Genetic Determinants of Protein Targeting from the Endoplasmic Reticulum to Lipid Droplets

HARVARD UNIVERSITY
Graduate School of Arts and Sciences

DISSERTATION ACCEPTANCE CERTIFICATE

The undersigned, appointed by the

Department of the Division of Medical Sciences

have examined a dissertation entitled

Genetic Determinants of Protein Targeting from the Endoplasmic Reticulum to Lipid Droplets

presented by Jiunn Song

candidate for the degree of Doctor of Philosophy and hereby certify that it is worthy of acceptance.

Signature _____

Typed name: Prof. Timothy Mitchison

Signature Anna Greka
Anna Greka (Aug 13, 2020 09:05 EDT)

Typed name: Prof. Anna Greka

Signature _____

Typed name: Prof. J.Wade Harper

Signature _____

Typed name: Prof. Michael Welte

Signature _____

Typed name: Prof.

Date: June 2, 2020

Genetic Determinants of Protein Targeting from the Endoplasmic Reticulum to Lipid Droplets

A dissertation presented

by

Jiunn Song

to

the Division of Medical Sciences

in partial fulfillment of the requirements

for the degree of

Doctor of Philosophy

in the subject of

Biological and Biomedical Sciences

Harvard University

Cambridge, Massachusetts

June 2020

Dissertation advisors: Robert V. Farese, Jr. and Tobias C. Walther Jiunn Song

Genetic Determinants of Protein Targeting from the Endoplasmic Reticulum to Lipid Droplets

Abstract

Lipid droplets (LDs) are cellular organelles specialized in storing triacylglycerol (TG). Aberrant LD accumulation is the basis of metabolic diseases like obesity and non-alcoholic fatty liver disease (NAFLD) and is associated with type 2 diabetes and cancer. Proteins on the LD surfaces facilitate organellar functions in energy homeostasis. For instance, glycero-3-phosphate acyltransferase 4 (GPAT4), which catalyzes the rate-limiting step of the TG synthesis pathway, targets from the endoplasmic reticulum (ER) to LDs and catalyzes TG synthesis on LDs. However, how proteins target LDs remains a fundamental unsolved problem in cell biology.

To investigate the mechanism of protein targeting from the ER to LDs, we performed a genome-scale RNAi imaging screen in *Drosophila* S2 R+ cells to identify genetic determinants of the targeting process, using GPAT4 as a model. We found that membrane fusion machinery—including Rab1 and its activating complex component (Trs20), a membrane tethering complex component (Rint1), and four SNAREs (Syx5, membrin, Bet1, and Ykt6)—is required for LD targeting of GPAT4 and other ER proteins but not of cytosolic proteins. Based on this finding, we propose a novel model of ER-to-LD protein targeting, in which the outer leaflet of the ER bilayer membrane is fused with the LD monolayer membrane by these components to establish membrane connections that mediate protein targeting. Electron microscopy of Rab1- or Syx5-depleted cells revealed ultrastructural changes consistent with this model. Finally, we provide evidence that there exist two types of ER-LD membrane connections, only one of which mediates GPAT4 targeting to LDs.

In the screen, knockdown of genes involved in phospholipid metabolism increased GPAT4 targeting to LDs. Knockdown of TMEM19, a previously uncharacterized gene associated with human cleft malformation, also increased GPAT4 targeting to LDs. We provide bioinformatic and experimental

evidence that TMEM19 is a novel enzyme involved in phospholipid metabolism and propose its catalytic activity.

My thesis leveraged the use of advanced microscopy and imaging analysis techniques to investigate a cellular protein trafficking process. Although more work is needed to elucidate the exact mechanisms, my findings open doors to understanding the fundamental cell biological process important for lipid homeostasis and human diseases.

Table of Contents

Acknowledgements

I would like to thank my PhD advisors, Professor Robert V. Farese, Jr. and Professor Tobias C. Walther, for taking me as their student. As one of the first students in their joint laboratory, I recognize the privilege of learning from two scientists who invest serious time and energy in establishing a research group with multifaceted expertise and in mentoring the next generation of scientists. I have been continuously inspired by their scientific rigor and enthusiasm about science, and I am glad to have found mentors whom I look up to as exemplary scientists. In addition, I owe them for their incredible patience and faith in me. You have been a constant source of encouragement and support, and your personal investment helped me get through this journey and become a better scientist and person.

I would also like to thank my dissertation advisory committee members, Professor Timothy Mitchison, Professor Norbert Perrimon, and Professor Adrian Salic, whose valuable feedback helped focus my research and make it most impactful. They, along with my advisors, helped me not lose sight of the big picture of my project and make the most out of my time in graduate school. I particularly want to thank Professor Timothy Mitchison who has taken a special interest in my career development and provided valuable counsel and perspective.

I extend my gratitude to my dissertation defense committee members, Professor Anna Greka, Professor Wade Harper, and Professor Michael Welte (University of Rochester), and Professor Timothy Mitchison.

I also thank the members of the Farese and Walther laboratory who institute a culture of collaborative learning. Not only were they instrumental in helping me acquire necessary skills to push my project forward, but they also helped me learn what it means to be a member of a community. I am happy to have worked with this multitalented group of individuals who provided me with feedback that challenged me to become a better scientist. I especially thank Jane Lee, our fearless lab manager, who has facilitated all my research with amazing organizational skills and care.

I am grateful for all my collaborators who inspire me with their knowledge as well as kindness. These include Dr. Stephanie E. Mohr and Rong Tao from the *Drosophila* RNAi Screening Center, HMS; Dr. Marcelo Cicconet from the Image and Data Analysis Center, HMS; Director Maria Ericsson at the

HMS Electron Microscopy Facility; and Dr. Zon Weng Lai from the Harvard Chan Advanced Multi-omics Platform. I especially thank Dr. Stephanie Mohr for supporting the design and the execution of my screening project with eagerness and unparalleled expertise in the field.

I would not have been able to get where I am without the support and encouragement of my programs, the Harvard/MIT MD-PhD Program and the Biological and Biomedical Sciences PhD Program. I especially thank Dr. Loren Walensky, Dr. Thomas Michel, and Amy Cohen from the MD-PhD program who work tirelessly to improve the MD-PhD student experience, advocate for students' needs, and provide guidance on almost everything one can imagine. I also thank Danny Gonzalez, Anne O'Shea, and Kate Hodgins from the PhD program for their personal and administrative support.

I gratefully acknowledge the funding received towards my dissertation: TL1-TR001101 training grant from the National Institute of Health and T32GM007753 from the National Institute of General Medical Sciences; the American Heart Association Predoctoral Fellowship; and the Aramont Fund for Emerging Science Research.

I also thank my previous research mentors. My undergraduate advisors at Cornell University, Professor Robin L. Davisson and Dr. Heinrich Lob, and my graduate school rotation advisors at HMS, Professor David E. Cohen and Professor Calum A. MacRae, have instilled in me a love for science and laid the groundwork for me to become a better scientist.

I am eternally grateful for my parents who have sacrificed so many things in their lives to allow me and my brothers to pursue our dreams. Your prayers have gotten me to where I am now. I also thank my brothers who are sources of constant support and amusement. Finally, I thank my grandparents in heaven who made me the person I am today.

I also thank my friends who stayed beside me and supported my journey near and far. All of you make me a better person, and your friendship and confidence in me have been indispensable to everything I do.

Lastly, I thank my God, Jesus Christ, Lord Almighty for giving me strength and resilience.

Contribution

Jiunn Song, Robert V. Farese Jr., and Tobias C. Walther conceived the projects and designed the experiments. Stephanie E. Mohr (*Drosophila* RNAi Screening Center, HMS) guided the screen design. Rong Tao (DRSC, HMS) prepared genome-scale dsRNA library. Marcelo Cicconet (Image and Data Analysis Core, HMS) and Jiunn Song designed the pipeline for screen image quantification, and Marcelo Cicconet trained the machine learning-based pipeline. Maria Ericsson, Louise Trakimas, and Anja Nordstrom (Electron Microscopy Facility, HMS) processed samples for electron microscopy and Jiunn Song imaged the samples. Zon Weng Lai performed mass spectrometry analysis. Flow Cytometry Core (Department of Immunology, HMS) performed cell sorting for cell line generation. Jiunn Song performed all other experiments and data analysis.

Chapter I. Introduction

Lipid droplets are cellular organelles important for physiology and disease

Lipid droplets (LDs) are cellular organelles found in nearly all eukaryotic cells across evolution[1–4]. They are specialized for storing neutral lipids including triacyclglycerols (TGs) and sterol esters (SEs) and have functions in cellular lipid homeostasis, protein degradation, transcription regulation, and viral replication. Originally thought of as inert depot for excess energy storage, LDs began to receive more attention in the past few decades as they became implicated in many disease pathologies. For instance, LD accumulation in hepatocytes and adipocytes is the hallmark of non-alcoholic fatty liver disease (NAFLD) and obesity respectively, both of which significantly increase the risks of cardiovascular diseases and type 2 diabetes[5–8]. NAFLD also predisposes individuals to developing non-alcoholic steatohepatitis (NASH) and liver cirrhosis, which can be fatal[9]. SE-rich LD accumulation in macrophages, called the foam cells, contributes to the formation of atherosclerotic plaque that narrows arteries[10]. LD accumulation is also associated with certain types of tumors such as breast cancer and prostate cancer[11] and correlates with aggressiveness in breast cancer cells[12] and drug resistance in laryngeal carcinoma cells[13]. In addition to diseases associated with increased LD accumulation, lack of LDs in adipocytes causes lipodystrophies[2]. Patients with lipodystrophies suffer from a variety of metabolic abnormalities including insulin resistance, hypertriglyceridemia, and metabolic syndrome[14]. Finally, LDs are also implicated in viral replication of RNA viruses, most notably hepatitis C virus (HCV) and dengue virus[15,16]. In the case of HCV, LDs allow for spatial separation between viral replication and coat assembly, such that RNA replicated in the replication complexes migrates to LDs where the capsid proteins are for assembly. Their extensive relevance to diseases makes LDs an attractive target for therapeutic development and highlights the importance of investigating cellular processes that govern LD biology.

Unique membrane structure of LDs

LDs are also fascinating organelles due to their unique structure (**Figure 1**). Unlike other organelles that are composed of an aqueous lumen and a surrounding phospholipid bilayer membrane, LDs are composed of a hydrophobic core of neutral lipids and a surrounding monolayer phospholipid

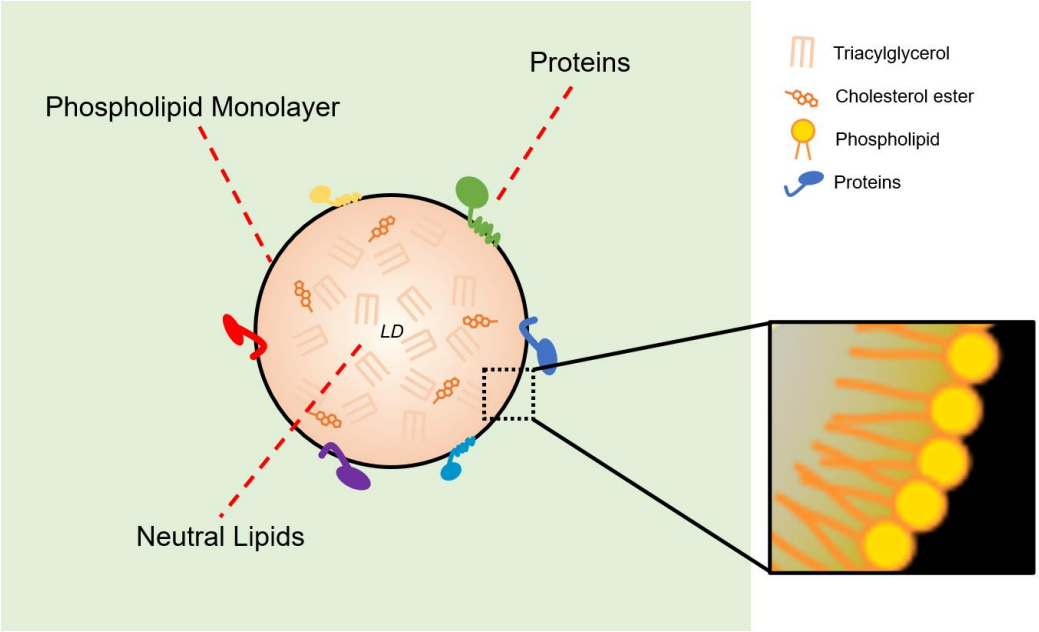

Figure 1. Structure of LDs
LDs are composed of a hydrophobic neutral lipid core and a surrounding phospholipid monolayer. In addition, hundreds of proteins reside on the surfaces of LDs.

membrane[17,18]. The monolayer membrane emulsifies neutral lipids in the aqueous environment of the cell: the hydrophobic acyl chains (or tails) of the phospholipids form hydrophobic interactions with neutral lipids, and the polar head groups form electrostatic interactions and hydrogen bonds with proteins on LD surfaces and water molecules in the cytosol. However, this emulsification is thought to be incomplete, resulting in a unique biophysical environment on LD surfaces[17]. Namely, the incomplete shielding of the neutral lipid core and acyl chains of phospholipids from the aqueous environment leads to prominent membrane packing defects on LD surfaces.

Interdigitation of neutral lipid molecules with membrane phospholipids is a unique factor that contributes to packing defect on LD surfaces[19–21]. Molecular dynamic simulations showed that neutral lipids between the bilayer membranes interdigitate between the phospholipid molecules and become exposed to the aqueous environment[19,21]. Although such interdigitation increased shallow lipid packing defects on LD surface, it seemed to modestly reduce deep packing defects. Surface packing defects as measured by the surface area per phospholipid molecule increased from 67Å^2 for bilayer membranes to 71Å^2 for monolayer membranes adjacent to neutral lipids[21].

The amount and type of phospholipids can modulate packing defects on LDs and other membranes. Increasing phospholipid amount relative to neutral lipids in the core results in a better emulsification and decreases packing defects, whereas deficiency in phospholipid due to limited synthesis or rapidly expanding neutral lipid core increases packing defects and surface tension[22]. Conical phospholipids with large polar heads compared to their tail, such as lysophosphatidylcholine (LPC) or lysophosphatidic acid (LPA), decrease packing defect, whereas phospholipids with comparatively smaller polar heads, such as phosphatidic acid (PA), phosphatidylethanolamine (PE), and cholesterol, increase packing defect, with cylindrical phospholipids including phosphatidylcholine (PC) and phosphatidylserine (PS) somewhere in-between[17,18,23]. In addition, saturation status of fatty acids affects packing defect such that decreased saturation increases the packing defect.

LDs are generated from the endoplasmic reticulum

LDs most likely originate from neutral lipid accumulation within the endoplasmic reticulum (ER) bilayer membrane (**Figure 2**) [24–27]. Both isoforms of enzymes that catalyze the final step of TG synthesis, diacylglycerol O-acyltransferase 1 (DGAT1) and DGAT2, reside in the ER membrane (first step in **Figure 2**)[28]. When TG is synthesized in the ER membrane and reaches a critical concentration, the oil is believed to phase-separate within the ER bilayer membrane and form a nucleation site ("oil lens"; second step in **Figure 2**) that eventually buds off towards the cytosol, taking the outer ER layer membrane as its monolayer membrane (third step)[29]. Molecular dynamics simulations showed that triolein molecules (TG with three oleic acid tails) spontaneously form aggregates of ~17nm diameter between the leaflets of phospholipid bilayer membranes and remain stable over a microsecond timescale, thereby supporting the potential existence of an "oil lens" intermediate in the ER bilayer as a precursor for LD[30]. Studies in cells also support the idea that LDs arise from the ER, as observed under confocal microscopy using various protein markers that recognize early LDs, including perilipins and acyl-CoA synthetase 3[24,31].

The precise mechanism behind LD biogenesis from the ER remains unknown. However, it is likely a highly regulated process involving many different proteins[25,29]. In addition to the enzymes required for activating fatty acids, such as long-chain acyl CoA synthetases (ACSLs), and for synthesizing TG,

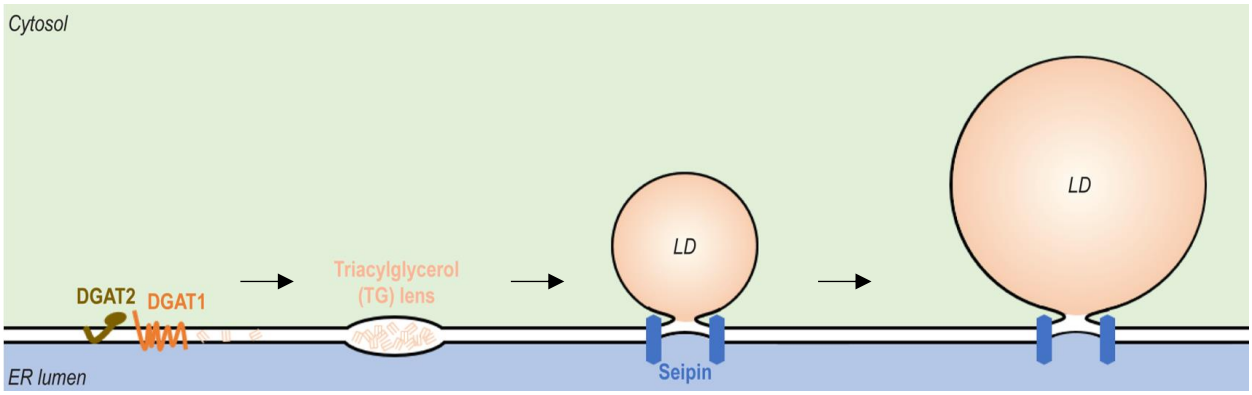

Figure 2. LD biogenesis from the ER
LDs are generated from neutral lipid accumulation between the two leaflets of the ER phospholipid membrane. DGAT1 and DGAT2 catalyze the synthesis of TG, which forms TG lens in the ER membrane. With the help of proteins like seipin, LDs bud towards the cytosol. LDs continue to grow and may remain connected to the ER via the membrane connections that are formed during the biogenesis and marked by seipin oligomeric complex.

such as DGAT1 and DGAT2, other proteins such as perilipins, seipin, and lipid droplet assembly factor 1 (LDAF1) have been implicated in LD biogenesis.

Perilipins (Plins) are best known for their roles in regulating lipolysis, a process by which TG is catabolized to release free fatty acids[32]. These 11-mer repeat amphipathic helix (AH)-containing proteins bind tightly to LD surfaces and block lipases from accessing the TG inside LDs[33]. Protein kinase A (PKA), upon activation downstream of a lipid catabolic signal such as β-adrenergic receptor activation, phosphorylates Plins and changes their conformation to allow for the access of hormone-sensitive lipase (HSL). There are five Plins (Plin1-5) in humans that are differentially expressed in various tissues. In particular, Plin3 (also called TIP47) and Plin4 are known to bind LDs early during their biogenesis[25,34]. It has been proposed that these early bindings allow for the generation of the curvature required for LDs to selectively bud towards the cytosol from the ER. In support of this idea, expression of Plin2 and Plin3 in cells containing elevated levels of neutral lipids in the ER bilayer induces LD formation[35]; depletion of Plin3 via small interference RNA (siRNA) suppresses LD formation in differentiated neutrophils[34]; Plin4 AH binds preferentially to TG over phospholipids *in vitro*[20]; and deletion of a distant yeast Plin Pet10p, which also binds LDs early, delays the appearance of small, nascent LDs from the ER upon LD induction with oleic acid (OA)[36]. Besides the 11-mer repeat AHs, Plins contain carboxy-terminal 4-helix bundles

which may be important in establishing the hierarchy of LD binding by different Plins[37]. However, it remains unknown how exactly different Plins contribute to LD biogenesis.

Seipin is another heavily studied protein with regards to LD biogenesis (see the third and the fourth step in **Figure 2**). Patients with Bernardinelli-Seip congenital lipodystrophy type 2 have mutations in the *BSCL2* locus that encodes seipin[38]. In addition to the lack of functional adipose tissues and ensuing metabolic abnormalities, these patients also suffer from mental retardation as well as upper and lower motor neuron disease symptoms[39–41]. Recent cryo-electron microscopy (cryo-EM) structural studies of human and *Drosophila* seipin suggest that seipin forms homo-oligomers (11-mer and 12-mer respectively) in the ER[42,43]. Altogether, this large, ~600kDa protein complex forms a ~150Å ring-like structure with 22~24 transmembrane domains and a pore of ~60Å. In cells, these oligomeric structures form puncta in the ER and potentially mark the sites of LD biogenesis, as BODIPY (neutral lipid dye that stains LDs)-positive spots arise from these puncta[44]. Without seipin, cells accumulate abnormally small LDs that likely coalesce over time due to abnormal phospholipid composition of the LD monolayer and increased packing defect[44].

The inner ring of the seipin oligomer that forms the pore is lined by ER luminal 11~12 hydrophobic α-helixes, one from each seipin monomer[42,43]. It has been proposed that this pore counteracts the ripening of LDs in the ER[45]. Ostwald ripening refers to the biophysical phenomenon by which smaller particles redeposit into larger particles in solutions with inhomogeneous particle sizes. In the context of LDs connected to the ER, ripening predicts that smaller LDs would transfer oil content to larger LDs due to the pressure difference among LDs (dictated by LD radius and surface tension). Indeed, TG embedded in giant unilamellar vesicles (GUVs), simulating LDs embedded in the ER *in vitro*, showed this predicted phenomenon as the smaller TG droplets disappeared and larger TG droplets appeared over time[45]. Importantly, incorporating the seipin oligomeric complex to the mix slowed down the ripening and stabilized smaller TG droplets. The potential role of seipin in stabilizing small LDs and counteracting ripening for equal partitioning of TG among growing LDs is consistent with observations in cells, since cells lacking seipin make heterogeneously sized LDs[44]. This interpretation makes two important assumptions: 1) the seipin ring allows for the transfer of TG from the ER lumen to LD core and 2) the LD core and ER lumen remain connected by seipin after biogenesis. The latter assumption is

supported by multiple observations: correlative light and electron microscopy (CLEM) shows seipin puncta at the junction of membrane continuity between the ER and budding LDs[45], and seipin puncta localize at ER-LD junctions in human cells[46] as well as in yeast where LDs are thought to stably associate with the ER over time after LD biogenesis[35,47]. Finally, seipin has been shown to bind anionic lipid species (particularly PA) *in vitro*[43], but whether seipin binds anionic lipids in cells or how such binding relates to the function of seipin needs to be further investigated.

A recent study from our laboratory identified an interactor of seipin that may be also important for LD biogenesis[48]. TMEM159, now re-named lipid droplet assembly factor 1 (LDAF1), was found to specifically interact with the hydrophobic α-helix that lines the inner pore of the seipin oligomeric ring. Like seipin, LDAF1 formed puncta in the ER that gave rise to LDs. Recruiting LDAF1 to the ER apposed to the plasma membrane using FKBP-FRB hetero-dimerizing system resulted in LD biogenesis in the ER next to the plasma membrane, indicating that LDAF1 can recruit machinery required for LD biogenesis including seipin. Intriguingly, purified LDAF1-seipin oligomeric complex contained TG, which suggests that the two proteins may mark the LD nucleation site in the ER. Current data support the idea that LDAF1 is a structural component of LD nucleation and may aid in the selective budding of LDs toward the cytosol instead of the ER lumen by sitting on the cytosolic leaflet of the ER bilayer and decreasing the packing defect of budding LDs, much like Plins. However, it is possible that LDAF1 has other functions in LD biogenesis. In addition, it remains to be studied whether there are other seipin-LDAF1 interactors that are involved in LD biogenesis.

There are still other proteins that have been implicated in LD biogenesis. Fat-inducible transcript 2 (FIT2) was originally identified as protein induced by a pharmacologic PPARα activation in mice[49]. Overexpressing FIT2 increased LD formation, whereas depleting FIT2 reduced LD accumulation in differentiated 3T3-L1 cells. Recently, our laboratory discovered that FIT2 catalyzes the hydrolysis of oleoyl-CoA to produce adenosine 3',5'-bisphosphate and oleoyl 4'-phosphopantetheine *in vitro* (Farese & Walther Laboratory, unpublished results). How this reaction relates to LD biogenesis remains unclear. Finally, yeast Pex30 and mammalian multiple C2 domain containing protein (MCTP2), both of which contain reticulon homology domain (RHD) that can generate curvatures in the ER membrane, have been

implicated in marking the sites of LD biogenesis in the ER[50,51]. Interestingly, data suggest that peroxisome biogenesis also shares the ER subdomains marked by Pex30 or MCTP2.

LDs remain connected to the ER upon biogenesis

Once LDs bud off from the ER (~100nm in diameter), they can grow, depending on the cell type, to >1μm and as large as 100μm in adipocytes[52]. Thin-section electron microscopy (EM) of various cell models and tissues shows continuity between the LD monolayer membrane and the outer leaflet of ER bilayer membrane on some LDs but not others[45,53,54], but given the limitations of 2D EM experiments, it is impossible to conclude whether some of the LDs are completely detached from the ER. Advancements in 3D electron microscopy techniques such as cryo-electron tomography (ET) and focused ion beam milling combined with scanning electron microscopy (FIB-SEM) allow for a better 3D resolution of the ER-LD membrane continuities[55], but no careful study has been performed across different cell types to answer this question. Still, recent studies suggest that upon biogenesis LDs may stay connected to the ER through their membranes. First, in yeast, it was found that Lro1, a diacylglycerol acyltransferase that catalyzes TG synthesis, moves freely between the ER membrane and LD surfaces, indicating that the two organelles are connected[47]. Second, in both yeast and mammalian cells, LD proteins artificially targeted to the ER lumen could still target LDs, indicating that LD surfaces are accessible to the ER luminal contents through the association between the two organelles[56]. Lastly, seipin puncta remain stably associated with LDs over many hours after LD biogenesis (see the fourth step in **Figure 2**)[57]. If this puncta indeed represent the oligomeric ring that mediates ER-LD membrane continuity as predicted by cryo-EM[42,43], then LDs must remain connected to the ER.

Membrane contact sites between the ER and LDs

Besides the membrane continuities between the ER and LDs, the two organelles are also associated by membrane contact sites. Membrane contact sites refer to the close apposition between organellar membranes that can span the distance of 10nm~80nm[58–60]. They have been implicated in a number of different functions, including transport of molecules (such as ions or lipids) between the organelles or recruitment of enzymes that act *in trans* from one organellar membrane to another[61]. In

particular, the ER has been shown to make extensive contact sites with many other cellular compartments, including mitochondria, plasma membrane, peroxisomes, and LDs.

To date, more than four pairs of ER-LD contact site proteins have been reported. In *C. elegans* lacking peroxisomal β-oxidation, fatty acid transport protein 1 (FATP1) and DGAT2 have been shown to reside in the ER and LD membranes respectively and associate with each other to facilitate TG synthesis and LD expansion[62]. In human cells, VPS13A and VPS13C have been shown to co-localize with VAPB in the ER via their FFAT motif and simultaneously associate with LDs via their C-terminal domain[63–65]. The crystal structure of the VPS13 N-terminal domain revealed a lipid binding pocket that binds glycerolipids and preferentially PC[64]. Furthermore, the domain was able to transfer PC between liposomes *in vitro*. Whether VPS13A/C mediate glycerolipid transfer between the ER and LD membranes still needs to be tested.

The NRZ (NAG-Rint1-Zw10) tethering complex and Rab18 have also been implicated in the formation of ER-LD membrane contact sites. NAG and Zw10 have been shown to interact with GTP-bound Rab18 and associate with LDs in a Rab18-dependent manner[66,67]. A SNARE protein classically associated with the NRZ complex, BNIP1, localized around LDs and recruited the ER around LDs when overexpressed together with Rab18 but not in the absence of NAG[67]. However, it remains unclear whether the endogenous complex localizes to the ER-LD interface and whether Rint1 is also involved in the contact site formation. In addition, the exact function of SNARE-NRZ-Rab18 complex at the ER-LD contact site is yet to be found, although depleting any of these complex components resulted in abnormally large LDs.

Yeast Mdm1, *Drosophila* Snazarus (Snz), and human sorting nexin protein 14 (Snx14), which are orthologs of each other, have been shown to mediate ER-LD contact sites[68–71]. These contact site proteins are unique in that they are proposed to bind more than two compartments simultaneously (ER, LD, and vacuole for Mdm1, and ER, LD, and plasma membrane for Snz) without binding partners. When overexpressed, Mdm1 in yeast localized at nuclear-ER-vacuole junction where starvation-induced LD biogenesis takes place[69]. The N-terminal integral membrane domain (IMD) region and PX-associated (PXA) domain of Mdm1 was sufficient to target ER and associate with LDs, whereas targeting these domains to the plasma membrane by fusing to plasma membrane-binding region of Ist2 resulted in LD

recruitment to the plasma membrane. In *Drosophila* fat bodies, Snz was found to associate with peripheral LDs (as opposed to medial LDs in terms of location) in the ER juxtaposed to the plasma membrane[70]. Finally, the amphipathic helix of the C-nexin domain of Snx14 was required for Snx14 association with LDs from the ER in U2OS cells, and overexpressing Snx14 increased LD association with the ER as observed under electron microscopy[71]. These sorting nexin orthologs seem to have a different function at their respective membrane contact sites in their respective model organisms. Mdm1 is proposed to bind fatty acids and recruit fatty acid-CoA ligase Faa1 to LD biogenesis sites in the ER[69]. Snz and Snx14 are shown to have genetic interactions with enzymes involved in TG metabolism, such as fatty acid desaturase (DESAT1) for Snz and DGAT2 for Snx14[70,71], but their exact role at the contact sites remain to be further elucidated.

LDs harbor proteins on their surfaces

Given the origination of LDs and the membrane continuities with the ER, LD membranes are thought to have similar composition to the cytoplasmic leaflet of the ER bilayer membrane[72]. Despite their close association, LDs maintain a distinct set of proteins from the ER[73–75]. This is partially due to the limitations imposed by the inherent physical properties of the organelle, namely the hydrophobic core that cannot accommodate aqueous moieties like proteins. This means that the LD lumen is considered protein-free, and no transmembrane proteins with luminal domains reside on LD membrane[53]. On the other hand, membrane-embedded proteins without luminal domains as well as peripheral membrane proteins can target LD membrane surfaces and are found to be crucial for LD functions including TG and sterol metabolism, phospholipid metabolism, protein degradation, glycosylation, and transcription[53,76].

LD surface proteins have been identified by a variety of methods. The most commonly used method is cellular fractionation, which leverages the fact that LDs have much lower density than all other cellular compartments. Proteins in the LD fraction can then be precipitated for identification by mass spectrometer. A major disadvantage of this method is that, like other cellular fractionations, the LD fraction is contaminated by other compartments, most commonly the ER. One way to increase the specificity of LD proteome from fractionations is to use protein correlation profiling, which relies on generating a migration pattern for a *bona fide* LD protein across a sucrose gradient and identifying

additional proteins with similar profiles. Such an experiment in *Drosophila* S2 cells has revealed proteins involved in TG and phospholipid metabolism, N-glycan biosynthesis, protein degradation, and ER organization[73]. In another study, the protein correlation profiling approach was used to track changes in organellar proteomes, including LD proteome, in mouse liver after normal chow diet or 3 or 10 weeks of high fat diet to mimic early and late stages of NAFLD[74]. The study revealed that the LD proteome dynamically changes over the progression of liver steatosis and sequesters many of the Golgi proteins, which may underlie the hepatic secretion defect observed in mice with NAFLD.

Recently, a proximity labeling technique has been applied to identify LD proteins. In this scheme, a proximity labeling enzyme is fused to a *bona fide* LD protein and the substrate for the biotinylating reaction is added so that LD proteins are labeled with biotin and thus can be isolated and identified[77,78]. A study using ascorbate peroxidase as the labeling enzyme (APEX2) and Plin2 or adipose triglyceride lipase (ATGL) as the *bona fide* LD proteins resulted in high-confidence LD proteomes that excluded common contaminating proteins[75]. However, this proteome may still include ER proteins that are in close proximity to LDs (such as those at the contact sites between the two organelles) and exclude proteins that are poorly labeled depending on whether the electron-rich residues are readily available for labeling. After identification of LD proteins, their localization is verified using immunofluorescence or other light microscopy techniques. Immuno-EM against endogenous proteins to locate them with relation to LD monolayer membranes remains the gold standard for confirming their LD localization.

Classes of LD proteins based on protein targeting

LD proteins have been classified into two categories based on their original, alternate localization in the absence of LDs (**Figure 3**)[53]. Class I LD proteins target LDs from the ER either during or after LD biogenesis (red in **Figure 3**). Enzymes that contribute to TG metabolism including ACSL3 and glycerol-3-phosphate acyltransferase 4 (GPAT4) belong to this class[24,54]. Class II LD proteins come from the cytosol (green), including perilipins that regulate TG hydrolysis and CTP:phosphocholine cytidylyltransferase 1 (CCT1) that catalyze the synthesis of CDP-choline in the PC synthesis (Kennedy) pathway[21,22,33].

How LD proteins selectively target to LD membranes merits further investigation. So far, evidence suggests that the packing defect characteristic of the LD monolayer surface is an important selective

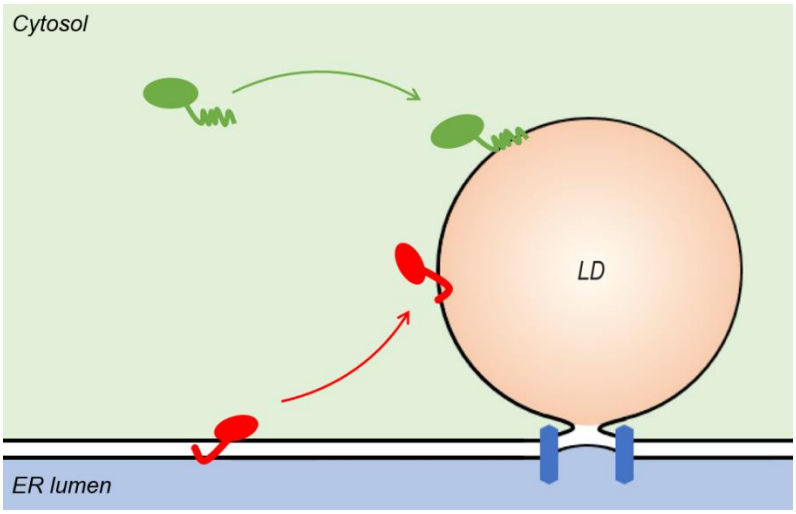

Figure 3. Protein targeting to LDs
LD proteins target from the ER membrane (Class I) or the cytosol (Class II). Many Class I proteins (red) contain hydrophobic hairpin-like domains that allow the proteins to insert into the membrane without containing luminal domains that would exclude them from targeting LD surfaces. Many Class II proteins (green) contain amphipathic helices that bind to LD monolayer surfaces. Blue, seipin oligomeric complex.

factor. Most class II LD proteins contain an amphipathic helix motif that is often necessary and sufficient to target LDs[21,79]. Molecular dynamics simulation of such an amphipathic helix from CCT1 binding to phospholipid monolayer covering neutral lipids showed that what is originally a disordered amphipathic helix folds into the secondary structure as it binds to the monolayer surface[21]. Notably, large hydrophobic residues of the amphipathic helix, such as phenylalanine, tyrosine, and tryptophan, were observed to insert into the packing defects of the phospholipid monolayer surface where the neutral lipid is exposed to the aqueous environment. Consistent with this observation, mutating large hydrophobic residues of amphipathic helices of class II LD proteins abrogated LD targeting. Interestingly, amphipathic helices of proteins that do not target LDs (such as the amphipathic lipid packing sensor (ALPS) motif of cis-Golgi protein GMAP210) also targeted LDs when expressed in isolation. In fact, it was also suggested that large hydrophobic residues of the ALPS motif, which is found in a variety of membrane binding proteins in bilayer membranes such as lipid transporters and nucleoporins, sense packing defects of curved membranes[80–82]. This indicates that packing defects of LD surfaces may not alone account for the specificity of protein binding on LD surfaces and that other mechanisms may prevent full-length proteins that contain amphipathic helices from promiscuously binding LDs.

CCT1 binding to LD packing defects is believed to play a homeostatic role on expanding LDs by catalyzing the rate-limiting step of the PC synthesis pathway that takes phosphocholine and CTP to create CDP-choline[22]. In *Drosophila* S2 cells, CCT1 shuttled between the nucleus and LD surfaces and bound LD surfaces when LDs were expanding after oleic acid treatment but not when LDs were shrinking

upon switching to lipid-free media. CCT1 depletion led to the coalescence of small LDs and the emergence of large LDs, which is consistent with relative phospholipid deficiency on LD surfaces. LD binding by CCT1 was associated with increased CCT1 activity in cells, and decreasing the PC:PE ratio in cell extract by supplying artificial droplets also increased CCT1 activity. This suggests that CCT1 binds to and is activated by PC-deficiency on LD surfaces and may help meet the increased need for PC synthesis on expanding LD membranes. Interestingly, CCTα, a CCT1 ortholog, was shown to bind LDs in murine macrophages[22] but not in differentiating 3T3-L1 adipocytes or human preadipocytes[83]. This inconsistency may reflect the difference in membrane compositions among various cell models, most notably the low PC to PE ratio in *Drosophila* S2 cells compared to mammalian systems, and the potential existence of alternative sensing mechanism for PC deficiency on expanding LD surfaces in adipocytes, since CCTα depletion still led to large LDs in these cells like in *Drosophila* S2 cells[22].

Class I LD proteins reside in the ER membrane but do not have an ER luminal domain that would exclude them from targeting LD membranes[53]. Some of these proteins such as ACSL3, methyltransferase-like protein 7A (Mettl7A; AAM-B), and Mettl7B (ALDI) contain an N-terminal hydrophobic domain that is predicted to mediate membrane insertion, with the remainder of the protein facing the cytosol[53,84,85]. Other proteins contain two predicted, consecutive transmembrane domains inside the protein with a proline kink in the middle, which would result in a V-shaped, hairpin-like topology that allows both the N- and C-termini of the protein to face cytosol (red in **Figure 3**)[54,84]. These include proteins such as GPAT4 and Ubxd8. Recent research from our laboratory suggests that the large hydrophobic residues, such as tryptophan, of the hairpin-like domain of GPAT4 are required for LD targeting (Farese & Walther Laboratory, unpublished results). As with amphipathic helices of class II LD proteins, these large hydrophobic residues have been predicted to insert and shield packing defects of LD surfaces under molecular dynamics simulation. *In vitro* reconstitution of membrane connections between monolayer and bilayer membranes in a microfluidics device using microsomes containing EGFP-GPAT4 and a neutral lipid stream showed that EGFP-GPAT4 preferentially accumulates on a monolayer membrane over a bilayer membrane[86]. This result predicts that if GPAT4 is allowed to move freely between the ER and LD membranes, it will accumulate on LD. It is currently under investigation whether this principle is generalizable to other class I LD proteins that also contain hairpin-like domains.

Another potential contributor to the accumulation of class I LD proteins on LDs over the ER membranes is selective degradation of LD proteins in the ER. In yeast, the class I LD protein phosphatidyl glycerol phospholipase C (Pgc1p) was found to be degraded by the Doa10 E3 ligase-dependent ER-associated protein degradation (ERAD) pathway[87]. Mutations in the ERAD pathway such as deleting *Doa10* increased Pgc1p amount in the absence or presence of LDs, and inducing LDs by oleic acid treatment or inhibiting lipolysis also increased Pgc1p, indicating that the ERAD pathway may preferentially degrade the ER pool over the LD pool of the protein. Interestingly, replacing the degron signal of Pgc1p, which overlaps with the hydrophobic ER and LD targeting motif, with the *Drosophila* GPAT4 hairpin domain recapitulated the ERAD-dependent degradation of wildtype Pgc1p[87]. However, it is difficult to conclude that preferential degradation of Pgc1p in the ER occurs, since *Doa10* deletion stabilized both the ER and LD pool of the protein, Pgc1p still preferentially accumulated on LDs under this condition, and it remains unclear whether the ER and LD pools of Pgc1p interchange with each other. In human cells, blocking ER-associated degradation pathway using a VCP inhibitor resulted in an accumulation of c18orf32 on LDs, highlighting the role of protein degradation in establishing LD proteome[75]

Finally, macromolecular crowding is an important selective factor for LD binding of both class I and class II proteins[88]. Shrinking the oil-water interface in a water-in-oil emulsion system (inverted emulsion droplets) revealed that lateral diffusion of LD proteins on the interface becomes limited as the surface area decreases, which is a hallmark of macromolecular crowding. Consistent with this idea, LD proteins such as fatty acid transport protein (FATP; class I) and CCT1 (class II) fell off LD surfaces during LD shrinkage, or lipolysis, in *Drosophila* S2 cells. Interestingly, some LD proteins fell off more prominently than the others during lipolysis, suggesting that proteins are differentially affected by shrinking LD surfaces[88]. Even when LD surfaces are not shrinking, overexpressing Lsd1, a perilipin ortholog in *Drosophila*, displaced LD proteins from the LD surfaces, indicating that proteins may compete for LD surfaces. Notably, LD proteins showed different amounts of displacement by Lsd1, which strongly correlated with the amount displaced during lipolysis. These findings suggest that LD proteins may compete for limited area on LD surfaces and strong binders may ‘crowd off’ weak binders. Indeed, there is additional evidence supporting the idea that competition among the AH regions of perilipins 1-3

determines their hierarchical binding to LDs in cells[37]. Thus, macromolecular crowding may be important for excluding certain weakly binding proteins from LD surfaces as well as regulating LD protein binding, for instance according to the metabolic state of the cells.

Trafficking of membrane-embedded proteins in cells

How class I LD proteins access LD surfaces remains largely unknown. In other parts of the cell, membrane-embedded proteins are transported in a number of ways. They can be imported into the membrane co-translationally or post-translationally through a translocation channel, as in the translocon of the ER membrane or the translocases of the inner and outer membrane complexes (TIM/TOM complexes) in the inner and outer mitochondrial membranes[89–92]. As the protein being imported goes through the channel in the bilayer membranes, hydrophobic domain of the protein exits to the side of the channel via lateral gate, thereby embedding into the hydrophobic phase of the membranes[89,93]. Alternatively, the hydrophobic domain of membrane-embedded proteins may be captured and inserted into the membrane, as is the case with tail-anchored proteins that become imported to the ER membrane by the GET (Golgi to ER Traffic) complex and with peroxisomal membrane proteins that get imported by various Pex complexes[94,95]. How proteins containing hairpin-like hydrophobic domains become inserted into the ER remains largely unstudied. One interesting report suggests that there may exist a specialized pathway by which these proteins become inserted into the ER. Ubxd8, a class I LD protein, was found to require Pex3 and Pex19 for post-translational insertion into the ER[96]. Pex19 bound to the hairpin-like domain of Ubxd8 in the cytosol, and incorporation of Ubxd8 into the ER required Pex3, a membrane-resident Pex19 receptor that also marks an ER subdomain. Importantly, sites of Ubxd8 insertion into the membrane co-localized with the ER subdomains marked by Pex3, but no direct insertion into the LD membrane was observed. Whether other class I LD proteins also require Pex3 or Pex19 for insertion into the ER has not been tested.

Once in bilayer membranes, membrane-embedded proteins may be transported to other bilayer compartments via vesicles[97–100]. For instance, ER membrane and luminal proteins that are to be transported to the Golgi are packaged in vesicles (30nm~100nm in diameter), which consist of a bilayer membrane and an aqueous lumen, by the COPII coat[101]. Vesicle formation starts with the activation of a

small GTPase on the cytosolic face of the bilayer compartment (e.g. Sar1 on the ER membrane or Arf1 in the Golgi) by its GDP-GTP exchange factor (GEF)[102]. Inner coat proteins such as Sec23/24 bind to the activated small GTPase and are thought to facilitate cargo selection by interacting with cargos or cargo receptors. The complex of the small GTPase, inner coat proteins, and the cargo-cargo receptors is termed the pre-budding complex. These pre-budding complexes are then polymerized by the outer coat proteins such as Sec13/31 to form a cuboctahedron structure, which deforms the ER membrane to generate the force required for the vesicle budding. COPII coat proteins surround vesicles that travel in an anterograde manner (from the ER to the Golgi), whereas COPI coat proteins surround vesicles that travel retrograde (from the Golgi to the ER)[103]. Importantly, vesicles contain proteins required for the next steps of vesicular trafficking, including a SNARE protein (vesicle or v-SNAREs).

After budding off from the original membrane, vesicles are transported towards the destination compartment by the motor proteins such as myosins, kinesins, or dyneins that walk along actin filaments or microtubules[104]. Once nearby, membrane tethering complexes tether the vesicles to the target membrane (**Figure 4**)[100,105]. Membrane tethering complexes are large protein complexes (such as the NRZ complex in the ER and TRAPP complexes in the Golgi) or coiled-coil proteins (such as giantin for the COPI vesicles, p115, and GM130, all of which are peripheral membrane proteins) that are thought to capture the vesicles by interacting with the proteins on the vesicles such as the coat proteins or small GTPases (step 1 in **Figure 4**), thereby anchoring the vesicle to the target membrane prior to membrane fusion (step 2 in **Figure 4**).

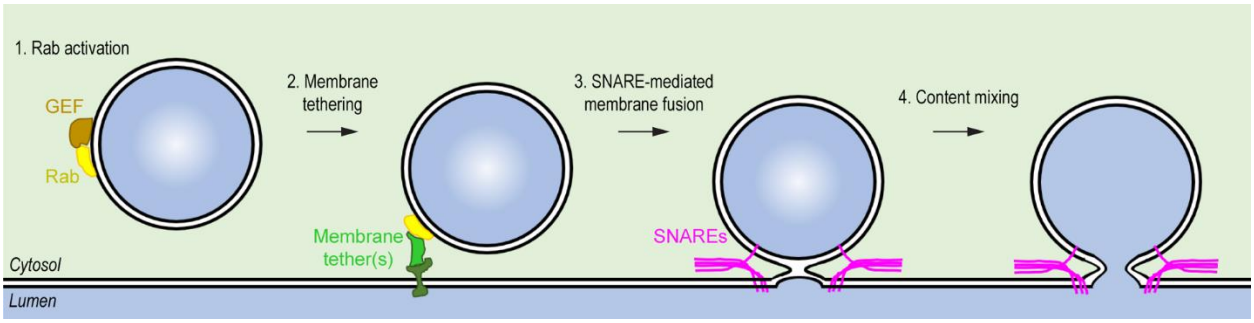

Figure 4. Steps of bilayer membrane fusion in vesicular trafficking
Typical bilayer membrane fusion in the context of vesicular trafficking in the secretory pathway involves (1) activation of a Rab protein by its GDP/GTP exchange factor (GEF), (2) membrane tethering by membrane tethers in the receiving membrane that interact with the activated Rab, (3) recruitment of SNAREs that fuse the two membranes together by intertwining tightly around each other (the intermediate hemi-fusion state is depicted above), and (4) complete fusion that allow for the content mixing. SNARE proteins are recycled by SNAP and NSF proteins for future fusion reactions.

In order for the vesicular bilayer membrane to fuse with the target bilayer membrane, it needs to be brought within few nanometers of distance. The force required for this reaction is generated by SNARE (SNAP receptors) proteins (step 3 in **Figure 4**)[106]. SNARE proteins contain helical domains that can interact with one another to form a four-helix bundle[107,108]. Based on structural homology, SNAREs are classified into four classes: Q_a, Q_b, Q_c, and R SNAREs in which Q and R denote the most critical residue in the helix that mediates bundle formation[106]. It is generally accepted that one of each four class of SNAREs is required for a productive fusion. Vesicles bring in one of the four SNAREs, most commonly an R SNARE, whereas the target membrane contains three SNAREs (target or t-SNAREs). *N*-ethylmaleimide-sensitive factor (NSF) is a AAA type ATPase that is thought to work with soluble NSF attachment proteins (SNAP) for disassembling the assembled four-helix SNARE bundle or SNAREpin[109,110]. In addition, there is evidence that NSF may also act in vesicle priming prior to the assembly of SNAREs[111]. Once the SNARE-mediated fusion is complete, contents of the vesicular membrane and lumen mix with the receiving membrane and lumen respectively (step 4 in **Figure 4**).

Each step of vesicular trafficking—budding, transport, membrane tethering, and SNARE-mediated fusion and recycling—likely contributes to selective cargo delivery. For instance, more than 60 SNAREs exist in mammals, and a specific combination of 4 SNAREs is thought to mediate selective fusion between a vesicle and a target membrane inside the cells[106,112,113]. Finally, a class of small GTPases called Rabs contributes to membrane identity and function in all steps of vesicular trafficking[114,115]. Like other small GTPases, Rabs, when activated by a GEF and bound to GTP, bind effector proteins. Rabs have been implicated in vesicle budding, uncoating, motility, tethering, and fusion. These diverse roles reflect the large number of Rabs (over 70 in humans) as well as the many effector proteins that can interact with each Rab for their function[97,115].

Currently, there is no evidence that class I LD proteins are directly imported to LDs by translocases or ‘insertases’ as neither of such machinery has been identified on LDs nor such phenomenon was observed on LDs. In addition, vesicular trafficking is unlikely since LDs have hydrophobic lumen and monolayer membrane whereas vesicles have aqueous lumen and bilayer membrane.

Membrane connections between the ER and LDs may mediate protein targeting

Alternatively, membrane-embedded proteins may directly diffuse from the ER to LDs given the membrane continuities between the two organelles (**Figure 5A**). In fact, a number of ER proteins have been shown to target LDs as LDs are being generated from the oil lens inside the ER bilayer membrane. These include ACSL3 and LDAF1, both of which are thought to be involved in LD biogenesis from the ER by generating substrate for TG synthesis and providing structural support for LD budding respectively[24,48]. On the other hand, GPAT4 has been shown to target LDs sometime after LD biogenesis[54]. In *Drosophila* S2 cells, endogenous GPAT4 as detected by immunofluorescence using an antibody against GPAT4 or transiently overexpressed, tagged GPAT4 localizes in the ER in the absence of LDs and targets LDs around 3 hours after oleic acid treatment for LD induction (as opposed to within minutes required for LD biogenesis). When overexpressed EGFP-GPAT4 on LDs were photobleached in a fluorescence recovery after photobleaching experiment (FRAP) experiment, projections from the surrounding ER were observed to mediate the fluorescence recovery on LDs, supporting the direct diffusion of the protein from the ER to LDs[54]. It remains to be tested whether these projections correspond to the ER-LD membrane continuities observed under electron microscopy (**Figure 5B**).

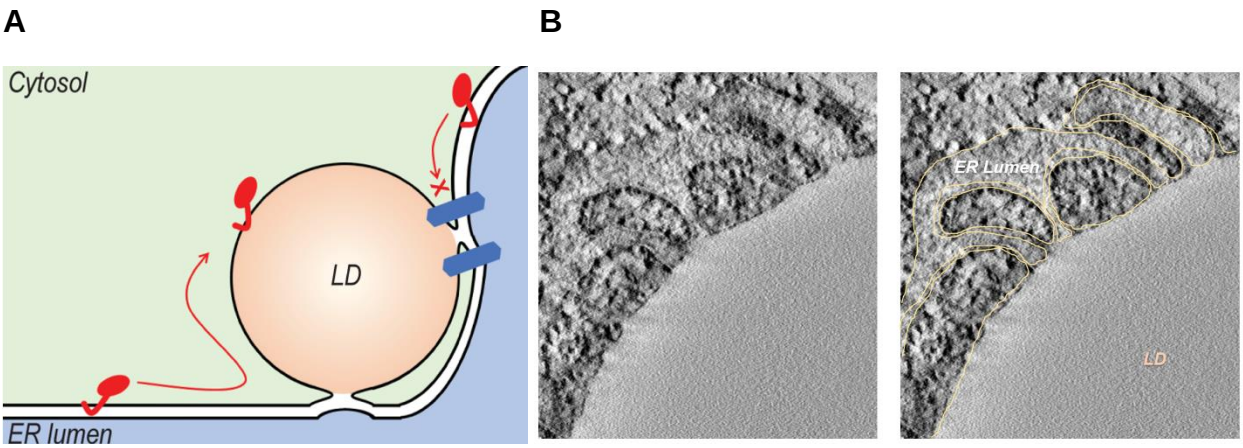

Figure 5. ER proteins target LDs via membrane connections between the two organelles
(A) ER proteins (red) may target LDs via membrane continuities between the outer leaflet of ER bilayer membrane and the LD monolayer membrane. There is evidence suggesting that seipin oligomeric complex (blue) acts as a diffusion barrier for protein targeting from the ER to LDs.
(B) ER-LD membrane connections under electron microscope. Electron microscopy revealed multiple membrane connections between the ER and LD membranes. See the right image for the annotations of ER and LD membranes (yellow)

The coordinated timing of GPAT4 targeting to LDs suggests that this protein targeting process may be regulated. It also warrants a question as to how GPAT4 does not target LDs during LD biogenesis in the ER when the ER and LD membranes are continuous, especially since the hydrophobic hairpin-like domain targets LDs within minutes after oleic acid treatment and has been in fact used as an early LD marker for this reason[44,54]. One possibility is that there is a lateral diffusion barrier between the ER and LDs during LD biogenesis that allows selective protein targeting. One such candidate is seipin oligomeric complex that localizes to the LD biogenesis sites in the ER and of which the large size may present a physical barrier to protein diffusion (blue in **Figure 5A**)[44,116]. Interestingly, depleting seipin resulted in early accumulation of GPAT4 and other ER proteins on LDs (minutes after oleic acid treatment)[44], which is consistent with the idea that GPAT4 is prevented from targeting LDs during LD biogenesis by the seipin complex.

Previous research from our laboratory suggests that new membrane continuities or 'bridges' between the ER and LDs may form sometime after LD biogenesis to mediate GPAT4 targeting[86]. A genome-scale imaging screen in *Drosophila* S2 cells revealed that Arf1/COPI machinery, which forms the coat complex for retrograde vesicular trafficking from the Golgi to the ER, are important determinants of LD number, size, and dispersion[117]. Wildtype *Drosophila* S2 cells form two populations of LDs upon oleic acid treatment distinguished by their sizes and GPAT4 targeting: one population of LDs that are small and do not obtain GPAT4 and the other that are large and obtain GPAT4[54]. When a component of the Arf1/COPI machinery is depleted by RNA interference, cells make uniformly sized LDs of which the diameters fall between the two populations in the wildtype cells[86]. Importantly, GPAT4 no longer targeted LDs upon Arf1/COPI component depletion, suggesting that Arf1/COPI machinery may be required for the formation of ER-LD membrane bridges that mediate protein targeting[86]. Inside cells, Arf1/COPI machinery was found to associate with LD surfaces in a punctate pattern, whereas purified Arf1/COPI components bound to and budded off 'nano-LDs' from purified LDs[118]. Together, these experiments indicate that Arf1/COPI machinery may act directly on LD surfaces.

Interestingly, RNAi against Arf1/COPI machinery increased phospholipid content of LDs (such as PC or PE) relative to TG amount, suggesting that Arf1/COPI may preferentially remove phospholipids over TG from LD surfaces[86]. We postulate that the removal of phospholipids from LD surfaces increases

packing defects and surface tension of LD surfaces such that LD surfaces are more likely to fuse with the nearby ER membranes. Consistent with this idea, knocking down CCT1 (which catalyzes the first step of PC synthesis on LDs) or providing cells with exogenous lipids or compounds that increase surface tension of membranes, such as cholesterol, stearylamine, or SR59230A, on LDs rescued the GPAT4 targeting defect from Arf1/COPI depletion. Conversely, providing cells with exogenous phospholipids prevented GPAT4 from targeting LDs.

Finally, other groups have found that Arf1/COPI is also required for ATGL targeting to LDs[119,120]. This could explain the intermediate size of LDs we observed in Arf1/COPI-depleted cells, as ATGL on LDs would decrease LD size and its absence increase LD size. One of these groups suggested a different model of protein targeting to LDs that involves Arf1/COPI machinery, in which small nascent LDs with ATGL arise from ER exit sites (ERES) and the ER-Golgi intermediate compartments (ERGIC) and fuse with mature LDs for protein delivery[120]. Currently, this model is supported by the observation of ERES and ERGIC markers (Sec23 and p58) near LDs, but neither the appearance of such small LDs nor the movement of ATGL from ERES or ERGIC to LDs has been observed. Given the diffuse localization of Arf1/COPI machinery in cells and its critical role in maintaining a functional Golgi apparatus, it is difficult to definitively rule out the potential indirect effect of Arf1/COPI depletion on GPAT4 targeting. If our model of Arf1/COPI modulating LD surface properties for ER-LD bridge formation is true, it remains to be investigated what upstream signal(s) initiate Arf1/COPI recruitment to LDs, whether LDs can fuse with all parts of the ER or only with specific subdomains of the ER), and whether other factors are involved in forming or maintaining the ER-LD membrane bridges.

Phospholipid composition of LD membranes affects protein targeting

Whereas Arf1/COPI machinery may modulate surface properties of LDs to facilitate GPAT4 targeting in a physiological state, non-physiological or pathological conditions have been associated with increased LD surface tension and thus increased GPAT4 targeting. For instance, depletion of CCT1 which catalyzes the rate-limiting step of PC synthesis on LDs increases GPAT4 targeting to LDs, even when Arf1/COPI machinery is not depleted[86]. Another example is seipin depletion, which causes Berardinelli-Seip lipodystrophy in humans[38] and is associated with various changes in cellular

phospholipid levels. RNAi against Seipin in *Drosophila* S2 cells increased GPAT4 targeting to LDs[44] and altered cargo delivery from the ER to LDs[57]. In both cases of CCT1 and seipin depletion, supersized LDs were observed, which are considered the products of LD coalescence. LD coalescence is another hallmark of increased surface tension and relative phospholipid deficiency on LDs. Consistent wit this idea, supplementing these cells with exogenous PC prevented the formation of supersized LDs[22,44].

The basis behind relative phospholipid deficiency in seipin-depleted cells is unknown. Interestingly, knocking out Seipin in yeast increased overall phosphatidic acid (PA), an important substrate for phospholipid synthesis, and particularly resulted in accumulation of PA in LD-forming subdomains in the ER as detected by PA-binding protein markers[121–123]. One potential explanation is that seipin depletion reduces phospholipid synthesis from PA at the ER-LD junctions. In support of this idea, depletion of CDP-diacylglycerol (DAG) synthase 1 (CDS1), which catalyzes the synthesis of CDP-DAG from CTP and PA for phospholipid synthesis, phenocopies the LD morphology of seipin depletion in yeast[124]. These findings highlight the importance of the phospholipid content of LD surfaces in modulating surface tension and LD protein targeting. However, it is currently unclear which of the two defects, phospholipid deficiency and abnormal protein targeting, comes first in these non-physiological conditions, especially since the seipin oligomeric complex may act a physical barrier for protein targeting to LDs during LD biogenesis in the ER, as discussed previously.

Enzymes target from the ER to LDs for their functions

Protein targeting from the ER to LDs is important for cellular TG homeostasis[54]. GPAT4 catalyzes the first and the rate-limiting step of the *de novo* TG synthesis pathway by transferring the acyl chain of acyl-CoA to glycerol-3-phosphate to produce lysophosphatidic acid (LPA) and CoA[125,126]. LPA is then converted to PA by 1-acylglycerol-3-phospohate-O-acyltransferases (AGPATs), then to diacylglycerol (DAG) by lipin phosphatases, and finally to TG by DGATs. Importantly, at least one isoenzyme for each step of the TG synthesis pathway, namely GPAT4, AGPAT3, and DGAT2, was found to localize around LDs in *Drosophila* S2 cells and mediate TG synthesis on LDs[54]. RNAi against of any of these enzymes resulted in small LDs that cannot expand, whereas the depletion of Arf1/COPI which leads to the failure of

GPAT4 and ATGL (enzymes that catalyze the rate-limiting steps of TG synthesis and hydrolyzing pathways respectively) altered LD phenotype[86,119,120].

GPAT activity is also important for phospholipid homeostasis because glycerolipids of the TG synthesis pathway can be used for phospholipid synthesis[127]. As mentioned previously, CDS combines PA and CTP to make CDP-DAG, which can be converted to phosphatidylserine (PS), a precursor to PC and PE, by phosphatidylserine synthase; to phosphatidylglycerol (PG), a precursor to cardiolipin, by phosphatidylglycerol synthase; and to phosphatidylinositol (PI) by phosphatidylinositol synthase. DAG can also be converted to PC and PE by choline/ethanolamine phosphotransferase (CEPT) in the CDP-choline pathway (also called the Kennedy pathway).

Research from our laboratory and others suggest that GPAT4-mediated phospholipid synthesis may be important for cellular lipotoxicity from saturated fatty acid[128,129]. Loss-of-function screens in cells using short hairpin RNA (shRNA) or CRISPR-Cas9 revealed that GPAT4 and its activator calcineurin B homologous protein 1 (CHP1) mediate palmitate-induced cell death. GPAT4 deletion reduced the accumulation of di-saturated PA and DAG and rescued palmitate-induced ER stress. Interestingly, DGAT1 depletion sensitized cells to palmitate-induced toxicity, which is consistent with the idea that sequestration of saturated fatty acids into neutral lipids like TG may protect cells from lipotoxicity[130]. So far, evidence suggests that GPAT4 targeting to LDs is important for TG expansion which correlates most with TG synthesis. However, it has not been investigated whether GPAT4 translocation to LDs preferentially enhances TG synthesis over phospholipid synthesis and whether the ER or LD pool of GPAT4 mediates palmitate-induced lipotoxicity in cells.

Further investigations revealed that in mammalian cells, both GPAT3 and GPAT4 target LDs from the ER[131]. There exist 4 different GPAT isoforms in mammalian cells: GPAT1 and GPAT2 in mitochondria and GPAT3 and GPAT4, which share significant sequence homology (>60%), in the ER and LDs[125,126]. Originally identified as AGPAT proteins based on sequence similarity, both GPAT3 and GPAT4 were later found to have GPAT activity[132,133]. Mouse knockout studies suggest that GPAT3 accounts for the majority of GPAT activity in adipose tissues and GPAT4 in the liver[134,135]. *GPAT3*$^{-/-}$ mice showed decreased adipose tissue mass, increased energy expenditure without altering food intake, and improved glucose tolerance when subjected to high fat diet (HFD)[134]. Interestingly, livers of *GPAT3*$^{-/-}$ mice were enlarged,

with increased levels of cholesterol and cholesterol esters but not TAG and elevated levels of markers for liver injury, AST and ALT. On the other hand, *GPAT4*$^{-/-}$ mice showed reduced hepatic and plasma TG levels but unaltered cholesterol content or inguinal adipose tissue mass under HFD[135]. Notably, these mice showed subdermal lipodystrophy. In addition, GPAT4$^{-/-}$ showed increased fatty acid oxidation in brown adipose tissue and reduced TG, suggesting a role of GPAT4 in TG storage in brown adipose tissue. Finally, insulin-mediated phosphorylation of GPAT3 and GPAT4 at Ser and Thr residues may be important for regulating their activities[136]. Altogether, these findings support the importance of GPAT3 and GPAT4 in tissue-specific TG synthesis and energy metabolism. However, it is currently unclear whether GPAT3 and GPAT4 target LDs in tissues and how their physiological functions relate to their potential localization on LDs.

Protein targeting from the ER to LDs is also implicated in disease. Genome-wide association studies (GWAS) have revealed the I148M variant in patatin-like phospholipase domain-containing protein 3 (PNPLA3) as a common, strong genetic risk factor for NAFLD[137,138]. *PNPLA3* encodes a paralog of PNPLA2 or ATGL that is proposed to target from the ER to LDs[119,120]. The PNPLA3 I148M mutant accumulates highly on LDs and has impaired TG hydrolase activity *in vitro*[139]. A lysine-less PNPLA3 mutant that is resistant to ubiquitin-mediated proteasomal degradation mimicked PNPLA3 I148M by accumulating on LDs and increasing hepatic TG in mice but without altering activity[140]. Conversely, reducing PNPLA3 I148M accumulation on hepatic LDs using genetic knockdown via shRNA or heterobifunctional proteolysis-targeting chimera (PROTAC3), which was used to recruit E3 ubiquitin ligase VHL to Halo-tagged PNPLA3 I148M, reduced hepatic TG accumulation. Altogether, these findings suggest that PNPLA3 I148M accumulation on LDs is the basis of hepatic LD accumulation[140]. Subsequent studies revealed that in mouse brown adipocytes and liver, PNPLA3 I148M competes with ATGL for its co-activator CGI-58 on LDs, thereby reducing the activity of the major TG hydrolase in cells and inducing TG accumulation[141].

Hydroxysteroid 17β dehydrogenase 13 (HSD17B13) is another protein that targets from the ER to LDs and is implicated in disease. A recent GWAS study revealed that a splice variant (rs72613567:TA) in *HSD17B13* reduces the risks for NASH and cirrhosis and reduced liver injury associated with PNPLA3 I148M mutant[142]. HSD17B enzymes have been primarily implicated in sex hormone metabolism[143].

However, substrate specificity of HSD17B13 is currently unknown. The *HSD17B13* rs72613567:TA variant results in a truncated protein with reduced enzymatic activity towards various steroid substrates and bioactive lipids *in vitro*[142]. In mice, deficiency of HSD17B13 alters hepatic lipid metabolism and induces liver inflammation in mice without affecting reproductive functions[144], indicating that the protein may be involved in metabolism of cholesterol and fatty acid instead of sex hormones[145]. It remains to be studied how the ER-to-LD targeting of HSD17B13 relates to its function and contribution to steatohepatitis.

Imaging screen as a tool to understand biology

Protein targeting from the ER to LDs is a fundamental process that affects lipid metabolism in physiology and disease. However, little is known about how the process occurs. Worse yet, we have no specific molecular handle of the process. Previous studies have utilized unbiased screening approaches to identify new molecular factors involved in protein transport and in LD biology[146–148]. For instance, a genome-wide RNA interference screen in *Drosophila* S2 cells using the secretion of horseradish peroxidase (HRP) into the surrounding media (as detected by chemiluminescence) as the readout revealed a class of proteins, now renamed transport and Golgi organization (TANGO) proteins, that are involved in protein transport from the ER to Golgi to plasma membrane[146]. Similarly, imaging screens using similar knockdown approaches but using LD morphology under confocal microscope as the readouts revealed new players in LD biology[117,119,149], namely CCT1 that catalyzes PC synthesis on LDs[22], Arf1/COPI that modulates LD surface tension for the formation of ER-LD membrane bridges[86], and MLX transcription factors of which LD binding modulates its transcriptional activity[149].

To understand how proteins target from the ER to LDs, I performed a genome-scale RNAi screen in *Drosophila* S2 R+ cells to identify genes required for GPAT4 targeting from the ER to LDs. This screening setup was chosen for many reasons. First, the process of GPAT4 targeting to LDs is most extensively studied in this system, including the observation of ER-LD connections that mediate protein targeting. Second, RNAi screens in *Drosophila* cells are efficient and easy to perform[150,151]. Unlike mammalian cells in which long double-stranded RNA (dsRNA) of ~500 base pairs leads to significant immune response and apoptosis, *Drosophila* cells manage to process the long dsRNA into many small

siRNA effectors that lead to efficient knockdown[152]. In addition, the genome of *Drosophila* is much less redundant than mammals, indicating that knockdown of a single gene leads to a clear phenotype[153]. Finally, a knockdown approach was chosen over a knockout approach (as in CRISPR-Cas9 screens) since a knockout screen may bias against essential genes that are also involved in ER-to-LD protein targeting, such as Arf1/COPI machinery that is required for cell survival and is implicated in priming LDs for establish ER-LD bridges. One major disadvantage of this method is the inability to perform a pooled screen which can drastically shorten the time for data collection and analysis. This problem was mitigated by using a state-of-the-art high throughput confocal microscope for imaging and a computing cluster to expedite imaging analysis.

Summary

In summary, LDs are cellular organelles important for TG homeostasis and implicated in a variety of metabolic diseases and cancer. The LD monolayer surface harbors many proteins that are important for TG homeostatic functions of the organelle and the development of metabolic diseases such as NAFLD and NASH. One such protein is GPAT4, an enzyme important for TG synthesis and LD expansion as well as for phospholipid synthesis and saturated fatty acid-induced lipotoxicity. How proteins like GPAT4 target from the ER to LDs remains a fundamental, unsolved problem. Current evidence suggests that GPAT4 targets from the ER to LDs via monolayer membrane connections or 'bridges' between the two organelles. Arf1/COPI machinery is thought to modulate LD surface tension to facilitate the formation of these bridges. However, we do not know how these bridges form, how the protein targeting is regulated, and what other factors are involved in the process. Answering these questions will be crucial for understanding how the LD proteome is dynamically controlled to facilitate LD function. Furthermore, elucidating the mechanisms behind the protein transport process will help understand the etiologies behind abnormal LD sizes in various metabolic diseases, including NAFLD and seipin lipodystrophy which have been associated with altered protein targeting to LDs.

Chapter II. Membrane Fusion Machinery Is Required for Protein Targeting from the ER to LDs

ER proteins target LDs early or late after LD induction

Previous studies identified proteins that target from the ER to LDs. To gain a systematic understanding of the targeting process, we overexpressed EGFP-fusion proteins in *Drosophila* S2 R+ cells and visualized their localization over time using confocal microscopy. Among the proteins that localized exclusively to the ER and LDs upon overexpression, EGFP-Ubxd8 and LDAH-EGFP targeted LDs as early as 30 minutes after LD induction using 1mM oleic acid (OA) treatment (**Figure 6A&C**). On the other hand, EGFP-GPAT4 and Ldsdh1-EGFP did not target LDs at the 30-minute timepoint but instead began to form the characteristic ring-shaped intensities around LDs starting 3 hours after LD induction (**Figure 6A&C**). HSD17B11-EGFP also began to target LDs starting 3 hours after LD induction, but only to a minor subset of LDs in contrast with other proteins that targeted to all LDs (**Figure 6A**). Before oleic acid treatment (0hr timepoint), most cells contained 0 to 2 LDs with HSD17B11-EGFP intensities (**Figure A1**) that were resistant to 1-day serum depletion. When treated with 1mM oleic acid, the number of cells with greater than 2 LDs with HSD17B11-EGFP intensities began to rise after 3 hours (**Figure 6C**).

Proteins that target LDs early (Ubxd8 and LDAH) may target during the LD biogenesis in the ER. Previous literature suggests that seipin, of which mutations or deficiency causes a severe congenital lipodystrophy in human, forms a homo-oligomeric complex at the junction of ER-LD connections during LD biogenesis in the ER and remain stably associated with the junction throughout LD maturation[45]. Importantly, it has been postulated that the ~600kDa seipin oligomeric complex may act as a diffusion barrier to prevent ER proteins from targeting LDs[57,116]. Consistent with this idea, GPAT4 targeting to LDs was enhanced in seipin-depleted cells[44].

To test the possibility that seipin acts as a selective barrier to protein targeting, we created Seipin KO *Drosophila* S2 R+ cells using CRISPR-Cas9 and tested the localization of EGFP-fusion proteins at different timepoints after OA treatment in these cells. Consistent with previous reports, seipin depletion

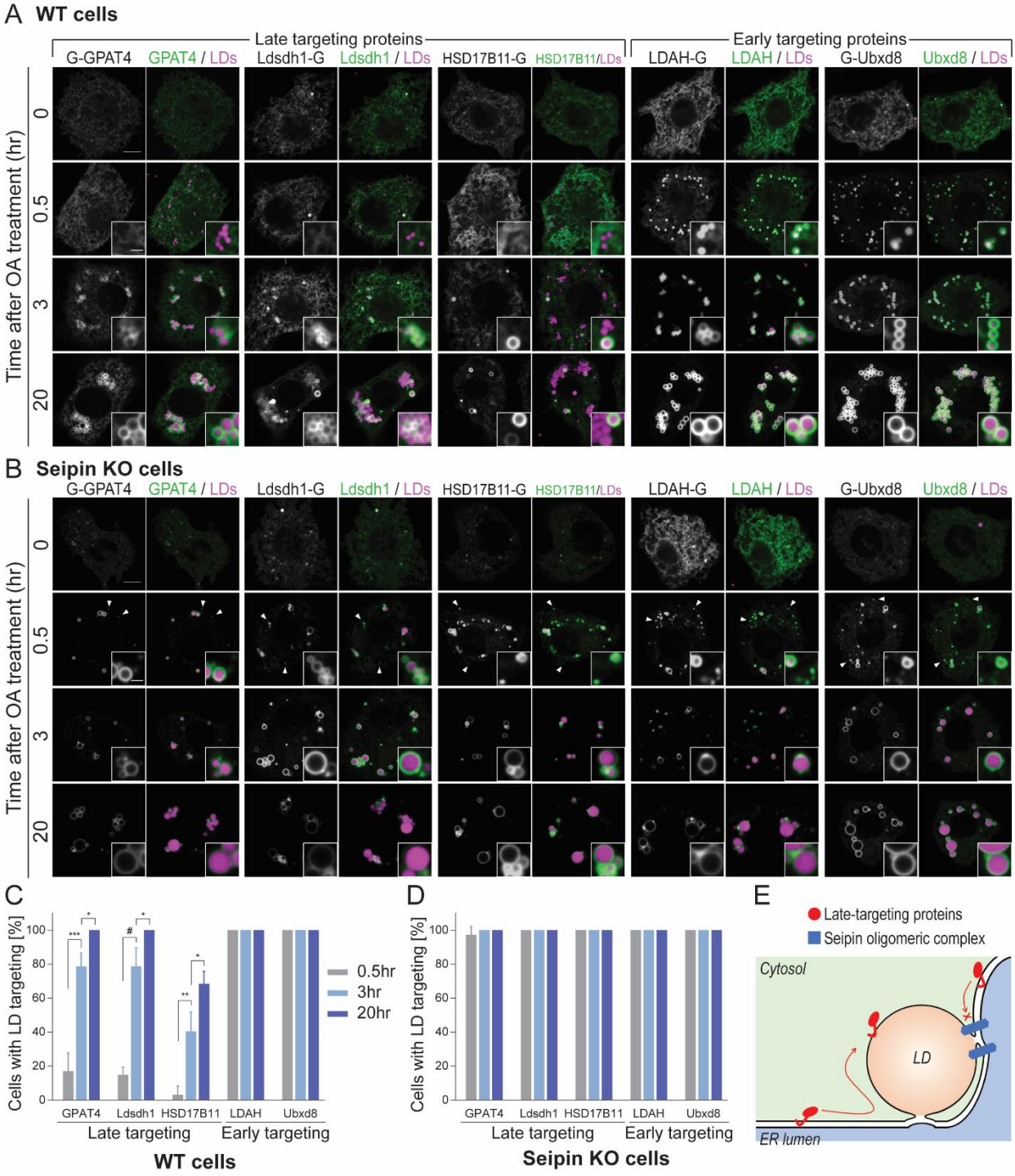

Figure 6. ER proteins target LDs early or late after LD induction

Figure 6 (continued). ER proteins target LDs early or late after LD induction
(A) Time course of localization of proteins that target from the ER to LDs upon LD induction. Wildtype *Drosophila* S2 R+ cells were transfected with EGFP-tagged constructs and treated with 1mM OA. LDs were stained with monodansylpentane (MDH). Representative images are shown. Scalebar, 5µm and 1µm (inlay)
(B) Time course of protein localization upon LD induction in Seipin KO cells. Arrowheads indicate MDH-negative EGFP construct puncta. Scale bar, 5µm and 1µm (inlay)
(C&D) Quantification of (A) and (B). Percentages of cells that show LD targeting of the transfected constructs at each timepoint were calculated. For HSD17B11, cells with LD targeting were defined as those that show protein targeting on >2 LDs in the imaging plane. Data are represented as mean + SD of the results from 3 independent experiments (8-13 cells each). One-way ANOVA for each construct with Bonferroni multiple comparisons correction, *p<0.05, **p<0.01, ***p<0.001, #p<0.0001.
(E) Diagram of a model of ER-LD bridges.

resulted in LD size heterogeneity and characteristic supersized LDs (**Figure 6B**). In contrast with the wildtype cells that showed a differential timing of LD targeting, all tested constructs including EGFP-GPAT4, Ldsdh1-EGFP, and HSD17B11-EGFP targeted LDs as early as 30 minutes after OA treatment in a remarkable consistency (**Figure 6B&D**). In addition, all tested constructs formed monodansylpentane (MDH)-negative puncta in the ER at this timepoint (arrowheads, **Figure 6B**), which resemble the early LD precursors that eventually give rise to LDs[44]. This indicates that in the absence of seipin, both early- and late-targeting ER proteins may target LDs during the LD biogenesis in the ER. Interestingly, HSD17B11-EGFP which targeted to only a subset of LDs in wildtype cells targeted all LDs in Seipin KO cells.

In summary, some ER proteins target LDs early during the LD biogenesis while other proteins are prevented by seipin from targeting LDs early. A previous study suggests that GPAT4 targets LDs via membrane connections or 'bridges' between the ER and LDs[54], analogous to the seipin-marked ER-LD connections that form during the LD biogenesis. Combined with the results of the current study, this supports the idea that alternative ER-LD membrane bridges unblocked by seipin oligomeric complex may form sometime after the LD biogenesis and mediate protein targeting (**Figure 6E**). However, how these bridges form have not been investigated.

Genome-scale imaging screen to identify genes required for GPAT4 targeting to LDs

To begin understanding how these ER-LD membrane bridges form and allow for late targeting of proteins like GPAT4, we performed a genome-scale imaging screen in *Drosophila* S2 R+ cells to identify genes required for GPAT4 targeting to LDs (**Figure 7A**). A cell line stably overexpressing EGFP-GPAT4-p2A-Puro^{R} was created in *Drosophila* S2 R+ cells and subjected to a genome-scale library of dsRNAs for RNAi in individual wells of imaging-compatible plates. At day 4 of RNAi, cells were treated with 1mM oleic acid to induce LDs. At day 5 of RNAi, cells were fixed, stained for nuclei with SiR-DNA and LDs with MDH, and imaged using an automated confocal microscopy system.

A custom image analysis pipeline was built to segment individual cells and regions of LDs within each cell based on the nuclear stain and the LD stain respectively (**Figure A2A-D**). A machine learning-based strategy was chosen over a simple thresholding method to improve the segmentation of the variable nuclei and LD stains induced by gene knockdowns, for instance RNAi of Arf79F or βCOP that

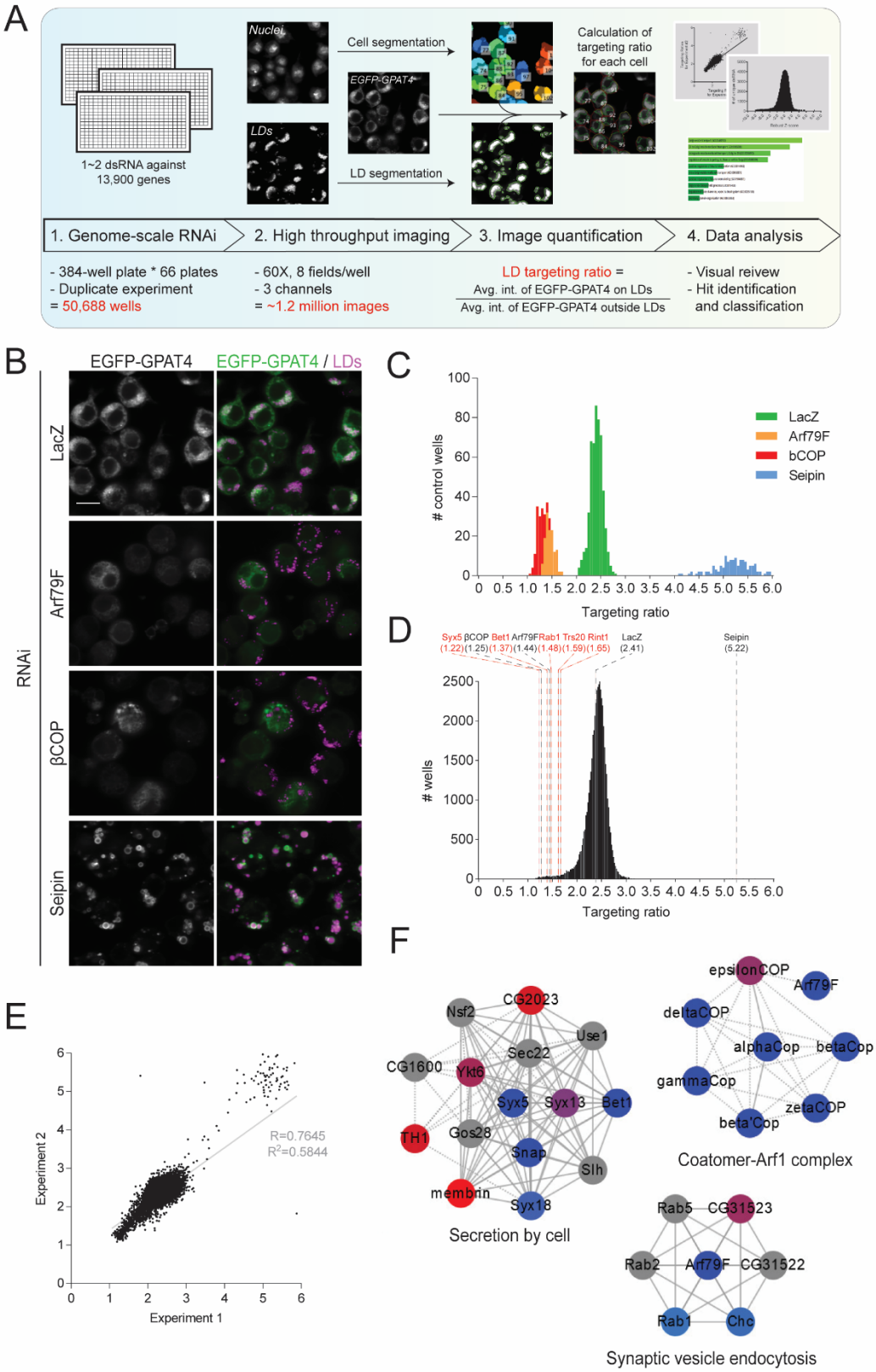

Figure 7. Genome-scale imaging screen to identify factors required for GPAT4 targeting from the ER to LDs

Figure 7 (continued). Genome-scale imaging screen to identify factors required for GPAT4 targeting from the ER to LDs
(A) Overview of screen design. *Drosophila* S2 R+ cells stably overexpressing EGFP-GPAT4 were subjected to a genome-scale library of dsRNA for RNAi. 20 hours after 1mM OA treatment, cells were fixed, stained for LDs and nuclei, and imaged using automated an confocal microscope. Using a machine learning-based analysis pipeline, cells and regions of LDs within each cell were segmented, and LD targeting ratios were calculated.
(B) Screen control images. Representative images for the screen negative control (RNAi against LacZ) and the positive controls (RNAi against Arf79F and βCOP which decrease GPAT4 targeting to LDs and RNAi against seipin which increases GPAT4 targeting) are shown. Scale bar, 10μm.
(C) LD targeting ratios for screen controls. Median LD targeting ratios for the screen control wells from all assay plates are shown. Total n = 528 for LacZ, n = 132 each for Arf79F, βCOP, and Seipin.
(D) Distribution of targeting ratios from all screen experiments. LD targeting ratios for screen controls (black) and select hits that reduce the targeting ratios (red) are highlighted. n =50,688.
(E) Scatter plot of LD targeting ratios from duplicate genome-scale screen experiments. A regression line, Pearson correlation coefficient (R), and the coefficient of determination (R^2) are shown. n = 25,344.
(F) Protein complexes enriched among screen hits. Screen hits with robust Z-score <-2.5 excluding ribosomal, proteasomal, and spliceosomal proteins were analyzed using the Protein Complex Enrichment Analysis Tool (COMPLEAT[154]). Complete list of results from the analysis is provided in **Online Supplementary Table 5** and additional visualization of complexes in **Figure A3D**. Node color: blue (smallest robust Z-score), red (highest robust Z-score), grey (non-hits; robust Z-score > 2.5). Line type: solid (known protein-protein interaction), dashed (known protein-protein interaction among orthologs in another species). p-values: coatomer-Arf1 complex (2.084e-20), secretion by cell (2.544e-05), synaptic vesicle endocytosis (5.788e-05).

induces variable shapes and intensities of nuclear staining (**Figure A2B&C**) and RNAi of seipin that leads to both tiny and super-sized LDs (**Figure A2D**). Training samples for the pipeline included annotated versions of these control images as well as other gene knockdowns known to affect LD size, such as DGAT2 RNAi. We performed two more rounds of iterative training with additional annotations using the failed segmentation results. Based on these segmentations, **LD targeting ratio**, defined as the ratio between the average intensity of EGFP-GPAT4 on LDs and the average intensity of EGFP-GPAT4 outside LDs, was calculated for each cell. After combining the data from 8 different fields of the same well, median LD targeting ratio among all segmented cells was determined as the final readout for the particular well with a unique dsRNA (**Figure A2E-H**).

The genome-scale screen was performed twice, which constituted a total of 132 384-well plates. Each plate contained 4 wells of dsRNA against LacZ as negative controls and 1 well each for dsRNA against Arf79F or βCOP as positive controls for genes of which knockdowns reduce GPAT4 targeting to LDs[86] and for dsRNA against Seipin as a positive control for genes of which knockdowns increase GPAT4 targeting to LDs[44]. Representative images for the control wells are shown in **Figure 7B** and the quantification results for the control wells from all plates are shown in **Figure 7C**. The screen workflow accurately captured the difference in the amount of GPAT4 targeting to LDs among the controls (median LD targeting ratios: LacZ = 2.410, Arf79F = 1.440, βCOP = 1.248, Seipin = 5.220). Importantly, the median LD targeting ratios from the negative control (range: LacZ = [2.034, 2.794]) and the two groups of positive controls (Arf79F = [1.282, 1.691], βCOP = [1.067, 1.474]; Seipin = [4.089, 5.967]) did not overlap, indicating that the working range of the readout from the screen is sufficiently wide.

LD targeting ratios from the screen formed a bell-shaped curve with a median value of 2.417, which juxtaposes very closely with the median LD targeting ratio of the screen negative control (LacZ = 2.410) (**Figure 7D**). The results from the duplicate experiments were well correlated (**Figure 7E**, slope = 0.7158, R = 0.7645), especially in either extremes outside the range of LacZ controls (**Figure A3A**, slope = 0.9435, R = 0.9242). Poor correlations among the LD targeting ratios of the screen controls from the same plate (**Figure A3B**, R values: Arf79F vs. βCOP = 0.09633, Arf79F vs. Seipin = 0.03938, βCOP vs. Seipin = 0.07207) suggested that there is no predictable variability across 132 plates. Therefore, LD targeting ratios and other quantification results from all screen plates were combined.

Robust Z-scores for the LD targeting ratios were calculated (**Figure A3C**, median absolute deviation = 0.1139). Initial analysis of the screen hits, defined as robust Z-score ≤ -2.5 (equivalent to LD targeting ratio ≤ 1.9950), revealed the enrichment of genes encoding ribosomal (Flybase gene group 0000130), proteasomal (FBgg000020), and spliceosome genes (FBgg0000519). These genes are commonly found false positives in the genome-scale screens and likely represent indirect effects on GPAT4 targeting to LDs. After excluding these genes, 896 genes (out of ~3,900 genes tested) were found to be required for GPAT4 targeting to LDs (**Online Supplementary Table 1**). A subsequent gene ontology analysis excluding those whose median LD area is 0 using GOrilla[155] showed a significant enrichment of genes involved in membrane trafficking (**Online Supplementary Table 2**). On the other side of the spectrum in which knockdowns significantly increase GPAT4 targeting to LDs (defined as robust Z-score ≥ 2.5 or targeting ratio ≥ 2.8398, n = 214 out of 13,900 genes tested; **Online Supplementary Table 3**), the gene ontology analysis was not informative (**Online Supplementary Table 4**). However, a simple inspection revealed a number of genes involved in phospholipid metabolism among the hits that increase GPAT4 targeting to LDs, including CCT1, CdsA, wun (PLPP1 ortholog), Desat1, ATP citrate lyase, and CTP synthase. These hits will be discussed more in detail in **Chapter III**.

Genes that resulted in robust Z-score <-2.5 were further analyzed using the Protein Complex Enrichment Analysis Tool (COMPLEAT[154]; **Online Supplementary Table 5**). As expected, components comprising the COPI and COPII coatomer complexes were found to be significantly enriched among the hits (the 'Coatomer-Arf1 complex' in **Figure 7F** and the 'COPII complex' in **Figure A3D**). In addition, complexes of small GTPases ('Synaptic vesicle endocytosis'), membrane tethers (the 'Dsl1p complex' which is an yeast ortholog of the NRZ complex and the 'Cog2-Cog3-Cog4 subcomplex'), and SNAREs that fuse membranes ('Secretion by cell') were highly enriched among screen hits. Some of these hits are highlighted in the overall distribution of targeting ratios (**Figure 7**) and robust Z-scores (**Figure A3C**).

A complete list of gene names and IDs, LD targeting ratios, robust-Z scores, and the segmentation results (absolute LD area (**Figure A3E**), relative LD area (**Figure A3F**; ratio of LD area to cell area), and total cell count) are provided in the **Online Supplementary Table 6**. Raw images from the screen will become available at lipidportal.org in the future.

Rab1 is required for GPAT4 targeting from the ER to LDs.

Membrane fusion involves (1) an activation of small Rab GTPase on the donor membrane, (2) a tethering between the donor and target membranes, and (3) a SNARE-mediated membrane fusion[97–100]. To determine if the genes involved in each step of membrane fusion are also required for GPAT4 targeting to LDs, we systematically analyzed and verified the screen results for the three categories of genes: (1) Rab GTPases (**Figure 8**), (2) membrane tethering proteins or complexes (**Figure 9**), and (3) SNAREs (**Figure 10**).

RNAi against Rab1, but no other Rabs, significantly reduced GPAT4 targeting to LDs in the genome-scale screen (**Figure 8A**). Many Rabs have been found to associate with LD membranes, some of which have reported functions on LDs[156]. Although Rab1 is found abundantly in many LD proteomes, its function on LDs remains unknown[73,75]. To further verify the screen results, we tested additional dsRNAs against Rab1 and other Rabs with reported functions on LDs (Rab7, Rab8, Rab18, Rab32, and Rab40)[156]. To increase the sensitivity of the readout in GPAT4 targeting, we used CRISPR-Cas9 to knock in EGFP sequence in front of the endogenous *GPAT4* loci (EGFP-GPAT4^{KI} cells) and tracked the localization of EGFP-GPAT4 using a spinning disk confocal microscope. In accordance with the screen results, only Rab1 was required for GPAT4 targeting to LDs in these cells (**Figure 8B&C**). In contrast with the LacZ control, no ring-shaped intensities of EGFP-GPAT4 was observed around LDs upon Rab1 RNAi (**Figure 8B**). Rab1 RNAi significantly reduced LD targeting ratios compared to LacZ control, whereas RNAi against other Rabs did not alter LD targeting ratios (**Figure 8C**). EGFP-GPAT4 signal in the ER upon Rab1 RNAi remained visually comparable to other conditions. In addition, the overall GPAT4 amount in the cells and the membrane fraction remained similar to the control (see **Figure 12**). When the intensity threshold was adjusted to a lower maximum to enhance contrast (**Figure 8B**; high contrast), the reticular pattern indicative of ER signal (see **Figure A8** for example) was observed around LDs, suggesting that GPAT4 is confined in the ER upon Rab1 depletion. Of note, Rab18, which has been implicated in tethering the ER and LD membranes[66,67], was not required for GPAT4 targeting to LDs.

RNAi using dsRNA against 5'UTR of Rab1 resulted in the same defect in GPAT4 targeting when soluble Halo was overexpressed, whereas the defect was reversed when Halo-Rab1 was overexpressed (**Figure 8D&F**). Importantly, Halo-Rab1 formed ring-shaped intensity around LDs, indicating the

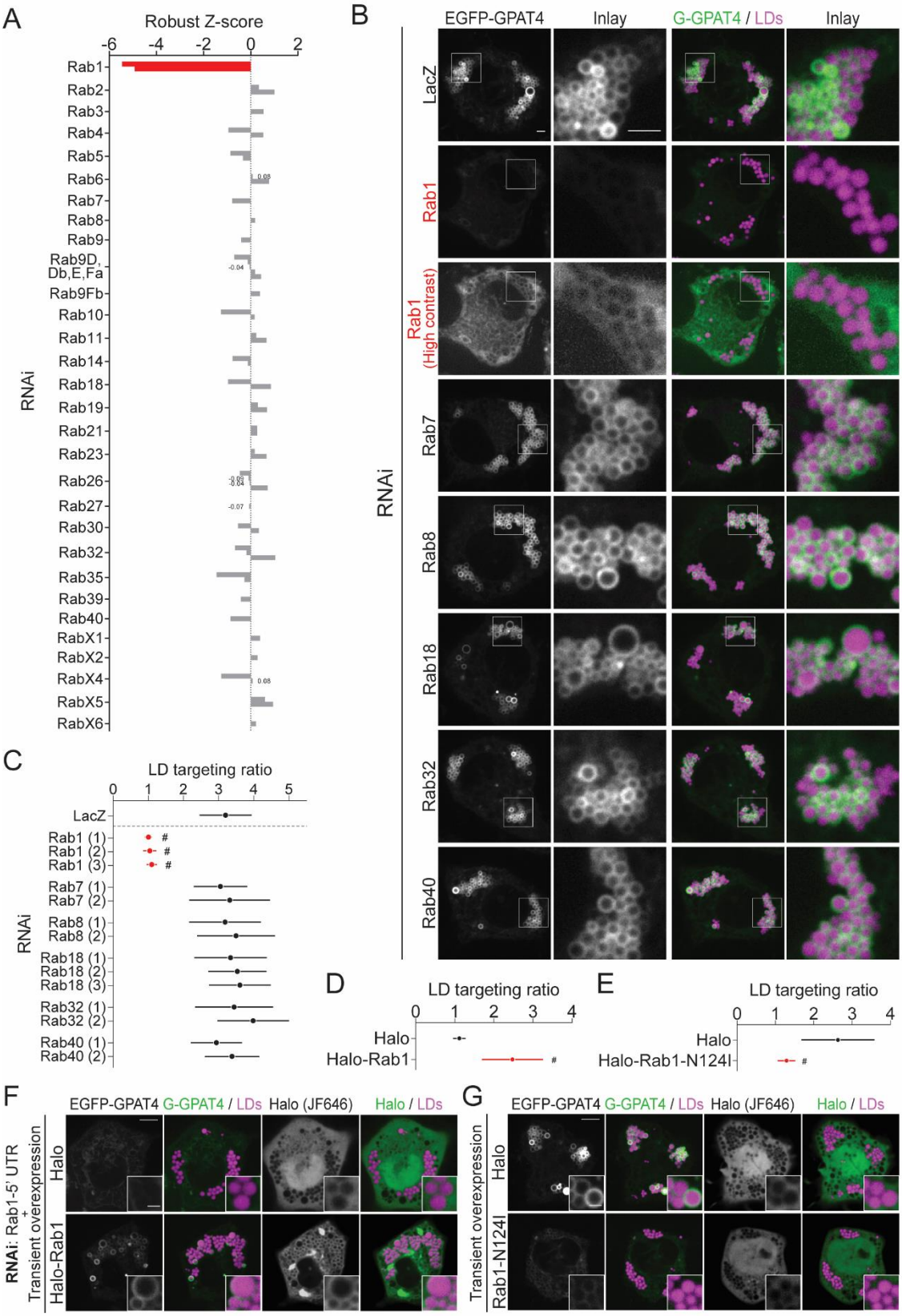

Figure 8. Rab1 is required for GPAT4 targeting from the ER to LDs

Figure 8 (continued). Rab1 is required for GPAT4 targeting from the ER to LDs
(A) Robust Z-scores for LD targeting ratios for all known Rabs. Each bar represents the mean of two robust Z-scores from the duplicate screen experiments. Different bars indicate unique dsRNA designs. Robust Z-score < -2.5 is highlighted in red.
(B) Screen result verification using EGFP-GPAT4^{KI} cells. Cells were subjected to 2-3 dsRNA's against select Rabs, treated with 1mM OA for 20 hours, stained with MDH, and imaged using a spinning-disk confocal microscope. Representative images for dsRNA that shows the largest effect on LD targeting are shown. High contrast images (same intensity minimum with lower intensity maximum) are provided for RNAi that show little GPAT4 intensity around LDs (red). Scale bar, 2μm and 2μm (inlay).
(C) Quantification of (B). LD targeting ratios were calculated from the confocal images. Number in () indicates a unique dsRNA design. Data are represented as mean ± SD of the results from 2-4 independent experiments (9-12 cells each). One-way ANOVA with Bonferroni multiple comparisons correction, #p<0.0001 compared to LacZ.
(D&F) Defect in GPAT4 targeting from Rab1 depletion is rescued by wildtype Rab1. EGFP-GPAT4^{KI} cells were subjected to dsRNA against the 5'UTR of Rab1 transcript, transfected with a plasmid encoding soluble Halo or Halo-Rab1, and incubated with Halo ligand JF646 and MDH for imaging. Representative images are shown in (F). Halo-Rab1 forms ring-like intensities around LDs. Scale bar, 5μm and 1μm (inlay). Quantification in (D) is represented as mean ± SD of the results from 3 independent experiments (16-18 cells each). t-test, #p<0.0001.
(E&G) Overexpression of Rab1-N124I mutant decreases GPAT4 targeting to LDs. EGFP-GPAT4^{KI} cells were transfected with a plasmid encoding soluble Halo or Halo-Rab1-N124I and incubated with Halo ligand JF646 and MDH for imaging. Representative images are shown in (F). Scale bar, 5μm and 1μm (inlay). Quantification in (G) is represented as mean ± SD of the results from 3 independent experiments (15-20 cells each). *t*-test, #p<0.0001.

localization of Rab1 on LDs (**Figure 8C**; inlay). Finally, transiently overexpressing Rab1-N124I mutant which tightly binds to and sequesters its endogenous GEF complex reduced GPAT4 targeting to LDs, suggesting that the mutant acts as a dominant negative to endogenous Rab1 (**Figure 8E&G**).

Rint1 localizes around LDs and is required for GPAT4 targeting to LDs

Membrane tethers reside in the target membrane and capture the donor membrane, often by binding to a small Rab GTPase on the donor membrane[100,105]. Membrane tethers can be classified into membrane tethering complexes or long coiled-coil proteins. In the imaging screen, none of the known long coiled-coil proteins in *Drosophila* was required for GPAT4 targeting to LDs (**Figure 9A**). Among the different membrane tethering complexes, RNAi against the components of the NRZ/RZZ complexes, the TRAPP complexes, and the COG complexes reduced GPAT4 targeting to LDs, but not the VPS-C (HOPS and CORVET), GARP, or Exocyst complexes (**Figure 9A**).

We used EGFP-GPAT4^{KI} cells and additional dsRNA designs to verify the screen results (**Figure 9B&C** and **Figure A4**). RNAi against the TRAPP complex component Trs20 (mammalian ortholog TRAPPC2) significantly reduced GPAT4 targeting to LDs in both the screen and the verification experiments. TRAPP complexes are unique in that they can act as either a GEF or a membrane tethering complex for Rab1[157–159]. Since Rab1 was required for GPAT4 targeting to LDs and the Rab1-N124I mutant acted as a dominant negative despite its ability to bind to TRAPP complexes (**Figure 8**), we postulate that the TRAPP complex act as a GEF rather than a membrane tethering complex in this process. Like Rab1 RNAi, RNAi of Trs20 resulted in a significantly reduced LD targeting ratio close to 1 and the absence of the ring-like intensities of EGFP-GPAT4 around LDs (**Figure 9B&C**) without reducing the GPAT4 amount in the cells and the membrane fraction (see **Figure 12**). High contrast images show that EGFP-GPAT4 is likely confined in the ER upon Trs20 knockdown. Interestingly, RNAi of the TRAPP complex components other than Trs20 and brun (yeast ortholog Trs120/mammalian ortholog TRAPPC9) did not significantly reduce LD targeting ratio. The extent of the reduction from RNAi of brun was small both qualitatively and quantitively, indicating that Trs20 may be the limiting component for the endogenous TRAPP complexes.

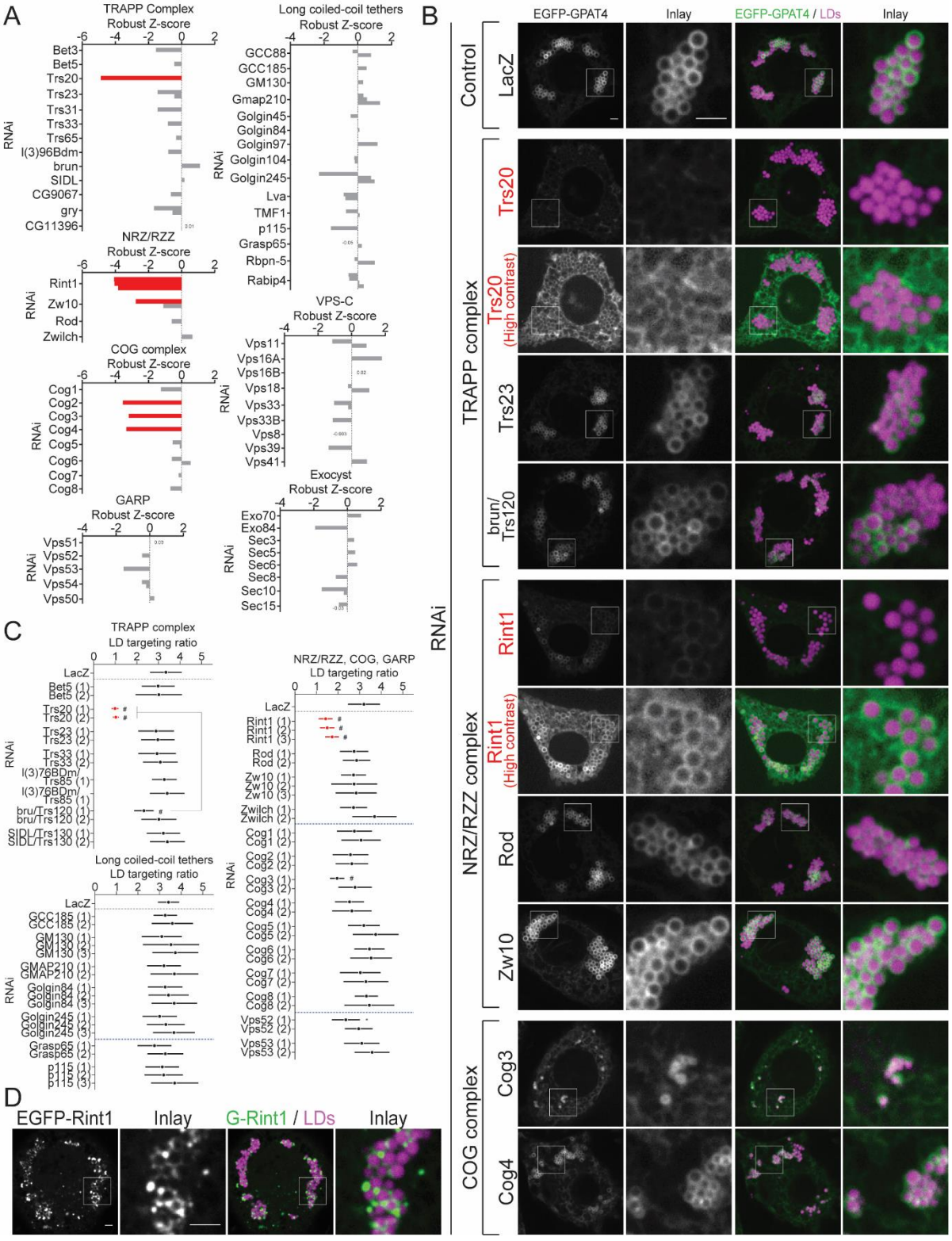

Figure 9. Membrane tether component Rint1 localizes around LDs and is required for GPAT4 targeting to LDs

Figure 9 (continued). Membrane tether component Rint1 localizes around LDs and is required for GPAT4 targeting to LDs

(A) Robust Z-scores for LD targeting ratios for all known membrane tethering complexes and long coiled-coil tethers. Each bar represents the mean of two robust Z-scores from the duplicate screen experiments. Different bars indicate unique dsRNA. Robust Z-score < -2.5 is highlighted in red.

(B) Screen result verification using EGFP-GPAT4^{KI} cells. Cells were subjected to 2-3 dsRNA's against select membrane tethering complex components, treated with 1mM OA for 20 hours, stained with MDH, and imaged using a spinning-disk confocal microscope. Representative images for dsRNA that shows the largest effect on LD targeting are shown. High contrast images (same intensity minimum with lower intensity maximum) are provided for RNAi that show little GPAT4 intensity around LDs (red). Images for additional targets in **Figure A4**. Scale bar, 2μm and 2μm (inlay).

(C) Quantification of (B). LD targeting ratios were calculated from the confocal images. Number in () indicates a unique dsRNA design. Data are represented as mean ± SD of the results from 2-4 independent experiments (8-16 cells each). RNAi that shows the largest effects is highlighted in red. One-way ANOVA with Bonferroni multiple comparisons correction, *p<0.05, #p<0.0001 compared to LacZ unless indicated otherwise.

(D) Localization of Rint1. Wildtype *Drosophila* S2 R+ cells were transfected with a plasmid encoding EGFP-Rint1, treated with 1mM OA, and stained with MDH for imaging. Representative images from 3 independent experiments (8-10 cells each) are shown. Scale bar, 2μm and 2μm (inlay).

RNAi of Rint1 significantly reduced GPAT4 targeting to LDs in both the screen and the verification experiments (**Figure 9A-C**). Compared to the Rab1 and Trs20 knockdowns which eliminated the ring-like GPAT4 intensities around LDs, endogenous EGFP-GPAT4 intensities were visible around LDs upon the Rint1 knockdown, albeit only to a modest level similar to the surrounding ER (**Figure 9B**). Rint1 interacts with NAG and Zw10 to form the NRZ complex in humans (orthologs of Tip20p, Dsl1p, and Sec39p that form Dsl1 complex in yeast)[160]. In *Drosophila*, however, no known NAG ortholog has been identified. Although RNAi of Zw10 using one but not the other dsRNA significantly reduced GPAT4 targeting to LD in the screen, none of the three dsRNAs against Zw10 in the verification experiments using EGFP-GPAT4^{KI} cells reduced GPAT4 targeting to LDs (**Figure 9C**). In addition, RNAi of Rod and Zwilch, which can bind with Zw10 to form another membrane tethering complex (the RZZ complex)[161], did not alter LD targeting ratios (**Figure 9B&C and Figure A4**). Combined, these results indicate that Rint1 may play an independent role from Zw10 or may be the limiting component for the endogenous NRZ complex.

RNAi against 3 of the 8 components of the COG complex—Cog2, Cog3, and Cog4—significantly reduced LD targeting ratios in the screen (**Figure 9A**). In EGFP-GPAT4^{KI} cells, RNAi of Cog3 only modestly reduced LD targeting ratio, whereas RNAi of Cog3 and Cog4 as well as the rest of the COG complex components did not alter LD targeting ratio (**Figure 9C**). Interestingly, the knockdowns of Cog2, Cog3, and Cog4, but not of other COG complex components, significantly reduced the LD size, and the effect was the most prominent with Cog3 RNAi (**Figure 9B & Figure A4**). The discrepancy between the screen and the verification experiments likely stems from two reasons: (1) the suboptimal resolution of screen images makes the segmentation of the LD regions less precise, and (2) dilating the LD mask, which was employed in calculating the LD targeting ratio to ensure the inclusion of the LD surfaces into the LD regions, reduces the LD targeting ratio to a greater extent when LDs are small. Indeed, the enrichment of EGFP-GPAT4 intensities was readily observed around LDs upon RNAi of Cog2, Cog3, and Cog4 (**Figure 9B & Figure A4**). Therefore, we conclude that the COG complex is dispensable for GPAT4 targeting to LDs.

As in the screen, components of the GARP complex and long coiled-coil tethers—including Rab1 interactor p115, Golgin proteins (GCC185, GM130, GMAP210, Golgin84, and Golgin245), and Grasp65 which tethers GM130 to a membrane—were dispensable for GPAT4 targeting to LDs in EGFP-GPAT4^{KI}

cells (**Figure 9C** and **Figure A4**). Of note, there is no known ortholog of giantin, CASP, Golgin67, and Golgin160 in *Drosophila*[162].

Among all the membrane tethering proteins and complexes tested (but excluding the TRAPP complex that can also act as a GEF for Rab1), only the knockdown of Rint1 significantly reduced GPAT4 targeting to LDs both qualitatively and quantitively. Rint1 knockdown did not significantly reduce the overall GPAT4 amount in the cells or the membrane fraction (see **Figure 12**). To test if Rint1 associates with LDs, we determined the localization of Rint1 by transiently overexpressing EGFP-Rint1 in cells. EGFP-Rint1 enveloped LDs and formed puncta around LDs, indicating that Rint1 may act directly around LDs to contribute to GPAT4 targeting to LDs (**Figure 9D**).

Select SNAREs are required for GPAT4 targeting to LDs

Final steps of membrane trafficking pathways involve the SNARE-mediated fusion of membranes. There exist four classes of SNAREs based on the central residue of the SNARE domain and sequence homology (Q_a, Q_b, Q_c, and R), and it is generally accepted that one SNARE from each class is required for a productive fusion reaction[106]. In the genome-scale screen that tested all known SNAREs in *Drosophila*, RNAi against a number of SNAREs in each of the SNARE classes (but none among the Q_{bc} SNAREs) reduced GPAT4 targeting to LDs (**Figure 10A**). Therefore, we used additional dsRNA designs to compare the magnitude of the effects of RNAi in EGFP-GPAT4^{KI} cells (**Figure 10B&C**).

Among the Q_a SNAREs, RNAi of Syx5 showed the largest reduction in LD targeting ratios compared to the LacZ control, which was also significantly larger than the reduction from RNAi of Syx13 and Syx18. Among Q_b SNAREs, membrin RNAi showed the largest reduction (compared to CG2023). Among Q_c SNAREs, Bet1 RNAi showed the largest reduction (compared to Use1) (**Figure 10C**). Indeed, no ring-like intensities of endogenous EGFP-GPAT4 was observed around LDs upon the knockdown of Syx5, membrin, or Bet1 (**Figure 10B**; see **Figure A5A** for high contrast images), as was the case for RNAi of Rab1 or Trs20. This contrasts with knockdowns of other Q_a, Q_b, or Q_c SNAREs which show ring-like EGFP-GPAT4 intensities around LDs despite significantly reduced LD targeting ratios. Importantly, the knockdown of Syx5 or Bet1 did not reduce GPAT4 amount in the cells or the membrane fractions (see **Figure 12**).

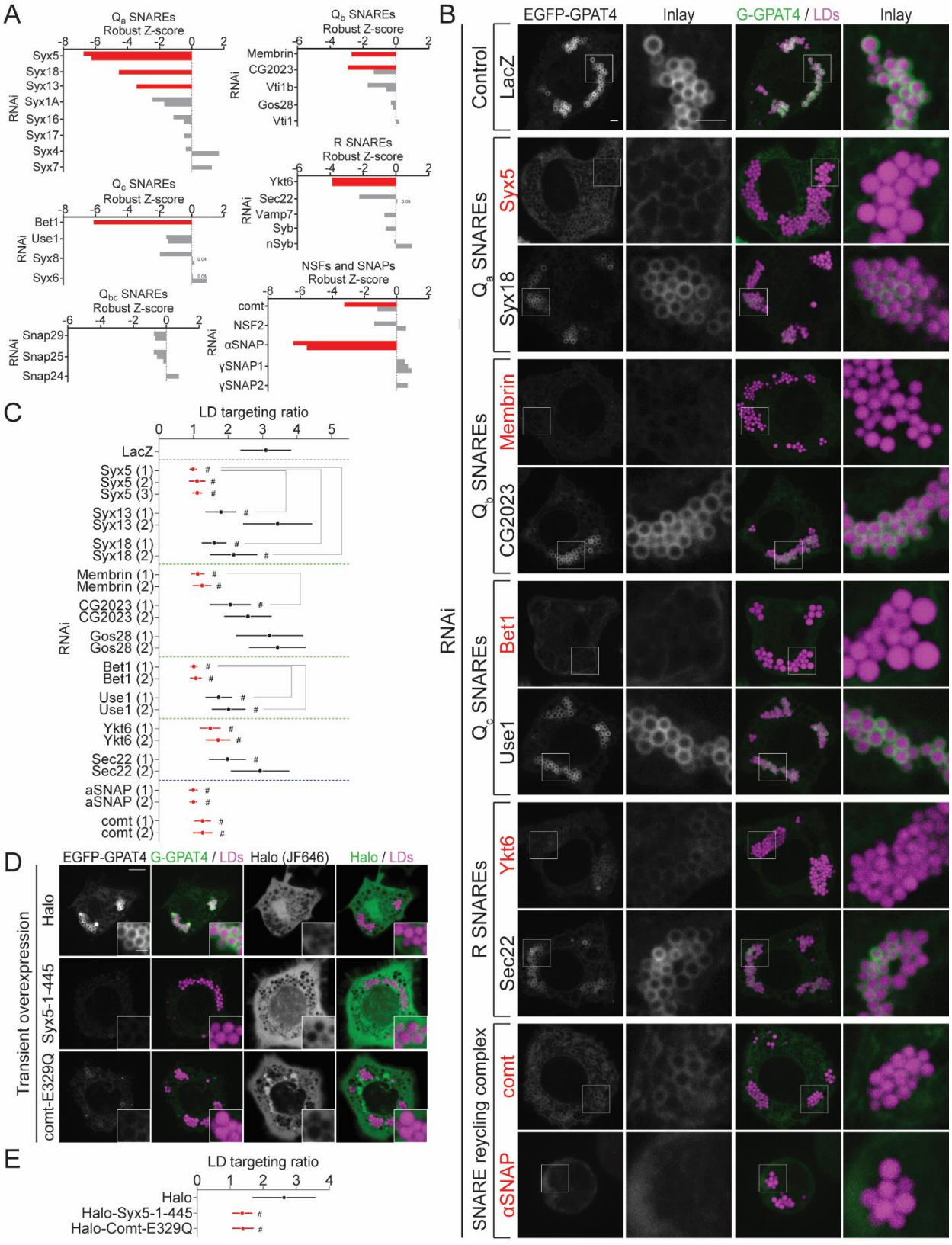

Figure 10. Select SNAREs are required for GPAT4 targeting from the ER to LDs

Figure 10 (continued). Select SNAREs are required for GPAT4 targeting from the ER to LDs
(A) Robust Z-scores for LD targeting ratios for all known SNAREs by class and the SNARE recycling components. Each bar represents the mean of two robust Z-scores from the duplicate screen experiments. Different bars indicate unique dsRNA designs. Robust Z-score < -2.5 is highlighted in red.
(B) Screen result verification using EGFP-GPAT4^{KI} cells. Cells were subjected to 2-3 dsRNA's against select SNAREs, treated with 1mM OA for 20 hours, stained with MDH, and imaged using a spinning-disk confocal microscope. Representative images for dsRNA that shows the largest effect on LD targeting are shown. Images for additional targets and high contrast images (same intensity minimum with lower intensity maximum) are provided in **Figure A5** for RNAi that show little GPAT4 intensity around LDs (red). Scale bar, 2μm and 2μm (inlay).
(C) Quantification of (B). LD targeting ratios were calculated from the confocal images. Number in () indicates a unique dsRNA design. Data are represented as mean ± SD of the results from 2-4 independent experiments (8-14 cells each). One-way ANOVA with Bonferroni multiple comparisons correction, **p<0.01, ***p<0.001, #p<0.0001 compared to LacZ unless indicated otherwise.
(D) Overexpression of the soluble Syx5 fragment or the comt-E329Q mutant decreases GPAT4 targeting to LDs. EGFP-GPAT4^{KI} cells were transfected with a plasmid encoding soluble Halo, Halo-Syx5-1-445, or comt-E329Q-Halo and incubated with Halo ligand JF646 and MDH for imaging. Scale bar, 5μm and 1μm (inlay).
(E) Quantification of (D). LD targeting ratios are calculated and represented as mean ± SD of the results from 3 independent experiments (13-20 cells each). One-way ANOVA with Bonferroni multiple comparisons correction, #p<0.0001 compared to the Halo transfection control.

Among R SNAREs, Ykt6 RNAi resulted in the largest reduction in LD targeting ratios (**Figure 10C**), to the extent comparable to Rint1 RNAi. Similar to Rint1 RNAi, slight EGFP-GPAT4 intensities were observed around LDs upon Ykt6 RNAi, but did not appear significantly more enriched than the surrounding ER, unlike Sec22 RNAi (**Figure 10B**; see **Figure A5A** for high contrast images).

In agreement with the idea that the SNARE-mediated membrane fusion is required for GPAT4 targeting to LDs, the SNARE recycling components, comt (NSF ortholog) and αSNAP were also required for GPAT4 targeting to LDs in both the screen (**Figure 10A**) and the verification experiments (**Figure 10B&C**). Overexpressing Syx5-1-445 truncation mutant, which lacks the transmembrane domain, or the ATPase-defective E329Q mutant of comt (NSF ortholog) significantly reduced GPAT4 targeting to LDs (**Figure 10D&E**). This result indicates that Syx5-1-445 and comt-E329Q act as dominant negatives to endogenous Syx5 and comt by competing for SNARE assembly and disassembly reactions, respectively, that are required for GPAT4 targeting to LDs. Finally, transiently overexpressed αSNAP-EGFP localized around LDs, supporting a direct action of the protein on LDs (**Figure A5B**).

We next sought to determine the localization of Syx5, membrin, Bet1, and Ykt6 to test if the SNAREs required for GPAT4 targeting to LDs localize near LDs. Transient overexpression of the fluorescently tagged SNAREs in *Drosophila* S2 R+ cells resulted in a diffuse ER and Golgi pattern for Syx5, membrin, and Bet1 and in a cytosolic pattern for Ykt6 with no obvious enrichment around or exclusion from LD surfaces (data not shown). As an alternative approach, we examined the public database for the organellar proteomes from a mouse model of non-alcoholic fatty liver disease (www.nafld-organellemap.org)[74]. In this study, murine livers were harvested upon chow (low fat) diet, 3 weeks of high fat diet, or 10 weeks of high fat diet, and fractionated into 22 sucrose-gradient fractions. Quantitative proteomic analysis using mass spectrometry revealed the migration pattern of proteins across different fractions, which was correlated with the migration pattern of organellar markers to determine the localization of detected proteins. This database is suitable for our purpose of identifying SNAREs potentially involved in the membrane fusion between the ER and LDs since (1) the progression of NAFLD correlates with increasing LD sizes, (2) LDs float to the top of sucrose gradient, making their separation from the majority of other fractions reliable, and (3) membrane associations often co-migrate into the same fraction, such that the ER around LDs may co-migrate and enrich in the LD fraction.

Data for all known murine SNARE proteins were extracted and reconstructed into a heatmap (**Figure A5C**). Intriguingly, the murine orthologs of three of the four SNAREs required for GPAT4 targeting to LDs in *Drosophila* cells were enriched in the top fraction after 10-week high fat diet feeding: STX5 (Syx5 ortholog), Bet1l (Bet1 ortholog), and Ykt6 (Ykt6 ortholog). The migration pattern for Syx5 contrasted with other SNAREs that co-migrated in the ER pattern under normal chow feeding, namely STX17 and STX18, which did not enrich in the LD fraction under high fat diet feeding. In addition, Ykt6 was enriched in LD fractions in all conditions, which is consistent with the previous reports of Ykt6 localization on LDs[73,75]. Among Q_b SNAREs, Gos28 was enriched in the LD fraction after 10-week high fat diet feeding but not Gos27, a related SNARE and the predicted murine ortholog of *Drosophila* membrin.

Membrane fusion machinery is required for LD targeting of a subset of ER proteins but not cytosolic proteins

To test whether the membrane fusion machinery identified to be required for GPAT4 targeting to LDs is also necessary for LD targeting of other proteins, we tested the effect of RNAi against Trs20, Rab1, Rint1, Syx5, or Bet1 on the localization of Ldsdh1, HSD17B11, LDAH, and Ubxd8 (**Figure 11A**). Transiently overexpressed EGFP-GPAT4, Ldsdh1-EGFP, and HSD17B11-EGFP, which targeted LDs later around 3 hours after OA treatment (**Figure 6**), failed to enrich around LDs when Trs20, Rab1, Rint1, Syx5, or Bet1 was silenced as opposed to the LacZ control. In contrast, LDAH-EGFP and EGFP-Ubxd8, which targeted LDs as early as 30 minutes after OA treatment, enriched around LDs in all the knockdowns. Quantified LD targeting ratios reflects this difference (**Figure 11B&C**). Whereas the targeting ratios for GPAT4 and Ldsdh1 were significantly reduced to ~1 upon RNAi of the membrane fusion machinery components, those for LDAH and Ubxd8 remained unchanged at values much greater than 1. For HSD17B11-EGFP which targeted only a subset of LDs, the percentage of cells with greater than 2 LDs with protein targeting was calculated (as in **Figure 6C**). In the LacZ control, >80% of cells showed greater than 2 LDs with HSD17B11 targeting, but the percentage was significantly reduced to <20% upon RNAi of the membrane fusion machinery components (**Figure 11C and Figure A6A&B**). This result is consistent with our prediction that the proteins that are blocked by seipin from targeting LDs early

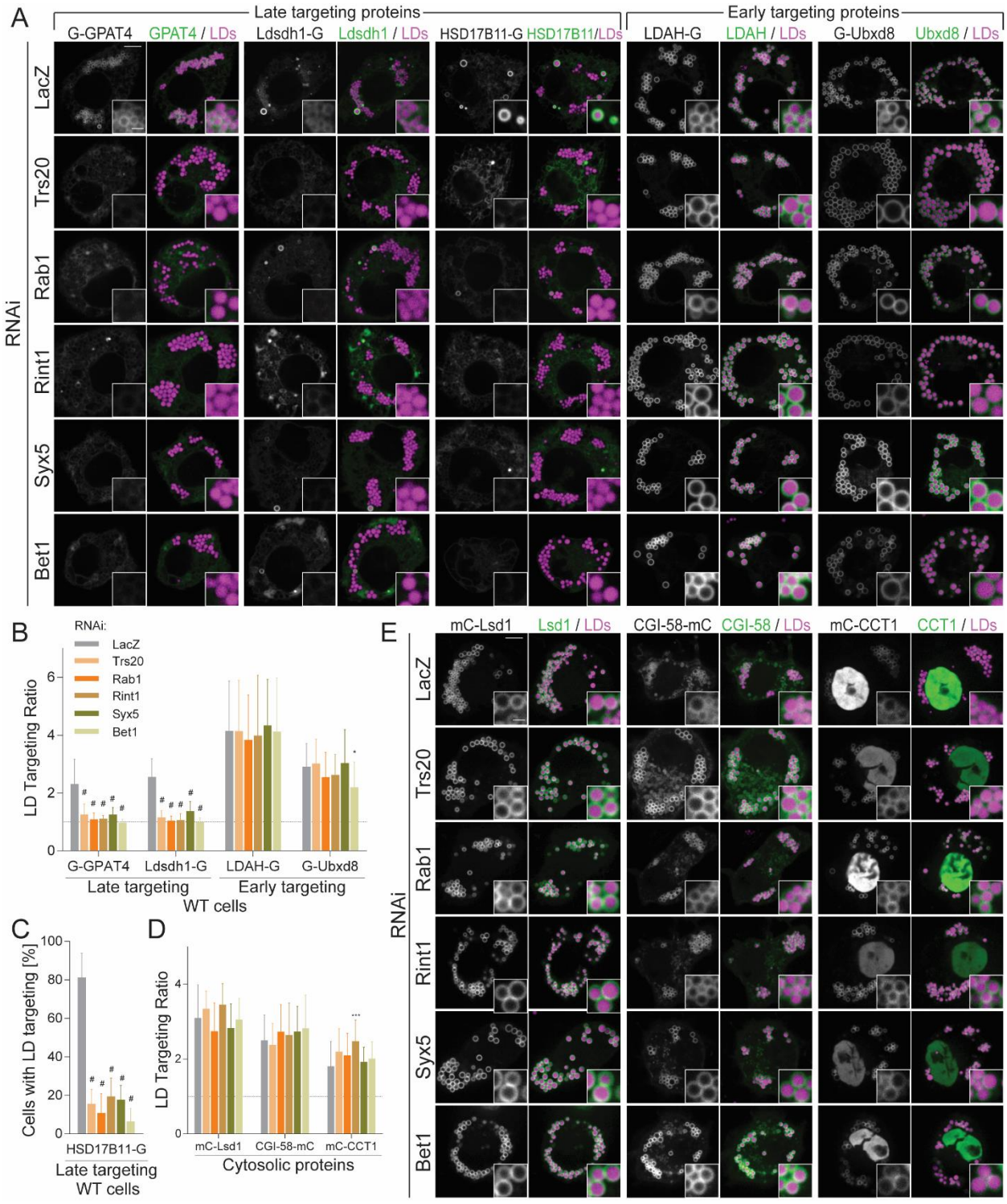

Figure 11. Rab1, Trs20, Rint1, Syx5, and Bet1 are required for LD targeting of ER proteins but not cytosolic proteins

Figure 11 (continued). Rab1, Trs20, Rint1, Syx5, and Bet1 are required for LD targeting of ER proteins but not cytosolic proteins
(A) GPAT4, Ldsdh1, and HSD17B11 require membrane fusion machinery for LD targeting. Wildtype *Drosophila* S2 R+ cells were subjected to dsRNA against LacZ, Trs20, Rab1, Rint1, Syx5, and Bet1, transfected with EGFP constructs, and stained with MDH for imaging. Proteins that target LDs later, but not those that target LDs early, required these components for LD targeting. Scale bar, 5μm and 1μm (inlay).
(B) Quantification of (A). LD targeting ratios are shown as mean + SD of the results from 3 independent experiments (12-18 cells each). Dashed line at LD targeting ratio = 1. One-way ANOVA with Bonferroni multiple comparisons correction for each construct, *p<0.05, #p<0.0001 compared to LacZ.
(C) Quantification of (A). Percentages of cells with >2 LDs with HSD17B11-G targeting were calculated per experiment. Data are represented as mean + SD of the results from 3 independent experiments (12-15 cells each). One-way ANOVA with Bonferroni multiple comparisons correction for each construct, #p<0.0001 compared to LacZ.
(D) Cytosolic proteins do not require membrane fusion machinery for LD targeting. EGFP-GPAT4^{KI} cells were subjected to dsRNA against LacZ, Trs20, Rab1, Rint1, Syx5, and Bet1, transfected with mCherry constructs, and stained with MDH for imaging. LD targeting ratios were calculated as done previously, except for CCT1 in which the nucleus was excluded from the calculation (LD targeting ratio for CCT1 = average intensity of mC-CCT1 on LDs / average intensity inside the cell excluding LDs and nucleus). EGFP channel images and quantification are shown in **Figure A7**. Data are shown as mean + SD of the results from 3 independent experiments (9-14 cells each). Dashed line at LD targeting ratio = 1. One-way ANOVA with Bonferroni multiple comparisons correction for each construct, ***p<0.001 compared to LacZ.
(E) Representative images for (D). Scale bar, 5μm and 1μm (inlay).

(i.e. GPAT4, Ldsdh1, HSD17B11) require an alternative pathway for protein targeting, whereas those that can bypass seipin to target LDs early (i.e. LDAH, Ubxd8) do not require an alternative pathway.

ER proteins accumulate on LDs likely by recognizing the packing defects on LD membranes via the large hydrophobic residues (Farese & Walther Laboratory, unpublished results). For instance, mutating the tryptophan residues of the hydrophobic hairpin-like domain of GPAT4 to alanine abolishes LD targeting of the domain. Similar mechanism is proposed for the cytosolic proteins that target LDs, which contain amphipathic helices with large hydrophobic residues that recognize membrane packing defects on LD surfaces[21,82]. To exclude the possibility that knockdown of the membrane fusion machinery alters intrinsic LD surface properties such as packing defects, we tested if cytosolic proteins target LDs when Trs20, Rab1, Rint1, Syx5, or Bet1 is knocked down (**Figure 11D&E**).

When overexpressed in EGFP-GPAT4^{KI} cells, cytosolic proteins mCherry-Lsd1, CGI-58-mCherry, and mCherry-CCT1 formed the characteristic ring-like intensities around LDs under LacZ RNAi (**Figure 11E**). mCherry-CCT1 also strongly localized to nucleus in accordance with a previous report[22]. Overexpression of these cytosolic proteins also modulated endogenous EGFP-GPAT4 targeting to LDs (**Figure A6D-F**): mCherry-Lsd1 overexpression resulted in a patchy pattern of GPAT4 targeting, with some LDs with higher amounts of EGFP-GPAT4 and some with lower amounts of EGFP-GPAT4 (**Figure A6D**), whereas CGI-58-mCherry overexpression increased GPAT4 targeting to LDs (**Figure A6E**). The former effect is consistent with the previously observed phenomenon of macromolecular crowding on LDs, in which Lsd1, a strong LD binding protein, competes with GPAT4 for LD surfaces[53]. The latter is likely due to the reduction in LD sizes that follow from the overexpression of CGI-58[163] which consequently concentrates EGFP-GPAT4 intensities around LDs. Still, EGFP-GPAT4 targeted LDs consistently under LacZ RNAi and was inhibited upon RNAi of Trs20, Rab1, Rint1, Syx5, or Bet1 in these conditions (**Figure A6C-F**). In contrast, mCherry-Lsd1, CGI-58-mCherry, and mCherry-CCT1 targeted LDs in all the knockdown conditions (**Figure 11E**), and their LD targeting ratios did not change upon RNAi of the membrane fusion machinery components (**Figure 11D**; note that nuclear signal was excluded when calculating LD targeting ratios for mCherry-CCT1). We therefore conclude that the protein targeting defect from silencing the membrane fusion machinery components is specific to a subset of ER proteins.

Silencing membrane fusion machinery reduces GPAT4 in LD fraction

Imaging experiments using the overexpression and the endogenous EGFP-GPAT4 cell lines showed that targeting of GPAT4 to LDs requires membrane fusion machinery components. To verify this finding biochemically, we compared LD fractions upon RNAi of LacZ, Trs20, Rab1, Rint1, Syx5, or Bet1 (**Figure 12**). We employed a simple two-step sucrose gradient that allows the separation of LD from the soluble cytosolic fraction, and the insoluble membrane fraction. As expected, CNX99A enriched in the membrane fractions, and α-tubulin in the cytosolic fraction (**Figure 12A&B**). GPAT4 and CCT1 were enriched in the LD fractions. The amount of GPAT4 in the LD fraction was reduced upon RNAi of Trs20, Rab1, Rint1, Syx5, and Bet1 compared to the LacZ control despite no reduction in the whole cell lysates (input; **Figure 12A&C**). In addition, GPAT4 amounts were modestly increased in the membrane fractions, supporting the idea that GPAT4 is confined in the ER in the absence of membrane fusion machinery

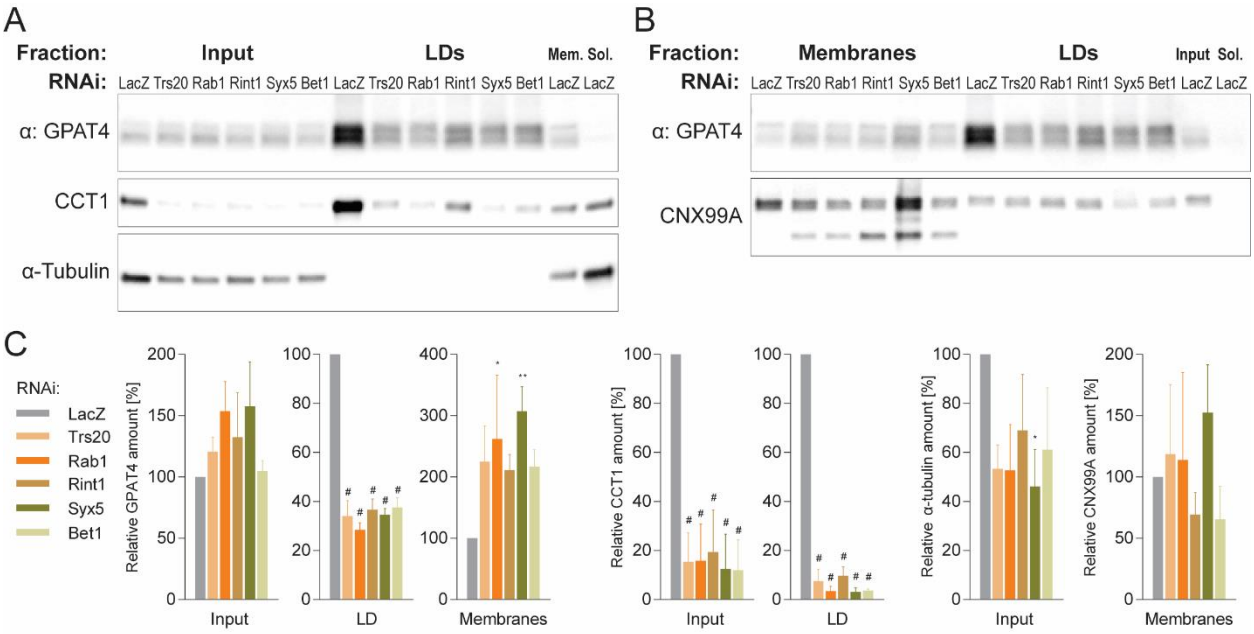

Figure 12. RNAi of membrane fusion machinery components reduces GPAT4 in LD fraction
(A&B) LD fractionation upon RNAi of membrane fusion machinery components. Wildtype *Drosophila* S2 R+ cells were subjected to dsRNA against LacZ, Trs20, Rab1, Rint1, Syx5, or Bet1 and fractionated into membrane, soluble, and LD fractions using a two-step sucrose gradient. Upon protein precipitation and normalization in protein amount (2.5µg for LDs and 7.5µg for the rest), western blot was performed using antibodies against GPAT4, CCT1, α-tubulin, or CNX99A. Input refers to the cell lysates prior to fractionation. Representative blots from 3 independent experiments are shown.
(C) Quantification of immunoblots in (A) and (B). Integrated intensity measurements were normalized to the LacZ control for each type of fraction. Data are represented as mean + SD of the results from 3 independent experiments. One-way ANOVA with Bonferroni multiple comparisons correction, *p<0.05, **p<0.01, #p<0.0001 compared to LacZ.

(**Figure 12B&C**). The amount of CCT1 was also significantly reduced in reduced in the LD fractions upon RNAi of the fusion machinery components, but the reduction was accompanied by a significant reduction in the total CCT1 amount in the whole cell lysates (**Figure 12A&C**).

SNARE depletion increases Rab1-dependent ER association with LDs

We performed the genome-scale imaging to identify factors required for GPAT4 targeting to LDs, which may occur via membrane connections or 'bridges' between the ER and LDs (see **Figure 6**). Therefore, we asked whether the depletion of the factors identified in the screen alters association between the ER and LD membranes. Under a confocal microscope, no noticeable difference in the ER association with LDs (as detected by endogenous CNX99A-EGFP) was observed upon RNAi of Trs20, Rab1, Rint1, or Syx5 (**Figure A7A**) compare to LacZ RNAi. Upon Bet1 RNAi, the ER seemed to enwrap LDs in a minor portion of the cells (**Figure A7A**; Bet1, second panel).

To get a finer detail of the organellar ultrastructure, we performed electron microscopy (EM) on chemically fixated *Drosophila* S2 R+ cells 20 hour after 1mM OA treatment. In this set of pilot experiments, the ER appears as tubular structures or spots with a bilayer membrane (**Figure 13**; additional images in **Figure A7B**). LDs have a translucent lumen with a monolayer membrane, but their spherical shape was disrupted likely by the fixation process. Under LacZ RNAi, spots of the ER were observed mostly in-between LDs (arrowheads) and around the outer boundaries of LD clusters (arrows). Upon RNAi against Rab1, the ER was rarely visible around LDs. Intriguingly, when Syx5 was silenced, the ER enwrapped LDs much more prominently (arrowheads). These observations are consistent with the idea that Rab1 initiates the fusion process leading to the ER-LD tethering, whereas the SNARE-mediated membrane fusion follows the ER-LD tethering. To test if the increased ER association with LDs upon Syx5 knockdown is dependent on Rab1, we simultaneously knocked down Syx5 and Rab1 and performed EM. Rab1 RNAi reversed the increased ER association with LDs induced by Syx5 RNAi. Combined, these results suggest that the Syx5 depletion leads to the accumulation of Rab1-dependent ER-LD associations. Given the limitations of chemical fixation process that altered morphologies of cellular ultrastructure in this pilot experiment, we plan to perform future experiments using a superior method of sample preservation such as high pressure freezing.

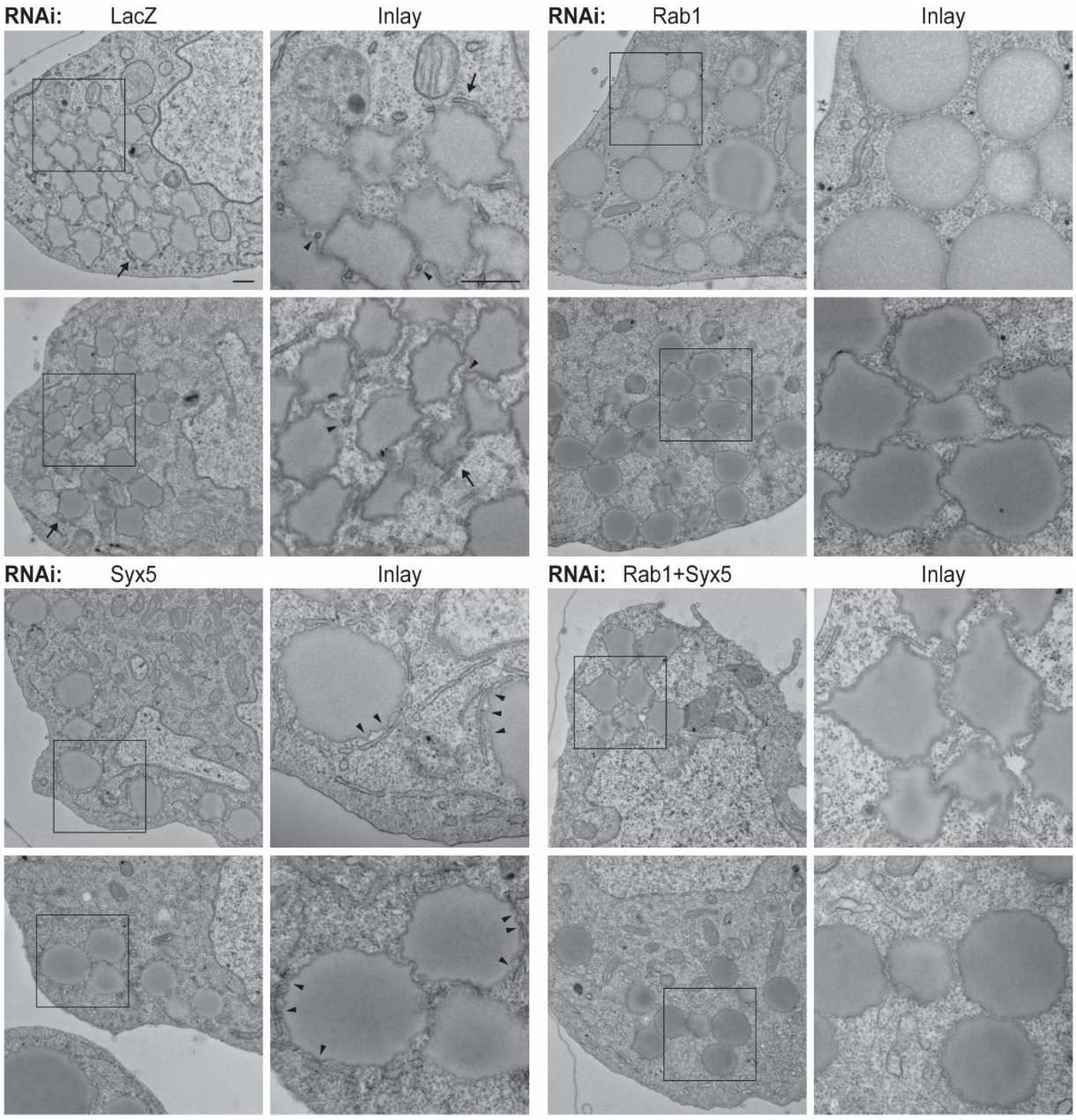

Figure 13. Syx5 depletion increases Rab1-dependent ER association around LDs
Ultrastructural changes upon RNAi against LacZ, Rab1, Syx5, or Rab1+Syx5. Wildtype *Drosophila* S2 R+ cells were subjected to RNAi and chemically fixated for EM. Representative images from 2 experiments for LacZ, Rab1, and Syx5 and from 1 experiment for Syx5+Rab1 are shown. Arrows and arrowheads indicate where the ER and LD membranes juxtapose closely. Additional images are shown in **Figure A7B**. Scale bar, 500nm and 500nm (inlay).

Membrane fusion machinery is dispensable for protein targeting from the ER to LDs in the absence of seipin

Since the proteins that were not prevented by seipin from targeting LDs early could target LDs in the absence of membrane fusion machinery (i.e. LDAH, Ubxd8), we tested if the depletion of seipin provides an alternative targeting pathway for the other group of proteins that could not target LDs in the absence of membrane fusion machinery (i.e. GPAT4, Ldsdh1, HSD17B11). In Seipin KO *Drosophila* S2 R+ cells, transiently overexpressed EGFP-GPAT4, Ldsdh1-EGFP, and HSD17B11-EGFP targeted LDs upon RNAi of Trs20, Rab1, Rint1, Syx5, or Bet1 (**Figure 14A**), and their LD targeting ratios remained comparable to the LacZ control (**Figure 14B**). Interestingly, HSD17B11-EGFP targeted to all LDs rather than to a subset of LDs as was observed in the wildtype cells. Therefore, quantifications using both the LD targeting ratios (**Figure 14B**) and the percentage of cells that contain >2 LDs with protein targeting (**Figure 14C**) are provided for HSD17B11. The reduction in LD targeting ratios for EGFP-GPAT4 upon RNAi of Rint1 and Bet1 compared to LacZ control may signify the additional contribution of the fusion machinery-dependent pathway to LD targeting in these cells. Finally, consistent with the idea that the seipin depletion allows for early targeting of LDs, GPAT4, Ldsdh1, and HSD17B11 targeted LDs as early as 30 minutes after OA treatment in Seipin KO cells in all the knockdown conditions (**Figure A8A&B**). Thus, we conclude that the depletion of seipin provides an alternative protein targeting pathway for the proteins that otherwise require membrane fusion machinery for the ER-to-LD targeting.

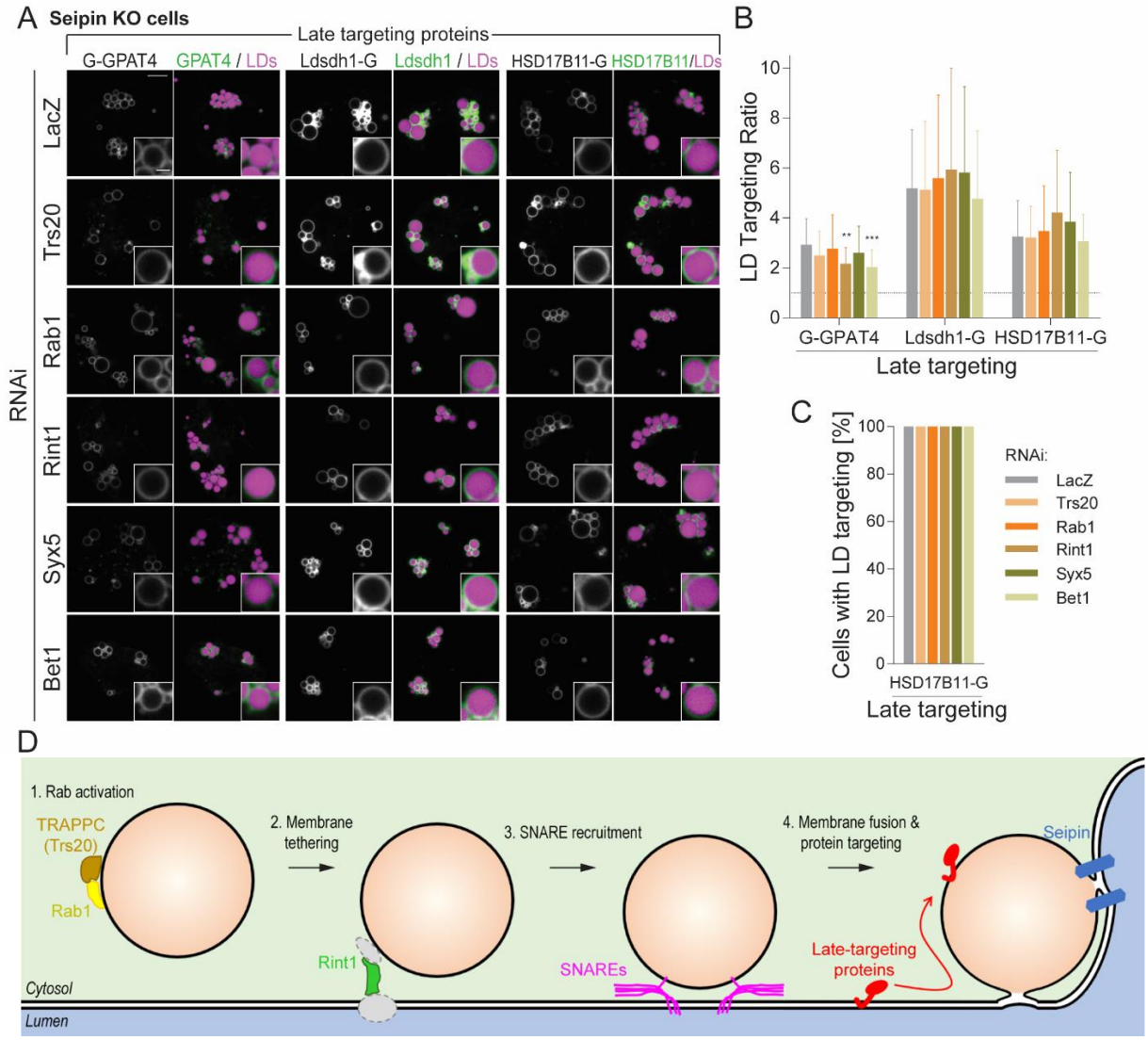

Figure 14. Membrane fusion machinery components are dispensable for ER-to-LD protein targeting in the absence of seipin

(A) GPAT4, Ldsdh1, and HSD17B11 do not require membrane fusion machinery for LD targeting in the absence of seipin. Seipin KO *Drosophila* S2 R+ cells were subjected to dsRNA against LacZ, Trs20, Rab1, Rint1, Syx5, and Bet1, transfected with EGFP constructs, treated with 1mM OA, and stained with MDH for imaging. Scale bar, 5μm and 1μm (inlay).

(B) Quantification of (A). LD targeting ratios are shown as mean + SD of the results from 3 independent experiments (13-18 cells each). Dashed line at LD targeting ratio = 1. One-way ANOVA for each construct, **p<0.01, ***p<0.001 compared to LacZ.

(C) Quantification of (A). Percentages of cells with >2 LDs with HSD17B11-G targeting were calculated per experiment. Data are represented as mean + SD of the results from 3 independent experiments (13-18 cells each).

(D) Model of the formation of ER-LD membrane bridges that mediate protein targeting from the ER to LDs. (1) Rab1 is activated by the TRAPP complex. (2) ER and LD membranes are tethered at least partially by Rint1. (3) SNAREs (Syx5, membrin, Bet1, and Ykt6) are recruited and (4) fuse the ER and LD membranes, thereby establishing membrane bridges that allow for the targeting of late-targeting proteins.

Chapter II. Discussion

A systematic analysis of the proteins that target from the ER to LDs revealed that some proteins target LDs early while others target LDs later (**Figure 6A**). The difference likely stems from the selective barrier function of seipin, which allows for some proteins to target LDs and prevent others from targeting LDs during the LD biogenesis in the ER (**Figure 6B**). Previous studies showed that GPAT4, an enzyme that catalyzes the rate-limiting step of the *de novo* TG synthesis pathway and targets LDs later, targets from the ER to LDs via membrane connections or 'bridges' between the two organelles[54,86]. To begin understanding how these bridges form to allow for the latter group of proteins to target LDs, we performed a genome-scale imaging screen in *Drosophila* S2 R+ cells to identify genes required for GPAT4 targeting to LDs (**Figure 7**). Bioinformatic analyses of the screen hits revealed that membrane trafficking-related genes, including those encoding small GTPases, membrane tethers, and SNARE proteins, are highly enriched among the genes of which knockdowns significantly reduce GPAT4 targeting to LDs.

We rigorously verified the screen results using EGFP-GPAT4^{KI} cells and determined that the small GTPase Rab1 and its GEF component Trs20; the membrane tethering complex component Rint1; Syx5 (Q_a SNARE), membrin (Q_b SNARE), Bet1 (Q_c SNARE), Ykt6 (R SNARE), and the SNARE recycling complex components αSNAP and NSF are specifically required for GPAT4 targeting from the ER to LDs (**Figures 8-10**). In addition, we localize Rab1 and Rint1 to LD membranes and find that the orthologs of Syx5, Bet1, and Ykt6 are highly enriched in the LD fractions of murine liver with NAFLD. We further show that Rab1, Trs20, Rint1, Syx5, and Bet1 are required for LD targeting of other proteins that target from the ER to LDs later, but not of those that target from the ER to LDs early or those that target from the cytosol (**Figure 11**). We also show that RNAi of the membrane fusion machinery components reduces GPAT4 amount in the isolated LD fractions but not in the whole cell lysates or the membrane fractions (**Figure 12**).

Upon establishing the specific requirement of these components in protein targeting, we used electron microscopy to show that Rab1 RNAi reduces the association between the ER and LD membranes, whereas Syx5 RNAi increases the association (**Figure 13**). Importantly, the increased association from Syx5 RNAi appeared to be dependent on Rab1, indicating that Syx5 acts downstream of

Rab1. In addition, these observations support the idea that membrane fusion machinery components remodel the ER-LD associations to facilitate ER-to-LD protein targeting. Lastly, we present the evidence that the ER-LD membrane bridges used by the late-targeting proteins are independent of seipin, which marks the membrane connections that form during the LD biogenesis from the ER, as depleting seipin allowed for the late-targeting proteins to target LDs in the absence of the membrane fusion machinery components (**Figure 14**).

Based on the results of this study, we propose the following model of protein targeting from the ER to LDs (**Figure 14D**). Some proteins embedded in the ER membrane target LDs during LD biogenesis or after LD budding via ER-LD membrane connections marked by seipin oligomeric complex (i.e. LDAH, Ubxd8). Sometime after LD biogenesis, **Step 1**: Rab1 is recruited to LDs and is activated on LD membrane by a TRAPP complex. **Step 2**: This in turn initiates membrane tethering between the ER and LD membranes, which is at least partially mediated by Rint1. **Step 3**: SNAREs (Syx5, membrin, Bet1, and Ykt6) are recruited to the vicinity of the tethered membranes and **Step 4**: assemble to fuse the LD monolayer with the outer leaflet of the ER membrane. The fusion results in ER-LD membrane bridges that allow for the LD targeting of proteins otherwise blocked by seipin (i.e. GPAT4, Ldsdh1, HSD17B11).

Although many aspects of the model remain to be tested, the current study documents two different groups of proteins that target from the ER to LDs; demonstrates the requirement of all the aforementioned molecular factors in the targeting of the late-targeting proteins to LDs; shows the effect of depleting the factors on the association between the ER and LD membranes and establishes the sequence of action by the factors; and deciphers the role of seipin as a selective barrier for protein targeting to LDs.

In addition to the factors discussed here, knockdown of many other genes has been found to reduce LD targeting ratios in the genome-scale screen. This includes the Arf1/COPI coatomer complex which may modulate LD surface tension to facilitate GPAT4 targeting to LDs[86] and used as positive controls in the screen. Arf1/COPI coatomers may contribute to establishing the ER-LD bridges in a number of different ways. First, the Arf1/COPI complex may act upstream of Rab1 and help activate LD membranes for Rab1 binding or activation. This hypothesis is most consistent with the potential action of Arf1/COPI machinery to bud off phospholipids from the monolayer surface (‘nano-LDs’), as was shown *in*

vitro[86,118]. Conversely, the Arf1/COPI complex may act downstream of Rab1 to facilitate ER-LD membrane tethering and/or fusion. Consistent with this idea, GBF1, a GEF for Arf1, was shown to interact with Rab1b in HeLa cells (*Drosophila* Rab1 is orthologous to both Rab1a and Rab1b in humans) and this interaction modulated Arf1/COPI recruitment to the Golgi[164]. In support of this idea, garz (a GBF1 ortholog in *Drosophila*) was also a hit in our screen, and both garz and the COPI component αCOP form punctate localization on LDs[86]. Therefore, Rab1 activation on LDs may lead to recruitment of garz and subsequently Arf1/COPI recruitment to LDs. Once recruited to LDs, the Arf1/COPI complex may bud off nano-LDs to make the membrane more favorable for fusion with the ER membrane as was previously proposed. Alternatively, the Arf1/COPI complex on LDs may contribute to the ER-LD tethering by interacting with the NRZ complex as was shown for COPI-coated vesicles and Dsl1p complex (NRZ complex ortholog in yeast)[165]. Thus, it will be important to determine whether Rab1 recruitment to LDs precedes or follows after Arf1/COPI recruitment to LDs and whether LD localization of one depends on another. Furthermore, it remains to be tested whether Rab1 directly interacts with Rint1 or recruits COPI coat to LDs for the interaction with Rint1.

Because it is not trivial to accurately localize the Arf1/COPI complex to LD membranes, there is a possibility that the Arf1/COPI complex does not localize to and act directly on LDs. In such a case, it would be important to test whether the Arf1/COPI complex is required for maintaining a reserve of SNAREs in the ER. Since the depletion of the Arf1/COPI complex halts the retrograde trafficking from the Golgi to the ER, such depletion could lead to the accumulation of Syx5, membrin, and/or Bet1 in the Golgi and their absence from the ER. This in turn would prevent the formation of ER-LD bridges and GPAT4 targeting to LDs. This hypothesis is consistent with the data from our screen that COPII coatomers are also required for GPAT4 targeting to LDs, albeit to a lesser extent than the Arf1/COPI complex, since the depletion of COPII coatomers would also disrupt the distribution of SNAREs in cells. This hypothesis can be tested by determining the localization of the respective SNAREs upon Arf1/COPI depletion.

The first step in our model involves the activation of Rab1 on LDs by the TRAPP complex. This is supported by the localization of Rab1 on LDs in this study (**Figure 8F**) and others and the requirement of both Rab1 and Trs20, a component of TRAPP complex, in GPAT4 targeting to LDs (**Figure 9**). As discussed above, it is unclear what triggers the recruitment of Rab1 to LDs, but it is possible that the

recruitment is coupled to the activation of Rab1 since the Rab1-N124I mutant, which binds TRAPP complex strongly but cannot be activated, did not localize to LDs (**Figure 8G**).

It is important to note that in our study, only Trs20 but not the other components of the TRAPP complex critical for its function, was required for GPAT4 targeting to LDs (**Figure 9**). This may be explained if only Trs20 is the limiting factor for TRAPP complex activity in cells and if the knockdowns against the remaining TRAPP complex components do not sufficiently deplete the components. Similarly, Rint1, but not Zw10, of the NRZ complex was required for GPAT4 targeting to LDs (**Figure 9**). Thus, it should be tested whether the knockdowns of the remaining TRAPP complex components and Zw10 reduces their respective amounts at the protein level.

The second step in our model involves tethering between the ER and LD membranes by Rint1. Rint1 and other components of the NRZ complex are soluble proteins that tether two membranes by interacting with proteins on both membranes[160]. In the retrograde trafficking from the Golgi to the ER, the NRZ complex is thought to be tethered to the ER membrane through interaction with SNAREs (Rint1 interaction with BNIP1 and NAG interaction with Use1) and capture vesicles from the Golgi via interaction with the COPI coatomer. As discussed above, it remains to be tested whether Rab1 on LDs directly interacts with Rint1 or indirectly by recruiting Arf1/COPI to LDs. Previous studies have identified Rab18 as an interactor of the NRZ complex on LDs[67]. In fact, the interaction was originally identified from a systemic screen of Rab effectors in *Drosophila* S2 cells using purified Rabs[66]. However, in our study, Rab18 was not required for GPAT4 targeting to LDs (**Figure 8**).

Consistent with the idea that Rint1 has an interactor on LDs, components of the NRZ complex have been localized to LDs. These include human Zw10 in COS cells (immortalized monkey kidney tissue)[66] and mouse NAG, Rint1, and Zw10 in differentiated 3T3-L1 adipocytes[67]. Their localization pattern resembled our results of EGFP-Rint1, which showed both punctate and enwrapping pattern around LDs (**Figure 9D**), but was dependent on the overexpression of Rab18 (in contrast to the diffuse cytosolic localization of the components without the Rab18 overexpression). It remains to be tested whether Rab1 overexpression results in a shift in the localization of the NRZ complex to LDs.

The discrepancy in the findings can be explained by the difference in cell types. Previously, Rab18 has been found to affect LD sizes in 3T3-L1 adipocytes and mouse testes cell line TM-3 Leydig

cells[67] but not in human breast carcinoma cell line SUM159 cells or *Drosophila* S2 cells[166]. These findings call into a question whether Rab1 and Rab18 have overlapping functions but manifest in different cell types. In support of this idea, the TRAPP II complex, which is a canonical GEF for Rab1, has been reported to function as a GEF for Rab18 in HEK293T cells[167]. Three different TRAPP complexes have been identified in yeast, the TRAPP I, TRAPP II, and TRAPP III complexes[157]. They share all the components of TRAPP I, but the TRAPP II and TRAPP III complexes contains additional subunits (Trs65, Trs120, and Trs130 for the TRAPP II complex and Trs85 for the TRAPP III complex). Interestingly, Trs20, which was required for GPAT4 targeting to LDs in our study, was also required for the activity and the assembly of the TRAPP II complex but not for the activity and assembly of the TRAPP I complex in yeast[168]. In addition, RNAi against the TRAPP II complex-specific subunit Trs120 resulted in a moderately significant reduction of LD targeting ratio, indicating that the TRAPP II complex may be involved in GPAT4 targeting to LDs in our system (**Figure 9C**). This further supports the idea that Rab1 and Rab18 may compete against or compensate for each other depending on the context. The complex interplay between Rab1 and Rab18 warrants further investigation.

The third step in our model involves the SNARE-mediated fusion between the LD monolayer membrane and the outer leaflet of the ER bilayer membrane. A productive SNARE fusion requires one SNARE from each of the four classes of SNAREs[106]. An unbiased screen followed by the targeted verification experiments revealed that one SNARE from each of the four classes is required for GPAT4 targeting to LDs, Syx5 (Q_a), membrin (Q_b), Bet1 (Q_c), and Ykt6 (R) (**Figure 10**), three of which have been found to be highly enriched in the LD fractions of murine liver with NAFLD (**Figure A5C**). None of the SNAREs that bind the NRZ complex in the retrograde trafficking (Syx18, BNIP1, and Use1 in the ER and Sec22 on the COPI vesicle) was required for GPAT4 targeting to LDs. Interestingly, ykt6 was previously found to interact with Dsl1p complex (yeast NRZ complex), although the significance of the interaction remains unknown[169].

It has been postulated that SNARE pairing contributes to the specificity of membrane fusion within cells, such that no same SNARE quadruples are found in different parts of the cells[106]. Consistent with this idea, the combination of four SNAREs in our model is unique. Interestingly, similar compositions of SNARE-pins are found elsewhere in cells: **Syx5**, Gos28, **Bet1L** (Bet1 ortholog) and **ykt6** that mediate

vesicle fusion from the early/recycling endosomes to *trans*-Golgi network; **Syx5**, **Gos27 (membrin ortholog)**, **Bet1**, and sec22b in the anterograde trafficking from the ER to the ER-Golgi intermediate compartment (ERGIC); and **Syx5**, Gos28, **Bet1**, and **ykt6** from the ERGIC to the Golgi. Our combination of SNAREs, Syx5, membrin/Gos27, Bet1/Bet1L, and ykt6, differs from these other combinations by one SNARE, supporting both the specificity and the likely productive fusion by the newly proposed SNARE quadruple. The combination of Syx5, membrin, Bet1 as the acceptor membrane-SNAREs and ykt6 as the donor membrane SNARE has not been tested for fusion capability, although a liposome fusion assay using Bet1 as the donor membrane SNARE did not produce productive fusion[112,113]. Besides liposome fusion assays, another useful assay for testing SNARE pairing is a cell-cell fusion assay in which 3 SNAREs are overexpressed in the plasma membrane of one group of cells (mimicking t-SNAREs) and the last SNARE is overexpressed in the plasma membrane of another group (mimicking v-SNARE)[170]. This method may be used to test if Syx5, membrin, Bet1, and ykt6 can produce a membrane fusion.

It is important to note that the fusion reaction we propose is a hemi-fusion in which only one of the two leaflets of the ER membrane fuses with the LD membrane which consists of a monolayer membrane. It has already been shown that SNAREs can mediate membrane hemi-fusion[171,172]; in fact, this state is considered an intermediate to the complete fusion of two bilayer membranes. Still, it should be tested whether the SNARE combination in our model can produce hemi-fusion between the monolayer and bilayer membranes, for instance by reconstituting purified SNAREs into liposomes and artificial LDs and testing for membrane phospholipid mixing between the liposomes and artificial LDs. Alternatively, one can purify LDs and microsomes from cells to test if they can fuse and if selectively depleting SNAREs from one compartment or another prevents this fusion.

Finally, the SNARE recycling complex components, comt (NSF ortholog) and αSNAP, were required for GPAT4 targeting to LDs (**Figure 10**), and αSNAP localized around LDs (**Figure A5B**), which supports the idea of SNARE action on LD membranes. In addition, expression of ATPase-defective comt-E329Q mutant acted as a dominant negative to prevent GPAT4 targeting to LDs (**Figure 10D**). This presents a valuable tool to investigate SNAREs in the future, as tthis mutant can potentially preserve and accumulate SNARE-pins that can be biochemically purified.

In our study, we showed that three late-targeting proteins require the membrane fusion machinery components for LD targeting (**Figure 11A-C**). Another protein speculated to use the same pathway is ATGL (brummer in *Drosophila*), an enzyme that catalyzes the rate-limiting step of TG hydrolysis on LDs. Previous studies have shown that Arf1/COPI components are required for ATGL targeting to LDs[119,120]. In addition, Arf1/COPI RNAi resulted in larger LDs, likely due to reduced TG hydrolysis on LDs[86,119,120]. Consistent with the hypothesis that ER-LD bridges mediate ATGL targeting to LDs, RNAi of Trs20, Rab1, Rint1, Syx5, and Bet1 resulted in larger LDs (see **Figure 11A**). Similarly, the database of an RNAi screen for LD morphology in the human macrophage cell line THP1 cells[149] revealed that RNAi of TRAPPC2 (Trs20 ortholog), Rab1b, GS27 (membrin), and NAPA (αSNAP) increase LD sizes (robust Z-score of +1.61, +3.74, +3.71, and +3.30 respectively), whereas knockdown of Ykt6 has been previously shown to increase LD size in differentiated 3T3-L1 adipocytes[67]. However, whether brummer targeting to LDs requires the fusion machinery components has not been directly tested. To determine which other proteins besides GPAT4, Ldsdh1, and HSD17B11 require these components for LD targeting, we plan to perform proteomics analysis on LD fractions upon factor RNAi, which accurately captured the changes in GPAT4 amount in LDs upon factor RNAi using western blot (**Figure 12**). In addition, since Syx5 RNAi increased associations between the ER and LDs under EM (**Figure 13**), it would be interesting to test if proteins that mediate this association are co-purified in the LD fractions upon Syx5 RNAi.

Our model assumes that once the ER-LD bridges are established, proteins would accumulate on LDs. This would mean that proteins that target LDs from the ER have intrinsic preference for the LD monolayer over the ER bilayer. This seems to be the case for GPAT4, as fluorescently tagged GPAT4 in microsomes selectively accumulated on the monolayer membrane when monolayer-bilayer connections were established *in vitro* by flowing the microsomes in a neutral lipid stream in a microfluidics device[86]. In addition, molecular dynamics simulations using the GPAT4 hydrophobic hairpin-like domain, which is sufficient to insert into the ER and target LDs, predicts that the domain favors a monolayer (lower free energy) to a bilayer (higher free energy) environment (Farese & Walther Laboratory, unpublished results). Whether these findings are generalizable to other ER-to-LD targeting proteins has not been untested.

As mentioned previously, both ER and cytosolic proteins that target LDs contain large hydrophobic residues that are critical for LD targeting[21,53]. Based on molecular dynamics simulations,

these large hydrophobic residues are thought to insert into the lipid packing defects on LDs. One consequence of this shared targeting mechanism is macromolecular crowding on LD surfaces, in which proteins that target LDs compete each other for LD binding[53]. As expected, overexpressing Lsd1 seemed to reduce GPAT4 targeting to LDs (**Figure A6B**). Conversely, reducing packing defects on LDs could reduce protein targeting from both the ER and LDs. In the current study, RNAi of membrane fusion machinery components reduced LD targeting of GPAT4 from the ER but not of Lsd1, CGI-58, or CCT1 from the cytosol in the same cells (**Figure 11D&E**). This indicates that the membrane fusion machinery components are required for a process specific for ER protein targeting to LDs but not for other processes shared by both ER and cytosolic proteins. Despite the unchanged targeting of overexpressed CCT1 to LDs upon RNAi of the membrane fusion machinery components, the endogenous CCT1 amount in the respective LD fractions was reduced (**Figure 12**). This may be attributed to the decline in the overall CCT1 amount in cells.

We also propose that there exist two different types of membrane connections between the ER and LDs: one that arises during the LD biogenesis in the ER and marked by seipin oligomeric complex (here on referred to as the 'seipin bridge') and the other that arises sometime after LD budding and mediates LD targeting of late-targeting proteins ('protein targeting bridge'). Evidence for the seipin bridge is well documented. This includes the findings that LDs arise from the seipin-marked sites in the ER[44,48]; seipin remains associated with LDs after budding from the ER[57]; and the seipin-mediated ER-LD connections have a uniform ultrastructural membrane architecture using correlative light electron microscopy[45]. There are also evidences suggesting that the seipin bridges connect the LD lumen with the space in-between the ER bilayer membranes where TG is deposited upon the synthesis in the ER membrane[42,43,45,48]. Importantly, each LD seems to possess only one seipin-mediated connection to the ER across different cell types.

Evidence supporting the existence of a second type of bridge includes the observation of multiple ER-LD membrane connections under EM[53,54]. A FRAP experiment using fluorescently labeled GPAT4 suggests that multiple protein targeting bridges form and recede dynamically around one LD, indicating that these bridges may account for the additional ER-LD membrane connections observed under EM[54]. In the current study, we propose the mechanism by which these protein targeting bridges may form. We

also functionally distinguish the two types of bridges based on the proteins they can accommodate for LD targeting and present evidence that seipin is the selective barrier for protein targeting.

One potential teleological explanation for the existence of the two different types of bridges is the need for the selective inclusion or exclusion of proteins during LD biogenesis. As discussed previously, LD biogenesis is a highly coordinated process involving many different proteins. For instance, LDAF (LD assembly factor 1) interacts with and accumulates in the middle of the seipin oligomeric complex at the site of LD biogenesis and may aid the directional budding of LDs towards the cytosol as opposed to the ER lumen[48]. Since budding LDs have a limited amount of space on their surfaces, absence of the seipin barrier may result in the competition for the space by different LD targeting proteins and disrupt LD biogenesis. Seipin depletion leads to the formation of aberrant small LDs[44], and we show in this study that absence of seipin results in early accumulation of late-targeting proteins to LDs (**Figure 6**). It remains to be investigated how the altered LD protein targeting affects the LD biogenesis from the ER.

The mechanism behind the selectivity of seipin barrier remains unknown. Interestingly, the hydrophobic hairpin-like domain of GPAT4 targets LDs early unlike full-length GPAT4 (**Appendix B**). Truncation analysis revealed that the C-terminal domain of GPAT4 is necessary and sufficient for the exclusion from early LDs (**Figure B1-3**). This effect was not related to the apparent size of the protein or the catalytic activity of GPAT4 (**Figure B4**). The exclusion mechanism may involve a complex interplay with the specific LD targeting domain of GPAT4, since the addition of the GPAT4 C-terminal domain to other early targeting proteins did not delay their timing of LD targeting (**Figure B5**). Finally, GPAT4 exclusion from early LDs was not dependent on its co-activator elm (CHP1 ortholog), which binds GPAT4 C-terminal domain (**Figure B6**). RNAi of elm reduced LD sizes, but GPAT4 still accumulated on LDs (**Figure B7A**), similar to the mTOR-inhibited conditions (**Figure B8**). Rather, localization of elm on LDs required GPAT4 (**Figure B7B**).

In addition to the seipin barrier, there are likely many additional mechanisms of regulation behind protein targeting to LDs. Among late-targeting proteins, HSD17B11 targeted only a subset of LDs unlike GPAT4 and Lsdsdh1 (**Figure 6**), which indicates that the presence of ER-LD bridges may not be sufficient for HSD17B11 targeting to LDs. On the other hand, HSD17B11 targeted early to all LDs in seipin KO cells, suggesting that this regulation is lost in the absence of seipin. There is also evidence for

a retention mechanism in the ER that prevents proteins from targeting LDs. Ubxd8, which targets LDs early, is retained in the ER via its interaction with the ER resident protein UBAC2, and reducing the expression of UBAC2 resulted in increased Ubxd8 targeting to LDs[173]. Finally, protein degradation may play an important role in regulating LD protein targeting. Treating cells with CB5083, a VCP inhibitor for blocking the ER-associated degradation pathway, led to the accumulation of ER-protein c18orf32 on LDs[75]. However, it is currently unknown how disrupting these regulations affects LD functions and cellular energy homeostasis.

In our current study, the genome-scale screen results were analyzed using previous annotations of gene functions, leading to the identification of previously studied membrane fusion machinery components as the factors required for protein targeting from the ER to LDs. Although current evidences suggest that the unique combination of the components—a Rab, a membrane tethering protein, and SNARE quadruple—may be sufficient to provide specificity to the fusion reaction, it is possible that a previously unidentified component that does not have a role elsewhere in the cell also contributes to the specificity of the membrane fusion between the ER and LDs. Thus, a closer look at the screen results that does not rely on previous gene annotations would be important for identifying such component.

One potential consequence of sharing the components of fusion reaction between different cellular contexts is an unspecific fusion. For instance, Rab GTPases are generally considered to provide membranes with identities, although instances of Rabs having multiple functions have already been documented[97,174]. In mouse liver, 10 weeks of high fat diet feeding, which leads to large hepatic LDs, resulted in a redistribution of the secretory pathway around LDs, including the Golgi collapsing onto LDs, and this retribution was associated with reduced hepatic protein secretion[74]. Since many of the fusion machinery components implicated in establishing ER-LD protein targeting bridges by this study have known functions in ER-Golgi or intra-Golgi trafficking, it is possible that these components drive this redistribution under the pathophysiological state. It remains to be tested whether silencing these components prevents the protein secretion defect *in vivo*.

Chapter II. Perspective

Implications of membrane fusion machinery in establishing the membrane connections between the ER and LDs encompass both old and new paradigms in protein targeting. We have long known the importance of these proteins in protein trafficking, and vesicular trafficking through membrane fusion stands as the central process enabling the secretory pathway of cells. Therefore, it is not entirely unexpected that the membrane fusion machinery is involved in protein transport elsewhere in the cell, especially for performing a task that they are built for. Nevertheless, it is exciting to imagine these well conserved proteins performing a previously unseen type of membrane fusion, namely between a monolayer and a bilayer membrane instead of between two bilayer membranes. Additionally, owing to the hemi-fusion instead of a full fusion, both compartments retain their original identities, making these transient membrane connections a unique type of membrane contact between two distinct organelles. As emphasized before, many aspects of the current model require further validation and investigation. Still, this work opens doors to the possibility of expanding the paradigm in cellular protein trafficking and understanding a fundamental biological process that has important implications in cell biology and beyond.

Chapter III. TMEM19 Modulates Protein Targeting from the ER to LDs by Altering Phospholipid Levels

Genome-scale imaging screen to identify genes modulating GPAT4 targeting to LDs

Proteins target from the ER to LDs for their functions on LDs. For instance, GPAT4 targets from the ER to LDs to catalyze the rate-limiting step of the *de novo* TG synthesis pathway and mediate LD expansion[54]. However, it remains unclear how the protein targeting from the ER to LDs is regulated. Whereas some proteins are required for the process, some proteins may limit protein targeting from the ER to LDs. For instance, deficiency of seipin (of which mutations cause a form of congenital lipodystrophy in humans) or CCT1 (which catalyzes the rate-limiting step of the CDP-choline pathway for PC synthesis) increases GPAT4 targeting to LDs[44,86].

To identify genes involved in regulating protein targeting from the ER to LDs, we performed a genome-scale imaging screen in *Drosophila* S2 R+ cells to identify genes of which RNAi alters GPAT4 targeting to LDs (see **Figure 7** in **Chapter II** for the details about the screen workflow). The screen revealed genes of which knockdowns decrease GPAT4 targeting to LDs (as discussed in **Chapter II**) as well as those of which knockdowns increase GPAT4 targeting to LDs. Among the screen controls were LacZ RNAi as a negative control and Seipin RNAi as a positive control (**Figure 15A**). Upon LacZ RNAi, EGFP-GPAT4 targeted to LDs and formed ring-like intensities around LDs as expected. In addition, an appreciable amount of EGFP-GPAT4 signal was observed in the ER as a reticular pattern outside LD stain. On the other hand, Seipin RNAi resulted in the characteristic supersized LDs with clear EGFP-GPAT4 intensities around them. In contrast with LacZ RNAi, the ER reticular pattern was barely visible upon Seipin RNAi. This relative increase in GPAT4 intensity on LDs as compared to the ER upon Seipin RNAi was accurately quantified as LD targeting ratios, defined as the ratio of the average intensity of EGFP-GPAT4 inside the regions of LDs to that outside LDs for each cell (**Figure 15B**). Median LD targeting ratios for each well of Seipin RNAi (1 well per plate) showed the median of 5.22, which was higher than that of LacZ RNAi (4 wells per plate) with the median of 2.41. In addition, the distribution of median LD targeting ratios for Seipin RNAi (range = [4.089, 5.967]) did not overlap with that for LacZ

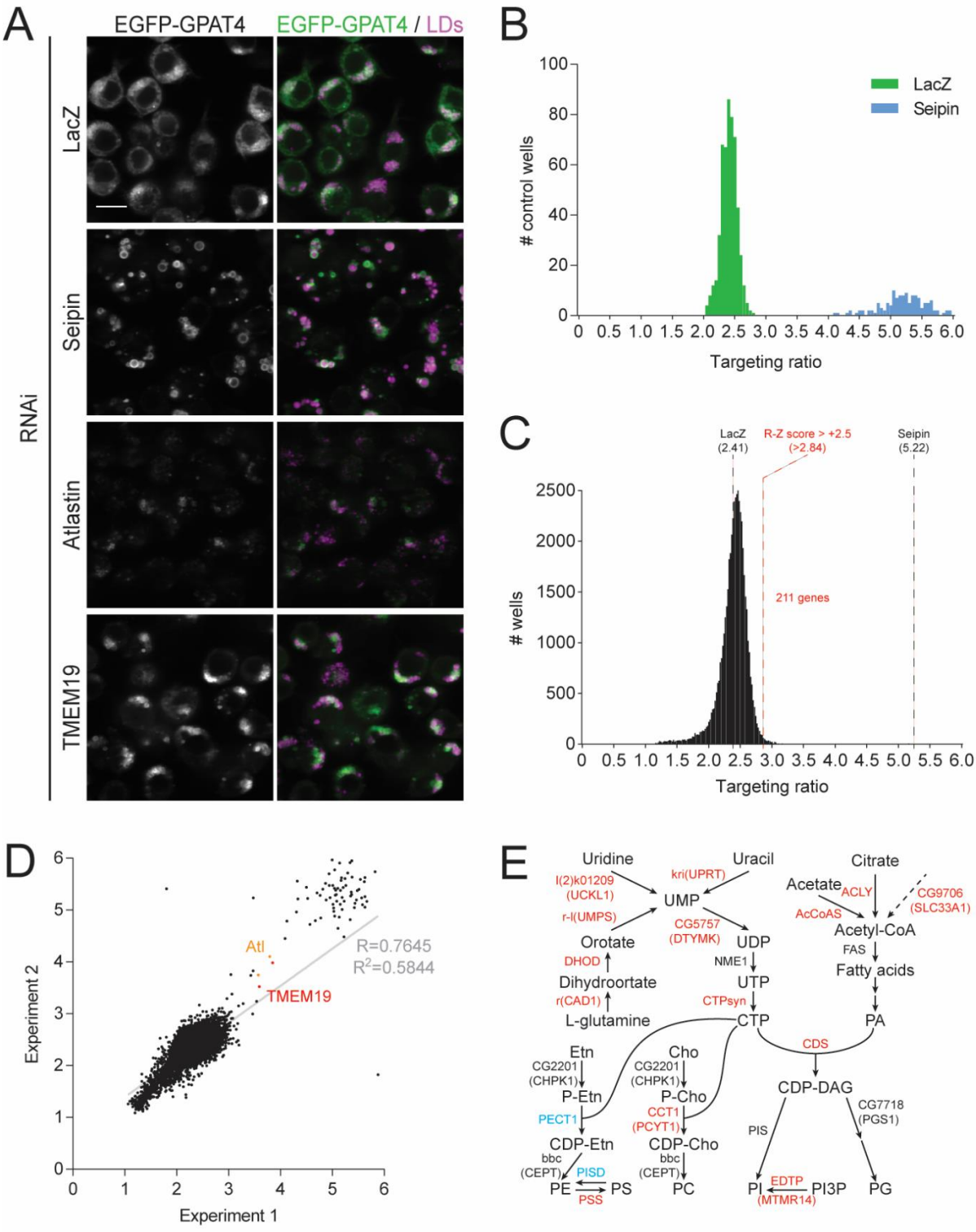

Figure 15. Genome-scale imaging screen identifies genes of which knockdowns increase GPAT4 targeting from the ER to LDs

Figure 15 (continued). Genome-scale imaging screen identifies genes of which knockdowns increase GPAT4 targeting from the ER to LDs

(A) Representative images from the imaging screen. *Drosophila* S2 R+ cell line stably overexpressing EGFP-GPAT4 was subjected to a genome-scale library of dsRNA for RNAi (see **Figure 7** for more details about the screen). Screen controls included a negative control (LacZ) and a positive control (Seipin) of which knockdown increases GPAT4 targeting to LDs. To quantify GPAT4 targeting to LDs, LD targeting ratios, which is the ratio of average intensity of EGFP-GPAT4 on LDs to that outside LDs, were calculated for each segmented cell. Representative images for the screen controls and RNAi that result in the next two highest LD targeting ratios (Atlastin and TMEM19) are shown. Scale Bar, 10μm.

(B) LD targeting ratios for screen controls. Median LD targeting ratios from the screen control wells of all assay plates are shown. Total n = 528 for LacZ, n = 132 for Seipin.

(C) Distribution of targeting ratios from all screen experiments. Median LD targeting ratios for the screen controls (black) and the cut-off for the screen hits (red) are indicated. n =50,688.

(D) Scatter plot of LD targeting ratios from the duplicate genome-scale screen experiments. A regression line, Pearson correlation coefficient (R), and the coefficient of determination (R^2) are shown. RNAi of genes that result in the next two highest LD targeting ratios (Atlastin and TMEM19) are highlighted in orange and red respectively. n = 25,344.

(E) Hits of the screen involved in CTP and phospholipid metabolism. A shortened, combined version of the CTP synthesis pathway, the CDP-choline pathway, and the CDP-DAG pathway is displayed. Enzymes that catalyze reactions are indicated mostly to the left of the arrows. Screen hits with RZ>+2.5 and RZ<-2.5 are highlighted in red and blue respectively. Dashed line, metabolite transporter.

RNAi ([2.034, 2.794]), indicating that the working range of the LD targeting ratios from the screen is sufficiently wide to identify genes of which knockdowns increase GPAT4 targeting to LDs.

RNAi of genes involved in phospholipid metabolism increases GPAT4 targeting to LDs

Robust Z-scores were calculated for all LD targeting ratios from the duplicate screen experiments. 211 genes with robust Z-score > +2.5 were classified as the screen hits that increase GPAT4 targeting to LDs upon knockdown (**Figure 15C** and **Online Supplementary Table 3**). LD targeting ratios from the duplicate genome-scale screen experiments were well correlated, indicating reproducibility of the results (**Figure 15D**). Importantly, no RNAi resulted in LD targeting ratio higher than the LD targeting ratios from Seipin RNAi. Gene knockdowns that result in the next two highest LD targeting ratios after Seipin controls were RNAi against Atlastin (Atl; [3.575, 4.103]) and CG10171 or TMEM19 ([3.523, 3.982]), which are highlighted in blue and red respectively in **Figure 15D**. All other data points with higher LD targeting ratios are Seipin controls or an artifact from control RNAi against Rho1 that results in cell death. Representative screen images for Atlastin and TMEM19 RNAi are shown in **Figure 15A**. Raw images from the screen will become available at lipidportal.org in the future.

Analysis of the screen hits using the Gorilla gene ontology analysis[155]showed no specific enrichment (**Online Supplementary Table 4**). Instead, a close inspection of the 211 genes revealed an enrichment of genes involved in CTP, acetyl-CoA, and phospholipid metabolism (**Figure 15E**). Screen hits, which are highlighted in red, essentially captured the entire *de novo* pyrimidine synthesis pathway for CTP as well as those involved in recycling uridine and uracil. CTP is an important substrate for phospholipid synthesis. In the *de novo* PC synthesis pathway (also called the Kennedy or the CDP-choline pathway), CCT1 catalyzes the rate-limiting step of CDP-choline synthesis from CTP and phosphocholine[22]. CCT1 was also a hit in the screen, which is in accordance with the previous reports that CCT1 knockdown increases GPAT4 targeting to LDs[86]. Alternatively, CTP can be used to make CDP-DAG by CDS (CDP-DAG synthase), which was also a hit in the screen. CDP-DAG can in turn be used for PI or PG synthesis.

A number of genes involved in acetyl-CoA metabolism were also found among the screen hits, including CG9706 (human ortholog SLC33A1), an acetyl-CoA transporter in the ER membrane, and

AcCoAS and ACLY which convert acetate and citrate into acetyl-CoA, respectively, which can be fluxed into fatty acid synthesis. Finally, EDTP (human ortholog MTMR14) which is a lipid phosphatase for PI3P and PI(3,5)P_2 was identified as a hit. Combined, these screen results indicate that a reduction in PC and/or PI synthesis may increase GPAT4 targeting to LDs.

On the other hand, RNAi of genes involved in PE metabolism significantly reduced GPAT4 targeting to LDs (robust Z-score < -2.5; highlighted in blue in **Figure 15E**). These included PECT1 which catalyzes the rate-limiting step of the PE synthesis pathway and PISD which converts PS to PE. Conversely, RNAi of PSS which converts PE to PS increased GPAT4 targeting to LDs. These results indicate that an increase in PE level and/or a decrease in PS level may increase GPAT4 targeting to LDs.

RNAi of Atlastin and TMEM19 increases GPAT4 targeting to LDs

Robust Z-scores for the genes highlighted in **Figure 15E** are shown in **Figure 16A**. Besides the genes involved in phospholipid metabolism, RNAi of two genes, Atlastin and TMEM19, stood out in the magnitudes of the effect on LD targeting ratios from the screen (Robust Z-socre > +8.0; **Figure 16A**, also see **Figure 15D**). Atlastin is a GTPase protein that mediates homotypic fusion of the ER to maintain its tubular structure. Knockdown of genes encoding other ER structural proteins, such as reticulons (Rtln), lunapark (Lnpk), and Reeps (receptor expression enhancing proteins) that are important for maintaining the curvature and junctions of the ER, did not significantly alter GPAT4 targeting to LDs (**Figure 16A**). On the other hand, both dsRNAs against TMEM19 significantly increased GPAT4 targeting to LDs. There is currently no literature on the molecular function of TMEM19.

To verify the screen results, we designed additional dsRNA against select genes and tested its effect on GPAT4 targeting to LDs using a spinning disk confocal microscope, which provides higher resolution images than the automated confocal microscope used in the screen. Using the stable cell line overexpressing EGFP-GPAT4, we confirmed that RNAi of CTPsyn, CDS, and TMEM19 increase GPAT4 targeting to LDs 20 hours after 1mM OA treatment (**Figure 16B&C**). We also additionally tested RNAi of CG32803, a potential ortholog of human LDAF1 (lipid droplet assembly factor 1) and yeast Ldo16 which are LD proteins and known interactors of seipin in their respective systems[48,175,176]. Previous unpublished pulldown experiments in our laboratory indicate that CG32803 indeed interacts with seipin in *Drosophila*

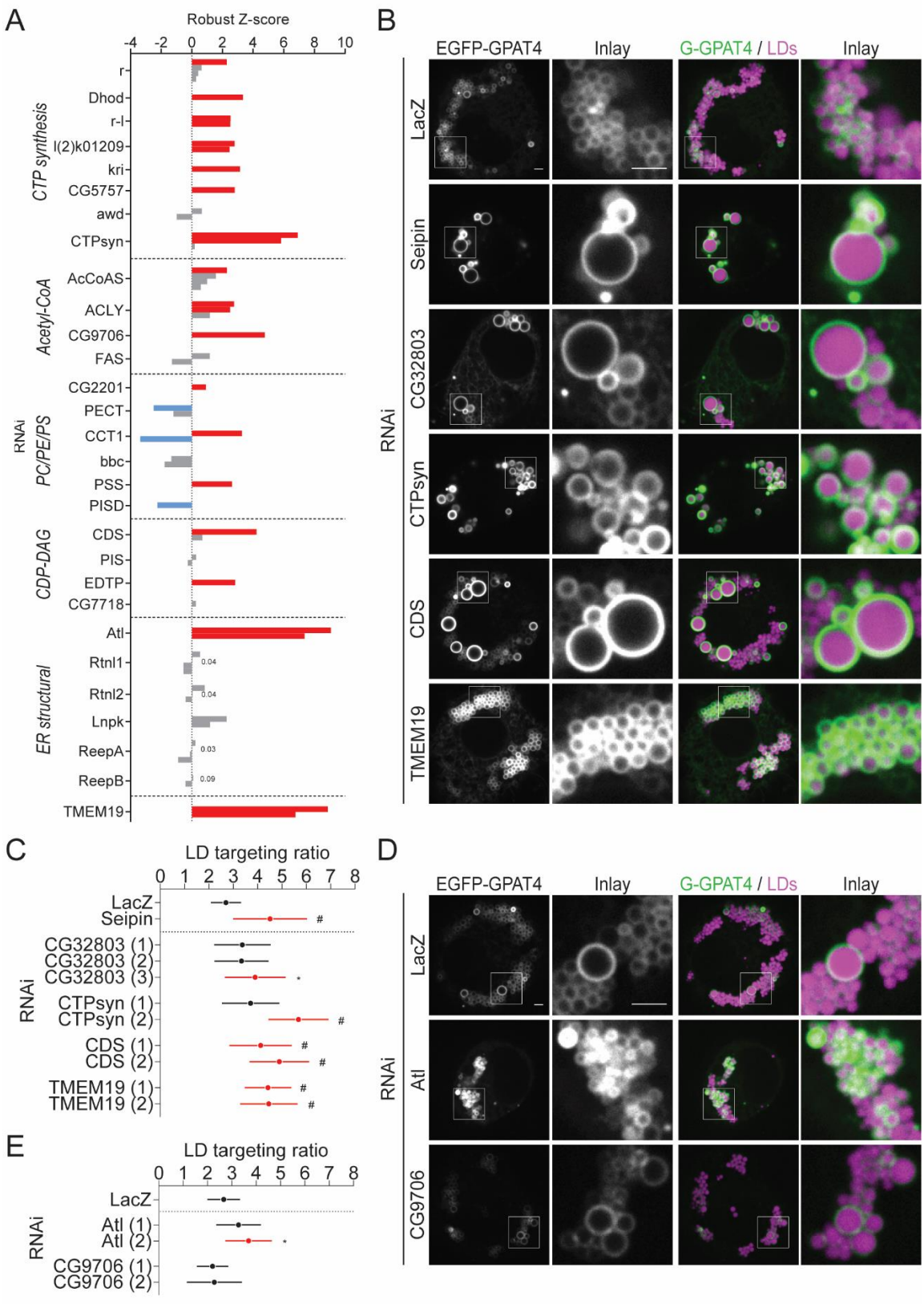

Figure 16. RNAi of genes involved in phospholipid metabolism and ER structural integrity increase GPAT4 targeting to LDs

Figure 16 (continued). RNAi of genes involved in phospholipid metabolism and ER structural integrity increase GPAT4 targeting to LDs

(A) Robust Z-scores for LD targeting ratios. Genes involved in the metabolism of CTP, acetyl-CoA, and phospholipids and in maintaining the ER structure are shown. Each bar represents the mean of two robust Z-scores from the duplicate screen experiments. Different bars indicate unique dsRNA designs. dsRNAs that result in a robust Z-score > +2.5 and <-2.5 in at least one experiment are highlighted in red and blue respectively.

(B) Screen result verification using additional dsRNA designs. Cells stably overexpressing EGFP-GPAT4 were subjected to 2-3 dsRNA's against select genes, treated with 1mM OA for 20 hours, stained with MDH, and imaged using a spinning-disk confocal microscope. Representative images for dsRNA that shows the largest effect on LD targeting are shown. Scale bar, 2μm and 2μm (inlay).

(C) Quantification of (B). LD targeting ratios were calculated from the confocal images. Number in () indicates a unique dsRNA design. Data are represented as mean ± SD of the results from 2-3 independent experiments (7-20 cells each). One-way ANOVA with Bonferroni multiple comparisons correction, *$p<0.05$, #$p<0.0001$ compared to LacZ.

(D) Screen result verification using EGFP-GPAT4^{KI} cells. RNAi of Select genes were tested with the endogenous knock-in cell line. Scale bar, 2μm and 2μm (inlay)

(E) Quantification of (D). LD targeting ratios were calculated from the confocal images. Number in () indicates a unique dsRNA design. Data are represented as mean ± SD of the results from 2 independent experiments (7-12 cells each). One-way ANOVA with Bonferroni multiple comparisons correction, *$p<0.05$ compared to LacZ.

S2 cells (not shown). RNAi of CG32803 increased GPAT4 targeting to LDs, albeit to a lesser extent than Seipin RNAi. Importantly, knockdown of Seipin, CG32803, CTPsyn, and CDS led to supersized LDs, which considered as the results of LD coalescence[44,124]. In contrast, TMEM19 knockdown did not result in apparent changes in LD size, although cells with supersized LDs were occasionally observed (not shown).

Additional screen hits were verified using EGFP-GPAT4^{KI} cells (**Figure 16D&E**). Knockdown of Atlastin in these cells resulted in smaller LDs and increased GPAT4 targeting to LDs. Knockdown of CG9706 (human ortholog SLC33A1) did not increase LD targeting ratio in the contrast to what was observed in the screen. A more thorough verification of additional screen results is needed in the future.

TMEM19 localizes to the ER and is not required for maintaining gross ER morphology

Since RNAi of TMEM19 had a large effect on GPAT4 targeting to LDs but its function has not been previously studied, we decided to investigate the molecular function of TMEM19. TMEM19 is predicted to contain 8 transmembrane domains[177,178] and no signal sequence[179] (**Figure 17A**). Transient overexpression of fluorescently tagged the protein (at either N- or C-terminus) revealed that the protein localizes to the ER (**Figure 17B**).

Given that the knockdown of the ER structural protein Atlastin increased GPAT4 targeting to the similar extent as the knockdown of TMEM19, we tested the possibility that TMEM19 is required for maintaining the ER morphology. To do so, we silenced TMEM19 in CNX99A-EGFP^{KI} cells. Under normal conditions (LacZ RNAi), CNX99A-EGFP was evenly found throughout the reticular ER and the nuclear envelop (**Figure 17C**). This reticular pattern was also observed interwoven between LDs (see inlay). On the other hand, Atlastin RNAi resulted in rounded cells with uneven, hyperintense CNX99A-EGFP signals throughout the cell and minor loss in the reticular pattern compared to LacZ RNAi. Nuclear envelop also showed hyperintensity. Finally, RNAi of seipin or TMEM19 did not result in changes in the gross ER morphology. CNX99A-EGFP signals were found in a reticular pattern throughout the cell and evenly around the nucleus and interwoven between LDs. Therefore, we conclude that TMEM19 is not required for maintaining the gross ER morphology.

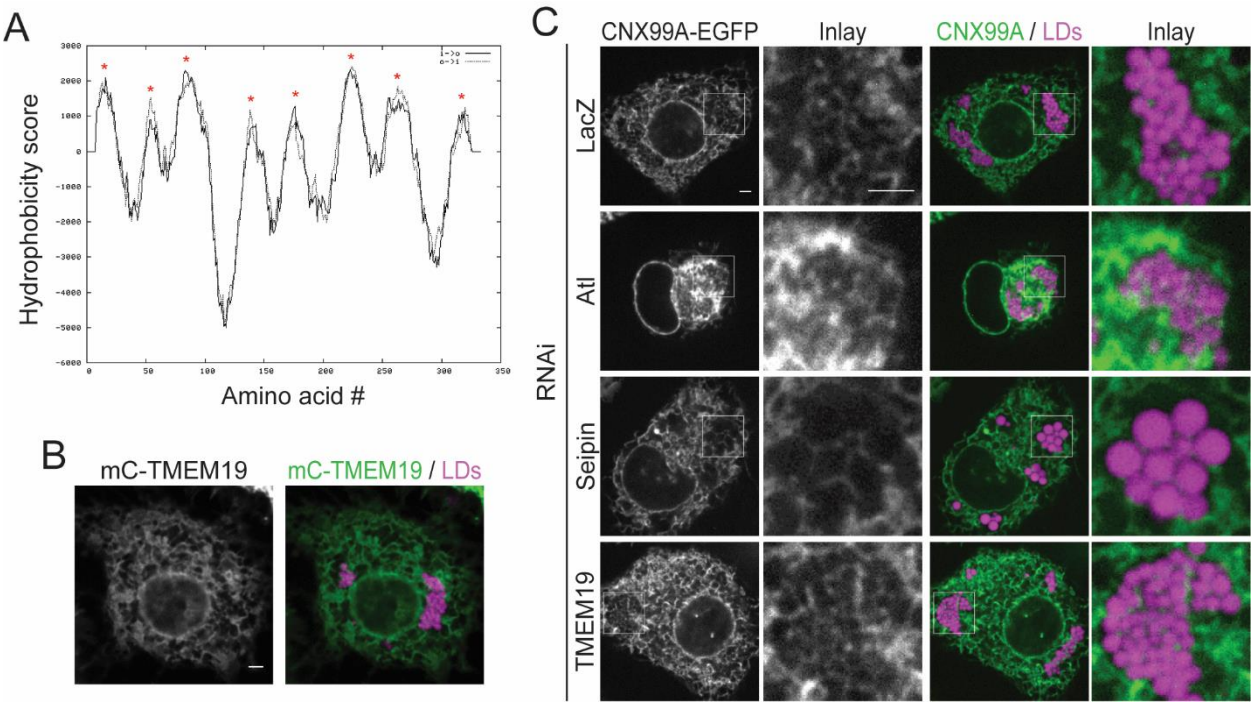

Figure 17. TMEM19 localizes to the ER and is not required for maintaining gross ER morphology
(A) Transmembrane prediction for TMEM19. TMPred[178] was used to predict the number of transmembrane domains in TMEM19. Red stars indicate the peaks in hydrophobicity scores indicative of predicted transmembrane domains.
(B) TMEM19 localization. Overexpressed mCherry-TMEM19 was visualized using a confocal microscope. LDs were stained with MDH. Scale bar, 2μm.
(C) Gross ER morphology upon gene knockdowns. The effect of gene RNAi on the gross ER morphology was tested using CNX99A-EGFP^{KI} cells. Scale bar, 2μm and 2μm (inlay).

TMEM19 is predicted to be a lipid-related enzyme

Predicted orthologs of TMEM19 were found in fly (*Drosophila melanogaster*; gene name CG10171, gene ID 39501), thale cress (*Arabidopsis thaliana*; AT5G19930, 832115), zebrafish (*Danio rerio*; tmem19, 415188), frog (*Xenopus tropicalis*; tmem19, 548833), rat (*Rattus norvegicus*; Tmem19, 299800), mouse (*Mus musculus*; Tmem19, 67226), and humans (*Homo sapiens*; TMEM19, 55266)[180], and their protein sequences were well conserved. Human and fly TMEM19 had 45% amino acid sequence identity (148 AAs out of 328) and 69% similarity (227 out of 328) with 4% gap (12 out of 328). Interestingly, much of the identical and similar regions were in the predicted transmembrane domains.

We then used HHpred[181] to find a potential structural homology to the proteins with known structures (**Table 1**). Although none of the predictions reached significance (low E-values and high P-values), it yielded many interesting predictions. For instance, N-terminal half of TMEM19 was predicted to

Table 1. Structural homology prediction for TMEM19 using HHPred[181]

No	Hit	Prob	E-value	P-value	HMM	Template HMM
1	4Q2G_B	Phosphatidate cytidylyltransferase	85.3	16	170-281	151-252 (290)
2	5NV9_A	Putative sodium:solute symporter	61.8	47	52-126	413-496 (496)
3	5XJ5_A	Glycerol-3-phosphate acyltransferase	53.8	1.60E+02	50-132	119-201 (201)
4	2XQ2_A	sodium/glucose cotransporter	52.8	1.10E+02	58-182	439-563 (593)
5	3DH4_D	sodium/glucose cotransporter	47.7	67	58-150	410-513 (530)
6	2LX0_A	Membrane fusion protein p14	30.9	99	92-113	11-32 (32)
7	5GUF_A	CDP-archaeol synthase	36.8	4.00E+02	216-281	58-113 (182)
8	1KVD_A	SMK TOXIN; TOXIN, HALOT	25.4	1.40E+02	209-236	17-44 (63)
9	4ZP0_A	Multidrug transporter MdfA	22.8	3.50E+02	62-150	134-224 (392)
10	4M64_A	Melibiose carrier protein	21	9.10E+02	72-150	154-244 (486)
11	1FFT_G	UBIQUINOL OXIDASE	20.8	1.00E+03	49-150	9-108 (315)
12	2JLN_A	MHP1; HYDANTOIN, TRANSPORTER	20.5	5.60E+02	50-124	369-462 (501)

have a structural homology to a sodium/sialic acid symporter from *Proteus mirabilis* (#2 among predictions) and a sodium/glucose cotransporter from *Vibrio parahaemolyticus* (#4). C-terminal half of TMEM19 was predicted to have a structural homology to CDS from *Thermotoga maritima* (#1), which was another hit in our screen (**Figure 15&16**), and to CDP-archaeol synthase from *Aeropyrum pernix* (#7). Importantly, CDS contains 8 transmembrane domains, as it is predicted for TMEM19.

D150 is critical for rescuing the effect of TMEM19 depletion on GPAT4 targeting

RNAi of TMEM19 resulted in one of the largest effects in GPAT4 targeting to LDs in the genome-scale screen, along with many genes encoding enzymes of various phospholipid metabolism pathways. TMEM19 also contains many predicted transmembrane domains that are highly conserved through evolution, which is a shared feature of lipid-related enzyme. In addition, TMEM19 is predicted to be structurally similar to CDS, an important enzyme in a phospholipid synthesis pathway. Therefore, we hypothesized that TMEM19 is a lipid-related enzyme involved in phospholipid metabolism.

To further investigate the function of TMEM19, we created TMEM19 knockout *Drosophila* S2 R+ cells using CRISPR-Cas9 ($TMEM19^{KO}$ cells). As expected, overexpressed EGFP-GPAT4 targeted LDs strongly in these cells (**Figure 18A&B**, mock transfection). Importantly, GPAT4 targeting to LDs was reduced upon the co-expression of mCherry-TMEM19 (**Figure 18A&B**).

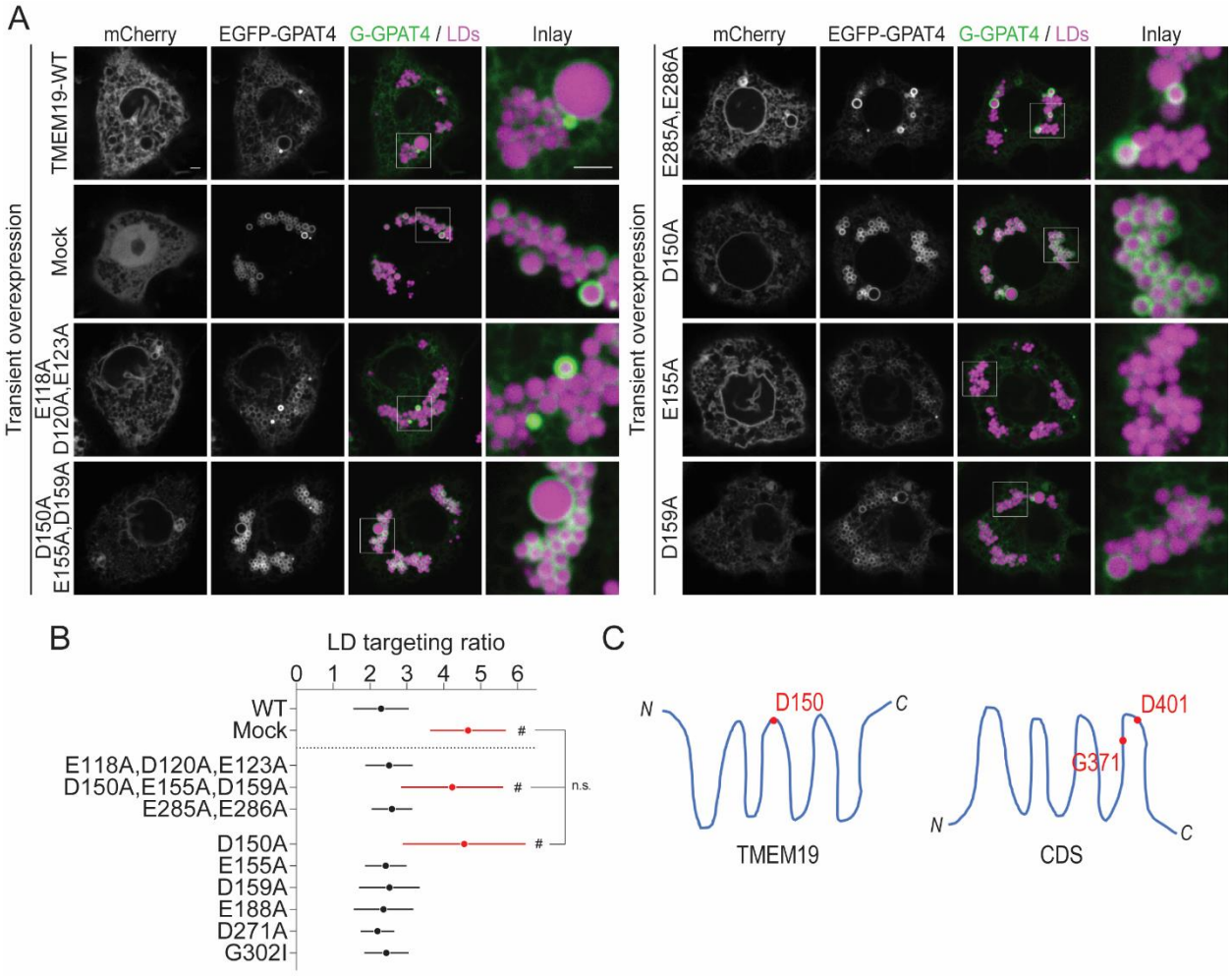

Figure 18. D150 of TMEM19 is critical for rescuing the effect of TMEM19 depletion on GPAT4 targeting to LDs

(A) Effect of overexpressing wildtype and mutant TMEM19 in GPAT4 targeting in TMEM19^{KO} cells. Cells were co-transfected with the constructs encoding EGFP-GPAT4 and mCherry (mock) or mCherry-TMEM19 (wildtype or mutants), treated with 1mM OA for 20 hours, and stained with MDH for imaging. Scale bar, 2μm and 2μm (inlay).

(B) Quantification of (A). LD targeting ratios were calculated from the confocal images. Data are represented as mean ± SD of the results from 2-3 independent experiments (6-21 cells each). One-way ANOVA with Bonferroni multiple comparisons correction, #p<0.0001 compared to WT.

(C) Position of D150 with regards to the predicted transmembrane domains of TMEM19. Critical catalytic residues of CDS are displayed for comparison. The two models were drawn upside down based on predictions from TMPred[178] (top is the cytosolic side and bottom is the ER luminal side of the ER membrane).

To identify a critical residue required for TMEM19 function, we mutated conserved negatively charged residues (aspartate and glutamate residues) to alanine and glycine residues to isoleucine and tested the ability of the mutants to reduce LD targeting ratio of GPAT4 in TMEM19^{KO} cells. These residues were chosen because they are critical for the enzymatic activity of CDS[182], which is predicted to be structurally similar to and had a similar effect on GPAT4 targeting upon RNAi as TMEM19. Residue D401 of CDS is thought to hold the cations Mg^{2+} and K^{+} in place so that they can interact with the negatively charged residues of the phosphate groups of CTP, whereas G371 of CDS is thought to accommodate the space necessary for these cations[182]. Among the different combinations of mutations in conserved aspartate, glutamate, and glycine residues of TMEM19, D150A+E155A+D159A triple mutant lost the ability to reduce LD targeting ratio as compared to wildtype TMEM19 (**Figure 18A&B**). When mutated individually, the D150A mutant but not the E155A or D159A mutants prevented TMEM19 from reducing GPAT4 targeting in TMEM19^{KO} cells.

D150 is predicted to be located at the soluble portion of the protein between 4th and 5th predicted transmembrane domains (**Figure 18C**). Of note, the aspartate residue critical for the catalytic activity of CDS is located at the soluble portion of the protein between 7th and 8th transmembrane domains[182].

Human TMEM19 cannot substitute for yeast CDS1

Given the similarities between CDS and TMEM19, we decided to test if TMEM19 can substitute for CDS. *Saccharomyces cerevisiae* was chosen since the organism does not have a predicted ortholog of TMEM19, and its CDS1 (systematic name: YBR029C) is essential for life. We found a yeast strain with temperature-sensitive CDS1 (ts-CDS1)[183] and transformed the cells, along with a wildtype yeast strain with the same background as the ts-CDS1 yeast, with constructs encoding human CDS1 (hCDS1), 3XFLAG-hCDS1, hTMEM19, or 3XFLAG-hTMEM19 under the constitutively active ADH promoter as well as the hygromycin resistance gene.

Successfully transformed colonies were selected using hygromycin and plated onto a new hygromycin plates (**Figure 19A**). All transformed colonies grew well at permissive temperature of 30°C (top). When grown at non-permissive temperature of 37°C (bottom), all colonies transformed with hCDS1 (6/6) or FLAG-hCDS1 (6/6) constructs grew, with a slight retardation for those with the hCDS1 construct.

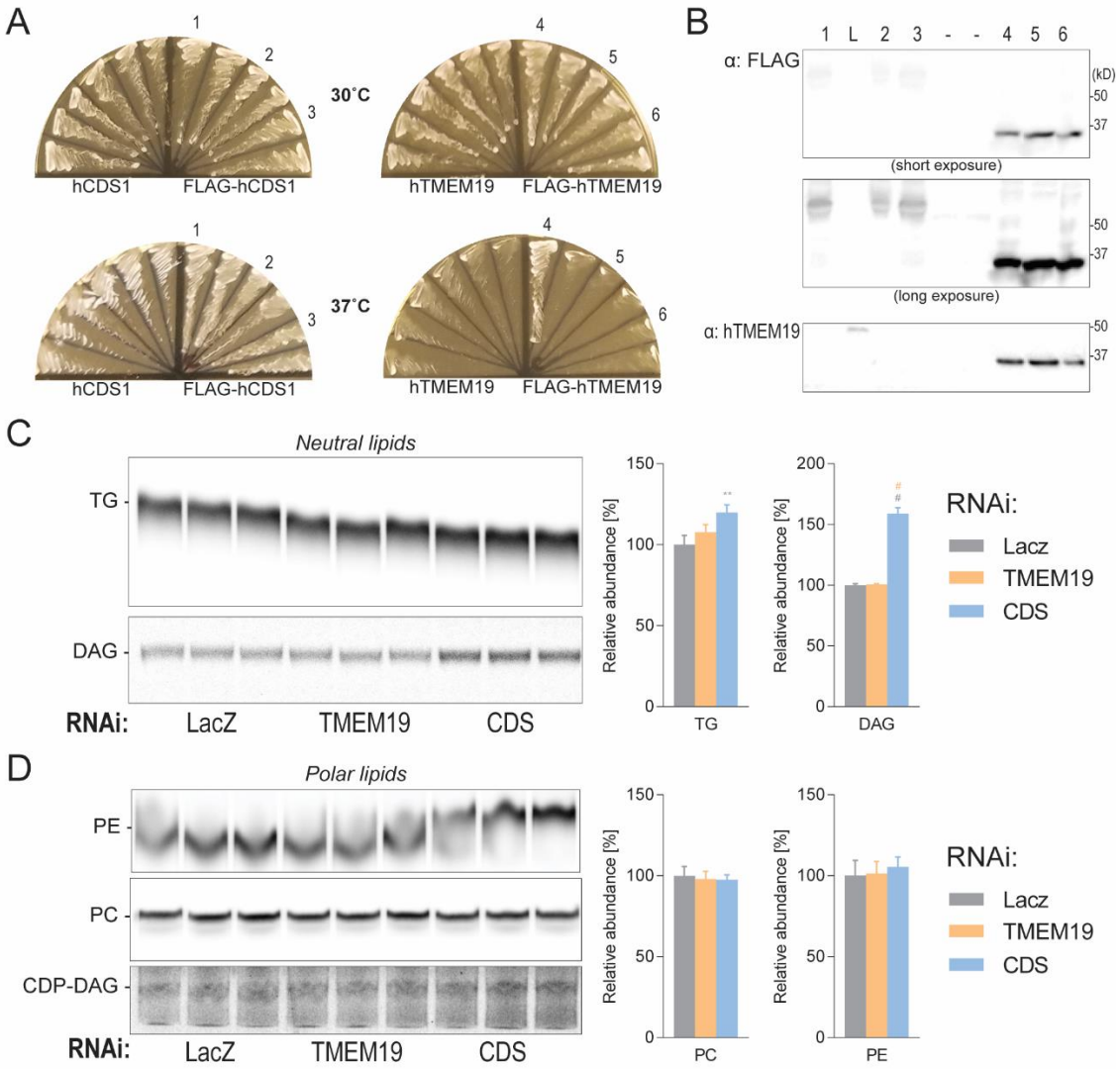

Figure 19. hCDS1, but not hTMEM19, can substitute for yeast CDS1

(A) Temperature-sensitive CDS1 mutant yeast rescue. The mutant yeast was transformed with a construct encoding human CDS1 or human TMEM19 (untagged or N-terminally tagged with 3XFLAG) under the ADH promoter along with hygromycin resistance gene. Cells stably expressing the constructs were selected using hygromycin and were subjected to permissive (30˚C) or non-permissive (37˚C) temperatures for growth.

(B) Western blot for yeast whole cell lysates from (A). Expressions of the transformed constructs (FLAG-hCDS1 or FLAG-hTMEM19) were verified. Sample numbers correspond to the yeast strains in (A). – indicates negative controls that do not express neither constructs. L, ladder. Predicted molecular weights, 3XFLAG-hCDS1: 56.1kDa and 3XFLAG-hTMEM19: 39.2kDa.

(C) Thin-layer chromatography using ^{14}C-oleic acid in *Drosophila* S2 R+ cells upon RNAi. WT cells were treated with dsRNA against LacZ, TMEM19, or CDS, and was treated with hot and cold oleic acid (1mM total). After 18 hours, lipids were extracted and run in TLC for detecting neutral lipids (hexane:DEE:AA=80:20:1). Three experimental replicates are run side-by-side. Locations of the standards were determined using iodine gas and are shown on the left. Each image was processed with the same intensity minimum but different intensity maximum. Band quantifications are shown on the right as mean + SD. One-way ANOVA with Bonferroni multiple comparisons correction, **p<0.01, #p<0.0001 compared to LacZ (grey) or TMEM19 RNAi (yellow).

(D) Polar lipids analysis. Same as (C), except for using a more polar solvent (chloroform:ethanol:water: triethylamine = 30:35:7:35) to detect phospholipid species.

On the other hand, none of the ts-CDS1 colonies transformed with hTMEM19 (0/6) grew at 37°C. 1 out of 6 ts-CDS1 colonies transformed with FLAG-hTMEM19 grew at 37°C (**Figure 19A**, bottom right, #4), but none of 16 colonies in an additional plate grew at 37°C (0/16; not shown), indicating that the one colony that grew likely had spontaneous mutation in the *CDS1* loci. Wildtype strains transformed with these constructs grew well at both 30°C and 37°C (6/6 for all conditions; not shown).

Expression of FLAG-hCDS1 or FLAG-hTMEM19 was confirmed in select colonies (#1~6) using western blot (**Figure 19B**). Notably, the expression level of FLAG-hTMEM19 was much higher in the transformed colonies compared to that of FLAG-hCDS1 in their respective colonies. The bands for 3XFLAG-hCDS1 were found at the expected height of 56.1kDa. The bands for 3XFLAG-hTMEM19 traveled right below 37kDa marker, which is slightly lower than the expected molecular weight (39.2kDa). The bands for 3XFLAG-hTMEM19 were further confirmed with hTMEM19 antibodies raised in a rabbit using a peptide from the C-terminal region of hTMEM19 (amino acids #280-307 out of 336) as the immunogen (**Figure 19B**). These results indicate that hCDS1 but not hTMEM19 can substitute for yeast CDS1.

To test if TMEM19 depletion causes similar changes in lipid levels as CDS depletion, we knocked down TMEM19 or CDS in wildtype *Drosophila* S2 R+ cells, labeled lipids with ^{14}C-oleic acid (in a trace amount within 1mM OA treatment for 20 hours), and performed thin-layer chromatography (TLC) to detect changes in lipid levels. Upon lipid extraction, lipids were normalized to the total protein amount and were subjected to TLC using two different solvent system, one for neutral lipids (hexane : DEE : AA = 80 : 20 : 1; **Figure 19C**) and another for polar lipids (chloroform : ethanol : water : triethylamine = 30 : 35 : 7 : 35; **Figure 19D**), which is the most commonly system for detecting CDP-DAG[184,185].

Compared to LacZ RNAi, CDS RNAi moderately but significantly increased TG (**Figure 19C**). This result is consistent with what appears to be increased LD area upon CDS RNAi in **Figure 16B**. In addition, DAG levels were highly increased upon CDS RNAi. This was expected, since the lack of CDS will flux more PA into the synthesis of DAG and TG via the *de novo* TG synthesis pathway instead of fluxing PA into the synthesis of CDP-DAG synthesis. In contrast, TMEM19 RNAi did not significantly alter the levels of TG or DAG (**Figure 19C**). Among the phospholipids, PE and PC levels did not change upon knockdown of TMEM19 or CDS (**Figure 19D**). CDP-DAG was not clearly separated from another band,

which runs close to the bands for LPI and LPC (which runs slightly above CDP-DAG). The lower of the two bands, which is suspected to be CDP-DAG, was very faint, indicating that the amount of CDP-DAG in cells is at most very low. This is not unexpected, since CDP-DAG is known to be a short-lived species. As a result, we could not conclude whether RNAi of TMEM19 or CDS alters the level of CDP-DAG in cells.

Depletion or overexpression of TMEM19 alters cellular lipid levels

To determine the potential enzymatic function of TMEM19, we performed lipid labeling experiment with ^{14}C-oleic acid (in a trace amount within 1mM OA treatment for 20 hours) under TMEM19 depleted or overexpressing conditions (**Figure 20**). Tested conditions included: wildtype S2 R+ cells as a control, TMEM19^{KO} cells, TMEM19^{KO} cells transiently overexpressing wildtype TMEM19, and TMEM19^{KO} cells transiently overexpressing the TMEM19-D150A mutant. Upon the lipid extraction and the normalization to the total protein amount, samples were subjected to TLC using two different solvent system, one for neutral lipids (hexane : DEE : AA = 80 : 20 : 1; **Figure 20A**) and another for polar lipids (chloroform : methanol : water : triethylamine = 65 : 25 : 4; **Figure 20B**, note that this system is different from the one used in **Figure 19D**).

Among neutral lipids, TMEM^{KO} cells showed increased DAG levels and a trend towards increased TG (p=0.06 compared to WT) compared to the wildtype cells (**Figure 20A**). This contrasts with what was observed for TMEM19 knockdown, which had little effect on the DAG and TG levels (**Figure 19C**). This may be due to the compensatory changes in various lipid pathways from the long-standing depletion of TMEM19 in TMEM19^{KO} cells, as opposed to cells under TMEM19 RNAi. The increases in TG and DAG levels in TMEM19^{KO} cells were reversed when either wildtype TMEM19 or TMEM19-D150A mutant was overexpressed, indicating that the intial changes are the results of TMEM19 depletion (**Figure 20A**).

Additional changes in lipid levels were observed between the bands for TG and DAG. Unknown lipid species (1) changed in the similar patterns as TG and DAG: lipid (1) was increased in TMEM19^{KO} cells compared to wildtype cells, and the increase was reversed by the overexpression of either wildtype or the TMEM19-D150A mutant (**Figure 20A**). On the other hand, unknown lipid species (2) remained unchanged in TMEM19^{KO} cells compared to WT cells but was increased upon the overexpression of wildtype TMEM19 and the TMEM19-D150A mutant, albeit to a smaller degree. Free fatty acids (FFA) is

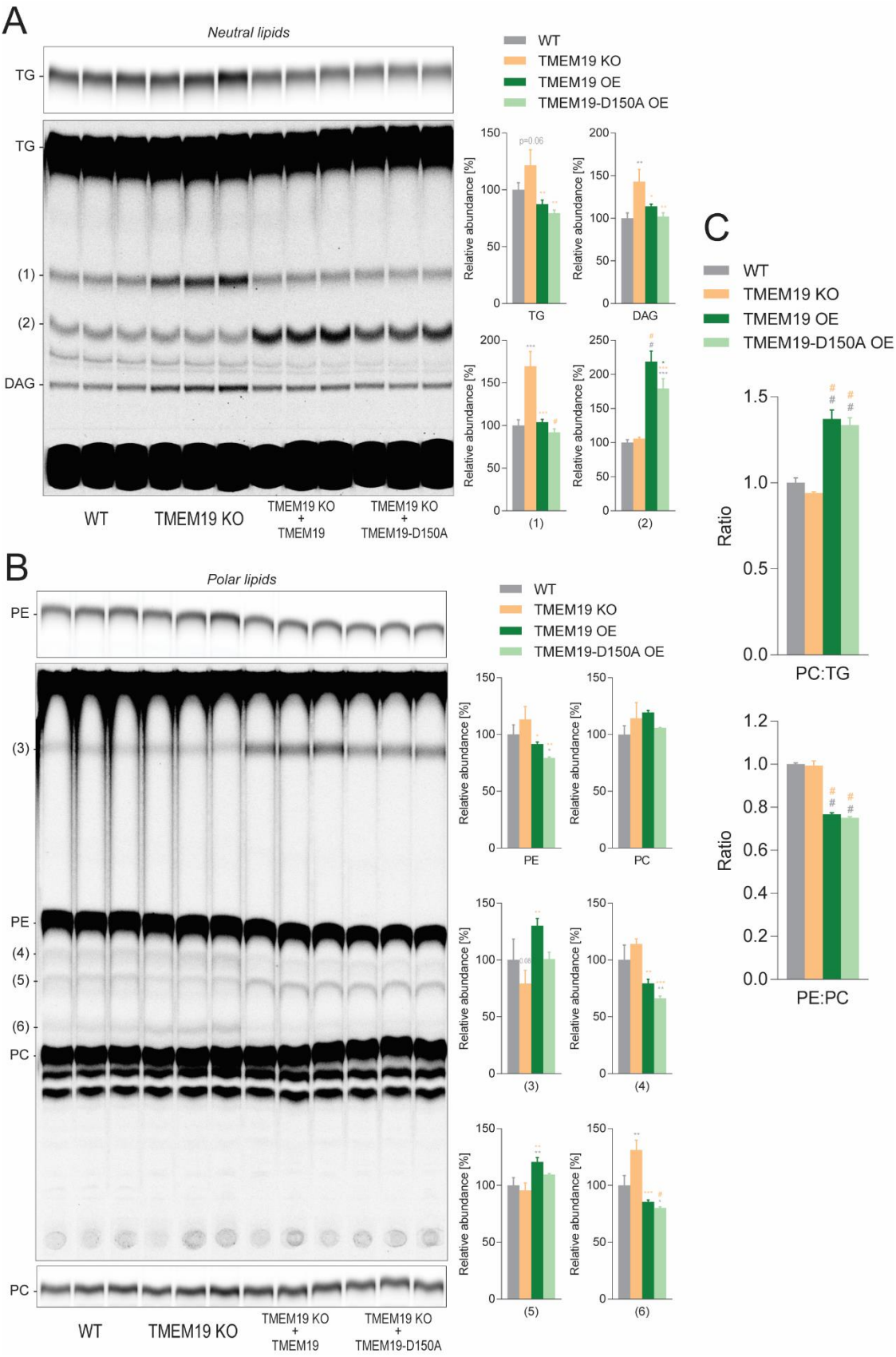

Figure 20. Depletion or overexpression of TMEM19 alters cellular lipid levels

Figure 20 (continued). Depletion or overexpression of TMEM19 alters cellular lipid levels
(A) Changes in neutral lipids upon deleting or overexpressing TMEM19. WT cells, TMEM19^{KO} cells, and TMEM19^{KO} cells overexpressing (OE) mCherry-TMEM19 or mCherry-TMEM19-D150A were treated with hot and cold oleic acid (1mM total). After 18 hours, lipids were extracted and run in TLC for detecting neutral lipids (hexane:DEE:AA=80:20:1). Three experimental replicates are run side-by-side in TLC. Locations of the standards were determined using iodine gas and are shown on the left. Lower contrast image for the TG bands are shown above the plate (same intensity minimum but higher intensity maximum). Band quantifications are shown on the right as mean + SD. One-way ANOVA with Bonferroni multiple comparisons correction, *p<0.05, **p<0.01, ***p<0.001, #p<0.0001 compared to WT cells (grey), TMEM19^{KO} cells (yellow), or TMEM19^{KO} cells overexpressing WT-TMEM19 (green).
(B) Changes in polar lipids upon deleting or overexpressing TMEM19. Same as (A), but using a polar solvent (chloroform:methanol:water=65:25:4). Lower contrast images for the PE and the PC bands are shown above and below the entire plate image respectively. Band quantifications are shown on the right as mean + SD. One-way ANOVA with Bonferroni multiple comparisons correction, *p<0.05, **p<0.01, ***p<0.001, #p<0.0001 compared to WT cells (grey) or TMEM19^{KO} cells (yellow).
(C) PC:TG and PE:TC ratios. The ratios were calculated and normalized to the ratios of the wildtype cells. One-way ANOVA with Bonferroni multiple comparisons correction, #p<0.0001 compared to WT cells (grey) or TMEM19^{KO} cells (yellow).

one of the lipids that run between TG and DAG in the solvent system used here. Although FFA was included among the standards, its band appeared as a long vertical smudge, making it impossible to tell the true location of the band. Based on previous TLC analyses in the laboratory, we suspect that unknown lipid species (2) may be FFAs.

Among polar lipids, PE levels decreased significantly upon overexpressing either wildtype TMEM19 or the TMEM19-D150A mutant in TMEM19^{KO} cells (**Figure 20B**). Magnitude of the decrease was larger with the overexpression of the mutant TMEM19. PC levels did not significantly change under any of the four conditions. Besides PC and PE, levels of unknown lipid species that are labeled with ^{14}C-oleic acid changed. Unknown lipid species (3), which ran close to the solvent front, increased upon overexpression of wildtype TMEM19 but not the D150A mutant. There was also a trend toward reduction in TMEM19^{KO} cells compared to WT cells ($p=0.08$). This pattern of a decrease upon depletion and an increase upon overexpression of wildtype but not the mutant TMEM19 makes unknown lipid species (3) a potential product of TMEM19 enzymatic activity.

There were additional changes in the levels of other unknown lipid species. Unknown lipid species (4) and (6), both of which ran between PC and PE standards, decreased significantly upon overexpression of either wildtype or the mutant TMEM19. Notably, unknown lipid species (6) was increased in TMEM19^{KO} cells compared to wildtype cells. Lastly, unknown lipid species (5) increased upon expression of wildtype TMEM19 but not the D150A mutant.

In summary, depletion or overexpression of TMEM19 changed levels of various lipids in cells labeled with ^{14}C-oleic acid. These results support the hypothesis that TMEM19 is a lipid-related enzyme. Importantly, TMEM19 overexpression increased PC to TG ratio (relative phospholipid excess) and decreased PE to PC ratio (relative increase in conical phospholipid; **Figure 20C**), both of which increase packing defects on LDs. These findings correlate well with the decreased GPAT4 targeting in TMEM19 overexpressing cells.

Since we did not know the identities of many of the visualized lipid bands, it was difficult to predict the enzymatic function of TMEM19 based on the results of this experiment. One unexpected observation was that the overexpression of TMEM19-D150A mutant, which could not rescue the effect of TMEM19 depletion on GPAT4 targeting to LDs, also changed the levels of various lipids in the patterns nearly

identical to the overexpression of wildtype TMEM19. This indicates that TMEM19-D150A mutant is likely also catalytically active.

Lipidomic analysis reveals that TMEM19 modulates the balance between TG and membrane phospholipids

To identify lipids of which abundance changes upon the depletion or the overexpression of TMEM19, we performed a lipidomic analysis of whole cell lipids under the same four conditions used for the TLC experiment: wildtype *Drosophila* S2 cells, TMEM19^{KO} cells, TMEM19^{KO} cells transiently overexpressing wildtype TMEM19, and TMEM19^{KO} cells transiently overexpressing TMEM19-D150A mutant (**Figure 21**). Each condition was prepared in quadruplet. One of the samples for TMEM19^{KO} cells did not segregate well with the rest of the samples in the same group in the principal component (PCA) analysis, so it was excluded from further analysis. The remaining samples correlated well within each group. The PCA plot for the accepted samples is shown in **Figure 21A**.

Although samples were normalized to the same protein amount prior to mass spectrometry, sum of the lipid abundance levels were significantly higher in wildtype cells (mean = 2.91E+11) than the other three groups (TMEM19^{KO}, 2.33E+11; TMEM19 OE, 2.13E+11; TMEM19-D150A OE, 2.22E+11), and wildtype cells contained highest lipid abundance in 15 out of 18 detected classes. This may reflect an intrinsic difference in the cell background that arises from cell sorting during cell line generation, such as cell size. Therefore, we decided to compare percentages of lipid abundance relative to total lipid abundance.

Among the lipids in the *de novo* TG synthesis pathway, TG, DAG, and PA were detected in the lipidomic analysis (**Figure 21B**). As was observed in the radiolabeling experiment (**Figure 20A**), TG was increased in TMEM19^{KO} cells compared to wildtype cells but to a smaller degree when TMEM19 was overexpressed (**Figure 21B**). DAG was moderately decreased upon the overexpression of wildtype TMEM19 and highly decreased upon the TMEM19-D150A overexpression. PA was only detected in a small amount and was significantly increased when the mutant TMEM19 was overexpressed.

Levels of various phospholipids also changed upon the deletion or the overexpression of TMEM19 (**Figure 21C&D**). Notably, PS level was decreased in TMEM19^{KO} cells compared to WT cells,

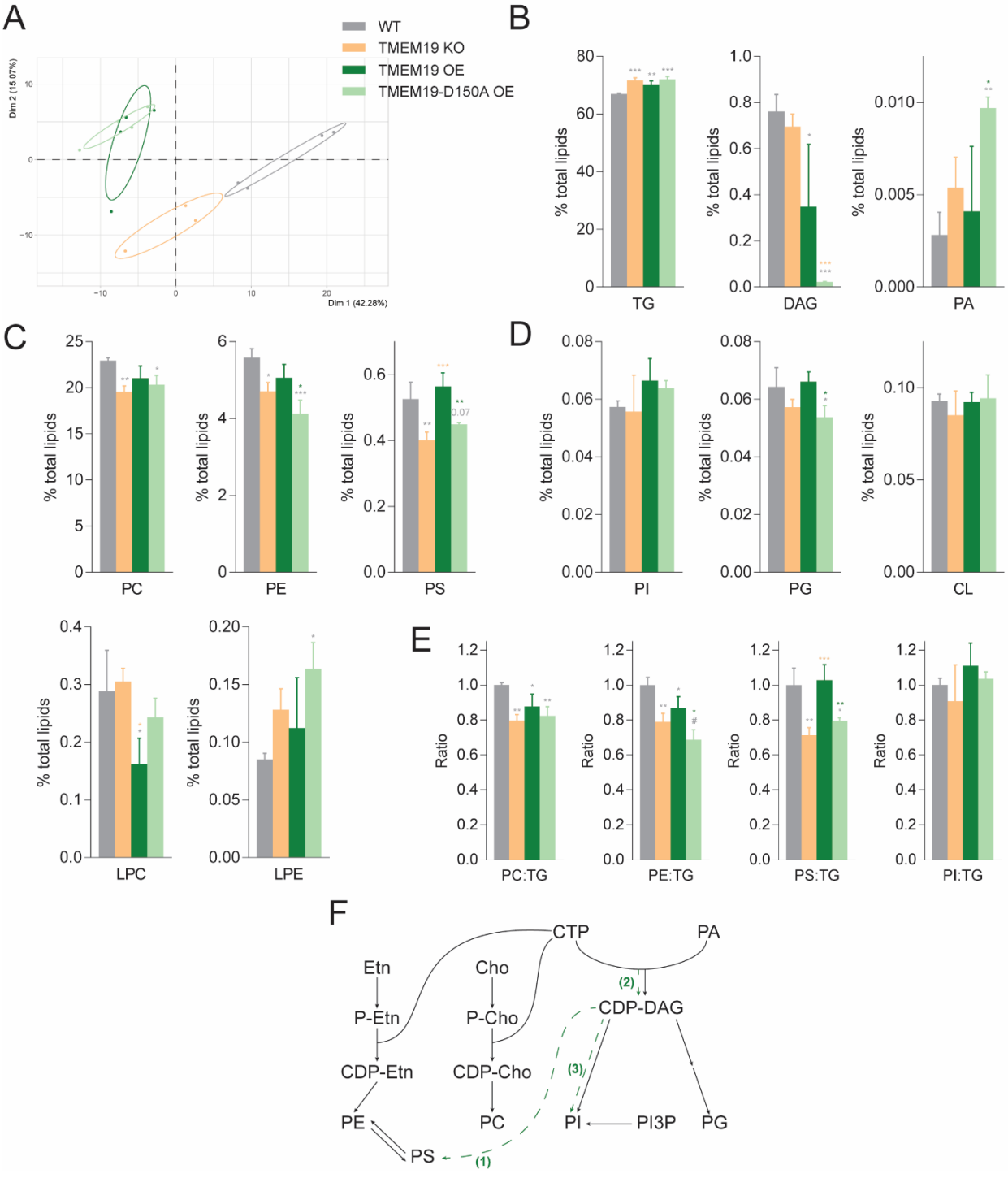
A
WT
TMEM19 KO
TMEM19 OE
TMEM19-D150A OE
Dim 2 (15.07%)
Dim 1 (42.28%)
B
% total lipids
TG
DAG
PA
C
PC
PE
PS
LPC
LPE
D
PI
PG
CL
E
Ratio
PC:TG
PE:TG
PS:TG
PI:TG
F
CTP
PA
Etn
Cho
(2)
P-Etn
P-Cho
CDP-DAG
CDP-Etn
CDP-Cho
(3)
PE
PC
PI
PI3P
PG
PS
(1)

Figure 21. Lipidomic analysis of cells lacking or overexpressing TMEM19 reveals changes in phospholipid content and composition

(A) PCA analysis of the results from lipidomics experiment. Groups separated well from each other except for the two conditions overexpressing wildtype TMEM19 or the D150A mutant.

(B-D) Lipidomic analysis results. % total lipids for various classes of lipids identified in the lipidomic analysis are shown as mean + SD. n = 4 for all groups except TMEM19 KO (n=3). One-way ANOVA with Bonferroni multiple comparisons correction, *p<0.05, **p<0.01, ***p<0.001 compared to LacZ (grey), TMEM19 KO (yellow), or TMEM19 OE (green).

(E) Phospholipid to TG ratios. The ratio of the abundance of PC, PE, PS, and PI to that of TG was calculated for each sample and normalized to the LacZ control. Data are shown as mean + SD for each group. One-way ANOVA with Bonferroni multiple comparisons correction, *p<0.05, ***p<0.001 compared to LacZ (grey).

(F) Potential enzymatic activity of TMEM19. A diagram of the phospholipid synthesis pathways from **Figure 15** was modified to demonstrate three potential enzymatic activity of TMEM19 that can explain the results from lipidomic analysis (green dashed lines (1)~(3)).

and recovered to the level in WT cells when the wildtype but not the mutant TMEM19 was overexpressed. Interestingly, two other major membrane phospholipid species, PC and PE, followed a similar pattern, although their increases upon TMEM19 overexpression were modest. Among related species, LPC level was significantly decreased upon overexpression of TMEM19.

PG in the CDP-DAG pathway also followed the similar pattern of a decrease upon TMEM19 depletion and an increase upon the overexpression of wildtype but not the mutant TMEM19, but its downstream product, cardiolipin, did not change in any of the conditions.

Since phospholipid amount is critical for shielding packing defects on the LD monolayer membranes, we calculated phospholipid (PC, PE, PS, and PI) to TG ratios (**Figure 21E**). We found significant decreases in the PC:TG, PE:TG, and PS:TG ratios in TMEM19^{KO} cells compared to wildtype cells, indicating that LDs in TMEM19^{KO} cells may exhibit more packing defects. No change was observed in the PI:TG ratio. Overexpressing TMEM19 in TMEM19^{KO} cells appeared to reverse the decrease in the phospholipid to TG ratios, although the change was statistically significant only for the PS:TG ratio. Importantly, overexpressing TMEM19-D150A mutant had no effect in the PS:TG ratio. These changes in phospholipid levels upon the deletion or the overexpression of TMEM19 correlate well with its effect on GPAT4 targeting to LDs. TMEM19 deletion decreased phospholipid to TG ratios and increased GPAT4 targeting to LDs, whereas TMEM19 overexpression (but not the overexpression of TMEM19 D150A mutant) attenuated the decrease in the phospholipid to TG ratios and rescued GPAT4 targeting to LDs to a normal level. These findings support the idea that TMEM19 modulates the balance between TG and membrane phospholipids to alter GPAT4 targeting to LDs.

Chapter III. Discussion

A genome-scale imaging screen revealed that genes involved in phospholipid metabolism pathways regulate protein targeting from the ER to LDs (**Figure 15**). Among the screen hits, depletion of TMEM19 and the ER structural protein Atlastin most drastically increased GPAT4 targeting to LDs (**Figure 16**). We determined that although TMEM19 also localizes to the ER like Atlastin, it is not required for maintaining the gross ER morphology of cells (**Figure 17**). Based on these results and the bioinformatic predictions of TMEM19 domains and structure (**Figure 18**), we hypothesize that TMEM19 is a lipid-related enzyme involved in phospholipid metabolism. By mutating key conserved residues, we identified D150 of TMEM19 as a critical residue for its effect on GPAT4 targeting to LDs (**Figure 19**). Finally, a radiolabeling experiment using ^{14}C-oleic acid (**Figure 20**) and lipidomic analysis (**Figure 21**) of cells lacking or overexpressing TMEM19 showed that TMEM19 affects the abundance of various phospholipids in cells. Importantly, our results suggest that TMEM19 modulates the ratio between TG and phospholipids, which may explain the role of TMEM19 in regulating protein targeting from the ER to LDs.

Silencing of genes involved in phospholipid synthesis generally increased GPAT4 targeting to LDs (**Figure 15E & Figure 16A**). Interestingly, RNAi of PECT1, which catalyzes the rate-limiting step of PE synthesis, reduced GPAT4 targeting to LDs, in contrast to RNAi of CCT1, which catalyzes the rate-limiting step of PC synthesis that increases GPAT4 targeting to LDs. This may be due to the difference in the shapes of PC and PE. PC is cylindrical, does not generate curvature, and effectively shields packing defects on LD surfaces, whereas PE is inverted conical, generates negative curvature, and poorly shields packing defects on LD surfaces[17,18]. Since both cytosolic and ER proteins that target LDs bind to these packing defects, the amount of packing defects likely correlates with protein binding.

PS is another major cylindrical phospholipid species in cells. Consistent with the idea that the shapes and packing defect-shielding abilities of phospholipids affect protein targeting to LDs, depleting PISD which converts PS to PE (increase PS, decrease PE) decreased GPAT4 targeting to LDs, while depleting PSS which converts PE to PS (increase PE, decrease PS) increased GPAT4 targeting to LDs in the screen. Interestingly, RNAi of genes encoding the enzymes shared by both the PC and PE synthesis pathways, CG2201 (human ortholog CHPK1) and bbc (human ortholog CEPT), did not significantly alter

LD targeting ratio, indicating that relative ratios between phospholipid species is likely also important, in addition to the total phospholipid amount.

Although CTP is required for the synthesis of both PC and PE, RNAi of genes involved in CTP synthesis (but no other nucleotides) significantly increased GPAT4 targeting to LDs. This is likely due to the requirement of CTP in the synthesis of other phospholipids through the CDP-DAG pathway. Consistent with this idea, depletion of CDS which catalyzes the rate-limiting step of PI synthesis increased GPAT4 targeting to LDs. PI is another major phospholipid species made in the ER. Unlike the other phospholipids we discussed, PI has a large hydrophilic head, rendering it with a conical shape that generates positive curvature and potentially making it more effective at shielding packing defects. Consistent with this idea, depletion of EDTP (human ortholog MTMR14) which removes phosphate from PI3P to generate PI in cytosolic face of various membranes in cells increased GPAT4 targeting to LDs. However, RNAi of PIS which catalyzes the conversion of CDP-DAG to PI had no effect on GPAT4 targeting to LDs in the screen.

In summary, the screen results indicate that a reduction in PC, PS, or PI and an increase in PE correlate with increased GPAT4 targeting to LDs.

A previous genome-wide RNAi screen for LD morphology in *Drosophila* S2 cells revealed that RNAi of genes involved in phospholipid synthesis results in fewer, larger LDs[117]. Genes identified in this category are CCT1, CCT2, CG2201, HLH106, SCAP, and FAS. The latter three genes are involved in the regulation of lipid synthesis through SREBP pathway, whereas the former three genes are the enzymes of phospholipid synthesis pathways, two of which are also identified in our current screen as determinants of protein targeting to LDs. This overlap is not surprising since the relative phospholipid deficiency on LD surfaces causes LD coalescence in cells lacking CCT1 or seipin[22,44]. Supplying cells with excess PC prevented the formation of the supersized LDs in both conditions. However, it has not been tested whether excess PC can prevent increased GPAT4 targeting to LDs under these conditions, although excess PC has been shown to reduce GPAT4 targeting to LDs in wildtype cells[86]. Conversely, most gene knockdowns that increased GPAT4 targeting to LDs in the current screen also resulted in large LDs (see **Figure 16B&D**). Exceptions included Atlastin and TMEM19, which may indicate that RNAi of Atlastin and TMEM19 alter LD membrane phospholipids in a way that is not as conducible for LD coalescence in

amount or in composition, reduce overall TG, and/or alter other processes that affect protein targeting to LDs.

To test the hypothesis that TMEM19 is a lipid-related enzyme with a similar catalytic activity as CDS, we attempted to identify the potential catalytic residue of TMEM19 by mutating conserved negatively charged or glycine residues, which comprise the catalytic residues of CDS[182] (**Figure 18**). We identified a point mutant (D150A) which can no longer reverse the GPAT4 targeting phenotype in TMEM19^{KO} cells. Surprisingly, overexpression of the mutant TMEM19 in TMEM19^{KO} cells altered the amounts of ^{14}C-oleic acid-labeled lipids in the thin-layer chromatography experiment (**Figure 20**), many of which were similarly altered by the overexpression of wildtype TMEM19. However, the effect of overexpressing TMEM19 D150A mutant was much less apparent in the lipidomics experiment (**Figure 21**). This discrepancy may be attributed to the fact that ^{14}C-oleic acid labeling experiment only traces lipid species with an oleic acid tail (or its derivative). Therefore, we predict that TMEM19-D150A mutant is also catalytically active but has an altered substrate specificity or a limited enzymatic activity. This could also explain why the TMEM19 mutant cannot rescue the effect of TMEM19 depletion on GPAT4 targeting to LDs. Finally, it remains to be tested whether the mutation alters protein stability and abundance.

Given the limitations of the ^{14}C-oleic acid labeling experiments, we relied on the results from lipidomic analysis to generate hypotheses for the potential TMEM19 enzymatic function (**Figure 21F**). **First, TMEM19 may catalyze the synthesis of PS from CDP-DAG and serine** ((1) in **Figure 21F**). Changes in the PS levels best fit the expected profile of the TMEM19 reaction product: its level is decreased in TMEM19^{KO} cells compared to wildtype cells and is increased back to the wildtype level when wildtype TMEM19 is overexpressed (but not the mutant). So far, no enzyme catalyzing such reaction has been identified in *Drosophila* or other higher organisms including humans. The only enzyme identified to generate PS in *Drosophila* is PSS, which exchanges ethanolamine group of PE with serine[186]. In their discovery, pulse-chasing *Drosophila* S2 cells with fluorescently labeled NBD-PE, but not NBD-PC, gave rise to NBD-PS. Interestingly, pulse-chasing with NBD-PA resulted in nearly equal amounts of NBD-PE and NBD-PS, whereas pulse-chasing with NBD-PE resulted in much smaller amount of NBD-PS. This experiment suggests a possibility that NBD-PA can be converted into NBD-PS without becoming NBD-PE first. This could happen through PA conversion to CDP-DAG, then to PS. PA levels in

our experiment are consistent with this hypothesis: although not statistically significant and detected in a small amount, the PA level increases upon TMEM19 depletion and decreases upon wildtype TMEM19 overexpression (but not the mutant). In addition, the predicted structural similarity between TMEM19 and CDS may represent the capacity of TMEM19 to bind CDP-DAG. Finally, an enzyme that catalyzes the conversion of CDP-DAG to PS is present in yeast (CDP-DAG--serine O-phosphatidyltransferase 1 or CHO1), but there is no known ortholog of CHO1 in higher organisms. Conversely, there is no predicted ortholog of TMEM19 in yeast.

Second, TMEM19 may catalyze the same reaction as CDS and **catalyze the synthesis of CDP-DAG from PA and CTP** ((2) in **Figure 21F**). Although TMEM19 could not substitute for CDS in yeast (**Figure 19**), it is possible that TMEM19 and CDS have distinct roles that cannot be compensated by each other, for instance access to a specific pool of substrates. Although it is difficult to explain the changes in PS level upon TMEM19 depletion or overexpression with this model (unless there exists a protein with CHO1 activity in *Drosophila* excluding TMEM19), it would explain the general decrease and increase in various phospholipid species (PC, PE, and PS) upon the depletion and the overexpression of TMEM19 respectively.

Third, TMEM19 may catalyze the synthesis of PI from CDP-DAG to inositol ((3) in **Figure 21F**). Decreased PI levels have been associated with increased protein targeting to LDs in murine liver[187]. In this study, treating mice with *Mboat7* (which converts LPI to PI) antisense oligonucleotide led to decreased PI level and increased LPI level, which was associated with increased enrichment of Plin2, Plin3, CCTα, and GPAT4 in the LD fractions. Another recent study suggests that in HEK293 cells, ORP5 exchanges PI(4)P on LD surfaces with PS in the ER at the ER-LD membrane contact sites[188]. Depletion of ORP5 increased PI(4)P and reduced PS on LDs, and also led to large LDs similar to those observed in cells lacking CCT1 or seipin. If indeed PI and its derivative(s) establish a concentration gradient on LDs so as to facilitate PS exchange from the ER, we may not observe much fluctuation in the PI levels upon depletion or overexpression of the enzyme responsible for the catalytic activity. Instead, we expect to see a change in PS levels, like we observe here.

There are additional bioinformatic inferences that support this hypothesis. In a binary protein-protein interaction database constructed using high throughput yeast two-hybrid screens (Human

reference interactome or HuRI[189,190]), TMEM19 was found to interact with both seipin and LDAF1 (*Drosophila* ortholog CG32803 as predicted by I-TASSER[191]). In *Drosophila* S2 R+ cells, CG32803 knockdown increased GPAT4 targeting to LDs and led to a LD phenotype similar to the seipin knockdown (see **Figure 16B**). A recent study from our laboratory revealed that seipin and LDAF1 interact with each other and mark the sites of LD biogenesis in the ER, where seipin remains associated at the junction of ER-LD membrane connections and LDAF1 moves from the ER onto the surface of LDs[48]. Fascinatingly, seipin and LDAF1 have been predicted by bioinformatic algorithms to share distant structural homology to lipid binding domains of Niemann-Pick C2 (NPC2) and NPC1 proteins which transport cholesterol by binding and handing it over to one another[192–194]. Seipin has been shown to bind anionic phospholipids *in vitro*, including PA and PI(3)P[43]. In addition, yeast ortholog of LDAF1 (Ldo16) was originally identified as protein enriched in LDs rich in the PI transfer protein Pdr16 and is required for LD targeting of Pdr16[175,176]. Finally, LDAF1 is also predicted to be structurally similar to a mannose-specific transporter, which may represent its inositol binding cavity. Similarly, the N-terminal domain of TMEM19 was predicted to have structural homology to sodium/sialic acid or sodium/glucose transporters, which indicate potential sugar binding capacity of the protein.

Based on these evidences, we propose that TMEM19 synthesizes PI from CDP-DAG and inositol, which is then transferred to seipin and LDAF1 via protein-protein interactions for the PI delivery to LD surfaces. The inability of ORP5 to exchange a derivative of PI on LDs with PS in the ER may explain the phenotypes we observe in the absence of TMEM19, namely decreased cellular PS levels and increased GPAT4 targeting to LDs. Consistent with this idea, RNAi of CDS in *Drosophila* leads to decreased levels of PI and phosphoinositides and LD accumulation in the salivary gland, which is phenocopied by the *Drosophila* lacking PIS[195]. Finally, this model of seipin and TMEM19 would explain the accumulation of PA in seipin-deficient cells[121–123].

However, there are evidences against this model: RNAi of PIS did not affect LD targeting ratios in the genome-scale screen, although it may indicate that TMEM19 and PIS have distinct functions. Second, RNAi of *Drosophila* orthologs of Orp5 and PI4K2A which is proposed to convert PI into PI(4)K on LDs (CG42668 and Pi4KIIα respectively) did not significantly alter LD targeting ratio in the screen.

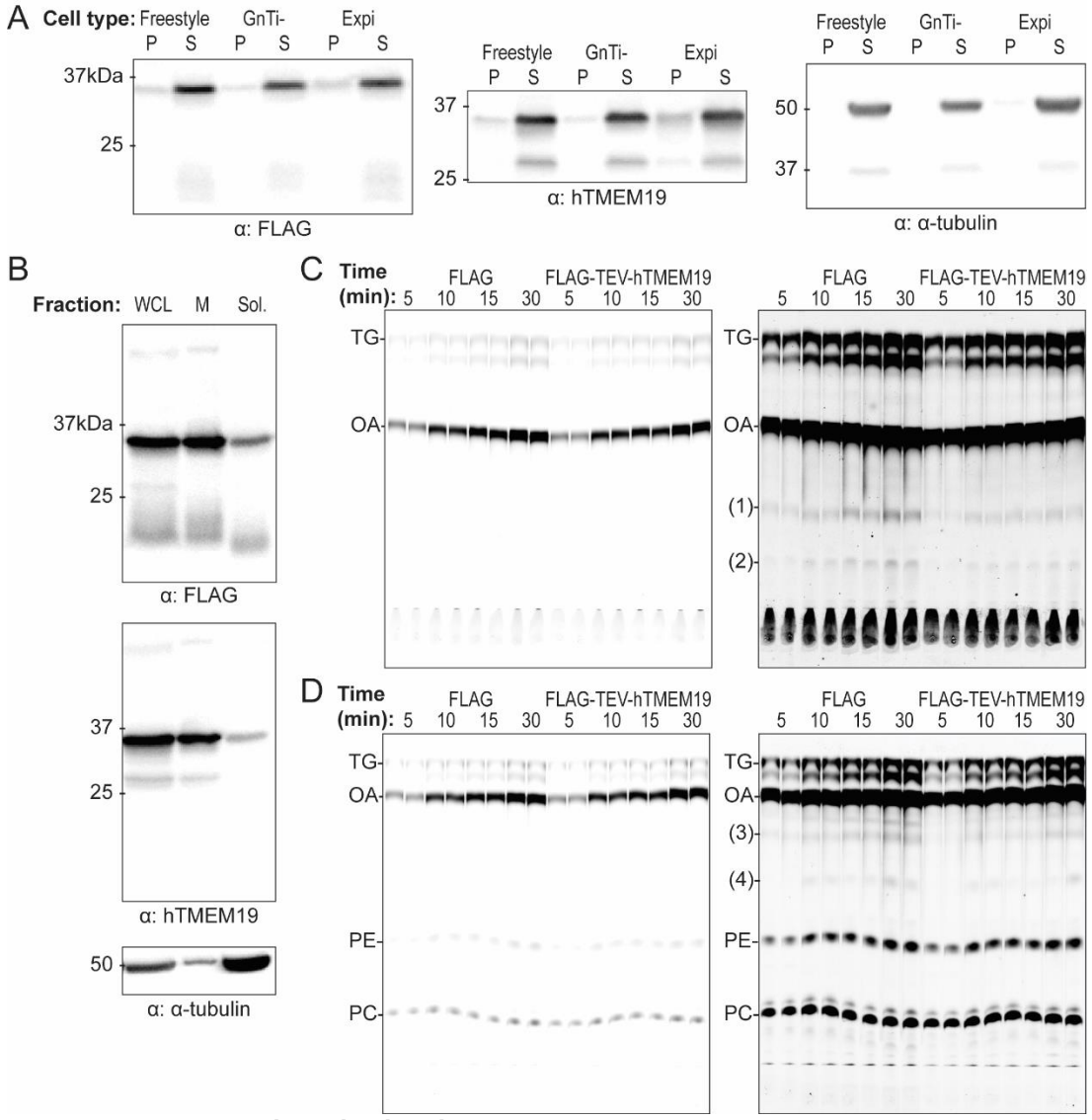

Figure 22. Human TMEM19 is active in microsomes

(A) hTMEM19 expression optimization. Three different human suspension cell lines, HEK293 Freestyle cells, HEK293 GnTi- cells, and Expi293 cells were tested for hTMEM19 expression. Upon PEI-mediated transfection of plasmid encoding 3XFLAG-TEV-hTMEM19, cells were dounced and solubilized with 1% GDN. Whole cell lysates were centrifuged for 30 minutes, 18,000g, at 4ºC to separate the solubilized proteins (supernatant; S) from the insoluble pellet (P). Each lane was normalized to the same number of cells prior to douncing. Expected size of 3XFLAG-TEV-hTMEM19: 39.2kDa, α-tubulin:50kDa.
(B) Isolation of microsomes containing hTMEM19. Expi293 cells were transfected with a plasmid encoding 3XFLAG-TEV-hTMEM19, dounced, and cleared of mitochondria (8,000g, 10 minutes, 4ºC). Microsome was isolated by centrifuging for 1 hour, 100,000g at 4ºC. Western blot was used to confirm hTMEM19 expression in the microsomes. WCL, whole cell lysate; M, microsomes; Sol, soluble fraction.
(C&D) ^{14}C-oleoyl CoA flux in microsomes. Microsomes from 3XFLAG or 3XFLAG-TEV-hTMEM19 overexpressing cells were treated with a trace amount of ^{14}C-oleoyl CoA in 0.5mM cold oleoyl CoA in 100mM KAc (pH 7.0), 1mM MgCl2, 20mM NaCl, 0.625mg/mL BSA buffer for the indicated amount of time. Lipids were extracted with 2:1 chloroform:methanol mix followed by 2% H_3PO_4 clearing of proteins and were loaded for thin-layer chromatography in (C) a neutral solvent (hexane:DEE:AA=80:20:1) or (D) a polar solvent (chloroform:methanol=96:4). Locations of standards visualized using iodine gas are shown on the left of the plate image. Both the low contrast and high contrast images are shown on the left and the right respectively.

There are many ways to test the three hypotheses about the potential enzymatic function of TMEM19 we propose. To conclusively determine whether the protein has an enzymatic activity, it can be purified and subjected to a variety of substrates *in vitro*. We have begun our efforts to optimize protein expression and purification in human suspension cells for this purpose (**Figure 22**). Expression of human TMEM19 (hTMEM19) was tested in different human suspension cell lines and the Expi293 cells were chosen. Microsomes from these cells were isolated and tested for hTMEM19 expression. Microsomes from 3XFLAG or 3XFLAG-TEV-hTMEM19 overexpressing cells were fluxed with hot and cold oleoyl-CoA, and lipids were extracted after 5, 10, 15, or 30 minutes to test if lipid levels change from hTMEM19 expression *in vitro*. Indeed, some bands appeared to differ between the two conditions (unknown lipids (1)~(4)), indicating that hTMEM19 is likely active when isolated. However, no striking changes were observed, indicating that this particular system (type of the radiolabeling substrate, buffer environment, etc.) is not ideal for investigating hTMEM19 catalytic activity and needs further optimization.

Besides this obvious and important approach of purifying the protein and testing for catalytic activity, there are cellular experiments that can inform the *in vitro* studies. For instance, we expect that reducing PS by overexpressing PISD which converts PS to PE or depletion of PSS which converts PE to PS would suppress the effect of TMEM19 overexpression if the changes in PS is the culprit behind altered GPAT4 targeting. Alternatively, supplying cells with excess PS or PI may rescue the effect of TMEM19 depletion on GPAT4 targeting if absence of either phospholipids on LDs reduces GPAT4 targeting to LDs.

It would also be important to determine the phospholipid composition of the LD monolayer membranes in above conditions, especially since such efforts have not been carefully made in the past. Although a fluorescent protein probe for PI(4)P has been used to show that PI is present on LDs and its association with LDs changes in response to various gene knockdowns[188], the exact abundance of PI and its derivatives on LD surfaces relative to other phospholipid species remains unclear. A more holistic approach such as purifying LDs, extracting phospholipids, and performing lipidomic analysis for both the nonpolar and polar phases (to measure both nonpolar and polar lipids) may prove to be useful.

Finally, although many studies clearly demonstrate the associations between the phospholipid amounts and composition with protein targeting to LDs and LD coalescence, the mechanism behind the

associations has not been explored. Since we hypothesize that phospholipid amount and composition affect LD packing defects that in turn alter protein binding to LD surfaces or LD coalescence, we can start testing the hypothesis by measuring and altering packing defects on LDs in cells using fluorescent protein probes and on artificial LDs using chemical probes such a C-laurdan[196] under various phospholipid compositions and testing for the changes in protein binding. We can also perform molecular dynamics simulations in parallel to predict the interaction of proteins, especially their large hydrophobic residues, with a monolayer membrane with various phospholipid compositions and calculate the binding affinity.

Physiological consequences of altering phospholipid compositions on LDs and LD protein targeting have not been investigated. Two human genetic studies revealed that mutations in TMEM19 loci (nonsense variant in exon 2 p.Trp54X and SNPs in promoter, rs2304269, and enhancer elements, rs7967428) are associated with facial dysmorphism including orofacial clefts, short stature, and language delay[197,198]. On the other hand, seipin deficiency in humans (which causes one of the most severe forms of congenital lipodystrophy) has been also associated with a number of motor neuron diseases including hereditary spastic paraplegia[39–41]. Interestingly, mutations of orthologs of two other screen hits, Atlastin1 and SLC33A1, also have been found to cause spastic paraplegia in humans[199,200]. Whether these defects come from altered LD biology in neurons or glial cells that produce myelin remains as an interesting topic for future investigation.

Chapter III. Perspective

As cells store excess energy in the form of TG, the demand for phospholipids increases to supply membrane for the growing LDs. Since there are excess fatty acyl chains, it is not surprising to find that the demand for CTP, another substrate required for the synthesis of most common phospholipids, becomes the bottleneck. Our screen revealed that restricting CTP synthesis in this setting alters protein targeting to LDs, presumably by affecting packing defects on LD surfaces. We also find that genes involved in phospholipid synthesis are essential for maintaining the normal level of protein targeting to LDs. Interestingly, depletion of a previously unstudied protein TMEM19 resulted in a large defect in this regulation. We propose that TMEM19 is critical for maintaining the balance between the amounts of TG and phospholipids in times of energy excess, by consuming a substrate shared by the TG and the phospholipid synthesis pathways, namely PA or DAG, for phospholipid synthesis. Elucidating the potential enzymatic activity of TMEM19 will help us understand how cells maintain this delicate balance to regulate LD protein targeting and fat storage.

Chapter IV. Methods

Special reagents

10mM oleic acid was prepared by dissolving 1.98g essentially fatty acid free BSA in 10mL PBS, adding 31.74μL oleic acid drop-by-drop, and shaking at 37°C for an hour. Solution was sterile-filtered (0.22μm) before use. All oleic acid treatment was performed with 1mM final concentration.

Janelia Fluor 646 HaloTag Ligand (JF646) was a kind gift from Luke Lavis (Janelia Research Campus).

Cell culture

The *Drosophila* S2 R+ cells (sex: male) used in this study were provided by Prof. Norbert Perrimon (Harvard Medical School). Cells were cultured at 26°C in Schneider's *Drosophila* Medium (Gibco, #21720001) supplemented with 10% fetal bovine serum, 50 units/mL of penicillin, and 50μg/mL of streptomycin. Cells were maintained by splitting 1:6-1:12 every 3-4 days.

Genome-scale imaging screen to identify genes involved in GPAT4 targeting to LDs

RNAi, fixation, and staining

Drosophila S2 R+ cells stably overexpressing EGFP-GPAT4 was subjected to a genome-scale library of dsRNA in imaging-compatible 384 well plates (PerkinElmer, #6057300) two times, prepared by the HMS *Drosophila* RNAi Screening Center (DRSC 2.0 genome-wide screening library) The library targets approximately 13,900 genes 1~2 times and consists of 66 384-well plates with 250ng dsRNA in 5uL per well. Confluent cells were resuspended from plates to $60x10^4$ cells/mL in Schneider's *Drosophila* Medium (Gibco, #21720001) without serum supplementation. 10uL of the cell suspension was dispensed into the dsRNA plates using the Thermo Scientific Matrix WellMate Microplate Dispenser. After mixing the contents gently, plates were sealed with parafilm and placed in a 'wet chamber' (airtight container with wet paper towels) inside 26°C incubator for 50 minutes. 30uL of Schneider's *Drosophila* Medium supplemented with 10% fetal bovine serum, 100 units/mL of penicillin, and 100μg/mL of streptomycin was added to each well, and plates were sealed with parafilm and placed in the wet chamber for 3.75 days.

After incubation, 6uL of 10mM OA solution and 14uL of fresh media was dispensed, and the plates were sealed with parafilm and placed in the wet chamber for 20 hours.

Next day, wells were washed once with 50uL PBS and about half the liquid were carefully aspirated using vacuum aspirator to avoid disrupting cells at the bottom of the plate, leaving ~50uL. 50uL of freshly prepared 8% paraformaldehyde in PBS solution was dispensed to each well and incubated at room temperature for 25 minutes. Again with careful aspiration, wells were washed with 70uL PBS three times. 17uL of 1μM SiR-DNA nuclear stain (Spirochrome, #SC007) and 133μM monodansylpentane LD stain (AUTOdot; Abcepta, #SM1000b) in PBS was added to each well (final concentration 0.25μM SiR-DNA & 33.3μM AUTOdot) and incubated for 35 minutes. Finally, each well was washed with 70uL PBS three times and 25uL PBS was added (final volume ~75uL) for imaging.

Confocal imaging

For automated confocal imaging, GE IN Cell Analyzer 6000 Cell Imaging System with robotics support for automated plate loading. Using the IN Cell Analyzer software, 3 channel images (FITC for EGFP-GPAT4, Cy5 for nuclei, and DAPI for LDs) were taken in 8 fields per well at the manually determined offset from auto-focusing using 60X objective.

Image quantification

A custom Matlab analysis pipeline was built in collaboration with the HMS Image and Data Analysis Core. Nuclei, cell, and LD compartments were obtained using supervised machine learning methods, specifically Random Forest pixel classifiers (http://github.com/HMS-IDAC/PixelClassifier). Three different models were trained, one for each compartment, using separate sets of annotated images (about 7 images per model). Nuclei and cells were segmented from the Cy5 channel, and LDs form the DAPI channel. Nuclei mask was used for segmenting cells as markers in a watershed algorithm. LD masks were post-processed by selecting only the intersection with cell masks. LD objects were then associated with cell objects depending on the area of intersection. Finally, the signal in the FITC channel was corrected for auto-fluorescence by subtracting the mean value of control images and was quantified inside and outside the LD mask in each segmented cell. From these measurements, we calculated LD targeting ratio for each segmented cell, defined as the ratio of the mean intensity of EGFP-GPAT4 signal inside the LD mask to that of EGFP-GPAT4 signal outside LD mask within the cell mask. Median LD

targeting ratio from all of the segmented cells from the 8 fields of the same well (with a unique dsRNA) was determined and employed as the final readout for the well.

Batch patch processing of screen images (total 1,216,512 images) through the custom analysis pipeline was performed using the Harvard O2 cluster.

Calculation of Robust Z-scores

Each median LD targeting ratio from the duplicate screen experiment was considered as a separate value. Robust Z-scores for all median LD targeting ratios (X) was calculated using the following formula:

$$\text{Robust Z-score} = (X_i - \text{median}(X))/(1.4826 * \text{median absolute deviation}(X))$$

$$\text{Where median absolute deviation} = \text{median}(|X_i - \text{median}(X)|)$$

In our screen, median = 2.147287 and median absolute deviation = 0.113917.

Plasmid construction

PCR of the insert was performed using PfuUltra II Fusion Hotstart DNA Polymerase (Agilent Technologies, #600672) following the manufacturer's protocol. Purified PCR product was first cloned into an entry vector using the pENTR/D-TOPO Cloning Kit (Invitrogen, #K240020) and then into a destination vector from the *Drosophila* Gateway vector collection system (Murphy Laboratory, Carnegie Mellon University) using the Gateway LR clonase Enzyme mix (Invitrogen, #11791019).

Halo destination vectors were created by replacing the EGFP sequence of pAGW and pAWG from the *Drosophila* Gateway vector collection system with Halo sequence using restriction-ligation (EcoRV & AgeI and SacI & AgeI respectively).

Backbone for the yeast plasmids was created by replacing _ of _ with pTEF-hph (hygromycin resistance gene) using restriction-ligation (NsiI & PfoI). hTMEM19 and hCDS1 sequences were inserted into the backbone using SpeI & XhoI.

For mutagenesis of constructs, mutations were made using the QuikChange II XL Site-Directed Mutagenesis Kit (Agilent, #200521) in an entry vector, which was then cloned into a destination vector to avoid undetected mutations elsewhere in the destination vector.

All final plasmids were verified by restriction analysis and sequencing of the insert region. All information about PCR template and primers are provided in **Tables C1-3**.

Transfection

Cells were transfected with the Effectene Transfection Reagent (Qiagen, #301425) following the manufacturer's protocol. When co-transfecting with more than one plasmid, equal amount (in µg) of the plasmids were used. Any further treatments took place 26 hours after transfection.

dsRNA synthesis for RNAi

Genomic DNA of the cells was isolated using the DNeasy Blood & Tissue Kit (Qiagen, #69504). PCR was performed using primers containing T7 promoter sequence (on both forward and reverse primers) with PfuUltra II Fusion Hotstart DNA Polymerase (Agilent Technologies, #600672). PCR products with the expected size was separated using 1% agarose gel. Purified PCR products were used as a template for RNA transcription using the MEGAscript T7 Transcription Kit (Invitrogen, #AM1334), which was then purified using the RNeasy Mini Kit (Qiagen, #74104). Sizes and quality of synthesized dsRNA were confirmed using 1% agarose gel before they were used for RNAi. PCR primer sequences are provided in **Table C4**.

RNAi

Cells were spun down at 300g for 5 minutes and resuspended with Schneider's *Drosophila* Medium (Gibco, #21720001) without serum supplementation at $60x10^4$ cells/mL. Cells were plated first and dsRNA was added at 20ng/uL. After carefully shaking the plate to mix the contents, plates were sealed with parafilm and placed in a 'wet chamber' (airtight container with wet paper towels) inside 26°C incubator to prevent evaporation for 50 minutes. After 50 minutes, serum-supplemented medium with 3 volumes of initial cell suspension was added carefully to avoid detaching cells. After sealing with parafilm, the plate was incubated in the wet chamber for 3.5-4 days prior to further treatments. If transfection, cells were transferred onto a new plate before following the transfection protocol.

Generation of a stable cell line overexpressing EGFP-GPAT4

Stable cell line overexpressing EGFP-GPAT4 was created by transfecting cells with pActin-EGFP-GPAT4-T2A-Puro^{R}. Information on PCR template and primers used for cloning the construct is provided in **Table C5**. Selection was started 3 days after transfection with 10μg/mL puromycin. 5 days later when most control cells (>75%) have died, transfected cells were recovered in medium without puromycin for 5 days. This selection and recovery were repeated one more time before cells were sorted.

For cell sorting, cells were suspended in sterile PBS supplemented with 1% fetal bovine serum. Using FACSAria-561 with 100μm gating, EGFP+ cells (488nm laser) were sorted into a 96-well plate (100 cells/well) containing conditioned media (media collected from cells growing at exponential phase, combined with equal volume of fresh Schneider's medium supplemented with 20% fetal bovine serum). After 2 weeks, cells were expanded and subjected to microscopy and western blot for verification of the cell line.

Generations of cell lines using CRISPR-Cas9 genome-editing

Knock-out and knock-in cell lines were created using CRISPR-Cas9, following protocols published by Housden et al.[201,202]. Guide RNA sequence and PCR primer sequences for donor construct cloning are provided in **Table C6**. 1 week after transfection, cells were suspended in sterile PBS supplemented with 1% fetal bovine serum and single-cell sorted into a 96-well plate containing conditioned media (media collected from cells growing at exponential phase, combined with equal volume of fresh Schneider's medium supplemented with 20% fetal bovine serum), using FACSAria-561 with 100μm gating. After 2~3 weeks, viable single-cell colonies were expanded and subjected to microscopy, western blot, and sequencing for verification of correct genome-editing.

Fluorescence microscopy

Cells that have undergone transfection or RNAi in 24-well plates were resuspended in the old medium and combined with equal volume of fresh medium to a 35mm dish with 14mm No. 1.5 coverslip bottom (MatTek Life Sciences, #P35G-1.5-14-C) coated manually with 0.1mg/mL Concanavalin A. Cells were allowed to settle for 1 hour at 26°C before further treatments, such as with 1mM oleic acid (OA).

Unless otherwise indicated, cells were imaged 20 hours after OA treatment. LDs were stained with 100μM monodansylpentane (AUTOdot; Abcepta, #SM1000b) 10 minutes before imaging. For JF646 treatment, cells were incubated with the Halo ligand 1 hour before imaging and washed once with PBS before resupplying medium (or medium with OA).

Nikon Eclipse Ti inverted microscope featuring CSU-X1 spinning disk confocal (Yokogama) and Zyla 4.2 PLUS scientific complementary metal-oxide semiconductor (sCMOS) (Andor, UK) was used for spinning disk confocal microscopy. NIS-elements software (Nikon) was used for acquisition control. Plan Apochromat VC 100X oil objective (Nikon) with 1.40 NA was used, resulting in 0.065μm pixel size. Solid state excitation lasers—405nm (blue; Andor), 488nm (green; Andor), 560nm (red; Cobolt), and 637nm (far-red; Coherent)—shared quad-pass dichroic beam splitter (Di01-T405/488/568/647, Semrock), whereas emission filters were FF01-452/45, FF03-525/50, FF01-607/36, and FF02-685/40 (Semrock) respectively.

Quantification of confocal images, immunoblots, and TLC plates

Confocal images, western blots, and TLC plates were quantified using FIJI software[203] to calculate LD targeting ratios. Cell boundaries were drawn manually based on fluorescence from protein channels such as EGFP-GPAT4 (Mask 1) and LD regions were distinguished by applying an automatic threshold (Otsu method) to the monodansylpentane channel within Mask 1 which was then dilated by 1 pixel to include LD surfaces (Mask 2). LD targeting ratios were measured by dividing the mean intensity of the fluorescent protein channel image in Mask 2 divided by that in Mask 1 – Mask 2 for all proteins except for CCT1. For CCT1, nuclei were distinguished by manually drawing the nuclear boundary from mCherry-CCT1 channel (Mask 3), which was excluded from Mask 1.

For western blots and TLC plate images, a rectangular ROI was drawn around the band of interest in the control lane (usually LacZ RNAi), and the measure function was used to measure total intensity inside the ROI. ROI was then moved to the next lane sequentially for measurements. For western blots, selected ROIs were all at equal heights (same y-position), whereas for TLC, ROI had to be moved up or down slightly based on the band migration pattern. Finally, the measured intensities were normalized to the level in the control lane for comparison.

Statistical analysis

All statistical analysis were performed using GraphPad Prism 7. Information about significance test is provided in detail in the respective figure legends.

LD fractionation

Cells were resuspended from plates and washed once with PBS, which was then placed on ice for all subsequent steps. Cell pellets were suspended in 1mL 250mM sucrose buffer containing 200mM Tris-HCl (pH 7.4), 1mM $MgCl_2$ (pH 7.4), and cOmplete Mini EDTA-protease inhibitor cocktail (Roche, #4693159001) and broken by passing through 25G syringe 30 times. 1unit/uL of benzonase nuclease (Millipore, #E1014) was added and incubated on ice for 10 minutes. 5% of the total volume was taken at this stage for **whole cell lysate or input** analysis. For the rest, unbroken cells and nuclei were fractionated by centrifuging for 5 minutes, 1,000g at 4°C. Top lipid layer and the supernatant was moved to the 5mL, Open-Top Thinwall Ultra-Clear Tube, 13x51mm (Beckman Coulter, #344057), where additional 1.5mL of the 250mM sucrose buffer was added. 2.5mL of 50mM sucrose containing 200mM Tris-HCl (pH 7.4), 1mM $MgCl_2$ (pH 7.4), and cOmplete Mini EDTA-protease inhibitor cocktail was layered on top. The two-step sucrose gradient was centrifuged for 16-20 hours, 100,000g, at 4°C using the SW 55 Ti Swinging Bucket rotor (Beckman Coulter, 342194).

Top of the tube (~5mm; 500uL) was sliced using the Beckman Coulter tube slicer, the content of which was taken as **LD fraction**. Supernatant was taken as **soluble fraction**, and the pellet resuspended in 500uL 250mM sucrose buffer was taken as **membrane fraction**.

For further analysis, proteins from the fractions were precipitated. Briefly, 1mL of methanol and 250uL of chloroform was sequentially added to 500~750uL of aqueous fractions with vigorous mixing after every addition. After centrifuging for 10 minutes, 14,000g, at 4°C, top layer was aspirated out. 1.7mL methanol was added and vigorously mixed. Precipitated proteins were then pelleted by centrifuging for 15 minutes, 18,000g, at 4°C. All liquid was aspirated, and after allowing the pellet to dry for 5 minutes, the pellet was resuspended in 100-250uL of 1.5% SDS, 50mM Tris-HCl (pH 7.4) buffer.

Immunoblotting

Protein concentrations owere measured using the Pierce BCA Protein Assay Kit (Thermo scientific, #23225), and the amount indicated in respective figure legends were mixed with 5X Laemmli buffer for the final concentration of 1X Laemmli buffer (2% SDS, 10% glycerol, 50mM Tris-HCl (pH 6.8), β-mercaptoethanol 100mM, 0.02% bromophenol-blue). After running samples in 4-15% gradient polyacrylamide gel (Bio-Rad, #4561084) at 100V for 1 hour 30 minutes in 1X Tris/Glycine/SDS buffer (Bio-Rad, #161-0772), proteins were transferred to a 0.2µm pore size nitrocellulose membrane (Bio-Rad, #1620112) in 1X Tris/Glycine buffer (Bio-Rad, #161-0771) at 70V for 1 hour 30 minutes in the cold room (4°C). Membrane was blocked by incubating in 5% non-fat dry milk (Santa Cruz Biotechnology, #sc-2325) in TBS-T buffer (20mM Tris at pH 7.6, 150mM NaCl, 0.1% Tween-20) for 30 minutes at room temperature. Membrane is incubated with 5% milk solution containing primary antibody (dilutions are indicated below) overnight in the cold room.

Next day, membranes are washed three times with TBS-T for 10 minutes each at room temperature, incubated with 1:5000 secondary antibodies conjugated to HRP proteins (Santa Cruz Biotechnology, #sc-516102 for primary antibodies from mouse or #sc-2357 for primary antibodies from rabbit) in 5% milk solution for 1 hour at room temperature, and washed three times with TBS-T for 10 minutes each at room temperature. SuperSignal West Pico PLUS Chemiluminescent Substrate (Thermo Scientific, #34580) was applied to the membrane, which was imaged using the Biorad Gel Doc XR system for signal acquisition.

For stripping the membrane of antibodies, membrane was washed with distilled water five times for 5 minutes each at room temperature and incubated with 100mM citric acid solution in distilled water for 10 minutes at room temperature. The membrane was then re-blocked with 5% milk solution for 30 minutes at room temperature before proceeding with incubation with another primary antibody.

Primary antibodies and their dilutions: rabbit anti-*dm*GPAT4[54] (1:1000), rabbit anti-*dm*CCT1[22] (1:1000), mouse anti-*dm*CNX99A (1:500; DSHB, #Cnx99A 6-2-1), mouse anti-FLAG (1:1000; Sigma-Aldrich, #F1804), rabbit anti-*hs*TMEM19 (1:1000; custom made, see below).

Generation of anti-human TMEM19 antibody

GenScript customized antibody service was used. Anti-hTMEM19 antibodies were raised by immunizing rabbits with the peptides from the C-terminal region of the protein (amino acids #280-307; QYTGLDESTGMVVNSPTNKARHIAGKPI) with an additional cysteine at the N-terminus for keyhole limpet hemocyanin (KLH) conjugation. After serum collection, SulfoLink Immobilization Kit for Proteins (Thermo Scientific, #44995) along with the immunogen peptide was used to affinity purify the polyclonal antibody.

Electron microscopy

Cells were washed once with PBS and fixed with 2.5% glutaraldehyde, 1.25% paraformaldehyde, and 0.03% picric acid in 0.1M sodium cacodylate buffer (pH 7.4) for 30 minutes. From this step until imaging, samples were processed by the HMS Electron Microscopy Core. After suspending and pelleting the cells, cells were washed in 0.1M cacodylate buffer; post-fixed with 1% osmium tetroxide (OsO4) / 1.5% potassium ferrocyanide (KFeCN6) for 1 hour; washed with water two times and with 0.05M maleate buffer (pH 5.15) once; incubated in 1% uranyl acetate in the maleate buffer for 1 hour; washed with water two times; and dehydrated using grades of alcohol (10min each; 50%, 70%, 90%, 100%, 100%). Samples were then put in propyleneoxide for 1 hour and infiltrated overnight in 1:1 mixture of propyleneoxide and TAAB Epon (TAAB Laboratories Equipment Ltd, UK, #T024).

The following day, samples were embedded in TAAB Epon and polymerized at 60°C for 48 hours. Ultrathin sections of ~60nm were cut using the Reichert Ultracut-S microtome and transferred to copper grids. Sections were stained with lead citrate before imaging with JEOL 1200EX Transmission electron microscope equipped with an AMT 2k CCD camera.

Yeast transformation

Yeast in exponential growth phase (OD_{600} = 0.4-0.8) was pelleted and resuspended in 1/50 the volume of TEL buffer (100mM LiAc, 10mM Tris-HCl (pH 8.0), 1mM EDTA (8.0)). Plasmid was added to the cell suspension (2µg/50uL cell suspension), along with 10 parts Salmon Sperm DNA (Invitrogen, AM9680). 6 volumes of PEG-TEL buffer (100mM LiAc, 10mM Tris-HCl (pH 8.0), 1mM EDTA (8.0), 40%

PEG-3350) was added to the cells and mixed vigorously. Cells were incubated at 25°C for 30 minutes and heat shocked in 42°C water bath for 10 minutes, after which cells were pelleted and resuspended in YPD media for recovery at 25°C with mild shaking. After 1 hour, cells were plated in an appropriate selection plate.

Thin-layer chromatography using radiolabeled fatty acids

Cells were treated normally with 1mM oleic acid overnight except with a trace amount of ^{14}C-oleic acid (American Radiolabeled Chemicals, #ARC 0297-50) to the final concentration of 0.25nCi/uL. In the following day, media containing the radiolabeled fatty acid is was away, and cells were carefully washed with PBS twice. For lipid extraction, 3:2 hexane:isopropanol mix was applied to cells and incubated at room temperature with gentle shaking for 10 minutes. After collecting the solubilized lipids into a tube, extraction was repeated one more time. Solvent was air dried and the extracted lipids were re-suspended in 2:1 chloroform:methanol mixture.

To the plate where lipids were extracted from cells, 0.3N NaOH 0.1% SDS buffer was applied for protein extraction. After rocking at room temperature for 2 hours (or until protein debris are no longer visible under light microscope), Pierce BCA Protein Assay Kit (Thermo scientific, #23225) was used to measure protein concentration.

For loading lipids for thin-layer chromatography, samples were normalized to the protein amount. After air drying the chloroform:methanol solvent, lipids were resuspended in the same amount of 2:1 chloroform:methanol buffer and loaded onto a silica gel (Analtech, #P43911) at the same height. After samples are dried, TLC plate is placed into a solvent chamber prepared at least 30 minutes prior with an appropriate solvent (as indicated in the figure legends). After solvent front reached the top of the plate, plates were removed from the chamber and air dried before assembling with the phosphor imaging cassette. After one day of exposure (or longer), phosphor imaging cassette screen was imaged using Typhoon FLA7000 phosphor imager. Bands for standards were detected using iodine vapors.

Lipidomic analysis

Cell culture and lipid extraction

Cells were pelleted and freeze-thawed three times using liquid nitrogen (15 seconds) and ultrasonic water bath sonicator at room temperature (5 minutes). All steps from here are conducted on ice (4°C). Ultrapure water was added to resuspend the ruptured cells and a small fraction was removed to determine relative protein concentration using the Pierce BCA Protein Assay Kit (Thermo scientific, #23225). Cell suspension equivalent of 250 µg of protein was aliquoted to a glass tube and brought up to equal volumes with ultrapure water. 1uL of SPLASH LIPIDOMIX Mass Spec Standard (Avanti, #330707) was added to each sample.

For lipid extraction, 20 volumes of 2:1 chloroform:methanol (v/v) was added to cell lysate, mixed vigorously, and placed in a shaking incubator for 1.5 hours at 4°C. 4 volumes of 0.88% NaCl (w/v) was added and mixed vigorously, and the tubes were centrifuged for 30 minutes, 1,800 x g, at 4°C. Using a sterile glass pipette, the lower organic phase was transfered to a new glass tube and dried under nitrogen flow (~1 hour). Dried lipids were resuspended in a small volume (150 uL) of 2:1 chloroform:methanol for lipidomic analysis.

Lipidomic measurements

LC-MS/MS analysis was using the same protocol as described in Gluchowski et al.[204]. Briefly, 5uL of each sample was analyzed separately using positive and negative acquisition modes, separated by the UHPLC system (consisting of Thermo Acclaim C30 reverse-phase column connected to a Dionex UltiMate 3000 UHPLC system) over 60 minute gradient of combinations of mobile phase (60:40 water/acetonitrile (v/v), 10 mM ammonium formate and 0.1% formic acid) and mobile phase (90:10 2-propanol/acetonitrile, also including 10 mM ammonium formate and 0.1% formic acid). UHPLC system was connected to Q Exactive orbitrap mass spectrometer (Thermo Fisher Scientific), which generated MS spectra of lipids using the full-scan/data-dependent MS^2 mode.

Data analysis

LipidSearch version 4.1 SP (Thermo Fisher Scientific) was used to analyze MS data. Identified species with grade A, B, or C were validated and quantified using R-script developed in-house.

Appendix A. Chapter II Supplementary Figures

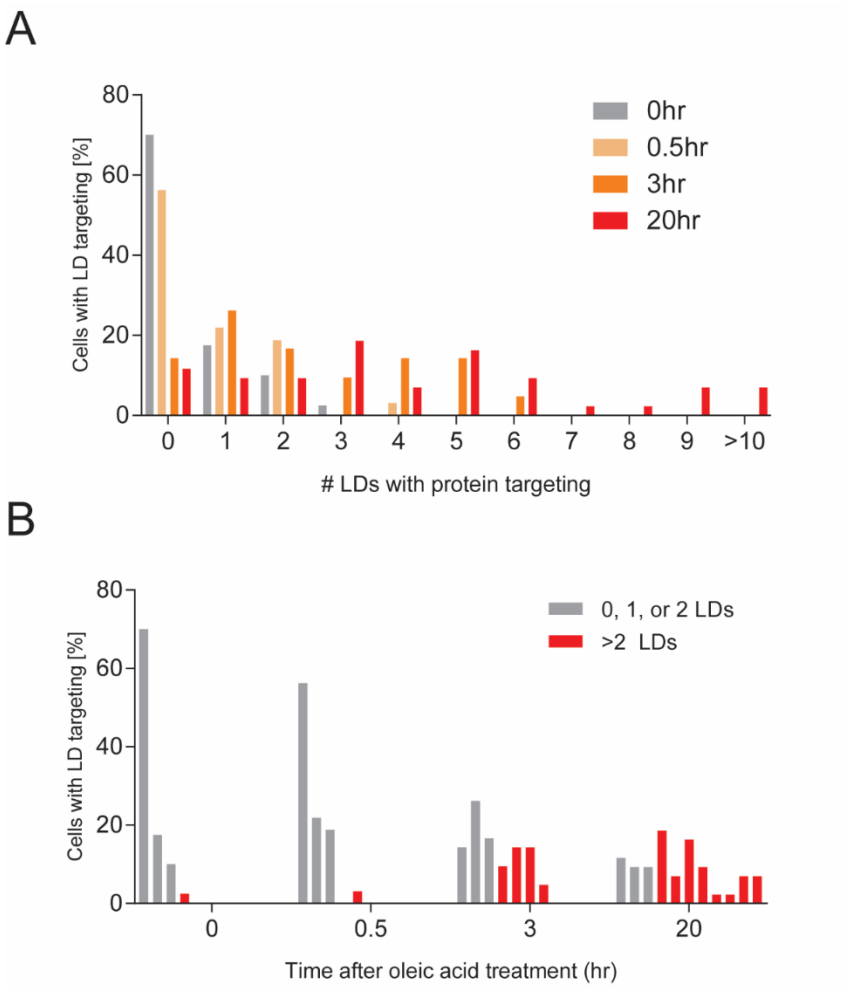

Figure A1. HSD17B11 targets a subset of LDs
(A) Frequency distribution for the percentage of cells per the number of LDs that show HSD17B11-G targeting. Wildtype *Drosophila* S2 R+ cells were transfected with a plasmid encoding HSD17B11-EGFP, treated with 1mM OA, and stained with MDH for imaging. For each observed cell, the number of LDs that show HSD17B11-G targeting was counted, and the percentage of cells containing the particular number of LDs with protein targeting over total number of observed cells was calculated for each timepoint after 1mM OA treatment. 3 independent experiments (10-14 cells each).
(B) Frequency distribution in (A) displayed by timepoint. At 0hr timepoint (prior to 1mM OA treatment), most cells show 0-2 LDs with HSD17B11-G targeting, and the percentages of cells with >2 LDs with HSD17B11-G targeting increases over time.

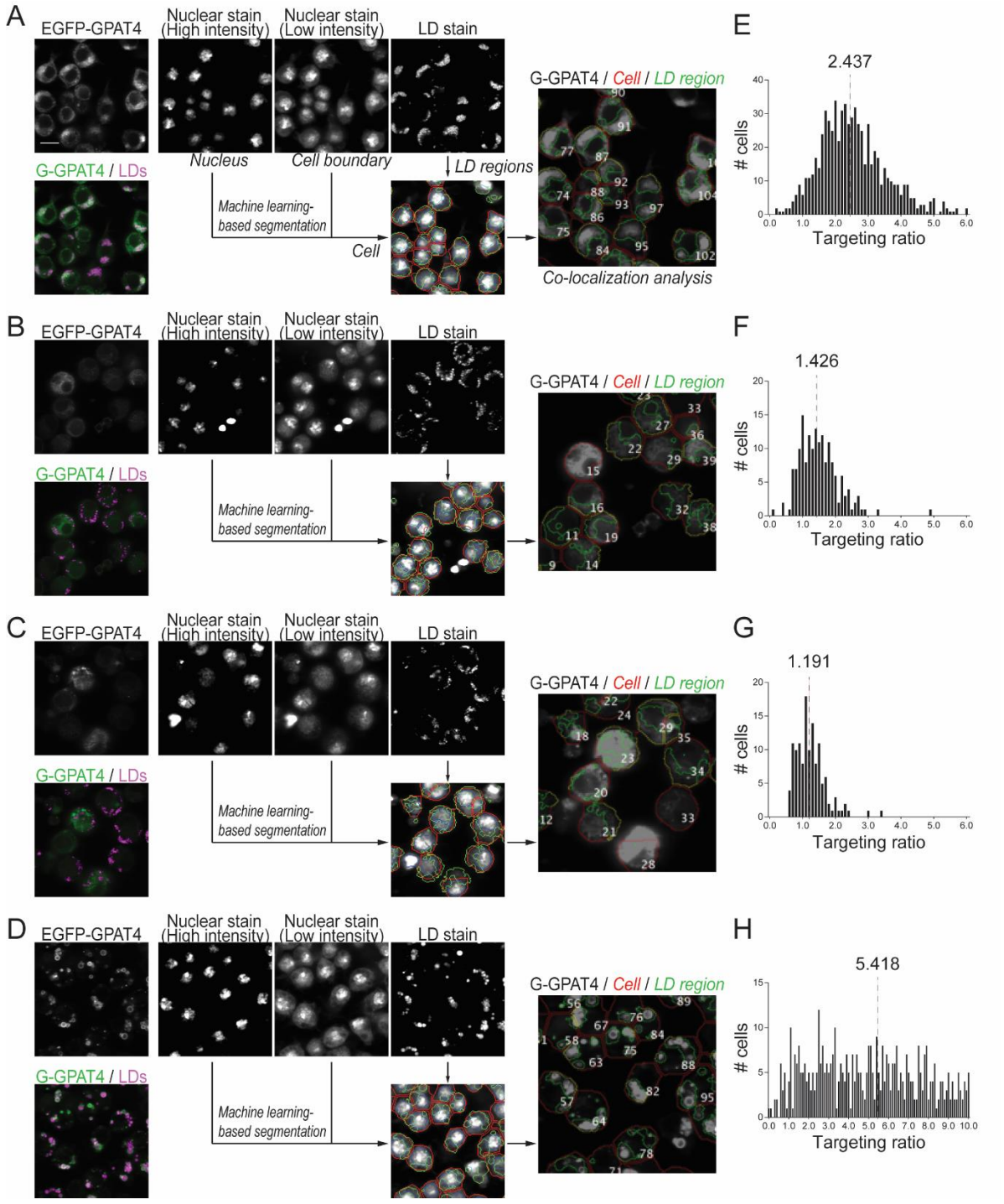

Figure A2. Segmentation of cells and regions of LDs for calculating LD targeting ratios
(A-D) Examples of segmentation in screen control wells ((A) LacZ, (B) Arf79F, (C) βCOP, (D) Seipin). Nuclei and cell boundaries are segmented using information from high and low intensities from nuclear stain image respectively, which are then combined to segment cells. Regions of LDs are segmented using information from LD stain image. Segmentation results are overlaid onto EGFP-GPAT4 channel for the calculation of LD targeting ratios.
(E-H) Examples of distribution of LD targeting ratios in individual screen control wells. Upon calculation of LD targeting ratios for all cells in a well, median LD targeting ratio (dotted line) is calculated as the final readout of the particular well.

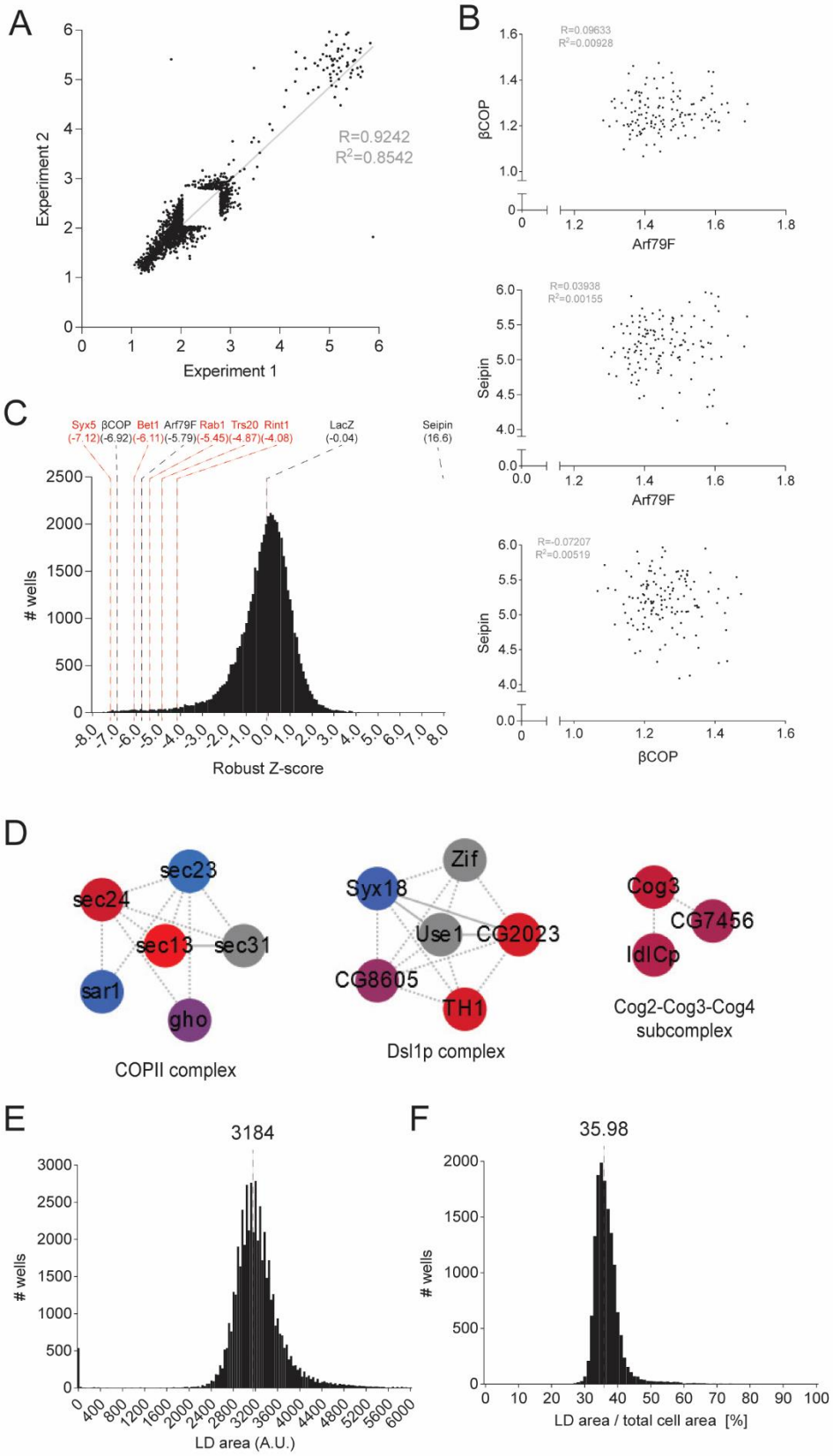

Figure A3. Screen quantification results and analysis

Figure A3 (continued). Screen quantification results and analysis
(A) Scatter plot of LD targeting ratios from duplicate genome-scale screen experiments in the extremes. Targeting ratio pairs of which both values fall within the range of LacZ control ([2.034, 2.794]) were excluded before performing linear regression. A regression line, Pearson correlation coefficient (R), and the coefficient of determination (R2) are shown. n = 2,290.
(B) Scatter plots of LD targeting ratios from screen positive controls. LD targeting ratios for positive controls from each plate was plotted against each other. Pearson correlation coefficient (R) and the coefficient of determination (R^2) are shown. n = 132 each.
(C) Distribution of robust Z-scores for LD targeting ratios. Robust Z-scores were calculated for all targeting ratios obtained from the duplicate genome-scale screen. Robust Z-scores for screen controls (black) and a number of hits that reduce the targeting ratios (red) are highlighted.
(D) Protein complexes enriched among screen hits. Screen hits with robust Z-score <-2.5 excluding ribosomal, proteasomal, and spliceosomal proteins were analyzed using the Protein Complex Enrichment Analysis Tool (COMPLEAT[154]). Complete list of results from the analysis is provided in **Online Supplementary Table 5** and additional visualization of complexes in **Figure 7F**. Node color: blue (smallest robust Z-score), red (highest robust Z-score), grey (non-hits; robust Z-score > 2.5). Line type: solid (known protein-protein interaction), dashed (known protein-protein interaction among orthologs in another species). p-values: COPII complex (6.942e-07), Dsl1p complex (1.647e-03), Cog2-Cog3-Cog4 complex (1.056e-02).
(E) Distribution of absolute LD area. Distribution of median LD areas obtained from the segmentation (in arbitrary unit) results for each well of the screen is shown. Median value is indicated with a dotted line.
(F) Distribution of relative LD area. Distribution of median percentage of total cell area occupied by LDs for each well is shown.

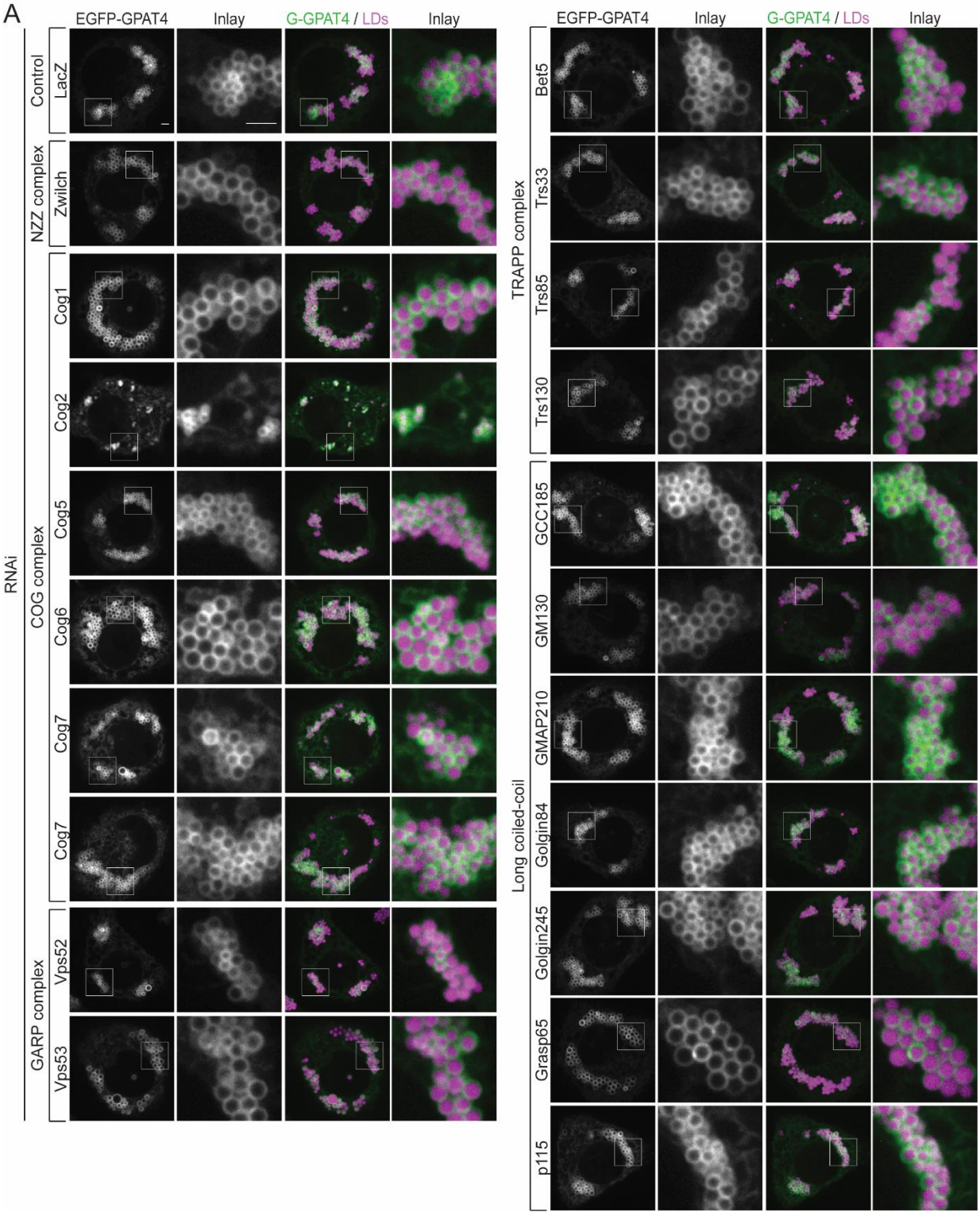

Figure A4. Membrane tether components dispensable for GPAT4 targeting to LDs
Screen result verification using EGFP-GPAT4^{KI} cells. Cells were subjected to 2-3 dsRNA's against select membrane tethering complex components, treated with 1mM OA for 20 hours, stained with MDH, and imaged with spinning-disk confocal microscope. Representative images for dsRNA that shows largest effect on LD targeting ratios are shown. Quantification in **Figure 9C**. Scale bar, 2μm and 2μm (inlay).

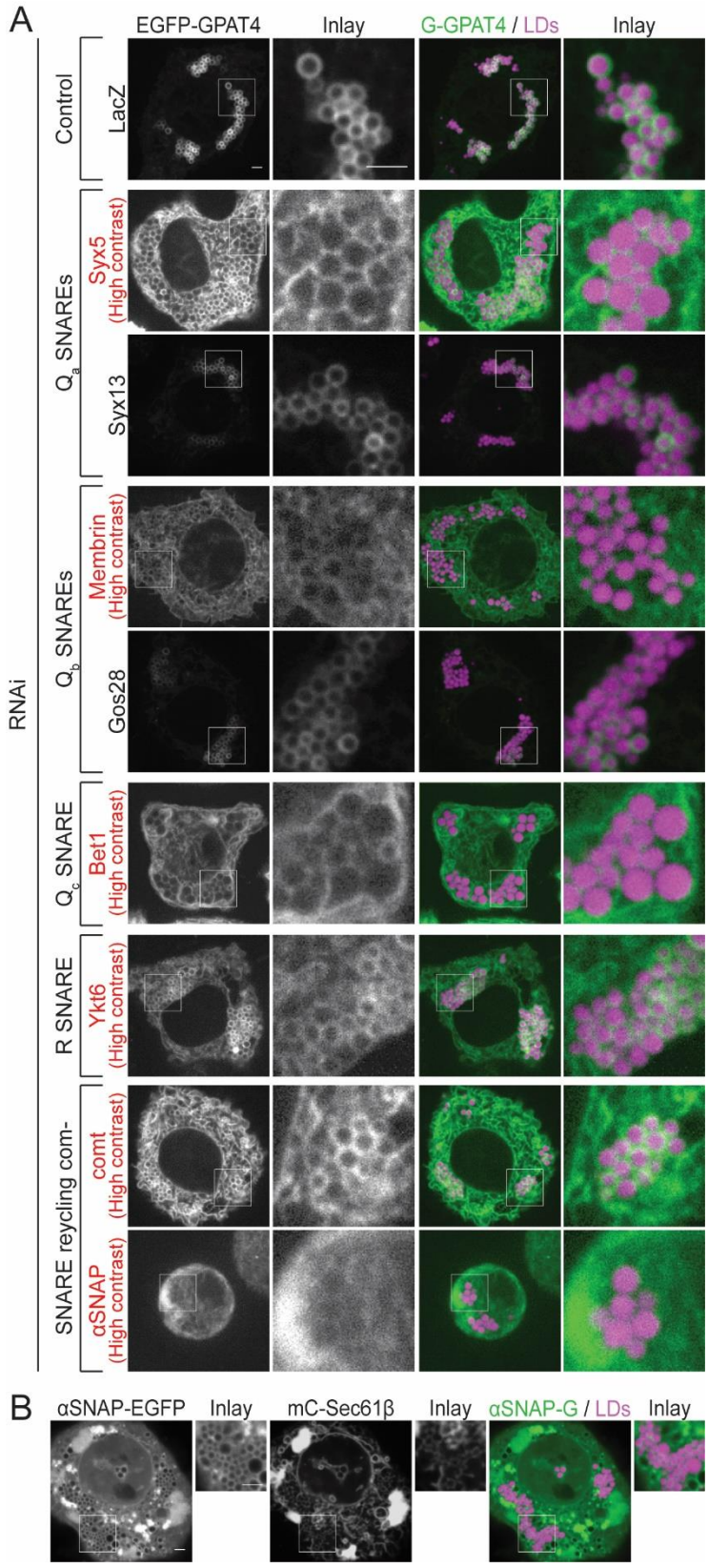

Figure A5. Select SNAREs are required for GPAT4 targeting to LDs and migrate to LD fraction in murine liver

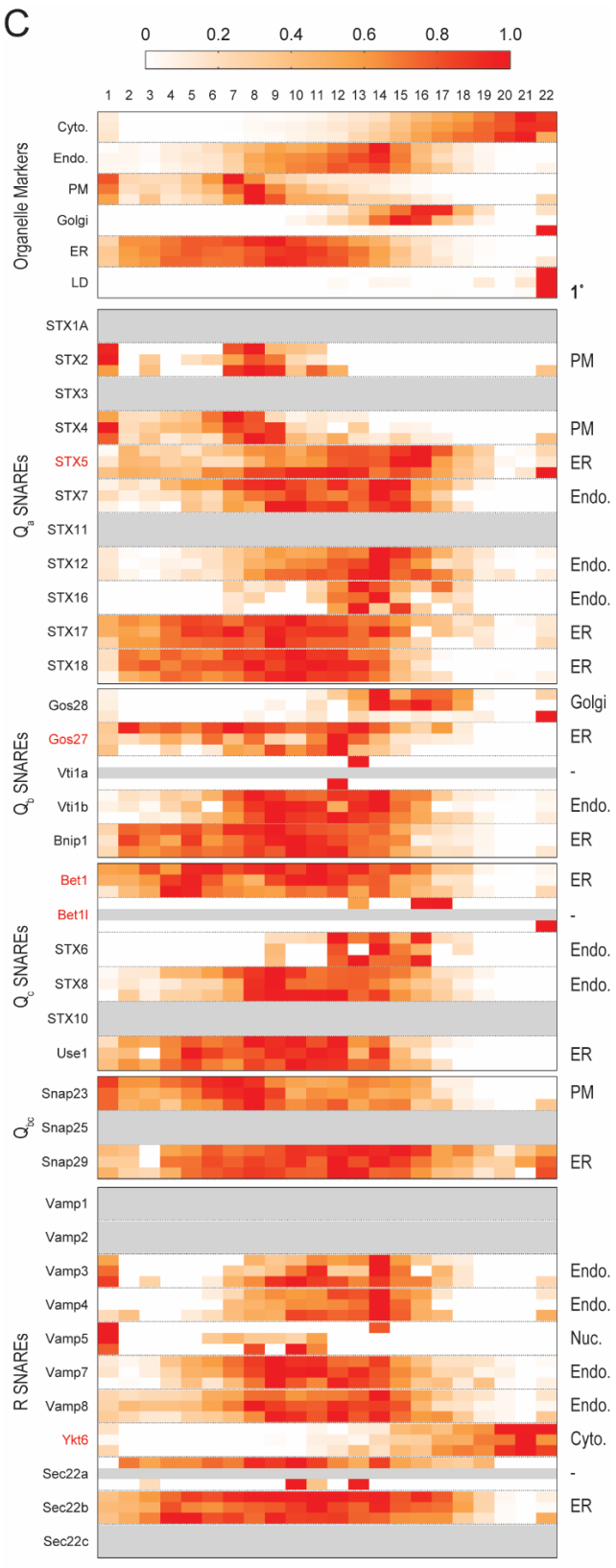

Figure A5 (continued). Select SNAREs are required for GPAT4 targeting to LDs and migrate to LD fraction in murine liver

Figure A5 (continued). Select SNAREs are required for GPAT4 targeting to LDs and migrate to LD fraction in murine liver

(A) Screen result verification using EGFP-GPAT4^{KI} cells. Cells were subjected to 2-3 dsRNA's against select membrane tethering complex components, treated with 1mM OA for 20 hours, stained with MDH, and imaged with spinning-disk confocal microscope. Representative images for dsRNA that shows largest effect on LD targeting are shown. High contrast images (same intensity minimum with lower intensity maximum) for RNAi that show little GPAT4 intensity around LDs are provided (red; see **Figure 10B** for regular contrast images). Quantification is shown in **Figure 10C**. Scale bar, 2μm and 2μm (inlay).
(B) Heatmap of relative SNARE enrichment across sucrose-gradient fractions of murine liver, original data from Krahmer et al.[74]. Numerical data was obtained from a public database (www.nafld-organellemap.org) and reconstructed into the heatmaps above. In this study, murine livers were harvested upon chow diet (low fat diet), 3 weeks of high fat diet, or 10 weeks of high fat diet, and fractionated into 22 sucrose-gradient fractions for quantitative proteomics using mass spectrometer. Organelle markers (top) were chosen based on GO-annotations and stable Euclidian hierarchical clustering across all conditions. Fractionation pattern for all known SNAREs from *Mus musculus* are shown by their class. The three consecutive rows for each protein represent the three conditions (low fat diet, 3w high fat diet, 10w high fat diet from top to bottom). Calculated peptide amounts were normalized to the highest value in each row as 1, with 0 representing undetected. Grey box represents no detection in all fractions in the particular condition. Predicted orthologs of *Drosophila* SNAREs required for GPAT4 targeting to LDs are highlighted in red. Cyto. = cytosol, Endo. = endosomes, PM = plasma membrane, Nuc. = nucleus, 1˚ = primary assignment, - = not assigned or inconsistently assigned.
(C) Localization of αSNAP. Wildtype *Drosophila* S2 R+ cells were co-transfected with plasmids encoding αSNAP-EGFP and mCherry-Sec61β, treated with 1mM OA, and stained with MDH for imaging. Representative images from 3 independent experiments (8-10 cells each) are shown. Scale bar, 2μm and 2μm (inlay).

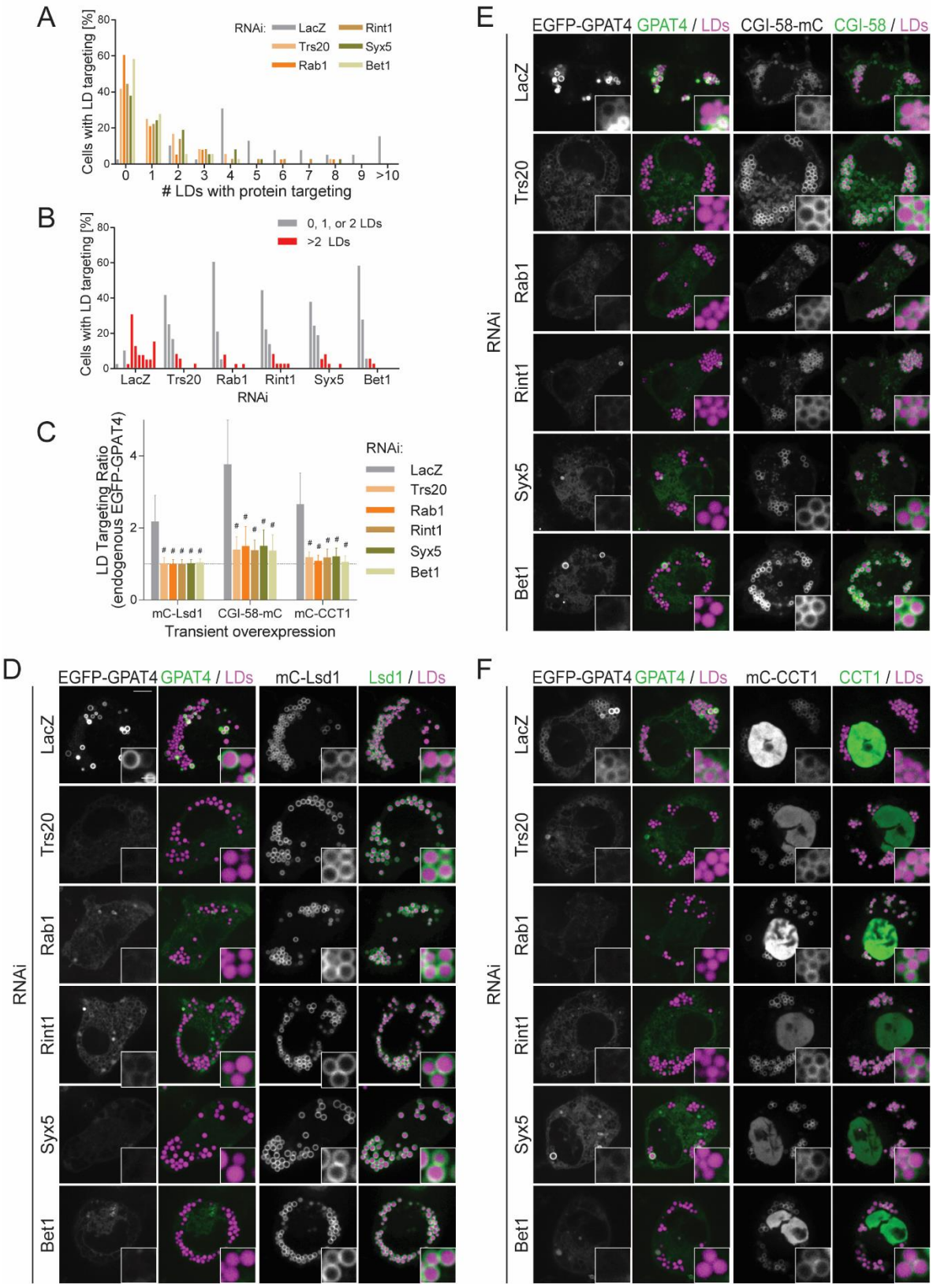

Figure A6. Membrane fusion machinery components are dispensable for LD targeting of cytosolic proteins but not ER proteins

Figure A6 (continued). Membrane fusion machinery components are dispensable for LD targeting of cytosolic proteins but not ER proteins
(A) Frequency distribution for the percentage of cells per the number of LDs that show HSD17B11-G targeting. Wildtype *Drosophila* S2 R+ cells were subjected to dsRNA against LacZ, Trs20, Rab1, Rint1, Syx5, and Bet1, transfected with a plasmid encoding HSD17B11-EGFP, treated with 1mM OA, and stained with MDH for imaging. For each observed cell, the number of LDs that show HSD17B11-G targeting was counted, and the percentage of cells containing the particular number of LDs with protein targeting over total number of observed cells was calculated for each RNAi condition. 3 independent experiments (10-14 cells each).
(B) Frequency distribution in (A) displayed by RNAi. In negative control (LacZ RNAi), most cells show >2 LDs with HSD17B11-G targeting, whereas upon RNAi of membrane fusion machinery components, most cells show 0, 1, or 2 LDs with HSD17B11-G targeting which correspond to the baseline level as shown in **Figure A1**.
(C) EGFP-GPAT4^{KI} cells were subjected to dsRNA against LacZ, Trs20, Rab1, Rint1, Syx5, and Bet1, transfected with mCherry constructs, and stained with MDH for imaging. Quantification here shows LD targeting ratios for EGFP-GPAT4 in different conditions. Data are shown as mean + SD of the results from 3 independent experiments (9-14 cells each). Dashed line at LD targeting ratio = 1. One-way ANOVA for each construct, #$p<0.0001$ compared to LacZ.
(D-F) Representative images for (C). mCherry channel images (also shown in **Figure 11**) are reproduced here. Scale bar, 5μm and 1μm (inlay).

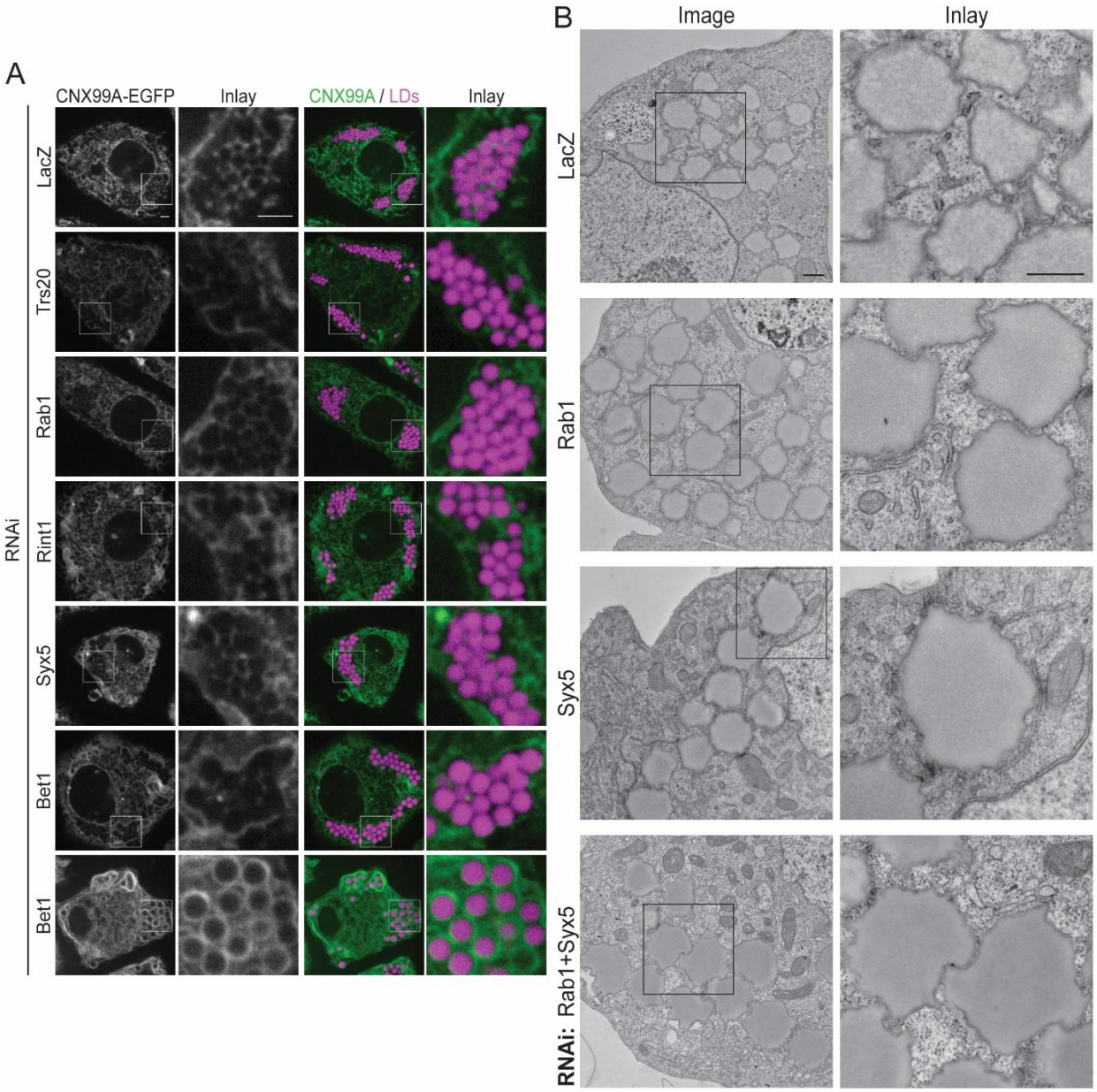

Figure A7. Changes in ER morphology upon RNAi of genes required for GPAT4 targeting from the ER to LDs

(A) CNX99A-EGFP^{KI} cells were subjected to dsRNA against LacZ, Trs20, Rab1, Rint1, Syx5, and Bet1, treated with 1mM OA, and stained with MDH for imaging. Representative images from 3 independent experiments (10-12 cells each) are shown, with two images for Bet1 RNAi. Scale bar, 2μm and 2μm (inlay).

(B) Ultrastructural changes upon RNAi against LacZ, Rab1, Syx5, or Rab1+Syx5. Wildtype *Drosophila* S2 R+ cells were subjected to RNAi and chemically fixated for EM analysis. Representative images from 2 experiments for LacZ, Rab1, and Syx5 and from 1 experiment for Syx5+Rab1 are shown. Additional images are shown in **Figure 13A**. Scale bar, 500nm and 500nm (inlay).

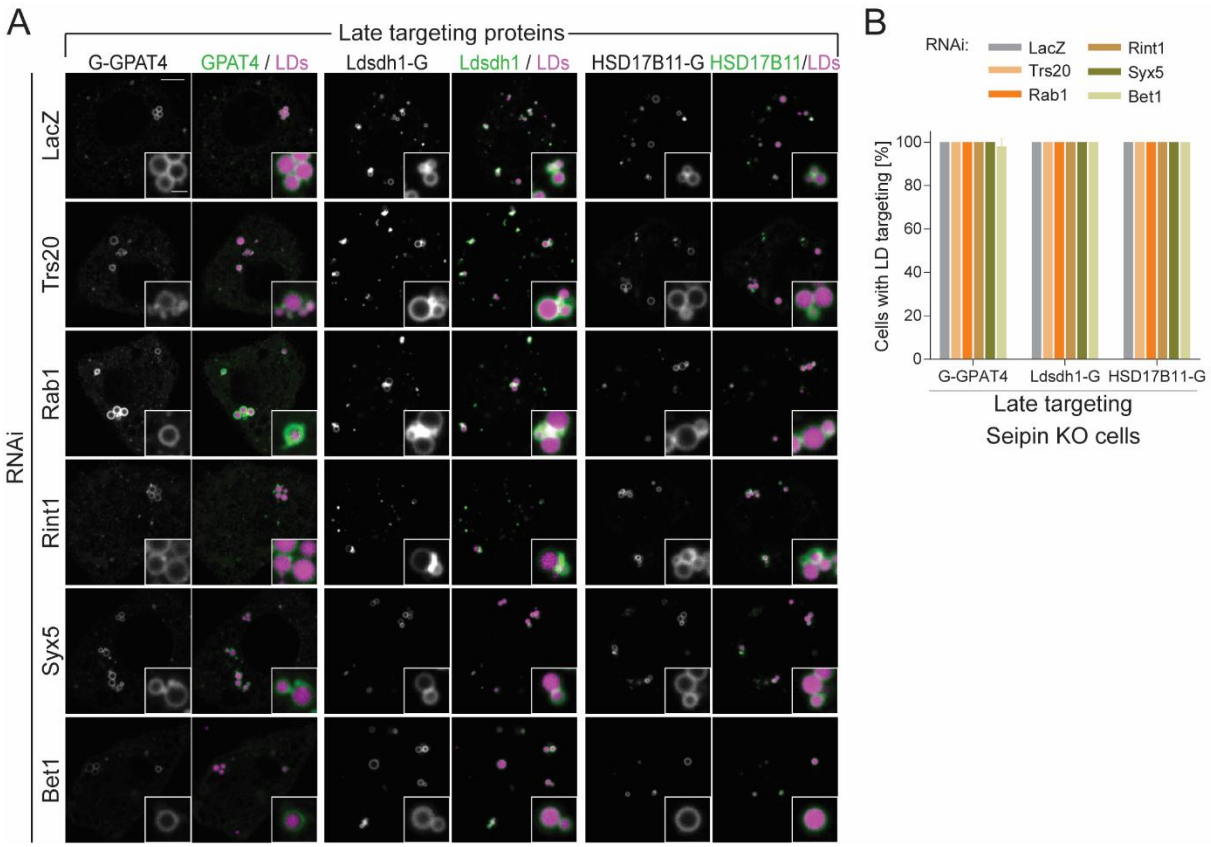

Figure A8. Membrane fusion machinery are dispensable for ER-to-LD protein targeting in the absence of seipin

(A) Seipin KO *Drosophila* S2 R+ cells were subjected to dsRNA against LacZ, Trs20, Rab1, Rint1, Syx5, and Bet1, transfected with EGFP constructs, treated with 1mM OA, and stained with MDH for imaging. Images were taken at 30 minutes after OA treatment. Scale bar, 5μm and 1μm (inlay).

(B) Quantification of (A). Percentage of cells with protein targeting were calculated per experiment, and data are represented as mean + SD of the results from 3 independent experiments (12-18 cells each).

Appendix B. C-Terminal Domain of GPAT4 Delays Its Timing of Targeting to LDs

GPAT4 targeted LDs late around 3 hours after OA treatment, whereas its hairpin-like hydrophobic domain (160-216) which is sufficient to insert into the ER and target LDs, targeted LDs as early as 30 minutes after OA treatment (**Figure B1**). Truncation analysis revealed that C-terminal domain of GPAT4 after the hairpin-like domain is necessary and sufficient to delay targeting of the protein to LDs.

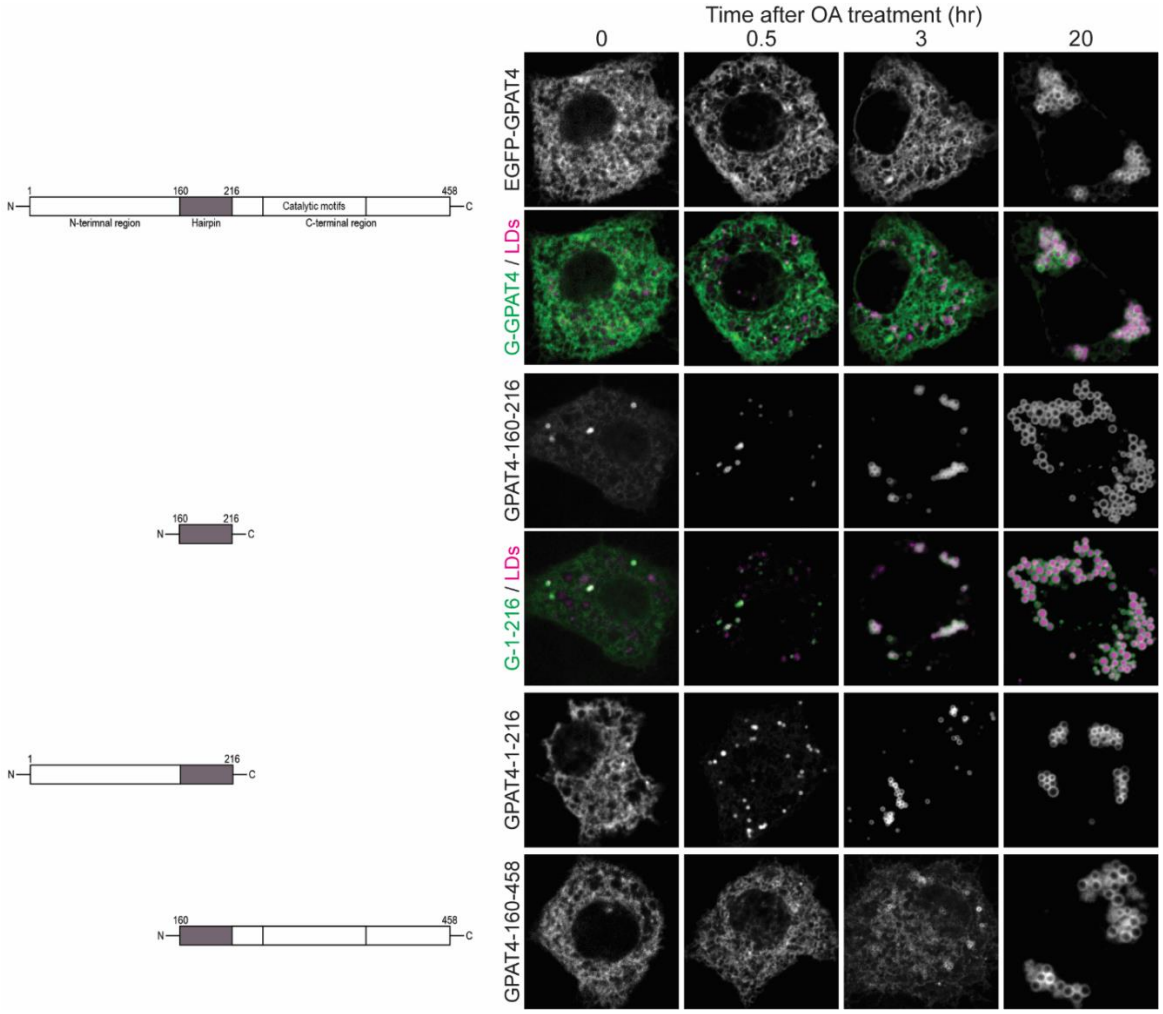

Figure B1. C-terminal domain of GPAT4 is necessary and sufficient to delay targeting of the protein to LDs
Drosophila S2 R+ cells were transfected with EGFP constructs of GPAT4 truncation mutants, and their LD targeting was observed over time after 1mM OA treatment. LDs were stained with MDH. Sequence features of GPAT4 is shown on the left. Shaded region indicates the location of hairpin-like hydrophobic domain sufficient to insert into the ER and target LDs.

Further truncation analysis revealed that GPAT4-160-376 domain may be necessary and sufficient to delay GPAT4 targeting to LDs (**Figure B2**). Truncation mutants 1-376 and 1-405 showed two distinct populations of LD targeting behavior starting 1.5 hours after OA treatment, in which one population show delayed LD targeting and the other showing early targeting.

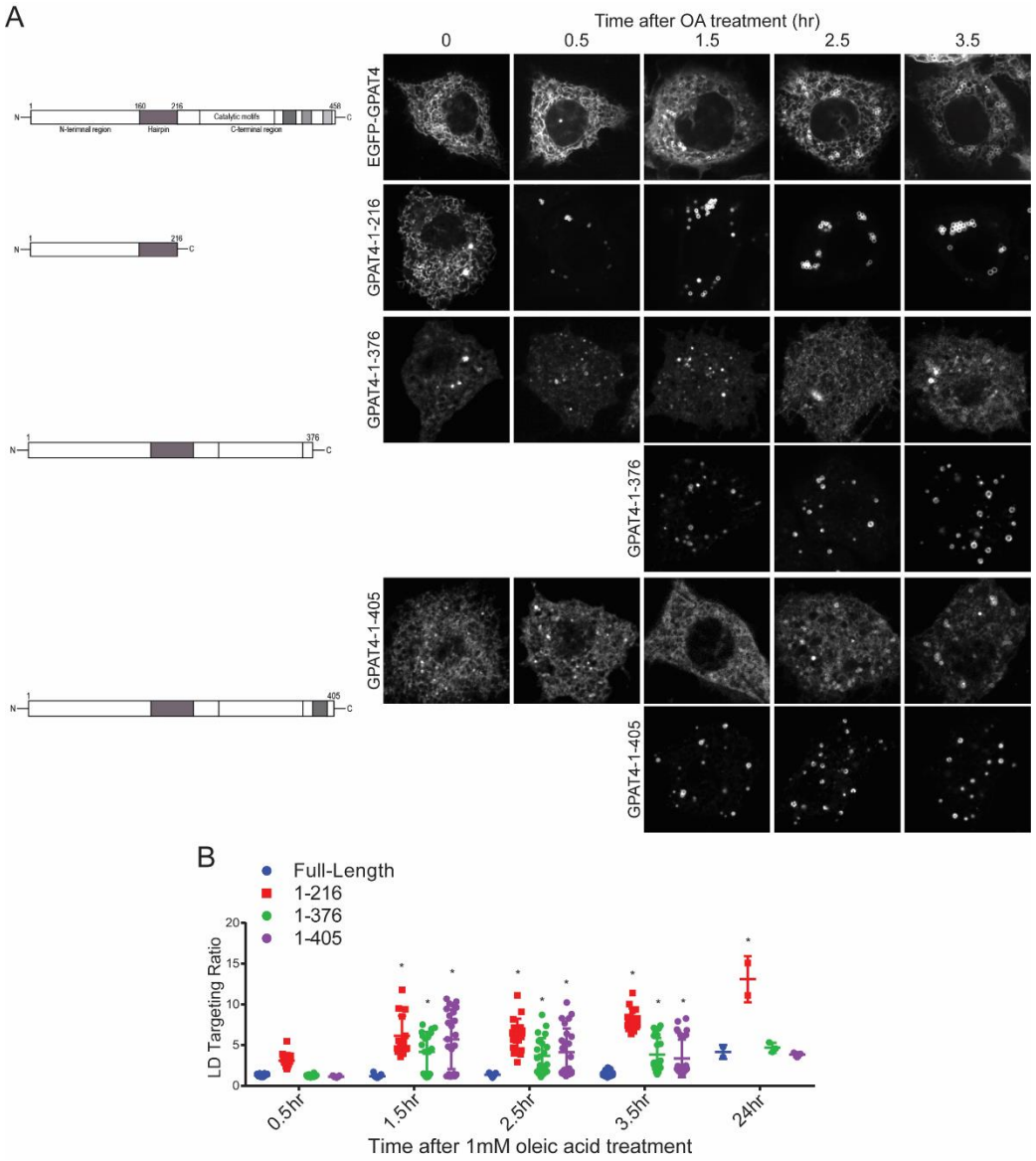

Figure B2. GPAT4-160-376 is necessary and sufficient to delay GPAT4 targeting to LD
(A) *Drosophila* S2 R+ cells were transfected with EGFP constructs of GPAT4 point or truncation mutants, and their LD targeting was observed over time after 1mM OA treatment. Sequence features of GPAT4 is shown on the left. Shaded region indicates the location of hairpin-like hydrophobic domain (160-216) or predicted amphipathic helices. Truncation mutants 1-376 and 1-405 showed two distinct populations of cells with different LD targeting behavior starting 1.5 hours after OA treatment. Above panels show delayed LD targeting and below early LD targeting.
(B) Quantification of (A). LD targeting ratios were calculated for conditions shown in (A). Two-way ANOVA, *p<0.05 compared to full-length.

Catalytic activity of GPAT4 was not required for the delayed targeting of GPAT4, since the catalytically dead mutant (H255A) still targeted LDs late (**Figure B3A**). In addition, GPAT4 C-terminal domain missing the catalytic domain (AA #361-458) was sufficient to delay LD targeting of the GPAT4hairpin-like hydrophobic domain (**Figure B3B**).

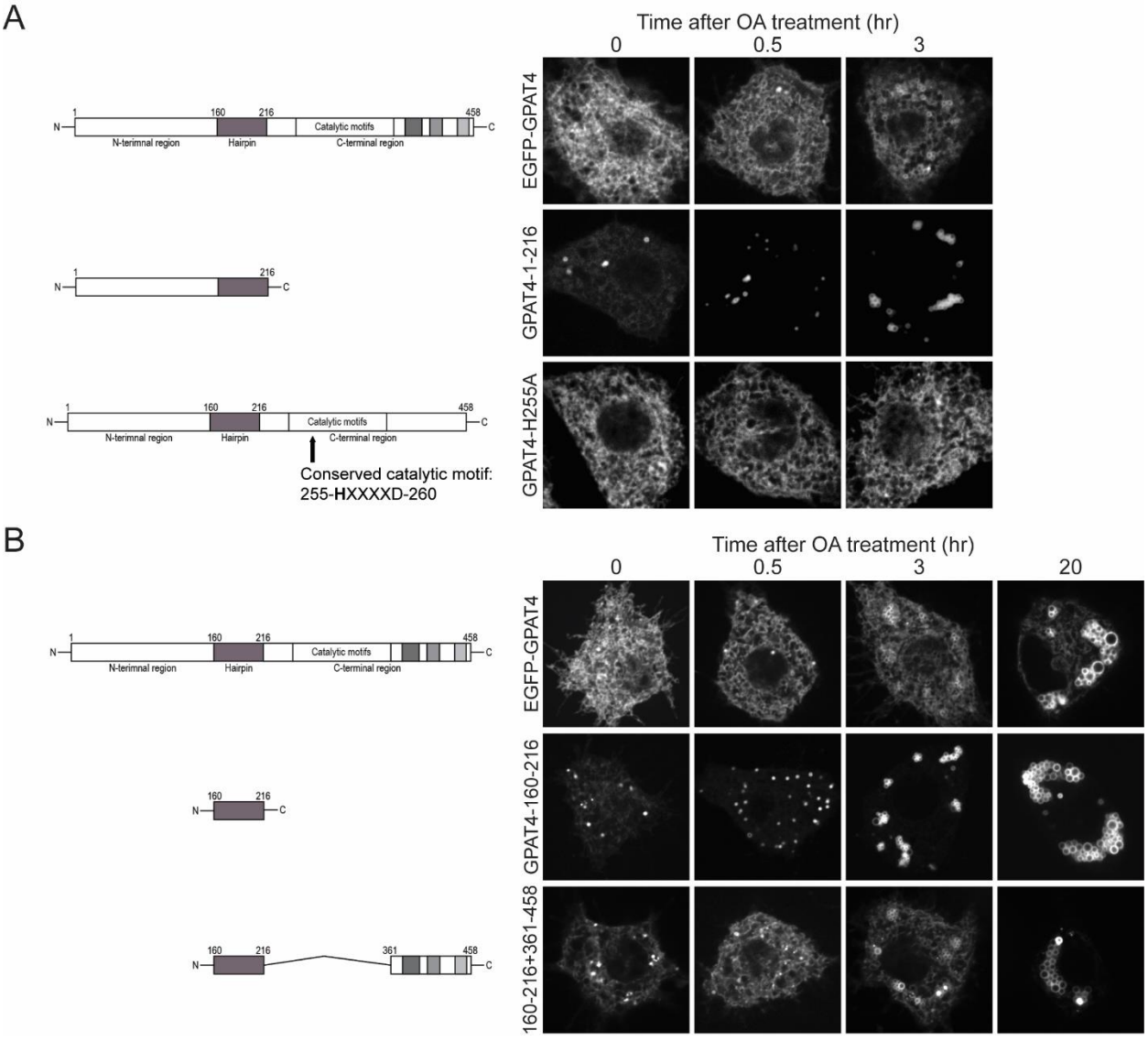

Figure B3. Catalytic activity of GPAT4 is not required for delaying GPAT4 targeting to LDs
(A&B) *Drosophila* S2 R+ cells were transfected with EGFP constructs of GPAT4 point or truncation mutants, and their LD targeting was observed over time after 1mM OA treatment. Sequence features of GPAT4 is shown on the left. Shaded region indicates the location of hairpin-like hydrophobic domain (160-216) or predicted amphipathic helices.

Delayed LD targeting was not attributable to the size or rigidity of the domain after the hairpin-like domain, since attaching EGFP, which is roughly the same size as GPAT4 C-terminal domain, did not delay GPAT4 targeting to LDs whether with or without a flexible linker (3*GGGGS) in-between (**Figure B4**).

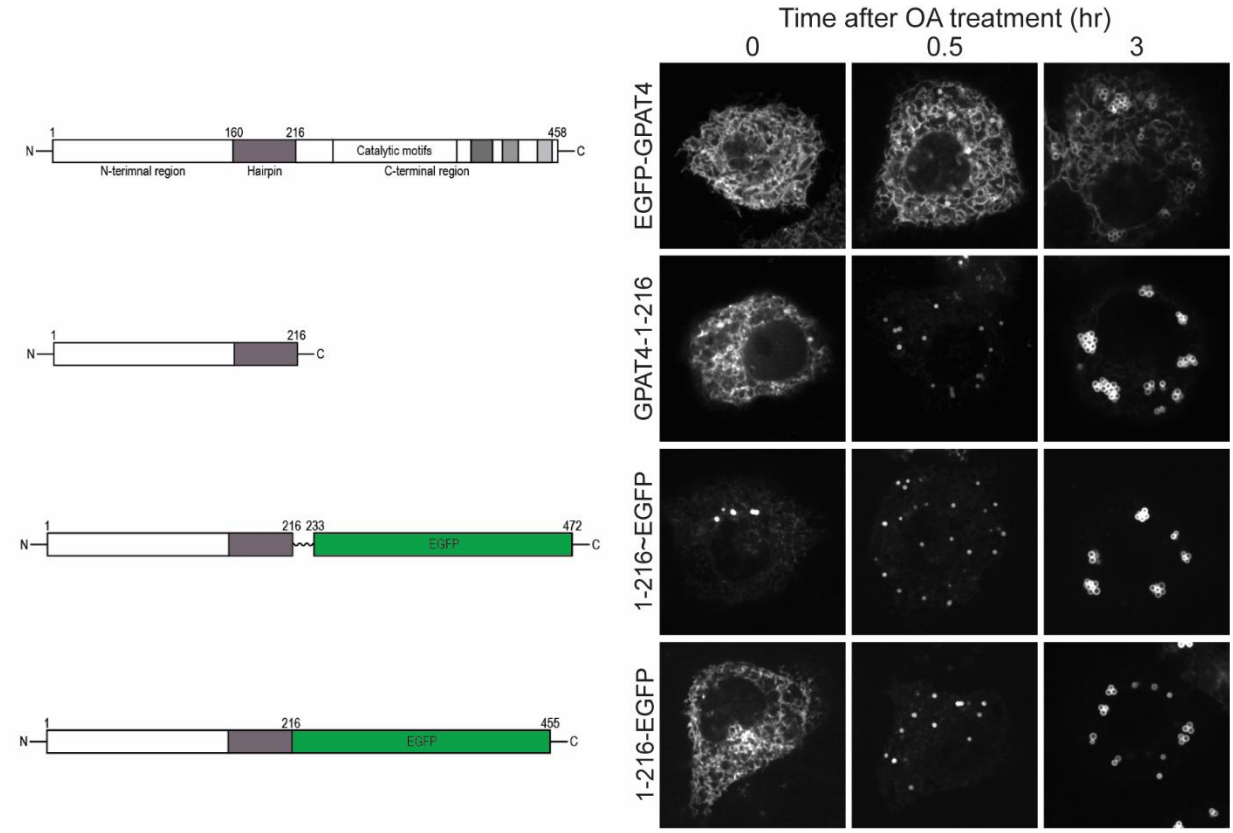

Figure B4. Size and rigidity do not affect timing of GPAT4 targeting to LDs
Drosophila S2 R+ cells were transfected with GPAT4 truncation mutants and chimeric constructs, and their LD targeting was observed over time after 1mM OA treatment. Sequence features of the mutants is shown on the left. Shaded region indicates the location of hairpin-like hydrophobic domain (160-216) and predicted amphipathic helices. ~ indicates 3*GGGGS linker.

Although GPAT4-361-458 was sufficient to delay LD targeting of GPAT4 hairpin-like domain, it was not sufficient to delay LD targeting of other early targeting proteins including HPos, Alg14 hairpin-like domain, and ACSL hairpin-like domain (**Figure B5**).

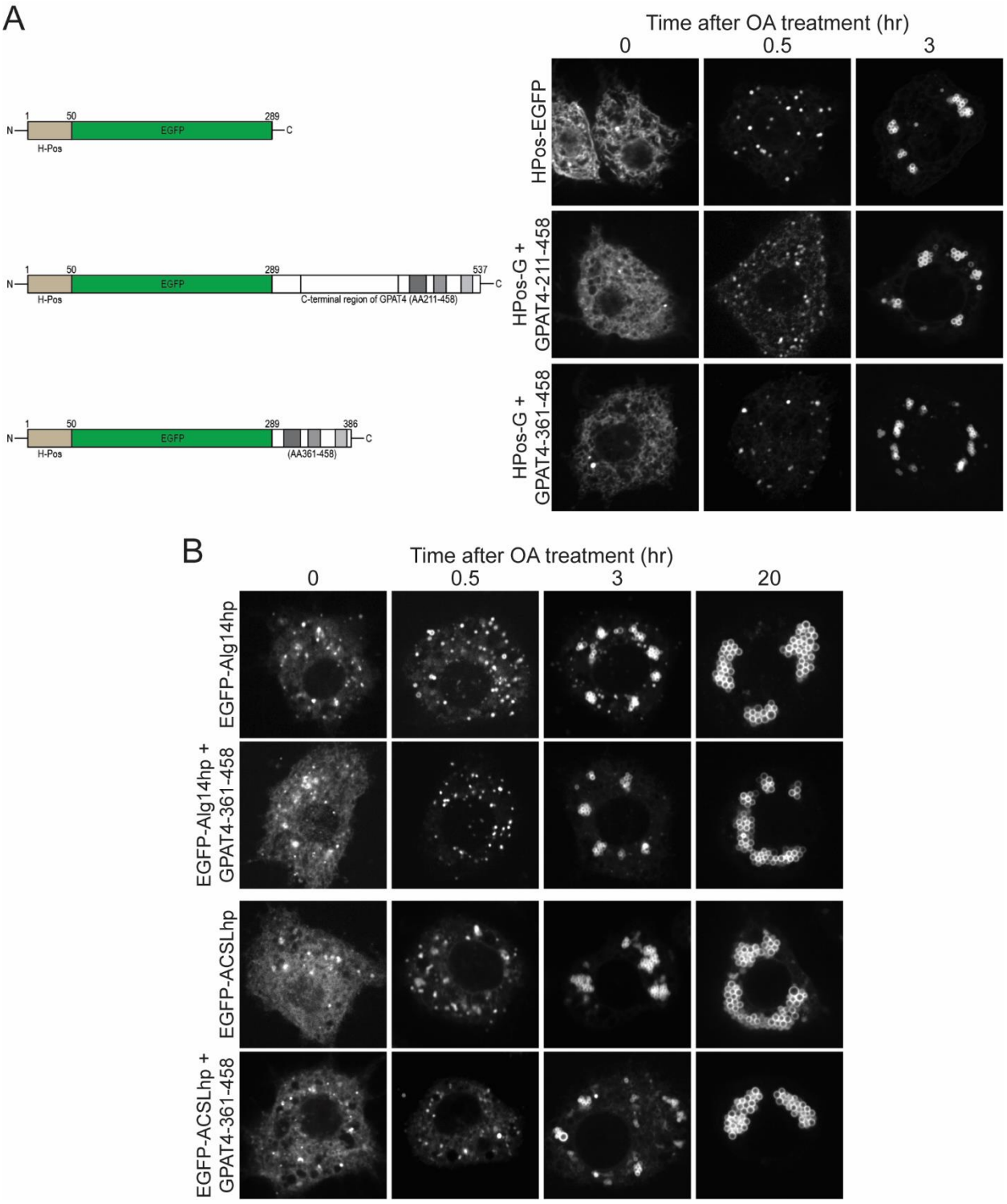

Figure B5. GPAT4-361-458 is not sufficient to delay LD targeting of other early targeting proteins. (A&B) *Drosophila* S2 R+ cells were transfected with constructs encoding early targeting proteins (HPos[24], Alg14 hairpin-like domain, ACSL hairpin-like domain) with or without GPAT4-361-458, and their LD targeting was observed over time after 1mM OA treatment.

To test if protein-protein interaction at the C-terminal region of GPAT4 delays LD targeting, we sought to determine interactors at this domain using co-immunoprecipitation coupled with tandem mass spectrometry for identification (**Figure B6**). Elm (human ortholog CHP1), which was recently identified as GPAT4 interactor and activator of catalytic activity[129], was found to co-precipitate in higher amount with full-length GPAT4 than the truncation mutant missing the C-terminal domain, in both basal and OA-treated conditions.

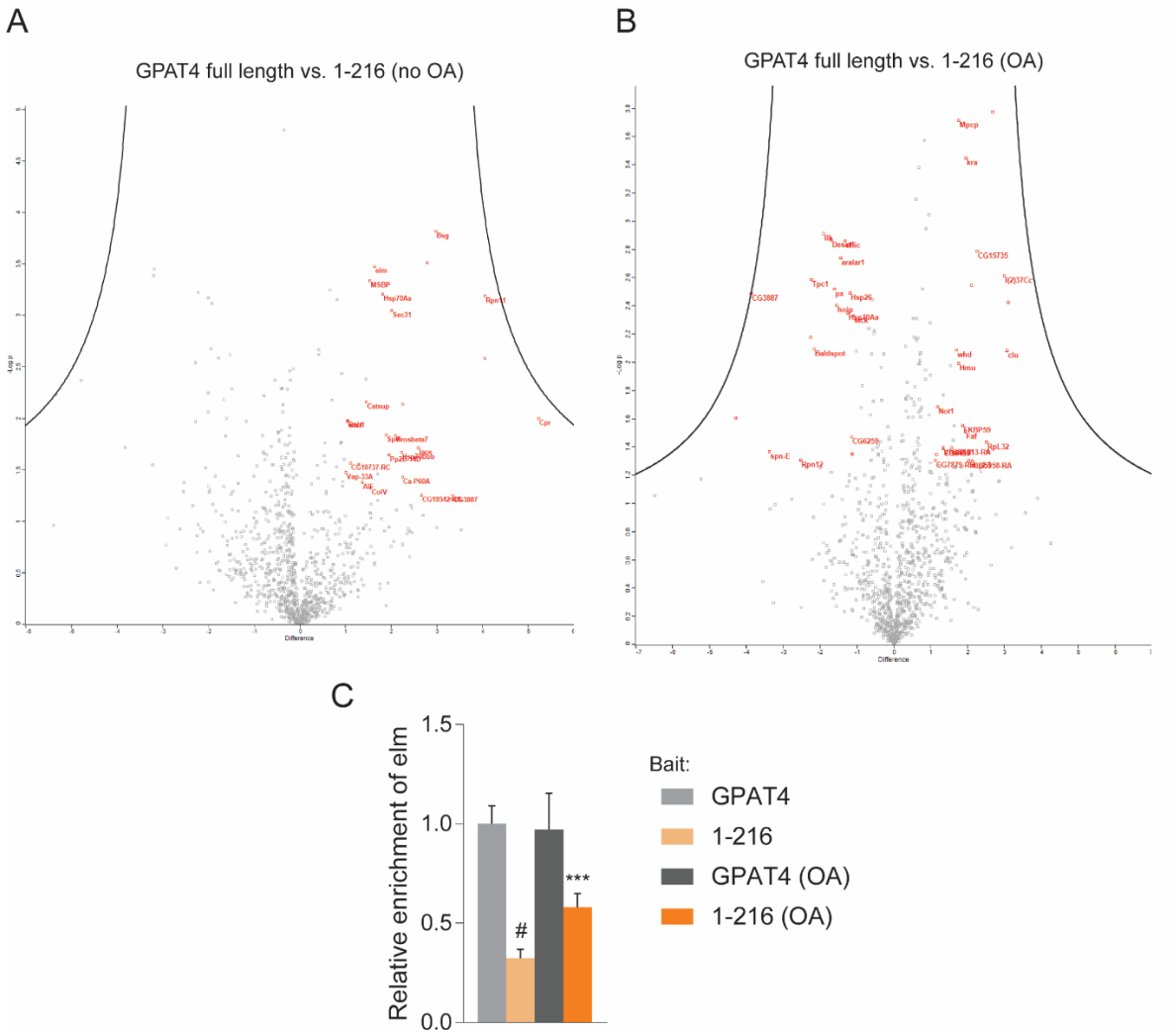

Figure B6. C-terminal domain of GPAT4 interacts with elm
(A&B) Co-immunoprecipitation of GPAT4 and GPAT4 truncation mutant missing the C-terminal domain. Co-IP was performed using full-length GPAT4 or GPAT4 truncation mutant 1-216 to identify interactors at the C-terminal domain in GPAT4 knock-out *Drosophila* S2 R+ cells. Upon transfection of EGFP fusion constructs with (A) or without (B) OA treatment, bait was enriched using GFP-Trap beads. Bait and prey were eluted and subjected to identification by tandem mass spectrometry. Results of the mass spectrometry analysis are displayed as volcano plots.
(C) Elm interacts with C-terminal domain of GPAT4. Relative enrichment of elm in the co-IP eluates normalized to GPAT4 co-IP without OA treatment (grey) is shown as mean + SD. One-way ANOVA, ***p<0.001, #p<0.0001 compared to GPAT4 without OA.

To determine if elm affects GPAT4 targeting to LDs, we tested if elm RNAi alters GPAT4 targeting to LDs (**Figure B7**). As expected, RNAi of elm resulted in slower LD maturation and smaller. GPAT4 could still target LDs, and the amount seemed comparable when comparing conditions with similar LD sizes (**Figure B7A**). On the other hand, elm localization to LDs depended on GPAT4 (**Figure B7B**). Whereas in wildtype cells only a faint enrichment of mC-elm was observed around LDs, mC-elm enrichment around LDs became much more apparent in EGFP-GPAT4 overexpressing cells. Finally, no ring-like enrichment of mC-elm was observed in GPAT4 knock-out cells, indicating that elm requires GPAT4 for LD targeting.

In the screen, RNAi of Wdr24, a component of GATOR complex required for mTOR activity, was found to decrease GPAT4 targeting to LDs. To determine if mTOR activity is required for GPAT4 targeting to LDs, we treated cells with mTOR inhibitors torin and rapamycin (**Figure B8**). Although pharmacological inhibition of mTOR pathway notably reduced LD sizes, EGFP-GPAT4 formed ring-like enrichment around LDs, indicating that mTOR activity is not required for GPAT4 targeting to LDs.

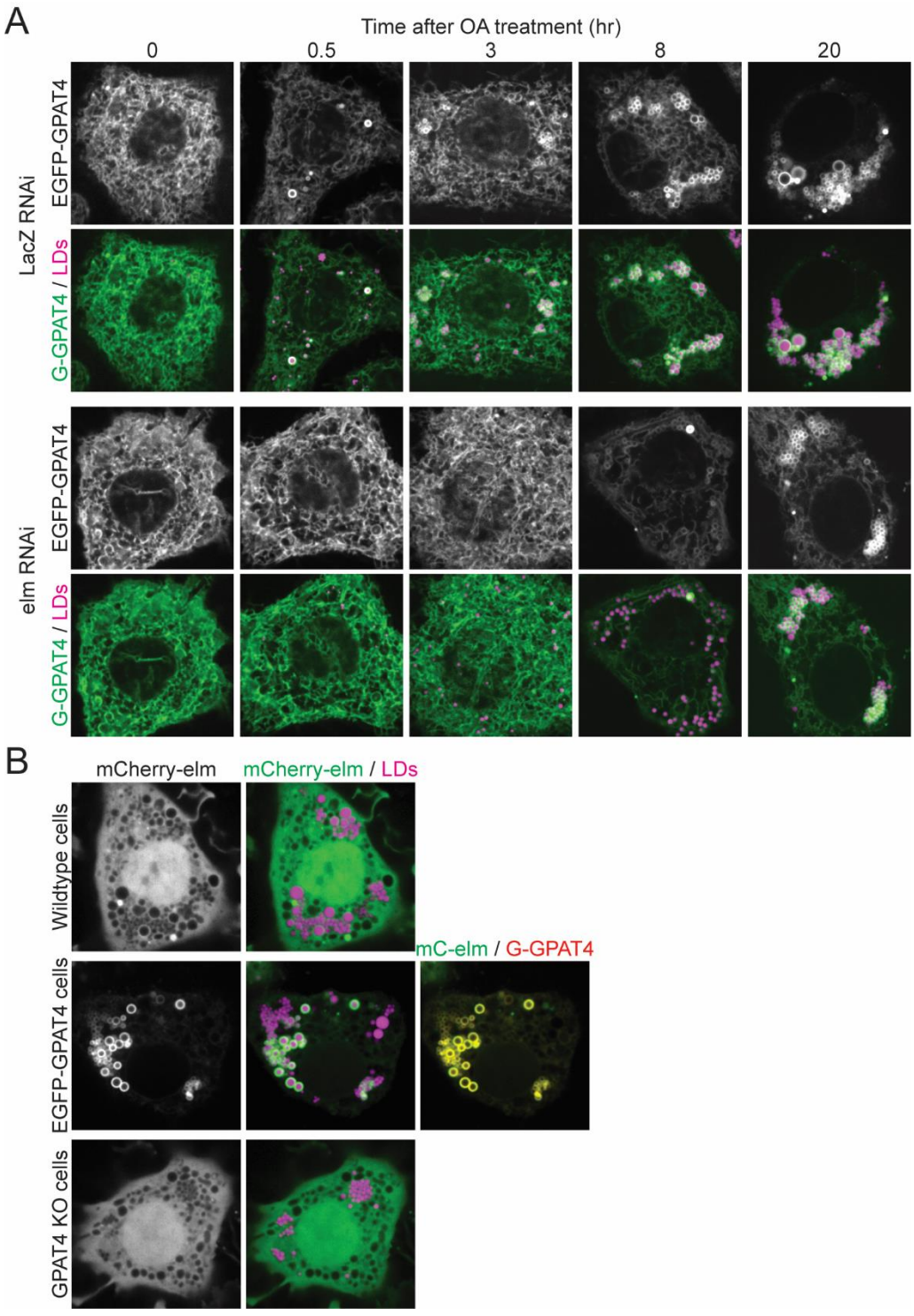

Figure B7. Elm depends on GPAT4 for LD targeting but not vice versa
(A) RNAi of elm does not prevent GPAT4 targeting to LDs. A stable cell line overexpressing EGFP-GPAT4 was subjected to LacZ or elm RNAi and GPAT4 targeting to LDs was observed over time after OA treatment. LDs were stained with MDH.
(B) Elm co-localizes with GPAT4 on LDs. mCherry-elm was transiently overexpressed in cells with various levels of GPAT4 expression (wildtype cells (medium), EGFP-GPAT4 stable cell line (high), and GPAT4 knock-out cells (none)) and its localization was determined. LDs were stained with MDH.

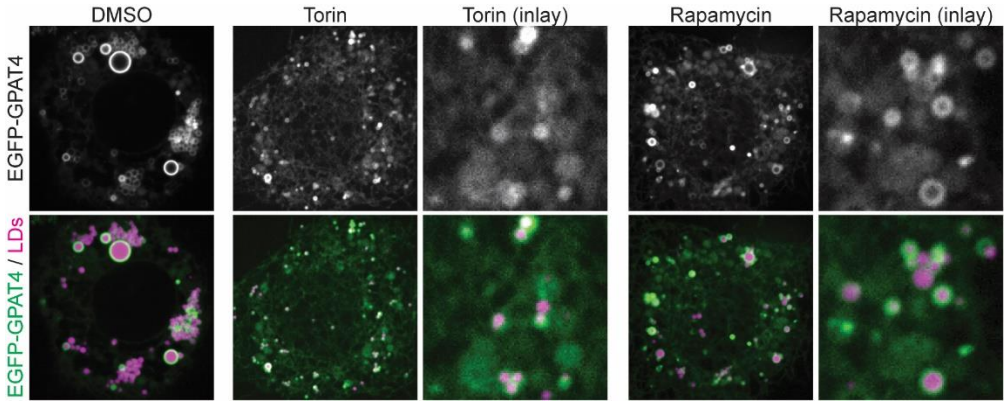

Figure B8. mTOR inhibition does not prevent LD targeting of GPAT4
Drosophila S2 R+ cells stably overexpressing EGFP-GPAT4 was pre-treated with DMSO, 250nM or 1.25μM torin, or 20nM or 100nM rapamycin before OA treatment. 14 hours after OA treatment, EGFP-GPAT4 localization was determined. LDs were stained with MDH.

Appendix C. Methods Supplementary Tables

Table C1. Gateway cloning

Plasmid	PCR template	Primer (forward)	Primer (reverse)
Chapter II			
pAG-GPAT4	pAC-GPAT4[54]	CACC ATGATCGCCGTGCTGTTGGAC ATATTC	TTAGGTGGAGTCCGACTTCAGCC G
pA-Ldsdh1-G	gBlock Gene Fragment Synthesis (Integrated DNA Technologies): CACC+gene sequence from flybase.org (FBgn0029994) excluding the stop codon		
pA-HSD17B11-G	gBlock Gene Fragment Synthesis (Integrated DNA Technologies): CACC+gene sequence from flybase.org (FBgn0032910) excluding the stop codon		
pA-LDAH-G	gBlock Gene Fragment Synthesis (Integrated DNA Technologies): CACC+gene sequence from flybase.org (FBgn0035206) excluding the stop codon		
pAG-Ubxd8	gBlock Gene Fragment Synthesis (Integrated DNA Technologies): CACC+gene sequence from flybase.org (FBgn0025608)		
pAHalo-Rab1	gBlock Gene Fragment Synthesis (Integrated DNA Technologies): CACC+gene sequence from flybase.org (FBgn0285937)		
pAG-Rint1	Bloomington Drosophila Stock Center (GH01880)	CACC ATGCATGCAGAACTCAGCGAA ATGG	AAACATCTTTATGTCCATCCTCCG CT
pAHalo-Syx5-1-445	Bloomington Drosophila Stock Center (SD07852)	CACC ATGCAAACCCGAAGACGCCTT CATC	TTAGCGATTTTTGGAGACGGATT GAAAG
pA-αSNAP-G	gBlock Gene Fragment Synthesis (Integrated DNA Technologies): CACC+gene sequence from flybase.org (FBgn0250791) excluding the stop codon		
pAC-Sec61 β	pAG-Sec61β[54]	CACC ATGCCCGCTCCAGCCAGTTCA ACG	TTAAGAACGATTGTATTTGCCCCA AATG
pAC-Lsd1	pAC-Lsd1[88]	CACC ATGGCAACTGCAACCAGCGGC AGTG	CTAGTAGACGCCGTTGATGTTATT GTG
pA-CGI-58-C	pA-CGI-58-C[88]	CACC ATGCTGCGTGCCGTGGAGAAG AAG	CTTCGGTTTGATGTTCGCCGCCA G
pAC-CCT1	pAC-CCT1[88]	CACC ATGGCCACCTCATCGATACTC GCC	TCAATTGCTTCGACGCTCGTACTC C
Chapter III			
pAC-TMEM19	gBlock Gene Fragment Synthesis (Integrated DNA Technologies): CACC+gene sequence from flybase.org (FBgn0036353)		

Table C2. Restriction-ligation cloning

Plasmid	Backbone	PCR template for insert	Primer (forward)	Primer (reverse)
Chapter II				
pA-Halo-W	pAGW	pSMART-Halo-Plin3[48]	GCACA GATATC G AGGCCT GTCTAGAGAAG CCC GCCACC atggcagaaatcggta ctg	GCACA ACCGGT G gccggaaatctcgagc gtcgac
pAW-Halo	pAWG	pSMART-Halo-Plin3[48]	GCACA GAGCTC CGCCACC atggcagaaatcggta ctg	GCACA ACCGGT G TCA gccggaaatctcgagc gtcgacag
Chapter III				
pADH_MCS_pTEF_hphMX6	pRS416 (Addgene #4898)	pFA6a-HBH-hphMX4 (Addgene #26873)	GCACA atgcat ttacttataatacagtttt TTATTCCTTTGC CCTCGGACGAG TG	GCACA tcccgga tttcggtttctttgaaatttttt tt GCCTCGTCCCC GCCGGGTCAC
pADH-hCDS1_hph	pADH_MCS_pTEF_hphMX6	gBlock Gene Fragment Synthesis (Integrated DNA Technologies): GCACA ACTAGT GCCACC + NM_001263.4 CDS region + CTCGAG TGTGC		
pADH-FLAG-hCDS1_hph	pADH_MCS_pTEF_hphMX6	gBlock Gene Fragment Synthesis: GCACA ACTAGT GCCACC ATG + 3XFLAG (GACTACAAAGACCATGACGGTGATTATAAAGATCATGA CATCGATTACAAGGATGACGATGACAAG) + GGGGS*3 linker (CACCGGTATACAAGTTTGTACAAAAAAGCAGGCTCCGC GGCCGCCCCCTTCACC) + NM_001263.4 CDS region + CTCGAG TGTGC		
pADH-hTMEM19	pADH_MCS_pTEF_hphMX6	gBlock Gene Fragment Synthesis (Integrated DNA Technologies): GCACA ACTAGT GCCACC + NM_018279.4 CDS region + CTCGAG TGTGC		
pADH-FLAG-hTMEM19_hph	pADH_MCS_pTEF_hphMX6	gBlock Gene Fragment Synthesis: GCACA ACTAGT GCCACC ATG + 3XFLAG (GACTACAAAGACCATGACGGTGATTATAAAGATCATGA CATCGATTACAAGGATGACGATGACAAG) + GGGGS*3 linker (CACCGGTATACAAGTTTGTACAAAAAAGCAGGCTCCGC GGCCGCCCCCTTCACC) + NM_018279.4 CDS region + CTCGAG TGTGC		

Table C3. Site-directed mutagenesis

Mutation	Primer (forward)	Primer (reverse)
Chapter II		
Rab1-N124I	gBlock Gene Fragment Synthesis (Integrated DNA Technologies): CACC + gene sequence from flybase.org (FBgn0285937), with nucleotide #371 changed from A to C	
Comt-E329Q	CTACATATCATCATCTTCGAC C AGATCGATGCCATTTGCAAG	CTTGCAAATGGCATCGATCT G GTCGAAGATGATGATATGTAG
Chapter III		
TMEM19-E118A, D120A, E123A	CGCACATGAAACGCCGTTTC GCG AGC GCT TTTCGC GCG GGCGAAGGCCAACGAAACTG	CAGTTTCGTTGGCCTTCGCC CGC GCGAAA AGC GCT CGC GAAACGGCGTTTCATGTGCG
D150A, E155A, D159A	TTGCATTGCTTTATCTGCTG GCC TGCGGTAGTGGC GCG CGGGCGGTG GCC TTCGCACGAGAATACCGAT	ATCGGTATTCTCGTGCGAA GGC CACCGCCCG CGC GCCACTACCGCA GGC CAGCAGATAAAGCAATGCAA
E285A, E286A	GCAGTTCTCGGGCATCAAT GCG GCA GGCAAGATTGTGGATACAC	GTGTATCCACAATCTTGCC TGC CGC ATTGATGCCCGAGAACTGC
D150A	TGCATTGCTTTATCTGCTGG C CTGCGGTAGTGGCGAGCG	CGCTCGCCACTACCGCAG G CCAGCAGATAAAGCAATGCA
E155A	CTGGACTGCGGTAGTGGCG C GCGGGCGGTGGACTTCGC	GCGAAGTCCACCGCCCGC G CGCCACTACCGCAGTCCAG
D159A	GTGGCGAGCGGGCGGTGG C CTTCGCACGAGAATACCGA	TCGGTATTCTCGTGCGAAG G CCACCGCCCGCTCGCCAC
E188A	GGCGACACCTGGTCCAGT GCA CTAGGATCCGTGCTGTCG	CGACAGCACGGATCCTAG TGC ACTGGACCAGGTGTCGCC
D271A	CTTTTTGGGTCCCTTTTGG C CTCTGTCCTAGGTGGTCTG	CAGACCACCTAGGACAGAGGCCAAA AGGGACCCAAAAAG
G302I	GGAGTGCGCCACGTAAGC AT ACTGCGCATCCTGGACAAC	GTTGTCCAGGATGCGCAGTATGCTTA CGTGGCGCACTCC

Table C4. Genomic DNA PCR to generate template for dsRNA synthesis

dsRNA target	Primer (forward)*	Primer (reverse)*
LacZ	tgtatgaacggtctggtctttg	aataaggttttcccctgatgc
Chapter II		
Arf79F	TAGCGATTAGCGTTCTTCA	CTGCCAAATGCAATGAACG
βCOP	CCAGTCAGTTGGGTGACCTT	CCTAGCAAGCCCATAACCAA
Seipin	ACGCCCTGCACCTTTCC	ACTATGGCCGACAATACGG
Rab1 (1) or Rab1	CACCATCACGTCTTCATATTATAGG	TGGTGTGGTCGACTACTTTCTTGG
Rab1 (2)	TGCAGTTTAATGGTCTTTCCGTCG	GCTGCTTATTGGAGACTCGGGC
Rab1 (3) or Rab1-5'UTR	TTCCGGATTCACAGATGACATTTTC	GTGTAGCCCTGGTTGGAAGAGG
Rab7 (1)	GACACTGCTGGTCAGGAACGCT	CTCCAACTCTAACGCATTCTTGGC
Rab7 (2)	AAACAATCGTCCTGGCAATCCTGAC	TGCCAGAGGCTCGTTAAGACTCAG
Rab8 (1)	CACTGCCGGCCAGGAGCGTTTT	CGGTCAATTCGCACTTGTTTCCC
Rab8 (2)	AGGACAGTTGGTTGTCCAGGTGC	ACCCTCGATCTGTGCGATACTAC
Rab18 (1)	GAAAGTTTGCCAGGAAGCACAGG	GTAACACGTAGACGCGCTTGCC
Rab18 (2)	GCATTAAGCGGAGCTCAAACCAC	ATGATGGCAATGTTGGGATTGTCG
Rab18 (3)	TCTATCGTGAGAATGTAAACAAAGCA	TGTGTGGTTTGAGCTCCGCTTAATG
Rab32 (1)	TGACATCCACCAGCGATAAGCGC	GGATGCACGGAATGGGACTGCC
Rab32 (2)	GTTGCTCATCCGTTTTCCAGTGC	CCAGGTCAGCAGGAACACTTGTTC
Rab40 (1)	CCCAGGAATTCCGAAGGTTCTTG	TTATTGCTGCGCCAGATGTGCTC
Rab40 (2)	GCTGTCGCTTCAGGAATTGTGCTG	ATCGCACAGCTATTCCGACTGCTG
Bet5 (1)	TCGTTCTCAACACGGACACGACG	ATATATTGCGAATGCCGAAGATGGG
Bet5 (2)	AGCCAAACTCACCTACGGAATGC	GTTTCCAGATAATGCAGGGCGTAG
Trs20 (1) or Trs20	GTCCACATACTACTTTGTTATTGTG	ACAAATACTTCCGACCAAAGATCTC
Trs20 (2)	AAGGAATTCAGCACCGTGAACAAG	TATTTGGCTGGCTGTGATGAAGG
Trs23 (1)	AGTCACCCTGGATGATGGACGC	TCCAGGGAGTAGAAGGGGTTCTT
Trs23 (2)	TCGGGTGGCCTTATATTCAACCT	TTCCATCCTTTCTGTTGAACGAGA
Trs33 (1)	GTCTGAAGAAATCCTTTTCGATTGC	TAGTTCCTGTTCACTTCTATGTGAA
Trs33 (2)	GACCTGGCCACTTTGGAGTATATA	CACGGTGCTGTTAATGCCTAGATT
l(3)76BDm (1)	GTCCTGAGCTGGGATTACTACCA	TTCTTCGGCCTGTTCGGCCAAT
l(3)76BDm (2)	CAAAAACTGCCCAAGTGGTTCCAT	GACTCCTTCCAGGAGCTGTGAC
Brun (1)	CCTCGAACTCATCTTCCTGCTC	ACATGAGGCGGTAACTTTGGTTC
Brun (2)	TCCAGTGGGTGCAAAATGATCTTA	TCCTGCTCCACATTTGAGTTGATG
SIDL (1)	AACTTCTACTGCGCTCTAAATGAG	ACGGGGAGGCAGTTAGGCTGA
SIDL (2)	TCTTTTCGAACGTCAAGCCTATTTG	AACTCTGCCAGCTCCAGGTAGA
GCC185 (1)	GCAGGAGAAGTTACAGAAGATCAAAC	TCCTTGCTGGCCAGTGATTCCTT
GCC185 (2)	CTACTGCCTCGAGACGTTCCCAC	GCATGTGTTGTTCACGTTCCTCGG
GM130 (1)	CAATCGCAGGCACAAATCAAGGAC	CTCGCTGGTTTCTTCCTTGGATG
GM130 (2)	ACCACGCCCACAGACAAGCAGC	AGCTCCACGCCCAAACTGACCAC
GM130 (3)	TCATTCGCACGATCACTCTCATCAG	CTCTGCGTTTGATAGAGGGCAATG
GMAP210 (1)	GGAACTGGACAAAAGAAATAAACTGC	GAGTTGCTCCTGCAACCTTGTTC
GMAP210 (2)	CTTCGTTCAATTCCTGGAGCAG	CGACACGATTGCACGTTTACAAGTG
Golgin84 (1)	GTGCTGGAAGCTCTGGTTAAAAGTC	CAACTCCTTTGCTAGTGTTTCCTCG
Golgin84 (2)	GACATGCGCCAAAAGATGACCAC	GAACCGCCTTGTCCCGCTCTTC
Golgin84 (3)	TTCTCATGCATCCAAGTCCATTCG	GGAGAGCAGCACAAACATGACCC
Golgin245 (1)	GCGAGAGATTCAAATACTACAAGATC	TTCGGCCAGCTTGGTGTTTTCGC
Golgin245 (2)	GGAGTCCAATATGCAGCAGGAG	GCTTAAGTCGCTCGTTGGACTG
Golgin245 (3)	CAAGGACGAAGCCGAATCGAAGC	CGCTCCATTTCCAGGCTCTTCTC
Grasp65 (1)	AGAACGACGACCTGTTCACGCTG	GGAACGGAAACGGGCTCGGCAAT
Grasp65 (2)	AGTCTCACCAACGTTGCCTTACATA	GTCCGGATAGTTCGTCGTTGCCT
P115 (1)	ATATACTCACGGAAACCATCAATGC	AGTAGCATTAGCAGACCCACCTTG

Table C4 (continued). Genomic DNA PCR to generate template for dsRNA synthesis

P115 (2)	CACAGGATGCGGAAGAGGTTGG	GGCAGGTCTGGGTGGACTGCTC
P115 (3)	ACTGGTCACGCCCAGTAATCAAC	GAGAAGAGTCCGGTGCAAAGGAG
Rint1 (1) or Rint1	GACCAGCACCTGGAACATTTCG	CAGTTTATGCGACTGCTGGACG
Rint1 (2)	TGAGATTGTAGTCCAGCTTACCC	TCTACGAGGGCAACGACTGCG
Rint1 (3)	TATTGTATTGCGACATGGTCACACTG	AGCTTGTCCTCGAAGTGAGCCAG
Rod (1)	TGGTGGAGATCATGGCTAACATC	CCTTGGCGCTTTCAATTTGCTGAA
Rod (2)	ATGTACACGGCTTTGAAGGGATC	AATAAGCTCGGTGGGGTTCTCAAC
Zw10 (1)	TGGCACCTACGTTCGATTGTCGC	ATCATGCAGCGTGGGAAGAGGAAG
Zw10 (2)	AGCGAGCATGTGCTAAGGATCGAC	GGCACTCGTCCACCAGTAATTTC
Zw10 (3)	CAGGAGTTCGAGTTCGAGAGCAC	CTATACAATCTGCGTAATGGCCTTG
Zwilch (1)	AACTCTCATTGAAAATAGCTACCAGG	CACATTGGAAGAGCATACTAAAGGC
Zwilch (2)	CCCACCTACTTGGTGAGCATGG	TTGACATCCGTGTGGTAGGAGAC
Cog1 (1)	GACCATCCAGGACATTAAGTCCG	AAACCTTTCAAATTGGATAAATACTCTG
Cog1 (2)	CACTTATGGAGCAAGTGCGACAC	GGTGCTGTTGAGCACGTTTAAGCT
Cog2 (1)	GCCAGGCACGCAACTCGGCACC	GAAAGCATATTTGGAAGTAAACCGG
Cog2 (2)	GCTGACATTCGCAAACTTGACGC	ACTAGCAACTTCCGCCAAGATTTG
Cog3 (1)	GGACACTGGTGTGCCTCTCAAG	GGGCGTGGCTGGAGTGGACTG
Cog3 (2)	TGACATCAGACTACCTGCGGAGG	GCATTCGTCGATCTTGTTGAGGC
Cog4 (1)	TGGAGGAGAGCGTACTGAAGGC	AATCAACGGTGGCTTTCAACGCG
Cog4 (2)	CAACAAGCTGAACGACCAGATCGT	TAGTTCCTTCTGCGCCTTGTTTGC
Cog5 (1)	CTGCTGAAAACGGCTCTCGAGCA	GCAGATTGGGCAGATCCACGACC
Cog5 (2)	TCCTTATCTTCTGAGCAGAGCTGAT	AAACGCAGCGGATTCGGATGATAAT
Cog6 (1)	AGCTGCAGAACGCTTTGGGCTAC	AGACAGTTCAAAAGGTACACACCC
Cog6 (2)	TGGATGCTCTGAGTGGTCTGTCC	TGCGACAGTGGTTCTGAGTCCATC
Cog7 (1)	CGCGCATGGTCATGTTGTCCAATA	GCGTAACGTACAGAACACAGCACT
Cog7 (2)	ATAGCCCTGCAAAAGTCCCTGCAC	AGTTTGCTTCCATTGCTGCTGCC
Cog8 (1)	CGACTTTCTGCAGACTCTGGAAC	AGCCGAACAAATGCCTCTCGTTC
Cog8 (2)	CGCAAGCAGGTTGATCCCGAGC	TTATCCCTCGGCAGTGACAGGCA
Vps52 (1)	CAGAGCGTTTTGAACAACATAAGCAC	GCCCATCGTATCGATGTATTCACTG
Vps52 (2)	TGGTTTTGGGCGTGTTGATGGAG	GGGCGTGAGGAGCTTGTGGAATC
Vps53 (1)	TTTGTTCGCCATCAACAAGACGCAG	TTGATAGATTCTGCATATCGCGCG
Vps53 (2)	CGCTGCAAACTAACCCTCTCGG	GGAAGTTGCCGTTGTTGTTTCAGTT
Syx5 (1) or Syx5	CACACAAACCTGCCAGCTAAGTG	GGTCTGTTTGATGAAGGCGTCTTC
Syx5 (2)	AAAAAGAAGAGCTTATTTGATGACAG	CTCAACGATGGTAGATTCTATATTTT
Syx5 (3)	GACGCGACGTGATCAGTTTAGCC	CATGGATAGGTACATGGGGCTTTT
Syx13 (1)	ACATTGGCCACAACATCACTGCC	CCCTGATCGTGCACCAGTCCAC
Syx13 (2)	GAACAGTATTGAGCAGACGGCCG	TGTTTGCGTGTGTTTGTTGAATATGG
Syx18 (1)	GCGCCAAGCGGAAGCCGCAG	GTCATCGTCGGCCTCCTGCTG
Syx18 (2)	GATCCCCTAAGCGCCGAGGATG	TTAATCGTAGTACCAGTCCAAGAAG
Membrin (1) or Membrin	TCCGACGATCCTCGACCAGCC	AGCTCAGTGCCCAGGAATCGC
Membrin (2)	AAGCAAGGTGACCACCACTCCTC	ACGAACTGCAGCATCATACGCAG
CG2023 (1)	TGCGTTTACATTACAGGCCATACG	TTCTCCTGCGAAACCAGACTGCC
CG2023 (2)	ACAGCCGCACCTCCATCGCCG	CGTCGTCCGTACTTTTTGAGCAG
Gos28 (1)	TCCTCGCTAAATGAGTCCATGTCC	ATCAGTGGGAATCGATTGGAGATAT
Gos28 (2)	CCACACGAAAGTCGAACAAATAAAG	AGCTCCGATTTTGCTGAATGCCAC
Bet1 (1) or Bet1	CGCCGCAACAACTACCCGTACC	ACTTAAACTTTAGGGTTATCCAGAGG
Bet1 (2)	GCTCGGCGACTAAAAATTGAATTGC	TGGGATATACGCTTCTTGGCTCAA
Use1 (1)	ATGCCCTGCGAAGACGTCGAGG	CAATTACGAAGGCAATCATCAGCC
Use1 (2)	GCCAAAAGCGAACAGAACTTCTGG	CAGTGCATTTTCCCCAGTTTCGC

Table C4 (continued). Genomic DNA PCR to generate template for dsRNA synthesis

Ykt6 (1)	GTGTCATGTCTATGTGCGGGCG	AATCATCAAAGCCCAAGTCGCAC
Ykt6 (2)	GATGGCCAGTTGCCAGTTACGAT	TTTATTGAAACGCCCACACATTCCG
Sec22 (1)	TAATCGAGAACGACGTCTGCTACC	CTGTGCCACGTTGGAGCACGTC
Sec22 (2)	ACCGGTGACGTGGTTACATTGCA	TCCTTCCACTGGCTGCTACTTATT
αSNAP (1)	CGTCAAGGACTACGACAGCATC	TTACGCATCCAAATGGAACATCAG
αSNAP (2)	CCAAGTCTATTCAGCACTATGAGC	TGATGAGCTTGAACTCCCTGGAG
Comt (1)	CCGTGCCGCCCAGTCGAGTG	CCCAATCGATCCGTAGTCCAGC
Comt (2)	ATAAACCCGGATTGGGACTTTGGC	AACATAGTTCCGATTTGGCGAGCC
Chapter III		
CG32803 (1)	CACTCCTGACCATTGTGTCCATG	CATATTTAAGTTGGGCAAGCAATATTG
CG32803 (2)	TGTGATGTCCGAGCTAGGTGGAAA	AAATCCGAAATAGGCAGCAACAGC
CG32803 (3)	CTCACTCGAACAAGGCTCGCAAA	AGCAAGCTCTCCAGGAACTGGTC
CTPsyn (1)	AGCAATGGCGAGATTTGGCGCG	GCCCAAGCGCATAGTGCCGC
CTPsyn (2)	AAATACATCCTGGTAACTGGTGGC	TGCTCATAAGGCGAAAAGGTTCC
CDS (1)	CGGCATCTTCACATGGATTATGATC	ATATTCCTGTAGATGAAATTGCATATT
CDS (2) or CDS	CTGAAGTTCCTGGTGACCTATCAC	ATTCCTGGGGCGTGAACAAATAGC
TMEM19 (1)	ATTTTCAAACACTAGTCAACGGCAT	CCCAGCGCAGCTCCAGATCGG
TMEM19 (2) or TMEM19	TCCATCGCCAGCCATCCGTTCT	ATTGTGGTGGGCTAATCAGAAGCA
Atl (1)	GGACTGGAGCTTTCCCTACGAG	AGTACGGCCGCGTTCCACCGC
Atl (2) or Atl	ACAGAACATCCAGGAGGACGACC	ACTCTTAAACTCGGGCGTGATGTC
CG9706 (1)	TACGCATCCACCTGCAATAGCGT	GTGGTCCGTTCGTATATCGACCG
CG9706 (2)	TTCTACAGGGCATTCCCATCGGG	GAAGTAGCCAGCTGTTTGGCCC

*All primers were flanked by T7 promoter sequence (TAATACGACTCACTATAGGG) at the 5' end.
Bold names indicate dsRNA that appears with two different names.

Table C5. Stable cell line overexpressing EGFP-GPAT4

Plasmid	PCR template	Primer (forward)	Primer (reverse)
pAG-GPAT4-T2A-Puro^{R}	pAC-GPAT4[54] (Left fragment containing GPAT4)	CACC ATGATCGCCGTGCTGTTG GACATATTC	CTTCCTCTGCCCTCaagcttGGTGGA GTCCGACTTCAGCCG
	pAc5-STABLE-Puro[205] (Right fragment containing T2A-Puro^{R})	CTTCCTCTGCCCTCaagctt GGTGGAGTCCGACTTCAG CCG	TCAGGCACCGGGCTTGCGGGTCA TG
Left and right fragments were combined using overlapping PCR, inserted into pENTR-D-TOPO vector, and cloned into the destination vector pAGW using Gateway cloning (LR cloning).			

Table C6. CRISPR-Cas9 genome editing

Plasmid	PCR template	Primer (forward)	Primer (reverse)
Seipin knock-out cells			
Pl18 (Cas9 and guide)[201]	S2 genomic DNA	GTTCG **CGCCCTGGATCCTCTGG GTC**	AAAC **GACCCAGAGGATCCAGGGCG** C
EGFP-GPAT4 knock-in cells			
Pl18 (Cas9 and guide)[201]	S2 genomic DNA	CTTCG **CATATTCTGGATCCCCAT CG**	AAAC **CGATGGGGATCCAGAATATG** C
pBH-donor vector DNA (using BsaI)[202]	S2 genomic DNA (left homology arm)	TAGT GGTCTC T GACC CCTCATGTAATCGGCTTC GTGGC	TAGT GGTCTC T GAAC TTTACATTTGTGTCATGCGACATTA G
	pAGW (insert)	TAGT GGTCTC T GTTC ATGGTGAGCAAGGGCGA GGAGCTG	TAGT GGTCTC T GCCC CC <u>tgagccacccctccgctcccgcctccaccagac cctccgccacc</u> CTTGTACAGCTCGTCCATGCCGAG
	S2 genomic DNA (right homology arm)	TAGT GGTCTC T GGGC ATGATCGCCGTGCTGTTG GACATATTC	TAGT GGTCTC T TATA GCAATGCCGGACTCCTTACCTTTG
TMEM19 knock-out cells			
Pl18 (Cas9 and guide)[201]	S2 genomic DNA	GTTCG **GGAATCACCCGGGACTC TGT**	AAAC **ACAGAGTCCCGGGTGATTCC** C

Bold sequences indicate portions encoding gRNA.
<u>Underlined sequence</u> indicates GGGGS*3 linker inserted between EGFP and GPAT4.

Appendix D. List of Online Supplemental Files

1. **Online Supplementary Table 1**. Genes of which RNAi reduce GPAT4 targeting to LDs
2. **Online Supplementary Table 2**. Gene ontology analysis of Online Supp. Table 1
3. **Online Supplementary Table 3**. Genes of which RNAi increase GPAT4 targeting to LDs
4. **Online Supplementary Table 4**. Gene ontology Analysis of Online Supp. Table 3
5. **Online Supplementary Table 5**. Protein complex enrichment analysis of Online Supp. Table 1
6. **Online Supplementary Table 6**. All screen results

Bibliography

1. Walther, T. C. & Farese, R. V. Lipid droplets and cellular lipid metabolism. *Annu. Rev. Biochem.* **81,** 687–714 (2012).

2. Krahmer, N., Farese, R. V & Walther, T. C. Balancing the fat : lipid droplets and human disease. *EMBO Mol. Med.* **5,** 973–983 (2013).

3. Gluchowski, N. L., Becuwe, M., Walther, T. C. & Jr, R. V. F. Lipid droplets and liver disease: from basic biology to clinical implications. *Nat. Rev. Gastroenterol. Hepatol.* **14,** 343–355 (2017).

4. Welte, M. A. Expanding roles for lipid droplets. *Curr. Biol.* **25,** R470–R481 (2015).

5. Targher, G., Bertolini, L., Padovani, R., Rodella, S., Tessari, R., Zenari, L., Day, C. & Arcaro, G. Prevalence of nonalcoholic fatty liver disease and its association with cardiovascular disease among type 2 diabetic patients. *Diabetes Care* **30,** 1212–1218 (2007).

6. Misra, V. L., Khashab, M. & Chalasani, N. Nonalcoholic fatty liver disease and cardiovascular risk. *Curr. Gastroenterol. Rep.* **11,** 50–55 (2009).

7. Bhupathiraju, S. N. & Hu, F. B. Epidemiology of obesity and diabetes and their cardiovascular complications. *Circ. Res.* **118,** 1723–1735 (2016).

8. Tana, C., Ballestri, S., Ricci, F., Di Vincenzo, A., Ticinesi, A., Gallina, S., Giamberardino, M. A., Cipollone, F., Sutton, R., Vettor, R., Fedorowski, A. & Meschi, T. Cardiovascular risk in non-alcoholic fatty liver disease: Mechanisms and therapeutic implications. *Int. J. Environ. Res. Public Health* **16,** 1–19 (2019).

9. Benedict, M. & Zhang, X. Non-alcoholic fatty liver disease: An expanded review. *World J. Hepatol.* **9,** 715–732 (2017).

10. Yu, X. H., Fu, Y. C., Zhang, D. W., Yin, K. & Tang, C. K. Foam cells in atherosclerosis. *Clin. Chim. Acta* **424,** 245–252 (2013).

11. Currie, E., Schulze, A., Zechner, R., Walther, T. C. & Farese, R. V. Cellular fatty acid metabolism and cancer. *Cell Metab.* **18,** 153–161 (2013).

12. Nieva, C., Marro, M., Santana-Codina, N., Rao, S., Petrov, D. & Sierra, A. The Lipid Phenotype of Breast Cancer Cells Characterized by Raman Microspectroscopy: Towards a Stratification of Malignancy. *PLoS One* **7,** (2012).

13. Rak, S., De Zan, T., Stefulj, J., Kosović, M., Gamulin, O. & Osmak, M. FTIR spectroscopy reveals lipid droplets in drug resistant laryngeal carcinoma cells through detection of increased ester vibrational bands intensity. *Analyst* **139,** 3407–3415 (2013).

14. Brown, R. J., Araujo-Vilar, D., Cheung, P. T., Dunger, D., Garg, A., Jack, M., Mungai, L., Oral, E. A., Patni, N., Rother, K. I., Von Schnurbein, J., Sorkina, E., Stanley, T., Vigouroux, C., Wabitsch, M., Williams, R. & Yorifuji, T. The diagnosis and management of lipodystrophy syndromes: A multi-society practice guideline. *J. Clin. Endocrinol. Metab.* **101,** 4500–4511 (2016).

15. Camus, G., Vogt, D. A., Kondratowicz, A. S. & Ott, M. *Lipid Droplets and Viral Infections*. *Methods in Cell Biology* **116,** (Elsevier Inc., 2013).

16. Zhang, J., Lan, Y. & Sanyal, S. Modulation of lipid droplet metabolism-A potential target for therapeutic intervention in Flaviviridae Infections. *Front. Microbiol.* **8,** (2017).

17. Thiam, A. R., Farese, R. V & Walther, T. C. The biophysics and cell biology of lipid droplets. *Nat. Rev. Mol. Cell Biol.* **14,** 775–86 (2013).

18. Bigay, J. & Antonny, B. Curvature, Lipid Packing, and Electrostatics of Membrane Organelles: Defining Cellular Territories in Determining Specificity. *Dev. Cell* **23,** 886–895 (2012).

19. Bacle, A., Gautier, R., Jackson, C. L., Fuchs, P. F. J. & Vanni, S. Interdigitation between Triglycerides and Lipids Modulates Surface Properties of Lipid Droplets. *Biophys. J.* **112,** 1417–1430 (2017).

20. Čopič, A., Antoine-Bally, S., Giménez-Andrés, M., La Torre Garay, C., Antonny, B., Manni, M. M., Pagnotta, S., Guihot, J. & Jackson, C. L. A giant amphipathic helix from a perilipin that is adapted for coating lipid droplets. *Nat. Commun.* **9,** 1–16 (2018).

21. Prevost, C., Sharp, M. E., Kory, N., Lin, Q., Voth, G. A., Farese, R. V & Walther, T. C. Mechanism and Determinants of Amphipathic Helix- Containing Protein Targeting to Lipid Droplets. *Dev. Cell* **44,** 73–86 (2018).

22. Krahmer, N., Guo, Y., Wilfling, F., Hilger, M., Lingrell, S., Heger, K., Newman, H. W., Schmidt-Supprian, M., Vance, D. E., Mann, M., Farese, R. V. & Walther, T. C. Phosphatidylcholine synthesis for lipid droplet expansion is mediated by localized activation of CTP:Phosphocholine cytidylyltransferase. *Cell Metab.* **14,** 504–515 (2011).

23. Vamparys, L., Gautier, R., Vanni, S., Bennett, W. F. D., Tieleman, D. P., Antonny, B., Etchebest, C. & Fuchs, P. F. J. Conical lipids in flat bilayers induce packing defects similar to that induced by positive curvature. *Biophys. J.* **104,** 585–593 (2013).

24. Kassan, A., Herms, A., Fernández-Vidal, A., Bosch, M., Schieber, N. L., Reddy, B. J. N., Fajardo, A., Gelabert-Baldrich, M., Tebar, F., Enrich, C., Gross, S. P., Parton, R. G. & Pol, A. Acyl-CoA synthetase 3 promotes lipid droplet biogenesis in ER microdomains. *J. Cell Biol.* **203,** 985–1001 (2013).

25. Pol, A., Gross, S. P. & Parton, R. G. Biogenesis of the multifunctional lipid droplet: Lipids, proteins, and sites. *J. Cell Biol.* **204,** 635–646 (2014).

26. Choudhary, V., Ojha, N., Golden, A. & Prinz, W. A. A conserved family of proteins facilitates nascent lipid droplet budding from the ER. *J. Cell Biol.* **211,** 261–271 (2015).

27. Walther, T. C., Chung, J. & Farese, R. V. Lipid droplet biogenesis. *Annu. Rev. Cell Dev. Biol.* **33,** 491–510 (2017).

28. Yen, C.-L. E., Stone, S. J., Koliwad, S., Harris, C. & Farese, R. V. Thematic review series: glycerolipids. DGAT enzymes and triacylglycerol biosynthesis. *J. Lipid Res.* **49,** 2283–301 (2008).

29. Wilfling, F., Haas, J. T., Walther, T. C. & Farese, R. V. Lipid droplet biogenesis. *Curr Opin Cell Biol.* **29,** 39–45 (2014).

30. Khandelia, H., Duelund, L., Pakkanen, K. I. & Ipsen, J. H. Triglyceride blisters in lipid bilayers: Implications for lipid droplet biogenesis and the mobile lipid signal in cancer cell membranes. *PLoS One* **5,** 1–8 (2010).

31. Brasaemle, D. L. The perilipin family of structural lipid droplet proteins: Stabilization of lipid droplets and control of lipolysis. *J. Lipid Res.* **48,** 2547–2559 (2007).

32. Brasaemle, D. L. Thematic review series: adipocyte biology. The perilipin family of structural lipid droplet proteins: stabilization of lipid droplets and control of lipolysis. *J. Lipid Res.* **48,** 2547–2559 (2007).

33. Sztalryd, C. & Brasaemble, D. L. The perilipin family of lipid droplet proteins: Gatekeepers of intracellular lipolysis. *Biochim Biophys Acta.* **1862,** 1221–1232 (2017).

34. Nose, F., Yamaguchi, T., Kato, R., Aiuchi, T., Obama, T., Hara, S., Yamamoto, M. & Itabe, H. Crucial Role of Perilipin-3 (TIP47) in Formation of Lipid Droplets and PGE2 Production in HL-60-Derived Neutrophils. *PLoS One* **8,** (2013).

35. Jacquier, N., Mishra, S., Choudhary, V. & Schneiter, R. Expression of oleosin and perilipins in yeast promotes formation of lipid droplets from the endoplasmic reticulum. *J. Cell Sci.* **126,** 5198–5209 (2013).

36. Gao, Q., Binns, D. D., Kinch, L. N., Grishin, N. V., Ortiz, N., Chen, X. & Goodman, J. M. Pet10p is a yeast perilipin that stabilizes lipid droplets and promotes their assembly. *J. Cell Biol.* **216,** 3199–3217 (2017).

37. Ajjaji, D., Mbarek, K. Ben, Mimmack, M. L., England, C., Herscovitz, H., Dong, L., Kay, R. G., Patel, S. & Saudek, V. Dual binding motifs underpin the hierarchical association of perilipins1-3 with lipid droplets . *Mol Biol Cell* **30,** 703–716 (2019).

38. Cartwright, B. R. & Goodman, J. M. Seipin: from human disease to molecular mechanism. *J. Lipid Res.* **53,** 1042–1055 (2012).

39. Ito, D. & Suzuki, N. Molecular pathogenesis of Seipin/BSCL2-related motor neuron diseases. *Ann. Neurol.* **61,** 237–250 (2007).

40. Patel, H., Hart, P. E., Warner, T. T., Houlston, R. S., Patton, M. A., Jeffery, S. & Crosby, A. H. The silver syndrome variant of hereditary spastic paraplegia maps to chromosome 11q12-q14, with evidence for genetic heterogeneity within this subtype. *Am. J. Hum. Genet.* **69,** 209–215 (2001).

41. Windpassinger, C., Wagner, K., Petek, E., Fischer, R. & Auer-Grumbach, M. Refinement of the 'Silver syndrome locus' on chromosome 11q12-q14 in four families and exclusion of eight candidate genes. *Hum. Genet.* **114,** 99–109 (2003).

42. Sui, X., Arlt, H., Brock, K. P., Lai, Z. W., DiMaio, F., Marks, D. S., Liao, M., Farese, R. V. & Walther, T. C. Cryo–electron microscopy structure of the lipid droplet–formation protein seipin. *J. Cell Biol.* **217,** 4080–4091 (2018).

43. Yan, R., Qian, H., Lukmantara, I. & Gao, M. Human SEIPIN Binds Anionic Phospholipids. *Dev. Cell* **47,** 1–9 (2018).

44. Wang, H., Becuwe, M., Housden, B. E., Chitraju, C., Porras, A. J., Graham, M. M., Liu, X. N., Thiam, A. R., Savage, D. B., Agarwal, A. K., Garg, A., Olarte, M.-J., Lin, Q., Fröhlich, F., Hannibal-Bach, H. K., *et al.* Seipin is required for converting nascent to mature lipid droplets. *Elife* **5,** 133–150 (2016).

45. Salo, V., Li, S., Vihinen, H., Hölttä-Vuori, M., Szkalisity, A., Horvath, P., Belevich, I., Peränen, J., Thiele, C., Somerharju, P., Santinho, A., Thiam, A. R., Jokitalo, E. & Ikonen, E. Seipin facilitates triglyceride flow to lipid droplet and counteracts droplet ripening via ER contact. *Dev. Cell* 1–16 (2019). doi:10.1016/j.devcel.2019.05.016

46. Szymanski, K. M., Binns, D., Bartz, R., Grishin, N. V., Li, W. P., Agarwal, A. K., Garg, A., Anderson, R. G. W. & Goodman, J. M. The lipodystrophy protein seipin is found at endoplasmic reticulum lipid droplet junctions and is important for droplet morphology. *Proc. Natl. Acad. Sci. U. S. A.* **104,** 20890–20895 (2007).

47. Jacquier, N., Choudhary, V., Mari, M., Toulmay, A., Reggiori, F. & Schneiter, R. Lipid droplets are functionally connected to the endoplasmic reticulum in Saccharomyces cerevisiae. *J. Cell Sci.* **124,** 2424–37 (2011).

48. Chung, J., Wu, X., Lambert, T. J., Lai, Z. W., Walther, T. C. & Farese, R. V. LDAF1 and Seipin Form a Lipid Droplet Assembly Complex. *Dev. Cell* **51,** 551–563.e7 (2019).

49. Kadereit, B., Kumar, P., Wang, W. J., Miranda, D., Snapp, E. L., Severina, N., Torregroza, I., Evans, T. & Silver, D. L. Evolutionarily conserved gene family important for fat storage. *Proc. Natl. Acad. Sci. U. S. A.* **105,** 94–99 (2008).

50. Wang, S., Idrissi, F. Z., Hermansson, M., Grippa, A., Ejsing, C. S. & Carvalho, P. Seipin and the

membrane-shaping protein Pex30 cooperate in organelle budding from the endoplasmic reticulum. *Nat. Commun.* **9,** 1–12 (2018).

51. Joshi, A. S., Nebenfuehr, B., Choudhary, V., Satpute-krishnan, P., Levine, T. P., Golden, A. & Prinz, W. A. Lipid droplet and peroxisome biogenesis occur at the same ER subdomains. *Nat. Commun.* **9,** 1–12 (2018).

52. Guo, Y., Cordes, K. R., Farese, R. V. & Walther, T. C. Lipid droplets at a glance. *J. Cell Sci.* **122,** 749–752 (2009).

53. Kory, N., Farese, R. V. & Walther, T. C. Targeting Fat: Mechanisms of Protein Localization to Lipid Droplets. *Trends Cell Biol.* **26,** 535–546 (2016).

54. Wilfling, F., Wang, H., Haas, J. T., Krahmer, N., Gould, T. J., Uchida, A., Cheng, J. X., Graham, M., Christiano, R., Fröhlich, F., Liu, X., Buhman, K. K., Coleman, R. A., Bewersdorf, J., Farese, R. V. & Walther, T. C. Triacylglycerol synthesis enzymes mediate lipid droplet growth by relocalizing from the ER to lipid droplets. *Dev. Cell* **24,** 384–399 (2013).

55. Mahamid, J., Tegunov, D., Maiser, A., Arnold, J., Leonhardt, H., Plitzko, J. M. & Baumeister, W. Liquid-crystalline phase transitions in lipid droplets are related to cellular states and specific organelle association. *Proc. Natl. Acad. Sci. U. S. A.* **116,** 16866–16871 (2019).

56. Mishra, S., Khaddaj, R., Cottier, S., Stradalova, V., Jacob, C. & Schneiter, R. Mature lipid droplets are accessible to ER luminal proteins. *J. Cell Sci.* **129,** 3803–3815 (2016).

57. Salo, V. T., Belevich, I., Li, S., Karhinen, L., Vihinen, H., Vigouroux, C., Magré, J., Thiele, C., Hölttä-vuori, M., Jokitalo, E. & Ikonen, E. Seipin regulates ER – lipid droplet contacts and cargo delivery. 1–18 (2016).

58. Wu, H., Carvalho, P. & Voeltz, G. K. Here, there, and everywhere: The importance of ER membrane contact sites. *Science (80-.).* **361,** (2018).

59. Scorrano, L., De Matteis, M. A., Emr, S., Giordano, F., Hajnóczky, G., Kornmann, B., Lackner, L. L., Levine, T. P., Pellegrini, L., Reinisch, K., Rizzuto, R., Simmen, T., Stenmark, H., Ungermann, C. & Schuldiner, M. Coming together to define membrane contact sites. *Nat. Commun.* **10,** 1–11 (2019).

60. Helle, S. C. J., Kanfer, G., Kolar, K., Lang, A., Michel, A. H. & Kornmann, B. Organization and function of membrane contact sites. *Biochim. Biophys. Acta - Mol. Cell Res.* **1833,** 2526–2541 (2013).

61. Chung, J., Torta, F., Masai, K., Lucast, L., Czapla, H., Tanner, L. B., Narayanaswamy, P., Wenk, M. R., Nakatsu, F. & De Camilli, P. PI4P/phosphatidylserine countertransport at ORP5- and ORP8-mediated ER - Plasma membrane contacts. *Science (80-.).* **349,** 428–432 (2015).

62. Xu, N., Zhang, S. O., Cole, R. A., McKinney, S. A., Guo, F., Haas, J. T., Bobba, S., Farese, R. V. & Mak, H. Y. The FATP1-DGAT2 complex facilitates lipid droplet expansion at the ER-lipid droplet interface. *J. Cell Biol.* **198,** 895–911 (2012).

63. Ramseyer, V. D., Kimler, V. A. & Granneman, J. G. Vacuolar protein sorting 13C is a novel lipid droplet protein that inhibits lipolysis in brown adipocytes. *Mol. Metab.* **7,** 57–70 (2018).

64. Kumar, N., Leonzino, M., Cerutti, W. H., Horenkamp, F. A., Li, P. & Lees, J. A. VPS13A and VPS13C are lipid transport proteins differentially localized at ER contact sites. 1–25 (2018).

65. Yeshaw, W. M., Zwaag, M. Van Der, Pinto, F. & Lahaye, L. L. Human VPS13A is associated with multiple organelles and influences mitochondrial morphology and lipid droplet motility . *Elife* **8,** (2019).

66. Gillingham, A. K., Sinka, R., Torres, I. L., Lilley, K. S. & Munro, S. Toward a Comprehensive Map of the Effectors of Rab GTPases. *Dev. Cell* **31,** 358 (2014).

67. Xu, D., Li, Y., Wu, L., Li, Y., Zhao, D., Yu, J., Huang, T., Ferguson, C., Parton, R. G., Yang, H. & Li, P. Rab18 promotes lipid droplet (LD) growth by tethering the ER to LDs through SNARE and NRZ interactions. *J. Cell Biol.* **217,** 975–995 (2018).

68. Hariri, H., Rogers, S., Ugrankar, R., Liu, Y. L., Feathers, J. R. & Henne, W. M. Lipid droplet biogenesis is spatially coordinated at ER –vacuole contacts under nutritional stress . *EMBO Rep.* **19,** 57–72 (2018).

69. Hariri, H., Speer, N., Bowerman, J., Rogers, S., Fu, G., Reetz, E., Datta, S., Feathers, J. R., Ugrankar, R., Nicastro, D. & Henne, W. M. Mdm1 maintains endoplasmic reticulum homeostasis by spatially regulating lipid droplet biogenesis. *J. Cell Biol.* **218,** 1319–1334 (2019).

70. Ugrankar, R., Bowerman, J., Hariri, H., Chandra, M., Chen, K., Bossanyi, M. F., Datta, S., Rogers, S., Eckert, K. M., Vale, G., Victoria, A., Fresquez, J., McDonald, J. G., Jean, S., Collins, B. M. & Henne, W. M. Drosophila Snazarus Regulates a Lipid Droplet Population at Plasma Membrane-Droplet Contacts in Adipocytes. *Dev. Cell* **50,** 557–572.e5 (2019).

71. Datta, S., Liu, Y., Hariri, H., Bowerman, J. & Henne, W. M. Cerebellar ataxia disease-associated Snx14 promotes lipid droplet growth at ER-droplet contacts. *J. Cell Biol.* **218,** 1335–1351 (2019).

72. Tauchi-Sato, K., Ozeki, S., Houjou, T., Taguchi, R. & Fujimoto, T. The surface of lipid droplets is a phospholipid monolayer with a unique fatty acid composition. *J. Biol. Chem.* **277,** 44507–44512 (2002).

73. Krahmer, N., Hilger, M., Kory, N., Wilfling, F., Stoehr, G., Mann, M., Farese, R. V & Walther, T. C. Protein correlation profiles identify lipid droplet proteins with high confidence. *Mol. Cell Proteomics* **12,** 1115–1126 (2013).

74. Krahmer, N., Najafi, B., Schueder, F., Quagliarini, F., ..., Walther, T. C., Jungmann, R., Zeigerer, A., Borner, G. H. H. & Mann, M. Organellar Proteomics and Phospho-Proteomics Reveal Subcellular Reorganization in Diet-Induced Hepatic Steatosis. *Dev. Cell* **47,** 205–221 (2018).

75. Bersuker, K., Peterson, C. W. H., To, M., Grossman, E. A., Nomura, D. K., Olzmann, J. A., Bersuker, K., Peterson, C. W. H., To, M., Sahl, S. J., Savikhin, V. & Grossman, E. A. Proximity Labeling Strategy Provides Insights into the Composition and Dynamics of Lipid Droplet Proteomes. *Dev. Cell* 1–16 (2018). doi:10.1016/j.devcel.2017.11.020

76. Bersuker, K. & Olzmann, J. A. Establishing the lipid droplet proteome : Mechanisms of lipid droplet protein targeting and degradation ☆. *BBA - Mol. Cell Biol. Lipids* 0–1 (2017). doi:10.1016/j.bbalip.2017.06.006

77. Rees, J. S., Li, X.-W., Perrett, S., Lilley, K. S. & Jackson, A. P. Protein Neighbors and Proximity Proteomics. *Mol. Cell. Proteomics* **14,** 2848–2856 (2015).

78. Kim, D. I., Jensen, S. C., Noble, K. A., KC, B., Roux, K. H., Motamedchaboki, K. & Roux, K. J. An improved smaller biotin ligase for BioID proximity labeling. *Mol. Biol. Cell* **27,** 1188–1196 (2016).

79. Rowe, E. R., Mimmack, M. L., Barbosa, A. D., Haider, A., Isaac, I., Ouberai, M. M., Thiam, A. R., Patel, S., Saudek, V., Siniossoglou, S. & Savage, D. B. Conserved amphipathic helices mediate lipid droplet targeting of perilipins 1-3. *J. Biol. Chem.* **291,** 6664–6678 (2016).

80. Drin, G. & Antonny, B. Amphipathic helices and membrane curvature. *FEBS Lett.* **584,** 1840–1847 (2010).

81. Giménez-Andrés, M., Čopič, A. & Antonny, B. The many faces of amphipathic helices. *Biomolecules* **8,** 1–14 (2018).

82. Vanni, S., Vamparys, L., Gautier, R., Drin, G., Etchebest, C., Fuchs, P. F. J. & Antonny, B. Amphipathic lipid packing sensor motifs: Probing bilayer defects with hydrophobic residues. *Biophys. J.* **104,** 575–584 (2013).

83. Aitchison, A. J., Arsenault, D. J. & Ridgway, N. D. Nuclear-localized CTP:phosphocholine cytidylyltransferase α regulates phosphatidylcholine synthesis required for lipid droplet biogenesis. *Mol. Biol. Cell* **26,** 2927–2938 (2015).

84. Zehmer, J. K., Bartz, R., Bisel, B., Liu, P., Seemann, J. & Anderson, R. G. W. Targeting sequences of UBXD8 and AAM-B reveal that the ER has a direct role in the emergence and regression of lipid droplets. *J. Cell Sci.* **122,** 3694–3702 (2009).

85. Ingelmo-Torres, M., Gonzalez-Moreno, E., Kassan, A., ..., Gross, S. P., Parton, R. G. & Pol, A. Hydrophobic and Basic Domains Target Proteins to Lipid Droplets. *Traffic* **10,** 147–162 (2009).

86. Wilfling, F., Thiam, A. R., Olarte, M. J., Wang, J., Beck, R., Gould, T. J., Allgeyer, E. S., Pincet, F., Bewersdorf, J., Farese, R. V. & Walther, T. C. Arf1/COPI machinery acts directly on lipid droplets and enables their connection to the ER for protein targeting. *Elife* **2014,** 1–20 (2014).

87. Ruggiano, A., Mora, G., Buxó, L. & Carvalho, P. Spatial control of lipid droplet proteins by the ERAD ubiquitin ligase Doa10 . *EMBO J.* **35,** 1644–1655 (2016).

88. Kory, N., Thiam, A. R., Farese, R. V. & Walther, T. C. Protein Crowding Is a Determinant of Lipid Droplet Protein Composition. *Dev. Cell* **34,** 351–363 (2015).

89. Zimmermann, R., Eyrisch, S., Ahmad, M. & Helms, V. Protein translocation across the ER membrane. *Biochim. Biophys. Acta - Biomembr.* **1808,** 912–924 (2011).

90. Ahting, U., Thun, C., Hegerl, R., Typke, D., Nargang, F. E., Neupert, W. & Nussberger, S. The TOM core complex: The general protein import pore of the outer membrane of mitochondria. *J. Cell Biol.* **147,** 959–968 (1999).

91. Bauer, M. F., Hofmann, S., Neupert, W. & Brunner, M. Protein translocation intomitochondria: therole of TIM complexes. *Trends Cell Biol.* **10,** 25–31 (2000).

92. Wasilewski, M., Chojnacka, K. & Chacinska, A. Protein trafficking at the crossroads to mitochondria. *Biochim. Biophys. Acta - Mol. Cell Res.* **1864,** 125–137 (2017).

93. Cymer, F., Heijne, G. vono & White, S. H. Mechanisms of integral membrane protein insertion and folding. *J Mol Biol.* **427,** 999–1022 (2015).

94. Schuldiner, M., Metz, J., Schmid, V., Denic, V., Rakwalska, M., Schmitt, H. D., Schwappach, B. & Weissman, J. S. The GET Complex Mediates Insertion of Tail-Anchored Proteins into the ER Membrane. *Cell* **134,** 634–645 (2008).

95. Mayerhofer, P. U. Targeting and insertion of peroxisomal membrane proteins: ER trafficking versus direct delivery to peroxisomes. *Biochim. Biophys. Acta - Mol. Cell Res.* **1863,** 870–880 (2016).

96. Schrul, B. & Kopito, R. R. Peroxin-dependent targeting of a lipid-droplet-destined membrane protein to ER subdomains. *Nat. Cell Biol.* **18,** 740–51 (2016).

97. Stenmark, H. Rab GTPases as coordinators of vesicle traffic. *Nat. Publ. Gr.* **10,** 513–525 (2009).

98. Bonifacino, J. S. & Glick, B. S. The Mechanisms of Vesicle Budding and Fusion. *Cell* **116,** 153–166 (2004).

99. Derby, M. C. & Gleeson, P. A. New Insights into Membrane Trafficking and Protein Sorting. *Int. Rev. Cytol.* **261,** 47–116 (2007).

100. Whyte, J. R. C. & Munro, S. Vesicle tethering complexes in membrane traffic. *J. Cell Sci.* **115,** 2627–2637 (2002).

101. Jensen, D. & Schekman, R. COPII-mediated vesicle formation at a glance. *J. Cell Sci.* **124,** 1–4 (2011).

102. Memon, A. R. The role of ADP-ribosylation factor and SAR1 in vesicular trafficking in plants. *Biochim. Biophys. Acta - Biomembr.* **1664,** 9–30 (2004).

103. Beck, R., Ravet, M., Wieland, F. T. & Cassel, D. The COPI system: Molecular mechanisms and function. *FEBS Lett.* **583,** 2701–2709 (2009).

104. Hehnly, H. & Stamnes, M. Regulating cytoskeleton-based vesicle motility. *FEBS Lett.* **581,** 2112–2118 (2007).

105. Spang, A. Membrane tethering complexes in the endosomal system. *Front. Cell Dev. Biol.* **4,** 1–7 (2016).

106. Hong, W. SNAREs and traffic. *Biochim. Biophys. Acta* **1744,** 493–517 (2005).

107. Ungar, D. & Hughson, F. M. SNARE Protein Structure and Function. *Annu. Rev. Cell Dev. Biol.* **19,** 493–517 (2003).

108. Fasshauer, D. Structural insights into the SNARE mechanism. *Biochim. Biophys. Acta - Mol. Cell Res.* **1641,** 87–97 (2003).

109. Littleton, J. T., Barnard, R. J. O., Titus, S. A., Slind, J., Chapman, E. R. & Ganetzky, B. SNARE-complex disassembly by NSF follows synaptic-vesicle fusion. *Proc. Natl. Acad. Sci. U. S. A.* **98,** 12233–12238 (2001).

110. Baker, R. W. & Hughson, F. M. Chaperoning SNARE assembly and disassembly. *Nat. Rev. Mol. Cell Biol.* **17,** 465–479 (2016).

111. Kuner, T., Li, Y., Gee, K. R., Bonewald, L. F. & Augustine, G. J. Photolysis of a caged peptide reveals rapid action of N-ethylmaleimide sensitive factor before neurotransmitter release. *Proc. Natl. Acad. Sci. U. S. A.* **105,** 347–352 (2008).

112. Scales, S. J., Chen, Y. A., Yoo, B. Y., Patel, S. M., Doung, Y. C. & Scheller, R. H. SNAREs contribute to the specificity of membrane fusion. *Neuron* **26,** 457–464 (2000).

113. Parlati, F., Varlamov, O., Paz, K., McNew, J. A., Hurtado, D., Söllner, T. H. & Rothman, J. E. Distinct SNARE complexes mediating membrane fusion in Golgi transport based on combinatorial specificity. *Proc. Natl. Acad. Sci. U. S. A.* **99,** 5424–5429 (2002).

114. Stenmark, H. Rab GTPases as coordinators of vesicle traffic. *Nat. Rev. Mol. Cell Biol.* **10,** 513–525 (2009).

115. Grosshans, B. L., Ortiz, D. & Novick, P. Rabs and their effectors: Achieving specificity in membrane traffic. *Proc. Natl. Acad. Sci. U. S. A.* **103,** 11821–11827 (2006).

116. Grippa, A., Buxo, L., Mora, G., Funaya, C., Idrissi, F. Z., Mancuso, F., Gomez, R., Muntanyï¿½, J., Sabidï¿½, E. & Carvalho, P. The seipin complex Fld1/Ldb16 stabilizes ER-lipid droplet contact sites. *J. Cell Biol.* **211,** 829–844 (2015).

117. Guo, Y., Walther, T. C., Rao, M., Stuurman, N., Goshima, G., Terayama, K., Wong, J. S., Vale, R. D., Walter, P. & Farese, R. V. Functional genomic screen reveals genes involved in lipid-droplet formation and utilization. *Nature* **453,** 657–61 (2008).

118. Thiam, A. R., Antonny, B., Wang, J., Delacotte, J., Wilfling, F., Walther, T. C., Beck, R., Rothman, J. E. & Pincet, F. COPI buds 60-nm lipid droplets from reconstituted water-phospholipid-triacylglyceride interfaces, suggesting a tension clamp function. *Proc. Natl. Acad. Sci. U. S. A.* **110,** 13244–13249 (2013).

119. M. Beller, C. Sztalryd, N. Southall, et al. COPI Complex Is a Regulator of Lipid Homeostasis. *PLoS Biol.* **6,** 2530–2549 (2008).

120. Soni, K. G., Mardones, G. a, Sougrat, R., Smirnova, E., Jackson, C. L. & Bonifacino, J. S.

Coatomer-dependent protein delivery to lipid droplets. *J. Cell Sci.* **122,** 1834–1841 (2009).

121. Fei, W., Shui, G., Zhang, Y., Krahmer, N., Ferguson, C., Kapterian, T. S., Lin, R. C., Dawes, I. W., Brown, A. J., Li, P., Huang, X., Parton, R. G., Wenk, M. R., Walther, T. C. & Yang, H. A role for phosphatidic acid in the formation of 'supersized' Lipid droplets. *PLoS Genet.* **7,** (2011).

122. Wolinski, H., Hofbauer, H. F., Hellauer, K., Cristobal-Sarramian, A., Kolb, D., Radulovic, M., Knittelfelder, O. L., Rechberger, G. N. & Kohlwein, S. D. Seipin is involved in the regulation of phosphatidic acid metabolism at a subdomain of the nuclear envelope in yeast. *Biochim. Biophys. Acta - Mol. Cell Biol. Lipids* **1851,** 1450–1464 (2015).

123. Han, S., Binns, D. D., Chang, Y. F. & Goodman, J. M. Dissecting seipin function: The localized accumulation of phosphatidic acid at ER/LD junctions in the absence of seipin is suppressed by Sei1pΔNterm only in combination with Ldb16p. *BMC Cell Biol.* **16,** 1–13 (2015).

124. Xu, Y., Mak, H. Y., Lukmantara, I., Li, Y. E., Hoehn, K. L., Huang, X., Du, X. & Yang, H. CDP-DAG synthase 1 and 2 regulate lipid droplet growth through distinct mechanisms. *J. Biol. Chem.* **294,** 16740–16755 (2019).

125. Yamashita, A., Hayashi, Y., Matsumoto, N., Nemoto-Sasaki, Y., Oka, S., Tanikawa, T. & Sugiura, T. Glycerophosphate/Acylglycerophosphate Acyltransferases. *Biology (Basel).* **3,** 801–830 (2014).

126. Yu, J., Loh, K., Song, Z. Y., Yang, H. Q., Zhang, Y. & Lin, S. Update on glycerol-3-phosphate acyltransferases: The roles in the development of insulin resistance. *Nutr. Diabetes* **8,** (2018).

127. Vance, J. E. Phospholipid Synthesis and Transport in Mammalian Cells. *Traffic* **16,** 1–18 (2015).

128. Piccolis, M., Bond, L. M., Kampmann, M., Pulimeno, P., Chitraju, C., Jayson, C. B. K., Vaites, L. P., Boland, S., Lai, Z. W., Gabriel, K. R., Elliott, S. D., Paulo, J. A., Harper, J. W., Weissman, J. S., Walther, T. C. & Farese, R. V. Probing the Global Cellular Responses to Lipotoxicity Caused by Saturated Fatty Acids. *Mol. Cell* **74,** 32–44.e8 (2019).

129. Zhu, X. G., Nicholson Puthenveedu, S., Shen, Y., La, K., Ozlu, C., Wang, T., Klompstra, D., Gultekin, Y., Chi, J., Fidelin, J., Peng, T., Molina, H., Hang, H. C., Min, W. & Birsoy, K. CHP1 Regulates Compartmentalized Glycerolipid Synthesis by Activating GPAT4. *Mol. Cell* **74,** 45–58.e7 (2019).

130. Chitraju, C., Mejhert, N., Haas, J. T., Diaz-Ramirez, L. G., Grueter, C. A., Imbriglio, J. E., Pinto, S., Koliwad, S. K., Walther, T. C. & Farese, R. V. Triglyceride Synthesis by DGAT1 Protects Adipocytes from Lipid-Induced ER Stress during Lipolysis. *Cell Metab.* **26,** 407–418.e3 (2017).

131. Pagac, M., Cooper, D. E., Qi, Y., Lukmantara, I. E., Mak, H. Y., Wu, Z., Tian, Y., Liu, Z., Lei, M., Du, X., Ferguson, C., Kotevski, D., Sadowski, P., Chen, W., Boroda, S., *et al.* SEIPIN Regulates Lipid Droplet Expansion and Adipocyte Development by Modulating the Activity of Glycerol-3-phosphate Acyltransferase. *Cell Rep.* **17,** 1546–1559 (2016).

132. Cao, J., Li, J. A., Li, D., Tobin, J. F. & Gimeno, R. E. Molecular identification of microsomal acyl-CoA:glycerol-3-phosphate acyltransferase, a key enzyme in de novo triacylglycerol synthesis. *Proc. Natl. Acad. Sci. U. S. A.* **103,** 19695–19700 (2006).

133. Nagle, C. A., Vergnes, L., DeJong, H., Wang, S., Lewin, T. M., Reue, K. & Coleman, R. A. Identification of a novel sn-glycerol-3-phosphate acyltransferase isoform, GPAT4, as the enzyme deficient in Agpat6 −/− mice. *J. Lipid Res.* **49,** 823–831 (2008).

134. Cao, J., Perez, S., Goodwin, B., Lin, Q., Peng, H., Qadri, A., Zhou, Y., Clark, R. W., Perreault, M., Tobin, J. F. & Gimeno, R. E. Mice deleted for GPAT3 have reduced GPAT activity in white adipose tissue and altered energy and cholesterol homeostasis in diet-induced obesity. *Am. J. Physiol. - Endocrinol. Metab.* **306,** 1176–1187 (2014).

135. Vergnes, L., Beigneux, A. P., Davis, R., Watkins, S. M., Young, S. G. & Reue, K. Agpat6

deficiency causes subdermal lipodystrophy and resistance to obesity. *J. Lipid Res.* **47,** 745–54 (2006).

136. Shan, D., Li, J. L., Wu, L., Li, D., Hurov, J., Tobin, J. F., Gimeno, R. E. & Cao, J. GPAT3 and GPAT4 are regulated by insulin-stimulated phosphorylation and play distinct roles in adipogenesis. *J. Lipid Res.* **51,** 1971–1981 (2010).

137. Romeo, S., Kozlitina, J., Xing, C., Pertsemlidis, A., Cox, D., Pennacchio, L. A., Boerwinkle, E., Cohen, J. C. & Hobbs, H. H. Genetic variation in PNPLA3 confers susceptibility to nonalcoholic fatty liver disease. *Nat. Genet.* **40,** 1461–1465 (2008).

138. Trépo, E., Romeo, S., Zucman-Rossi, J. & Nahon, P. PNPLA3 gene in liver diseases. *J. Hepatol.* **65,** 399–412 (2016).

139. Huang, Y., Cohen, J. C. & Hobbs, H. H. Expression and characterization of a PNPLA3 protein isoform (I148M) associated with nonalcoholic fatty liver disease. *J. Biol. Chem.* **286,** 37085–37093 (2011).

140. BasuRay, S., Wang, Y., Smagris, E., Cohen, J. C. & Hobbs, H. H. Accumulation of PNPLA3 on lipid droplets is the basis of associated hepatic steatosis. *Proc. Natl. Acad. Sci. U. S. A.* **116,** 9521–9526 (2019).

141. Yang, A., Mottillo, E. P., Mladenovic-lucas, L., Zhou, L. & Granneman, J. G. Dynamic interactions of ABHD5 with PNPLA3 regulate triacylglycerol metabolism in brown adipocytes. *Nat. Metab.* **1,** (2019).

142. Abul-Husn, N. S., Cheng, X., Li, A. H., Xin, Y., Schurmann, C., Stevis, P., Liu, Y., Kozlitina, J., Stender, S., Wood, G. C., Stepanchick, A. N., Still, M. D., McCarthy, S., O'Dushlaine, C., Packer, J. S., *et al.* A protein-truncating HSD17B13 variant and protection from chronic liver disease. *N. Engl. J. Med.* **378,** 1096–1106 (2018).

143. Hilborn, E., Stål, O. & Jansson, A. Estrogen and androgen-converting enzymes 17β-hydroxysteroid dehydrogenase and their involvement in cancer: With a special focus on 17β-hydroxysteroid dehydrogenase type 1, 2, and breast cancer. *Oncotarget* **8,** 30552–30562 (2017).

144. Adam, M., Heikelä, H., Sobolewski, C., Portius, D., Mäki-Jouppila, J., Mehmood, A., Adhikari, P., Esposito, I., Elo, L. L., Zhang, F. P., Ruohonen, S. T., Strauss, L., Foti, M. & Poutanen, M. Hydroxysteroid (17β) dehydrogenase 13 deficiency triggers hepatic steatosis and inflammation in mice. *FASEB J.* **32,** 3434–3447 (2018).

145. Su, W., Mao, Z., Liu, Y., Zhang, X., Zhang, W., Gustafsson, J. A. & Guan, Y. Role of HSD17B13 in the liver physiology and pathophysiology. *Mol. Cell. Endocrinol.* **489,** 119–125 (2019).

146. Bard, F., Casano, L., Mallabiabarrena, A., Wallace, E., Saito, K., Kitayama, H., Guizzunti, G., Hu, Y., Wendler, F., DasGupta, R., Perrimon, N. & Malhotra, V. Functional genomics reveals genes involved in protein secretion and Golgi organization. *Nature* **439,** 604–607 (2006).

147. Bassaganyas, L., Popa, S. J., Horlbeck, M., Puri, C., Stewart, S. E., Campelo, F., Ashok, A., Butnaru, C. M., Brouwers, N., Heydari, K., Ripoche, J., Weissman, J., Rubinsztein, D. C., Schekman, R., Malhotra, V., Moreau, K. & Villeneuve, J. New factors for protein transport identified by a genome-wide CRISPRi screen in mammalian cells. *J. Cell Biol.* **218,** 3861–3879 (2019).

148. Rabouille, C. & Kondylis, V. TANGOing along the protein secretion pathway. *Genome Biol.* **7,** (2006).

149. Mejhert, N., Kuruvilla, L., Gabriel, K. R., Elliott, S. D., Guie, M. A., Wang, H., Lai, Z. W., Lane, E. A., Christiano, R., Danial, N. N., Farese, R. V. & Walther, T. C. Partitioning of MLX-Family Transcription Factors to Lipid Droplets Regulates Metabolic Gene Expression. *Mol. Cell* **77,** 1251–1264.e9 (2020).

150. Mohr, S. E. & Perrimon, N. RNAi screening: New approaches, understandings, and organisms. *Wiley Interdiscip. Rev. RNA* **3,** 145–158 (2012).

151. Mohr, S. E. RNAi screening in Drosophila cells and in vivo. *Methods* **68,** 82–88 (2014).

152. Heigwer, F., Port, F. & Boutros, M. Rna interference (RNAi) screening in Drosophila. *Genetics* **208,** 853–874 (2018).

153. Gu, Z., Cavalcanti, A., Chen, F. C., Bouman, P. & Li, W. H. Extent of gene duplication in the genomes of Drosophila, nematode, and yeast. *Mol. Biol. Evol.* **19,** 256–262 (2002).

154. Vinayagam, A., Hu, Y., Kulkarni, M., Roesel, C., Sopko, R., Mohr, S. E. & Perrimon, N. Protein complex-based analysis framework for high-throughput data sets. *Sci. Signal.* **6,** 1–12 (2013).

155. Eden, E., Navon, R., Steinfeld, I., Lipson, D. & Yakhini, Z. GOrilla: A tool for discovery and visualization of enriched GO terms in ranked gene lists. *BMC Bioinformatics* **10,** 1–7 (2009).

156. Li, C. & Yu, S. S. B. Rab proteins as regulators of lipid droplet formation and lipolysis. *Cell Biol. Int.* **40,** 1026–1032 (2016).

157. Barrowman, J., Bhandari, D., Reinisch, K. & Ferro-Novick, S. TRAPP complexes in membrane traffic: Convergence through a common Rab. *Nat. Rev. Mol. Cell Biol.* **11,** 759–763 (2010).

158. Cai, H., Yu, S., Menon, S., Cai, Y., Lazarova, D., Fu, C., Reinisch, K., Hay, J. C. & Ferro-Novick, S. TRAPPI tethers COPII vesicles by binding the coat subunit Sec23. *Nature* **445,** 941–944 (2007).

159. Thomas, L. L., Joiner, A. M. N. & Fromme, J. C. The TRAPPI II complex activates the GTPase Ypt1 (Rab1) in the secretory pathway. *J. Cell Biol.* **217,** 283–298 (2017).

160. Tagaya, M., Arasaki, K., Inoue, H. & Kimura, H. Moonlighting functions of the NRZ (mammalian Dsl1) complex. *Front. Cell Dev. Biol.* **2,** 1–9 (2014).

161. Wainman, A., Giansanti, M. G., Goldberg, M. L. & Gatti, M. The Drosophila RZZ complex - roles in membrane trafficking and cytokinesis. *J. Cell Sci.* **125,** 4014–4025 (2012).

162. Gillingham, A. K. & Munro, S. Long coiled-coil proteins and membrane traffic. *Biochim. Biophys. Acta - Mol. Cell Res.* **1641,** 71–85 (2003).

163. Yamaguchi, T., Omatsu, N., Morimoto, E., Nakashima, H., Ueno, K., Tanaka, T., Satouchi, K., Hirose, F. & Osumi, T. CGI-58 facilitates lipolysis on lipid droplets but is not involved in the vesiculation of lipid droplets caused by hormonal stimulation. *J. Lipid Res.* **48,** 1078–1089 (2007).

164. Monetta, P., Slavin, I., Romero, N. & Alvarez, C. Rab1b Interacts with GBF1 and Modulates both ARF1 Dynamics and COPI Association. *Mol. Biol. Cell* **18,** 2400–2410 (2007).

165. Reilly, B. A., Kraynack, B. A., VanRheenen, S. M. & Waters, M. G. Golgi-to-endoplasmic reticulum (ER) retrograde traffic in yeast requires Dsl1p, a component of the ER target site that interacts with a COPI coat subunit. *Mol. Biol. Cell* **12,** 3783–3796 (2001).

166. Jayson, C. B. K., Arlt, H., Fischer, A. W., Weng Lai, Z., Farese, R. V. & Walther, T. C. Rab18 is not necessary for lipid droplet biogenesis or turnover in human mammary carcinoma cells. *Mol. Biol. Cell* **29,** 2045–2054 (2018).

167. Li, C., Luo, X., Zhao, S., Siu, G. K., Liang, Y., Chan, H. C., Satoh, A. & Yu, S. S. COPI–TRAPPII activates Rab18 and regulates its lipid droplet association. *EMBO J.* e201694866 (2016). doi:10.15252/embj.201694866

168. Taussig, D., Lipatova, Z., Kim, J. J., Zhang, X. & Segev, N. Trs20 is Required for TRAPP II Assembly. *Traffic* **14,** 678–690 (2013).

169. Andag, U., Neumann, T. & Schmitt, H. D. The Coatomer-interacting Protein Dsl1p Is Required for

Golgi-to-Endoplasmic Reticulum Retrieval in Yeast. *J. Biol. Chem.* **276,** 39150–39160 (2001).

170. Hu, C., Ahmed, M. & Melia, T. J. Fusion of Cells by Flipped SNAREs. *Science (80-.).* **1745,** 1745–1750 (2009).

171. Xu, Y., Zhang, F., Su, Z., McNew, J. A. & Shin, Y. K. Hemifusion in SNARE-mediated membrane fusion. *Nat. Struct. Mol. Biol.* **12,** 417–422 (2005).

172. Giraudo, C. G., Hu, C., You, D., Slovic, A. M., Mosharov, E. V., Sulzer, D., Melia, T. J. & Rothman, J. E. SNAREs can promote complete fusion and hemifusion as alternative outcomes. *J. Cell Biol.* **170,** 249–260 (2005).

173. Olzmann, J. A., Richter, C. M. & Kopito, R. R. Spatial regulation of UBXD8 and p97 / VCP controls ATGL-mediated lipid droplet turnover. **8,** (2012).

174. Hutagalung, A. & Novick, P. Role of Rab GTPases in Membrane Traffic and Cell Physiology. *Physiol Rev* **91,** 119–149 (2011).

175. Castro, I. G., Eisenberg-Bord, M., Persiani, E., Rochford, J. J., Schuldiner, M. & Bohnert, M. Promethin Is a Conserved Seipin Partner Protein. *Cells* **8,** 268 (2019).

176. Eisenberg-Bord, M., Mari, M., Weill, U., Rosenfeld-Gur, E., Moldavski, O., Castro, I. G., Soni, K. G., Harpaz, N., Levine, T. P., Futerman, A. H., Reggiori, F., Bankaitis, V. A., Schuldiner, M. & Bohnert, M. Identification of seipin-linked factors that act as determinants of a lipid droplet subpopulation. *J. Cell Biol.* **217,** 269–282 (2018).

177. Krogh, A., Larsson, B., Von Heijne, G. & Sonnhammer, E. L. L. Predicting transmembrane protein topology with a hidden Markov model: Application to complete genomes. *J. Mol. Biol.* **305,** 567–580 (2001).

178. Hofmann, K. & Stoffel, W. TMbase-a database of membrane spanning proteins segments. *Biol. Chem.* (1993).

179. Almagro Armenteros, J. J., Tsirigos, K. D., Sønderby, C. K., Petersen, T. N., Winther, O., Brunak, S., von Heijne, G. & Nielsen, H. SignalP 5.0 improves signal peptide predictions using deep neural networks. *Nat. Biotechnol.* **37,** 420–423 (2019).

180. Hu, Y., Flockhart, I., Vinayagam, A., Bergwitz, C., Berger, B., Perrimon, N. & Mohr, S. E. An integrative approach to ortholog prediction for disease-focused and other functional studies. *BMC Bioinformatics* **12,** (2011).

181. Söding, J., Biegert, A. & Lupas, A. N. The HHpred interactive server for protein homology detection and structure prediction. *Nucleic Acids Res.* **33,** 244–248 (2005).

182. Liu, X., Yin, Y., Wu, J. & Liu, Z. Structure and mechanism of an intramembrane liponucleotide synthetase central for phospholipid biosynthesis. *Nat. Commun.* **5,** 1–10 (2014).

183. Ben-Aroya, S., Coombes, C., Kwok, T., O'Donnell, K. A., Boeke, J. D. & Hieter, P. Toward a Comprehensive Temperature-Sensitive Mutant Repository of the Essential Genes of Saccharomyces cerevisiae. *Mol. Cell* **30,** 248–258 (2008).

184. Vaden, D. L., Gohil, V. M., Gu, Z. & Greenberg, M. L. Separation of yeast phospholipids using one-dimensional thin-layer chromatography. *Anal. Biochem.* **338,** 162–164 (2005).

185. Tamura, Y., Harada, Y., Nishikawa, S. I., Yamano, K., Kamiya, M., Shiota, T., Kuroda, T., Kuge, O., Sesaki, H., Imai, K., Tomii, K. & Endo, T. Tam41 is a CDP-diacylglycerol synthase required for cardiolipin biosynthesis in mitochondria. *Cell Metab.* **17,** 709–718 (2013).

186. Yang, X., Liang, J., Ding, L., Li, X., Lam, S. M., Shui, G., Ding, M. & Huang, X. Phosphatidylserine synthase regulates cellular homeostasis through distinct metabolic mechanisms. *PLoS Genet.* **15,** 1–23 (2019).

187. Helsley, R. N., Varadharajan, V., Brown, A. L., Gromovsky, A. D., Schugar, R. C., Ramachandiran, I., Fung, K., Kabbany, M. N., Banerjee, R., Neumann, C., Finney, C., Pathak, P., Orabi, D., Osborn, L. J., Massey, W., *et al.* Obesity-linked suppression of membrane-bound o-acyltransferase 7 (MBOAT7) drives non-alcoholic fatty liver disease. *Elife* **8,** 1–69 (2019).

188. Du, X., Zhou, L., Aw, Y. C., Mak, H. Y., Xu, Y., Rae, J., Wang, W., Zadoorian, A., Hancock, S. E., Osborne, B., Chen, X., Wu, J. W., Turner, N., Parton, R. G., Li, P. & Yang, H. ORP5 localizes to ER-lipid droplet contacts and regulates the level of PI(4)P on lipid droplets. *J. Cell Biol.* **219,** 1–16 (2020).

189. Rual, J. F., Venkatesan, K., Hao, T., Hirozane-Kishikawa, T., Dricot, A., Li, N., Berriz, G. F., Gibbons, F. D., Dreze, M., Ayivi-Guedehoussou, N., Klitgord, N., Simon, C., Boxem, M., Milstein, S., Rosenberg, J., *et al.* Towards a proteome-scale map of the human protein-protein interaction network. *Nature* **437,** 1173–1178 (2005).

190. Rolland, T., Taşan, M., Charloteaux, B., Pevzner, S. J., Zhong, Q., Sahni, N., Yi, S., Lemmens, I., Fontanillo, C., Mosca, R., Kamburov, A., Ghiassian, S. D., Yang, X., Ghamsari, L., Balcha, D., *et al.* A proteome-scale map of the human interactome network. *Cell* **159,** 1212–1226 (2014).

191. Yang, J. & Zhang, Y. I-TASSER server: New development for protein structure and function predictions. *Nucleic Acids Res.* **43,** W174–W181 (2015).

192. Kwon, H. J., Abi-Mosleh, L., Wang, M. L., Deisenhofer, J., Goldstein, J. L., Brown, M. S. & Infante, R. E. Structure of N-Terminal Domain of NPC1 Reveals Distinct Subdomains for Binding and Transfer of Cholesterol. *Cell* **137,** 1213–1224 (2009).

193. Gong, X., Qian, H., Zhou, X., Wu, J., Wan, T., Cao, P., Huang, W., Zhao, X., Wang, X., Wang, P., Shi, Y., Gao, G. F., Zhou, Q. & Yan, N. Structural insights into the Niemann-Pick C1 (NPC1)-mediated cholesterol transfer and ebola infection. *Cell* **165,** 1467–1478 (2016).

194. Pfeffer, S. R. NPC intracellular cholesterol transporter 1 (NPC1)-mediated cholesterol export from lysosomes. *J. Biol. Chem.* **294,** 1706–1709 (2019).

195. Liu, Y., Wang, W., Shui, G. & Huang, X. CDP-Diacylglycerol Synthetase Coordinates Cell Growth and Fat Storage through Phosphatidylinositol Metabolism and the Insulin Pathway. *PLoS Genet.* **10,** (2014).

196. Ballweg, S., Sezgin, E., Doktorova, M., Covino, R., Reinhard, J., Wunnicke, D., Hänelt, I., Levental, I., Hummer, G. & Ernst, R. Regulation of lipid saturation without sensing membrane fluidity. *Nat. Commun.* **11,** 756 (2020).

197. Lopez, E., Callier, P., Cormier-Daire, V., Lacombe, D., Moncla, A., Bottani, A., Lambert, S., Goldenberg, A., Doray, B., Odent, S., Sanlaville, D., Gueneau, L., Duplomb, L., Huet, F., Aral, B., Thauvin-Robinet, C. & Faivre, L. Search for a gene responsible for Floating-Harbor syndrome on chromosome 12q15q21.1. *Am. J. Med. Genet. Part A* **158 A,** 333–339 (2012).

198. Yu, Y., Zuo, X., He, M., Gao, J., Fu, Y., Qin, C., Meng, L., Wang, W., Song, Y., Cheng, Y., Zhou, F., Chen, G., Zheng, X., Wang, X., Liang, B., *et al.* Genome-wide analyses of non-syndromic cleft lip with palate identify 14 novel loci and genetic heterogeneity. *Nat. Commun.* **8,** 1–11 (2017).

199. Sanderson, C. M., Connel, J. W., Edwards, T. L., Bright, N. A., Duley, S., Thompson, A., Luzio, J. P. & Reid, E. Spastin and atlastin, two proteins mutated in autosomal-dominant hereditary spastic paraplegia, are binding partners. *Hum. Mol. Genet.* **15,** 307–318 (2006).

200. Lin, P., Li, J., Liu, Q., Mao, F., Li, J., Qiu, R., Hu, H., Song, Y., Yang, Y., Gao, G., Yan, C., Yang, W., Shao, C. & Gong, Y. A Missense Mutation in SLC33A1, which Encodes the Acetyl-CoA Transporter, Causes Autosomal-Dominant Spastic Paraplegia (SPG42). *Am. J. Hum. Genet.* **83,** 752–759 (2008).

201. Housden, B. E., Hu, Y. & Perrimon, N. Design and generation of Drosophila single guide RNA

expression constructs. *Cold Spring Harb. Protoc.* **2016,** 782–788 (2016).

202. Housden, B. E. & Perrimon, N. Design and generation of donor constructs for genome engineering in Drosophila. *Cold Spring Harb. Protoc.* **2016,** 789–793 (2016).

203. Schindelin, J., Arganda-Carreras, I., Frise, E., Kaynig, V., Longair, M., Pietzsch, T., Preibisch, S., Rueden, C., Saalfeld, S., Schmid, B., Tinevez, J. Y., White, D. J., Hartenstein, V., Eliceiri, K., Tomancak, P. & Cardona, A. Fiji: An open-source platform for biological-image analysis. *Nat. Methods* **9,** 676–682 (2012).

204. Gluchowski, N. L., Gabriel, K. R., Chitraju, C., Bronson, R. T., Mejhert, N., Boland, S., Wang, K., Lai, Z. W., Farese, R. V. & Walther, T. C. Hepatocyte Deletion of Triglyceride-Synthesis Enzyme Acyl CoA: Diacylglycerol Acyltransferase 2 Reduces Steatosis Without Increasing Inflammation or Fibrosis in Mice. *Hepatology* **70,** 1972–1985 (2019).

205. González, M., Martín-Ruíz, I., Jiménez, S., Pirone, L., Barrio, R. & Sutherland, J. D. Generation of stable Drosophila cell lines using multicistronic vectors. *Sci. Rep.* **1,** (2011).